Fluid Flow and Heat Transfer in Porous Media Manufactured by a Space Holder Method

Thesis submitted in accordance with the requirements of the University of Liverpool for the degree of Doctor in Philosophy by

XIANKE LU

January 2020

Abstract

Porous metals are attracting growing attentions due to their unique properties such as light weight, high surface area, fluid permeability and good thermal conductivity, and a wide range of applications in many fields such as thermal management, chemical catalysis, energy absorption and filtration. In particular, as technology advances, the conventional cooling methods and components have become difficult to meet the rapidly growing cooling demand in modern electrical and electronic devices. Open-cell porous metals have been proven to be an ideal and effective cooling solution because of their excellent thermal and permeability properties. The Lost Carbonate Sintering (LCS) process, invented in the University of Liverpool, is an efficient and low cost manufacturing process to produce open-cell porous copper with controllable porosity, pore size and pore shape.

The heat transfer performance of porous metal is determined by three factors, identified as the thermal properties of the solid skeleton, the thermal properties of the fluid within the skeleton and the interactions between the solid and the fluid flow. Fluid flow behaviour in porous metal is also crucial when considering the heat transfer performance of porous metal. However, the flow behaviour in porous media and how it affects the heat transfer performance of the solid-fluid system have not been fully studied in the past.

The aim of this study is to understand the interactions between fluid flow and heat transfer in porous media. Four kinds of porous media, porous copper and porous glass with LCS structure, sintered copper and sintered glass, were manufactured. The fluid flow behaviour was visualized and the pressure drop was measured in the porous glass. Flow behaviour in sintered glass was also studied to explore the commonality of the experimental results. The heat transfer performance such as heat transfer coefficient and thermal conductivity of porous copper with wide ranges of porosity and pore size was studied. Effect of flow regime on heat transfer performance of porous copper was evaluated.

Pressure drop in porous media was measured at a wide range of flow rate using a purpose-built apparatus. The relationship between pressure drop and flow velocity fitted well with the Forchheimer extended Darcy equation, from which four flow regimes, pre-Darcy, Darcy, Forchheimer and turbulent, were identified. The flow regime boundaries were different for each sample and also different from the porous media reported in previous studies. In sintered glass samples, the permeability increased and form drag coefficient decreased dramatically with increasing particle size. In porous samples, the permeability increased and form drag coefficient decreased with increasing porosity. The values of permeability and form drag coefficient depended on the flow regime in which they were calculated.

Flow visualization showed that the velocity magnitude distribution at the pore scale was similar to that in an open pipe flow, with the highest velocity located at the centre and gradually decreasing to zero towards the wall. Velocity profiles across a specific channel/pore were parabolic in the Darcy and Forchheimer regimes, and

became more uniform in the turbulent regime. Strong velocity fluctuations were located at the channel junctions in sintered glass samples and at the near wall region in porous glass samples with LCS structure. The critical Reynolds number identifying the transition from laminar to turbulent flow obtained by quantifying velocity fluctuations agrees well with the critical Reynolds number from Forchheimer to turbulent flow identified from the pressure drop measurements.

The thermal conductivity of porous copper was greatly affected by porosity and copper particle size, but was less affected by pore size. It decreases along a power law with porosity, with exponent around 2.3. For a given porosity, the porous copper with the copper particle size range of 45-70 μm had the highest thermal conductivity. Fluid in the porous copper also contributed to thermal conductivity through natural convection. For high porosity samples, the contribution could account for up to 50% of the total thermal conductivity.

The heat transfer performance of porous copper through natural convection and forced convection was characterised by measuring the heat transfer coefficient. Under natural convection, the heat transfer coefficient increased nearly linearly with temperature difference. For a given porosity, the porous copper with a pore size range of 700-1000 μm performed best. The effect of porosity on natural convective heat transfer performance was insignificant. Sample orientation also affected the heat transfer performance; orientating the larger surface on the horizontal plane increased the heat transfer coefficient by more than 10%. Under forced convection, there was an optimal porosity (around 0.65) for heat transfer performance at a given pore size and flow rate. The relationship between Nusselt number and Reynolds number can be divided into three sections, each of which followed a power func-

tion, $Nu = C_t Re^n$, where C_t and n are parameters constant for each section. The value of n was largely independent of porosity, except at the lowest porosity. The three sections broadly corresponded to the pre-Darcy, Darcy and non-Darcy regimes.

Acknowledgements

Primarily, I would first like to express my utmost gratitude to Professor Yuyuan Zhao and Dr. David Dennis for their supervision and invaluable support throughout the PhD programme. The way and attitude they do research will benefit me for the rest of my life.

I would also like to thank Dr. Liping Zhang for her help with my experiment and her guidance for overseas life. I will miss the delicious food she made in every Christmas holiday.

I'm also grateful to Mr. D. Atkinson for his assistance in sample preparation, advice on chemicals, optical microscope setup, discussions on structures and many other assistances.

I would also like to thank my colleague Dr. K. K. Diao for training me on machine operation and discussing the experiment results.

I wish to acknowledge the funding from the Chinese Scholarship Council and University of Liverpool.

Finally, I would like to show my deepest gratitude to my wife, Nan Niu, and my family. I will use the rest of my life to repay their eternal support and understanding. I wish my lovely daughter, Anna, a healthy and happy growth.

Publications

Lu, Xianke, and Yuyuan Zhao. "Effect of flow regime on convective heat transfer in porous copper manufactured by lost carbonate sintering." International Journal of Heat and Fluid Flow 80 (2019): 108482.

Lu, Xianke, Yuyuan Zhao, and David JC Dennis. "Flow measurements in microporous media using micro-particle image velocimetry." Physical Review Fluids 3.10 (2018): 104202.

Contents

List of Figures

List of Tables

Nomenclature

List of Symbols

A	Cross-sectional area	m^2
A	Parameter in Eq. 4.3	
a	Constant in Eq. 2.4	
B	Parameter in Eq. 4.3	
b	Constant in Eq. 2.4	
C	Form drag coefficient	m^{-1}
c, c_p	specific heat	J/KKg
c_a	Acceleration coefficient	
c_F	inertial coefficient	
C_T	Correlation parameter in Eq. 2.17	
D	Diameter	m
d	Distance	m
D_m	Mean diameter	m

f	Friction factor	
h	Convective heat transfer coefficient	kW/m^2K
h_f	Heat transfer coefficient under forced convection	kW/m^2K
h_n	Heat transfer coefficient under natural convection	kW/m^2K
J	Heat transfer rate	W
K	Permeability	m^2
L	Distance	m
M	Mass	Kg
n	Correlation parameter in Eq. 2.17	
Nu	Nusselt number	
P	Pressure	kPa
Pr	Prandtl number	
Ra	Rayleigh number	
Re	Reynolds number	
s_v	Surface area per unit volume	m^{-1}
T	Temperature	$^oC, K$
u	Velocity component in x direction	m/s
U'	Local velocity fluctuation intensity ($= \sqrt{u'^2 + v'^2}/\bar{U}$)	
u'	Velocity fluctuation in x direction	m/s

V	Darcy velocity	m/s
v	Velocity component in y direction	m/s
v'	Velocity fluctuation in y direction	m/s
V_i	Interstitial velocity, $= \frac{V}{\epsilon}$	m/s
Vm	Volume	m^3
$\bar{U}$	Local averaged velocity magnitude $(= \sqrt{\bar{u}^2 + \bar{v}^2})$	m/s
$\bar{u}$	Time averaged velocity component in x direction	m/s
$\bar{v}$	Time averaged velocity component in y direction	m/s

Greek symbols

α_m	Thermal diffusivity of porous medium	m^2/s
β	Thermal volume expansion coefficient	K^{-1}
ϵ	Porosity	
κ	Kozeny-Carman constant	
λ	Effective thermal conductivity	W/mK
μ, μ_b, μ_w	Viscosity	Pas
ρ	Density	Kg/m^3

Subscript

Agent	Pore agent (space holder)
amb	Ambient

b Bottom

c Critical

cof Contribution of fluid

Cu copper

$Cu - f$ Porous Cu - fluid

D Darcy regime

f fluid

g Glass sphere

in Inlet

ND Non-Darcy regime

t Top

TD Transition to Darcy regime

TN Transition to non-Darcy regime

v Vacuum

Chapter 1

Introduction

Porous metals are attracting more and more attentions in many engineering fields such as heat exchange, sound insulation, catalyst, mechanical damping and shock wave buffer, due to their unique thermal, acoustic, chemical, mechanical properties and special structure (Gibson & Ashby 1999, Ashby et al. 2000, Banhart 2001). Open-cell porous metals, in particularly, have proven to be a competitive candidate to substitute traditional component in compact heat exchangers, due to their high surface area and superior thermophysical properties, together with permeability for fluid flow. Heat transfer performance of porous metals depends greatly on the structural properties and fluid flow behaviour in the porous structure. The present study focuses on the visualization of porous flow in porous media and heat transfer performance of porous copper produced by Lost Carbonate Sintering (LCS) under natural and forced convections.

1.1 Background and motivation of research

Heat dissipation is a new challenge facing the developments of technologies in various fields. Traditionally used heat dissipation methods and heat sinks are difficult to meet the requirements of modern devices. For example, ten years ago, heat dissipation of cell phone was by heat conduction to transfer heat from the chip to the surface of the phone. The designer did not need to consider the heat dissipation of the cell phone because the heat was too little to be noticed. But today, the high demand for more powerful and more compact cell phones has led to high amounts of heat generated at the chip level. The heat could lead to damage to the chip and decrease of the phone's performance if the heat is not removed in time. Another example is the heat dissipation of LED lamp beads, which have been widely used in daily life as they have multiple advantages such as compact size, low energy consumption and long life. A high power LED lamp can easily heat the ambient temperature to over one hundred degrees and this can be destructive to other components close to it. As a consequence, the demand for effective cooling techniques has increased dramatically over the recent years. Porous metals are one of the promising effective cooling solutions due to their superior thermophysical characteristics and good mechanical properties.

Several methods for manufacturing porous metals have been invented in the past few decades. The simplest and most popular method is by powder metallurgy through sintering metallic particles together without using space holders. This method was only able to produce sintered packed beds with a low and narrow porosity range (below 0.5) (Zhang et al. 2009). Another method used to produce porous metals is investment casting, which has been commercially used in industry. Investment

casting involves using a prefabricated ceramic template as mould to cast the porous metal. This route can produce porous metals of excellent quality and with a high and narrow porosity range (above 0.8) (Zhang et al. 2009). However, the cost of investment casting is extremely high because the process needs to be operated under high temperature and requires special equipment. Neither of the porous metals produced by these two methods is suitable for heat exchanger, because packed beds are not very permeable for fluid flow due to low porosity, while the porous metals produced by investment casting have poor thermal conductivity due to high porosity. Porous metals with porosity in the range of 0.5 to 0.8 are good for heat exchanger, but they are rarely reported in the literature.

The Lost Carbonate Sintering (LCS) process, which was invented by Zhao and his colleagues (Zhao, Fung, Zhang & Zhang 2005), is found to be an excellent method for manufacturing porous metals with controlled pore size, porosity and pore shape. This process uses metal powder and carbonate particles as raw materials. By mixing them uniformly with a binder and sintering the mixture at the solid state, porous metals such as aluminium, copper, nickel and steel can be achieved. Pores produced by this process have the same shape as the space holder particles, providing an easy way to control the pore shape. LCS has provided an efficient process by which porous metals with various pore sizes and a large range of porosity from 0.4 to 0.85 can be produced. Porous metals produced by this process have a higher permeability than packed beds and a higher thermal conductivity than the porous metals made by investment casting with the same material. Porous copper made by this method has been found to be a potential candidate for thermal management applications due to its large inner surface area, controllable porous structure and excellent mechanical properties (Xiao & Zhao 2013).

The high pressure drop of porous metal when fluid flow passes through it is a big concern. It has limited the applications of porous metals where high pressure cannot be achieved. The pressure drop is mainly produced by the large amount of inner surface area of porous metal, but it is also affected by other structural properties such as porosity, pore size, pore shape and the flow state within the porous metal. The relationship between pressure drop and velocity has been proved to be linear at low flow rates and nonlinear at high flow rates both in packed beds (Fand et al. 1987, Kececioglu & Jiang 1994) and in investment cast porous metals (Dukhan et al. 2014). These studies also found the existence of different flow regimes (pre-Darcy, Darcy, Forchhrimer and turbulent flow) in porous materials as flow rate varies. However, the pressure drop and flow behaviour in porous media made by the space holder methods have not been fully studied to date.

As a recent development of flow visualization techniques, micro particle image velocimetry (μ-PIV) becomes a powerful and effective tool to study the flow behaviour at micro scale. μ-PIV can obtain a large amount of flow information that cannot be obtained by pressure drop measurements, such as velocity distribution, statistical distribution and velocity fluctuation distribution, which are important for thermal transfer study and porous structure design. Unfortunately, experimental data on the visualization of fluid flow in complex structures (e.g. porous materials) is limited in literature because of the difficulties of such experiments, such as requirement for transparent samples, matched refractive index between solid and fluid and suitable seed particles. So far, research on visualization of porous flow has only been conducted in packed bed and within a narrow flow rate range. The flow behaviour in other porous structures such as LCS structure has not been studied before, and the

effect of structure characteristics on flow behaviour is not clear.

Although flow behaviour in porous structures and heat transfer performance of porous metals have been studied previously, the effect of flow behaviour on the heat transfer performance in porous metal is not well understood. This is because these two experiments have never been conducted simultaneously. In the present study, the flow behaviour in porous glass and sintered glass were studied by pressure drop measurements and μ-PIV measurements; pressure drop and forced convective heat transfer performance of porous copper were investigated. Natural convective heat transfer performance and the thermal conductivity of porous copper were also studied and the effects of porosity, pore size and natural convection were analysed.

1.2 Research aim and objectives

This project aims to establish a relationship between heat transfer performance and flow behaviour in porous media manufactured by the LCS process through measuring heat transfer coefficient of porous copper under forced convection and visualizing the flow in porous glass with the same structure.

The main objectives are:

- To fabricate porous copper by the LCS process and transparent porous media with same pore structure.
- To identify the flow regimes, visualize the flow behaviour and determine the velocity and fluctuation distributions at the pore scale in the transparent porous

media.

- To determine the flow regimes in porous copper and heat transfer performance of porous copper under forced convection.

- To determine the correlation between the heat transfer coefficient and flow behaviour in porous copper samples.

1.3 Structure of thesis

Chapter 2 reviews the literature on the relevant work in this field. Porous metal, including open-cell and closed-cell, is briefly introduced. The existing manufacture methods and the applications of porous metals are reviewed. Previous studies of hydrodynamics of porous media by pressure drop measurements and visualization methods are discussed. Thermal properties of porous metals including thermal conductivity, heat transfer performance under natural convection and forced convection are also reviewed.

Chapter 3 details the experimental procedures involved in this study, including the preparation of porous glass, porous copper, sinter copper and sintered glass, and experimental equipment and test procedure for flow behaviour and heat transfer performance investigations.

Chapter 4 presents and discusses the results obtained from the pressure drop measurements and μ-PIV measurements. It is composed of four sections, presenting results from sintered packed bed, porous glass with spherical pores, porous glass with irregular pores and porous copper, respectively. In each section, the pressure

drop, identification of different flow regimes, velocity distribution in pore scale and velocity fluctuations in porous structure are presented and discussed. At the end, the effects of structural characteristics (porosity, pore shape) on flow regime boundary, permeability, form drag coefficient and friction factor are discussed.

Chapter 5 mainly presents and discusses the results from the heat transfer experiments in porous copper. First, the thermal conductivity values of porous copper samples containing different fluids are presented and the effects of structural characteristics (porosity, pore size and copper particle size) and natural convection are discussed. Second, the heat transfer coefficient of LCS porous copper under natural convection is shown and the effects of structural characteristics (porosity and pore size) and temperature are discussed. Third, the heat transfer coefficient of LCS porous copper under forced convection is presented and the effects of porosity and flow rate are discussed. The effect of flow regime on the heat transfer coefficient is also discussed.

Chapter 6 summarises the findings in this project and presents recommendations for future work.

Chapter 2

Literature review

Porous metals are a new class of materials with low densities and novel physical, thermal and many other properties. Many approaches have been developed to achieve porous structures. In this chapter, the definition of porous metal, production methods and thermal applications are introduced. A detailed review on fluid flow behaviour when flow through porous media is provided. The thermal properties such as thermal conductivity, heat transfer performance under natural convection and forced convection of porous metals are described in details.

2.1 Introduction to porous metals

Porous metal, also known as metal foam, is made up of an interconnected network of solid metal struts or plates which form the edges and faces of pores or voids. Its density is lower than that of the bulk metal from which the solid struts are made due to the presence of pores. The pores can be either sealed or interconnected, depending on the production method. Porous metals can be classified into closed-cell

and open-cell from the point view of the connectivity of the pores. The pores in open-cell porous materials are interconnected, providing pathway for fluid flow and making them useful for heat exchanger applications. The pores in closed-cell porous metals are not connected and are separated by the solid struts. Closed-cell porous metals can be used as impact energy absorption box.

The unique physical and structural properties are one of the reasons why porous metals have attracted so much attention in engineering fields and are still receiving a growing interest in recent years. One of the most important parameters of porous metal is porosity (or relative density), i.e., the fraction of pores in a porous metal (the density of the porous material divided by the density of the solid from which the cell walls are made). Some metal foams, such as aluminium foam produced by template casting, have porosity as high as 0.95 (Ashby et al. 2000). In this thesis we are mainly concerned with porous copper and porous glass manufactured by the LCS method, which have a porosity between 0.5 and 0.85, and some sintered packed beds with a porosity around 0.4.

Pore structure is another important parameter of porous metals. The pore structure of porous metals ranges from the nearly perfectly ordered bee's honeycomb to disordered, three-dimensional networks of foams. The honeycombs are manufactured from metal and paper for use as the cores and panels. Most have cells which, like those of bee honeycombs, are hexagons, but they can also be made of square or triangular cells (Gibson & Ashby 1999). Cells in some other metal foams, such as the aluminium foam manufactured by the air bubbling method, have completely irregular shapes and different cell sizes. Likewise, the cell faces (solid struts) have different sizes and are distributed in various orientations.

So far, many techniques and processes have been developed to manufacture porous metal. Early production methods for metal foam are mainly based on the concepts of introducing air into solid metals. The most successful example of foaming and also the most mature commercial process, is obtained by injecting air into and mechanically agitating a mixture of molten aluminium and SiC particles. Another method is the solid forming process which usually refers to the powder metallurgy technique, where the metal powder can be sintered independently or mixed with a foaming agent (e.g. TiH_2). Recently, some other new production methods have been developed, such as electrodeposition, laser forming and self-propagation synthesis.

Porous metals are widely used in the engineering field either as a structural material or a functional material, or a combination of both. In recent years, a large number of porous metals based on different metallic materials, such as aluminium, copper, steel, magnesium, zinc and their alloys, have been exploited. So far, several commercially available porous metals, such as porous aluminium, porous nickel and porous copper, have been used in engineering applications.

2.2 Production techniques for porous metals

A range of manufacturing processes have been developed to achieve a wide variety of pore structures (closed-cell, open-cell, different pore sizes and porosities) and metal foams. Some of the common manufacturing processes are summarized and listed in Table. 2.1.

Table 2.1: Common manufacturing processes for porous metals.

Process	Relative cost	Pore size(mm)/porosity	Cell topology	Metal foamed
Melt gas injection	Low	5-20/0.9-0.97	Closed-cell	Al, Mg
Gas-releasing particle decomposition	Low	0.5-5/0.8-0.93	Closed-cell	Al
Casting using a template	Medium	1-5/0.85	Open-cell	Al, Mg, Ni-Cr, Stainless steel, Cu
Metal deposition on cellular preforms	High	0.01-0.3/0.95-0.98	Open-cell	Ni, Ti
Entrapped gas expansion	Medium-High	0.01-0.3/0.9-0.98	Closed-cell	Ti
Hollow sphere structures	High	0.1/0.95	Closed-/open-cell	Ni, Co, Ni-Cr
Casting of two materials	Low	0.01-10/0.5-0.7	Open-cell	Al
Gas-metal eutectic solidification	High	0.01-10/0.25-0.95	Closed-cell	Cu, Ni, Al
Space-holder	Low	0.05-1.5/0.5-0.85	Open-cell	Cu, Ni, Al, Steel, Ti

2.2.1 Melt gas injection

The melt gas injection process was developed simultaneously and independently by AlCAN and NORSK-HYDRO in the late 1990s (Surace et al. 2009). This process is normally used to manufacture porous aluminium alloys with closed cells. A variety of gases (CO_2, O_2, inert gases and even water vapour) can be used to create bubbles within liquid aluminium, but the gas bubbles created in the high density liquid melt rise to the surface due to the high buoyancy forces. Fine ceramic powders or alloying elements (e.g. SiC, Al_2O_3 and MgO) that form stabilising particles (5-15% wt) are often added to the melt before foaming to allow the ascension of the bubbles (Jin et al. 1991, Banhart & Baumeister 1998). Fig. 2.1 shows an example of aluminium foams produced by the gas injection technique.

Figure 2.1: Aluminium slabs of two different porosities and cell sizes produced by the gas injection method. (Banhart 2001).

The bubble size can be controlled by adjusting the gas flow rate and the propeller design (number of nozzles and their size) (Surace et al. 2009). This approach is the

least costly to implement and results in a foam with a porosity in the range 0.9 to 0.97. It is at present limited to the manufacture of aluminium foams (Ashby et al. 2000).

2.2.2 Gas-releasing particle decomposition

Aluminium and its alloys can be foamed by mixing into them a foaming agent that releases gas when heated. Titanium hydride (TiH_2) is widely used as foaming agent as it begins to decompose into Ti and gaseous H_2 when heated above 465^oC (Speed 1976). The process begins by melting Al and stabilizing the melt temperature between 670 and 690 ^oC. 1%-2% of calcium is added in the melt to raise the viscosity by forming finely dispered CaO and $CaAl_2O_4$ particles. The melt is then aggressively stirred and 1%-2% of TiH_2 is added in the form of 5-20 μm diameter particles. The stirring system is withdrawn when the TiH_2 particles are uniformly dispersed in the melt so that the foam can be formed.

Porosities ranging from 0.8 to 0.93 can be achieved by adjusting the volume fractions of calcium and titanium hydride added to the melt. The cell size can be varied from 0.5 to 5 mm by changing the TiH_2 content and the foaming and cooling conditions. This approach is also limited to aluminium at present because hydrogen embrittles many metals and the decomposition of TiH_2 occurs too quickly in higher melting point alloys (Ashby et al. 2000).

2.2.3 Casting using a template

Open-cell polymer foams with low relative densities can be used as templates to create investment-casting moulds into which a variety of metals and their alloys can be cast. An open-cell porous polymer/wax with the desired cell size and relative density is selected as a template. This can be coated with a mould casting slurry which is then dried and embedded in casting sand. The casting slurry is then baked to harden the casting material and to decompose the polymer template, leaving behind a negative image of the polymer foam. The molten metal is then filled into the open channels. After the metal solidifies and the mould material is removed, an open-cell porous metal is formed. The DUOCEL foam sold by ERG Ltd (Oakland, US) is made in this way. Fig. 2.2 shows a micrograph of aluminium foam made by this approach. This method gives open-cell foam with pore sizes of 1 mm - 5 mm and porosity as high as 0.95 (Ashby et al. 2000).

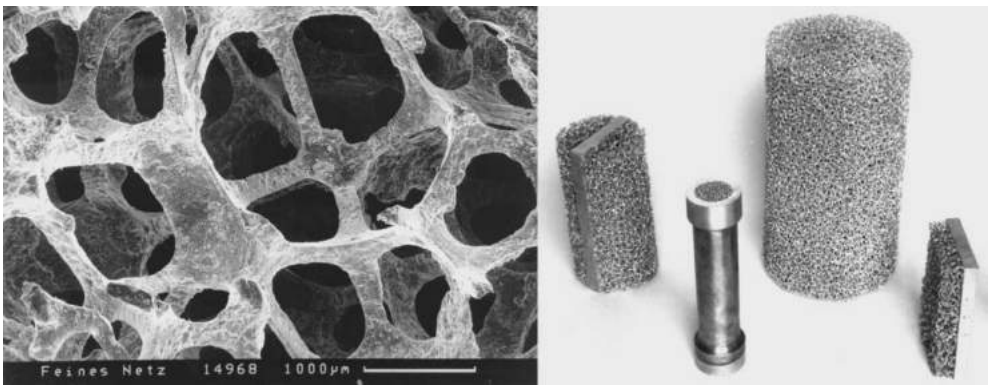

Figure 2.2: Left: SEM image of DUOCEL foam, right: some parts made by the template method (Hintz et al. 1999) (large cylinder is about 40 mm in diameter). (Wadley 2002).

2.2.4 Metal deposition on cellular preforms

In the metal deposition method, metals are deposited on an open-cell template by chemical vapor decomposition (CVD), by evaporation or by electrodeposition. For example, nickel foam can be achieved by heating nickel carbonyl, ($Ni(CO)_4$). An open-cell polymer is placed in a CVD reactor and $Ni(CO)_4$ is introduced. This gas decomposes into nickel and carbon monoxide at the temperature of 100 ^oC and coats all the exposed heated surfaces within the reactor. Then the metal-coated porous polymer is removed from the CVD reactor after a certain thickness of nickel is deposited. By heating the mixture in air, the polymer burns out, resulting in a cellular metal structure with hollow ligaments (Babjak et al. 1990), as shown in Fig. 2.3. The inset of the photograph shows that the struts are hollow. Foams with open pore sizes in the diameter range of 100 μm - 300 μm and porosity range of 0.95 - 0.98 can be made by this method.

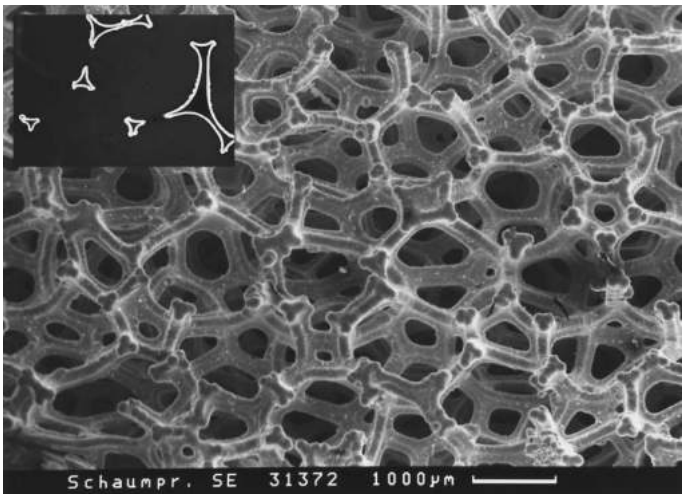

Figure 2.3: Nickel foam prepared by chemical vapor decomposition. Inset: micrograph of the edges of some of the hollow struts (Banhart 2001).

2.2.5 Entrapped gas expansion

This process has been used to create low-density core Ti-6Al-4V sandwich panels with pore fractions up to 50%. The process steps are shown in Fig. 2.4. In the process, metal powder is sealed in a canister of the same alloy. The canister is evacuated to remove any oxygen and then backfilled with argon between 3 to 5 atmospheres. Then the canister is sealed and consolidated to a high relative density (0.9 - 0.98) by Hot Isostatic Pressing (HIPing). In this procedure, the quantity of pores decreases dramatically. In order to increase the number of pores, hot rolling at 900 - 940 ^{o}C is adopted. As the voids become flattened and elongated after hot rolling, void faces come into contact and diffusion bond, creating strings of smaller gas-filled pores. Finally the panel is expanded by heating at 900 ^{o}C for 20 - 30 hours. The high temperature raises the internal pore pressure causing creep dilation and a reduction in the overall density of the sample (Ashby et al. 2000). This process gives the porous metal a porosity up to 0.5 and a pore size of 10 - 300 μm (Ashby et al. 2000).

2.2.6 Hollow sphere structures

Metallic hollow spheres (e.g. Cu, Ni, Ti) can be produced by several approaches, e.g., depositing metal onto a polymer sphere followed by sintering to remove the polymer, leaving a dense metal shell (Yi et al. 2009). In an alternative method, hollow spheres are formed from a slurry composed of a decomposable precursor such as TiH_2, together with organic binders and solvents. The spheres are hardened by evaporation during their flight in a tall drop tower, heated to drive off the solvents and to volatilize the binder. A final heat treatment decomposes the metal hydride, leaving hollow metal spheres (Kendall et al. 1982). In a third method, inert gas

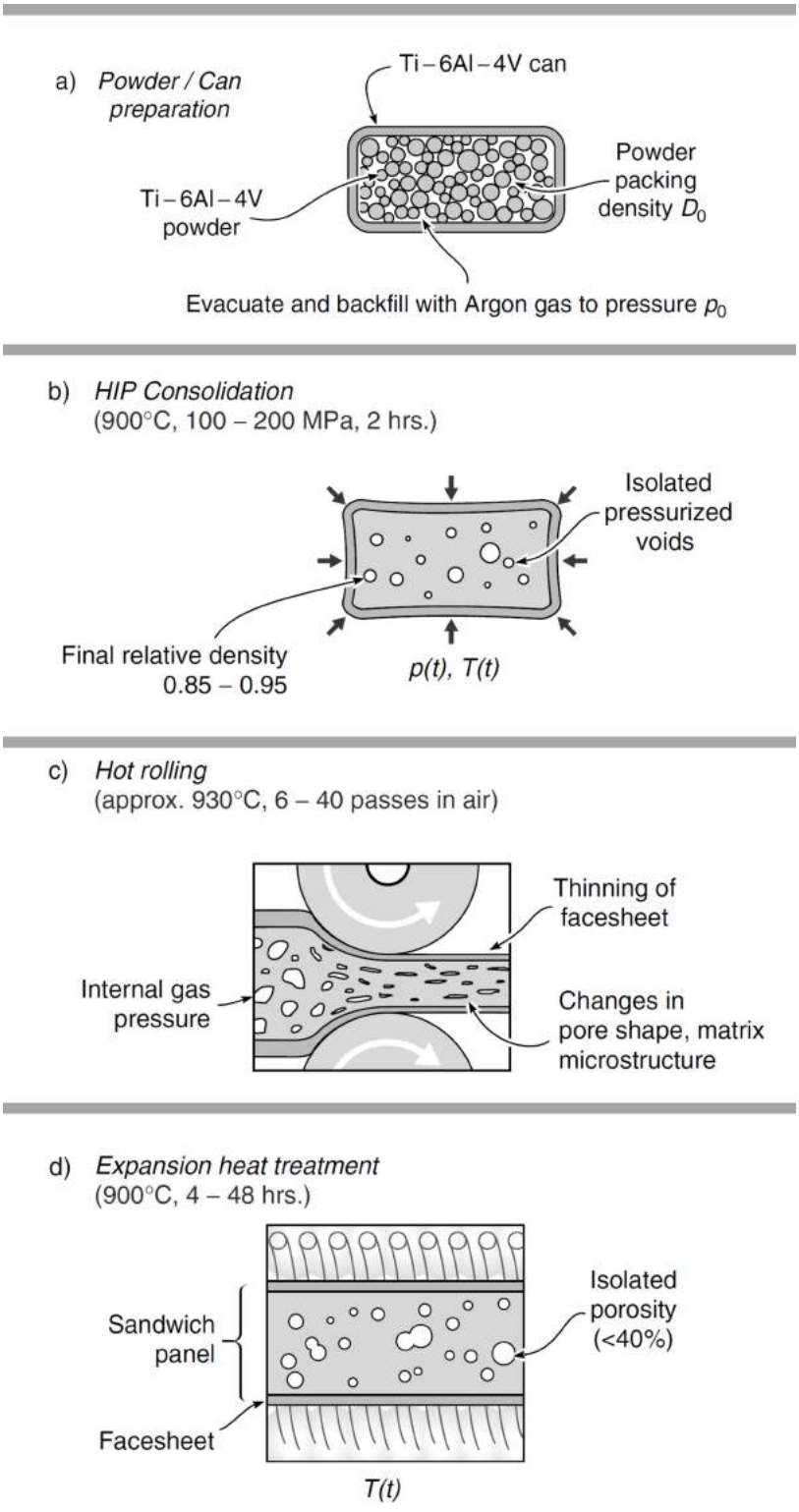

Figure 2.4: Entrapped gas expansion process steps used to manufacture titanium alloy sandwich panels with highly porous closed-cell cores. (Ashby et al. 2000).

atomization often results in a small fraction (1 - 5%) of large diameter (0.3 - 1 mm) hollow metal alloy spheres with relative densities as low as 0.1. These hollow particles can then be consolidated by HIPing, by vacuum sintering, or by liquid-phase sintering. Fig. 2.5 shows one of the samples made by this method.

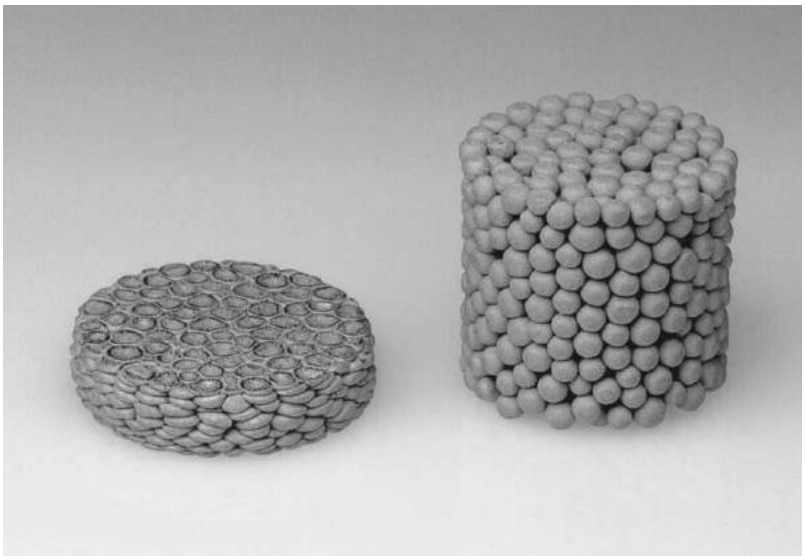

Figure 2.5: Open hollow sphere structure made from stainless steel spheres by sintering: after and before axial deformation. Diameter of parts is about 20 mm (Banhart 2001).

This approach gives a structure with a mixture of open and closed porosity. The ratio of the two types of porosity and the overall relative density can be tailored by varying the starting relative density of the hollow spheres and the extent of densification during consolidation. Overall porosity as high as 0.95 is feasible with a pore size in the range 100 μm to several millimetres (Ashby et al. 2000).

2.2.7 Casting of two materials

Open-cell porous metals (e.g. aluminium and its alloys) can be manufactured by infiltrating liquid metal into a leachable particle bed. In this method, a salt powder, for example, is consolidated and used as a bed of leachable particles. Then, the metallic melt is infiltrated into the bed under pressure. After the metal is solidified, the salt can be rinsed away in water, leaving an open-cell structure.

This method is used to manufacture porous metals with porosity between 0.5 and 0.7. The pore size is determined by the powder particle size and lies in the range 10 μm to 10 mm (Ashby et al. 2000).

2.2.8 Gas-metal eutectic solidification

The gas-metal eutectic solidification method involves melting the metal (e.g. Cu, Ni, Al, and Mg) in the hydrogen atmosphere (50 atm) to obtain a homogeneous melt charged with hydrogen (Banhart 2001). A eutectic transition to a solid+gas phase occurs when the temperature is lowered, leading to directional solidification advancing through the liquid melt. The hydrogen content close to the plane of solidification is enhanced and as a consequence, gas bubbles are created. Fig. 2.6 is an image of the resultant foam, also known as “gasar” or “lotus-type” foam, which contains large directional pores with diameters of 10 μm - 10 mm and pore length of 100 μm - 30 cm (Shapovalov & Withers 2008).

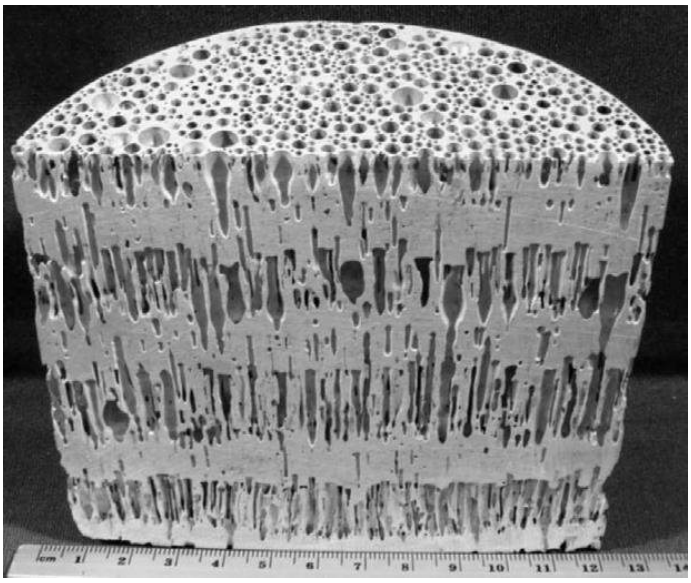

Figure 2.6: Gasar sample manufactured using the solid-gas eutectic solidfication method. (Shapovalov 2007).

2.2.9 Space-holder sintering

Open-cell porous metals (e.g. Cu, Al, stainless steel, nickel and their alloys) with porosity of 0.5 - 0.85 can be produced by space-holder sintering. Ceramic particles, polymer grains, salts or hollow spheres are just some of the types of space holders currently used. The process involves mixing the space holder with the metal powder at the target porosity ratio, with the addition of a suitable binder (e.g. ethanol). The mixture is pressed in a mould and then sintered at high temperature. The space holder is decomposed during sintering or rinsed away in solvent after sintering.

The Lost Carbonate Sintering (LCS) and Sintering Dissolution Process (SDP), which are based on the space holder principle, were developed by Zhao and his colleagues (Zhao & Sun 2001, Zhao, Fung, Zhang & Zhang 2005). A variety of porous metals (e.g. Al, Cu, Ti, steel and their alloys) have been made with this method. The processes involve mixing metal particles and space holder particles, compacting the

powder mixture, sintering, and decomposition or dissolution. These two processes have been proved to be an efficient powder metallurgical manufacturing method to produce porous metals with controllable pore parameters, such as porosity, pore size, pore shape and pore distribution. Porous copper manufactured by the LCS process is shown in Fig. 2.7.

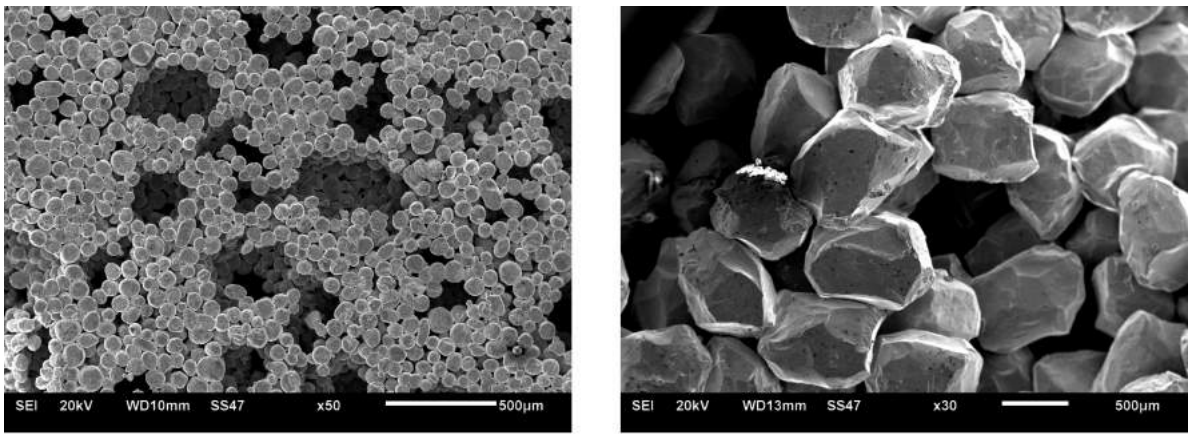

Figure 2.7: SEM image of porous copper produced by LCS process. (a)Sephrical copper particles and (b) irregular copper particles.

The porous metals made by the above processes show a strong bonding between the metal particles, leading to good thermal and mechanical properties. These foams have two types of pores, as can be seen from the SEM images (Fig. 2.7): the primary pores produced by the space holder, and secondary pores which are the gaps between the metal particles. The space-holder method has a very low cost compared with other methods.

2.3 Fluid flow in porous media

Fluid flow through porous media is very common in every area of science and technology, including hydrology, soil physics, soil mechanics, petroleum technology, chemical engineering, mining and mineral processing, and oil and gas production. Flow through porous media can also be found in many applications, e.g., heat exchangers, packed bed reactors (Sutherland et al. 1963, Mandal et al. 2013, Mandal 2015), fluid contacting filtration and various separation and purification devices (Harris 1977, Kundu et al. 2014). Flow in porous media is very complex due to the complex structure of porous media and the complex interaction between fluid and solid phases.

2.3.1 Pressure drop and flow rate

2.3.1.1 Darcy's law and the modifications

Fluid flow through porous media has been studied for a long time. Darcy (Darcy 1856) was the first to establish a linear relationship between pressure drop and flow rate when he studied the fluid flow through packed sand. The relationship, known as Darcy's law, after being modified to include the fluid viscosity, is stated as follows:

$$-\frac{\Delta P}{L} = \frac{\mu V}{K} \tag{2.1}$$

where V is the Darcian velocity, which equals to the volume flow rate divided by the entire cross-section area of the entire porous medium, μ is the viscosity of the fluid, K is the permeability of the porous media, and $\Delta P/L$ is the pressure gradient in the direction of flow. It is not difficult to conclude that viscous force dominates the flow in Darcy flow within porous media.

A number of researchers have verified that Darcy's law only applies for sufficiently slow and single phase fluid flow through porous media. Mokadam (1961) derived a general equation for flow through porous media using irreversible thermodynamics and showed that Darcy's equation is a special case. After a critical velocity, the non-linearity appears in the pressure drop-velocity relationship. This deviation from the Darcy's law is attributed to the increasing role of inertial force, which comes from the interactions between the fluid flow and the solid matrix (Chauveteau & Thirriot 1967). Dupuit (1863), Forchheimer (1901) are generally believed as the first suggesting a non-linear relationship between the pressure drop and Darcian velocity. They suggested that the inertial resistance can be accounted for by the kinetic energy per unit volume of the fluid, i.e. on ρV^2. Therefore, in general engineering applications, the law governing this fluid flow is a modified version of Darcy's equation, with inertial resistance superimposed on the viscous resistance:

$$-\frac{\Delta P}{L} = \frac{\mu}{K}V + \rho C V^2 \tag{2.2}$$

where K is the permeability in the Darcy regime, ρ is the density of the fluid and C is the drag form coefficient of the medium. The term $\rho C V^2$ accounts for the inertial effects or non-linear flow resistance in the flow. The above equation is known as the Forchheimer extended Darcy equation.

Recently, Joseph et al. (1982) modified the Forchheimer equation based on the work of Ward (1964) by introducing an inertial coefficient, c_F to Eq. 2.2, where c_F =

$CK^{1/2}$. Then the equation can be expressed as

$$-\frac{\Delta P}{L} = \frac{\mu}{K}V + c_F K^{-1/2}\rho V^2 \tag{2.3}$$

The value of inertial coefficient, c_F, has been discussed in previous literature. Ward (1964) suggested that c_F is a universal constant for all porous materials and equals to 0.55. Later work found that c_F does vary with the nature of the porous medium, and can be as small as 0.1 in the case of fibrous porous metal.

Irmay (1958) derived an alternate equation for unidirectional flow. The study was based on the gas flow through crushed porous solids. By introducing porosity and sphere diameter, the equation was obtained as

$$-\frac{\Delta P}{L} = a\frac{(1-\epsilon)^2}{\epsilon^3}\frac{\mu V}{D^2} + b\frac{1-\epsilon}{\epsilon^3}\frac{\rho V^2}{D} \tag{2.4}$$

where a and b are dimensionless constants, ϵ is porosity and D is the diameter of spheres. The degree to which the above equation may be applied to various porous media is dependent on the constants a and b. Ergun (1952) concluded that a large quantity of experimental data could be fitted when $a = 150$ and $b = 1.75$, and the above equation is known as Ergun's equation. However, subsequent experimental data from porous media consisting of smooth particles shown that these values are not definitive. Macdonald et al. (1979) suggested that $a = 180$ and $b = 1.8$ should be used for engineering applications.

Another alternative extension to Darcy equation is Brinkman's equation (Brinkman

1949*a*,*b*). With inertial terms omitted it takes the form

$$-\frac{\Delta P}{L} = \frac{\mu}{K}V + \mu_e \nabla^2 V \tag{2.5}$$

The first viscous term is the usual Darcy term and the second is analogous to the Laplacian term that appears in the Navier-Stokes equation. The coefficient μ_e is an effective viscosity.

The value of effective viscosity has been widely discussed in the literature. Brinkman set μ and μ_e equal to each other, but this is not always the case. On the one hand, straight volume averaging as presented by Ochoa-Tapia & Whitaker (1995) gives $\mu_e/\mu = 1/\epsilon$, greater than unity. On the other hand, analyses such as that by Saez et al. (1991) give μ_e/μ close to a tortuosity, a quantity that is less than unity. Liu & Masliyah (2005) suggest that the difference between μ_e and μ as being due to momentum dispersion and it has been generally accepted that the value of effective viscosity is strongly dependent on the type of porous media as well as the strength of the flow.

2.3.1.2 Other correlation functions

The Darcy's law, Forchheimer-extended Darcy equation, and Ergun equation are the most well known functions to represent the relationship between pressure drop and velocity in porous media. Other researchers have also tried to find new functions for the correlation.

Cheng et al. (2008) used quadratic and power law formulations in terms of seepage Reynolds number for correlating the experimental results covering Darcy to non-

Darcy flows through porous media. The results showed that the quadratic law is applicable to both linear and non-linear flow regimes but the two coefficients vary at different regimes. In comparison, the power law appears not working if the seepage velocity varies over a wide range. However, a similar experiment conducted by Moutsopoulos et al. (2009) showed a different case. Their experiment indicated that, for a wide spectrum of velocities, both the Forchheimer and power law equations offer excellent descriptions of the flow processes. Only for moderate values of Reynolds number, a discontinuity in the velocity-hydraulic gradient curve was detected.

2.3.2 Flow regimes in porous media

Considering that there are linear and nonlinear relationships between the pressure drop and velocity as fluid flows through the porous media, researchers conclude that there may be more undiscovered flow regimes. Dybbs & Edwards (1984) published a comprehensive review paper on the laser anemometry and flow visualization studies on the fluid flow in porous structures. The porous medium was either packed bed of spheres or a rod structure as shown in Fig. 2.8. They indicated the existence of four regimes of flow in porous media according to the flow behaviour analysis. The four flow regimes were identified as Darcy flow regime, inertial flow regime, unsteady laminar flow regime and unsteady and chaotic flow regime.

There is an easy way to identify the different flow regimes in porous media. By comparing the relationship between pressure drop and velocity, the flow regimes can be identified more accurately. To do this, the Forchherimer-extended Darcy equation

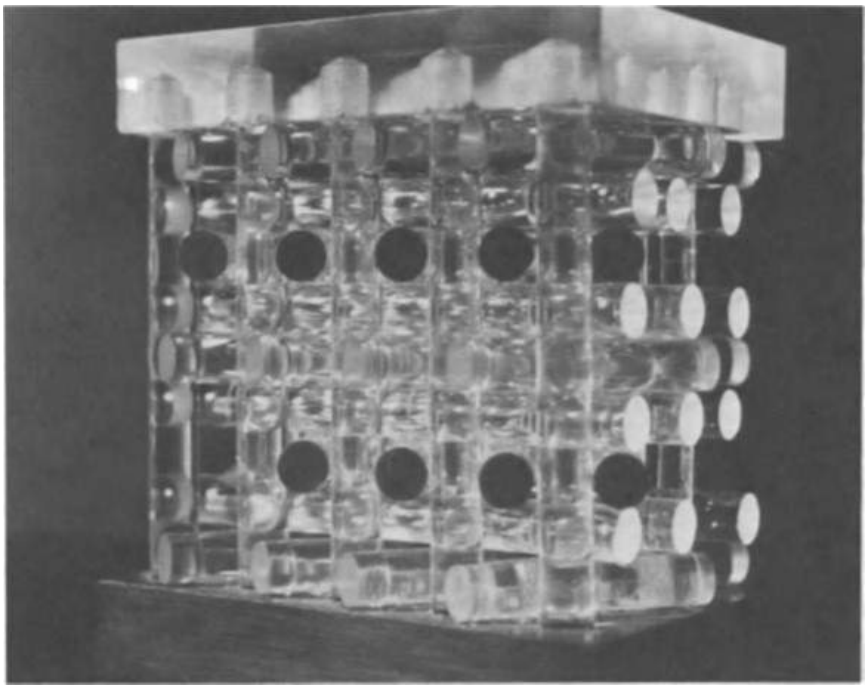

Figure 2.8: Photograph of half-scale model of complex rod structure porous medium.

need to be rewritten as:

$$-\frac{\Delta P}{LV} = \frac{\mu}{K} + \rho C V \tag{2.6}$$

where the term $-\Delta P/LV$ is called reduced pressure drop. Then plot $-\Delta P/LV$ against V, different flow regimes can be identified according to the slope differences. Most recent studies (Fand et al. 1987, Kececioglu & Jiang 1994, Bear 2013) have confirmed the existence of four flow regimes, namely pre-Darcy, Darcy, Forchheimer and turbulent regimes when fluid passes through the porous media. Fig. 2.9 schematically shows a typical plot between reduced pressure drop and velocity. It should be noted that there is a transition region between each pair of adjacent flow regimes and the range of the transition region depends on many factors related to the porous material and fluid properties.

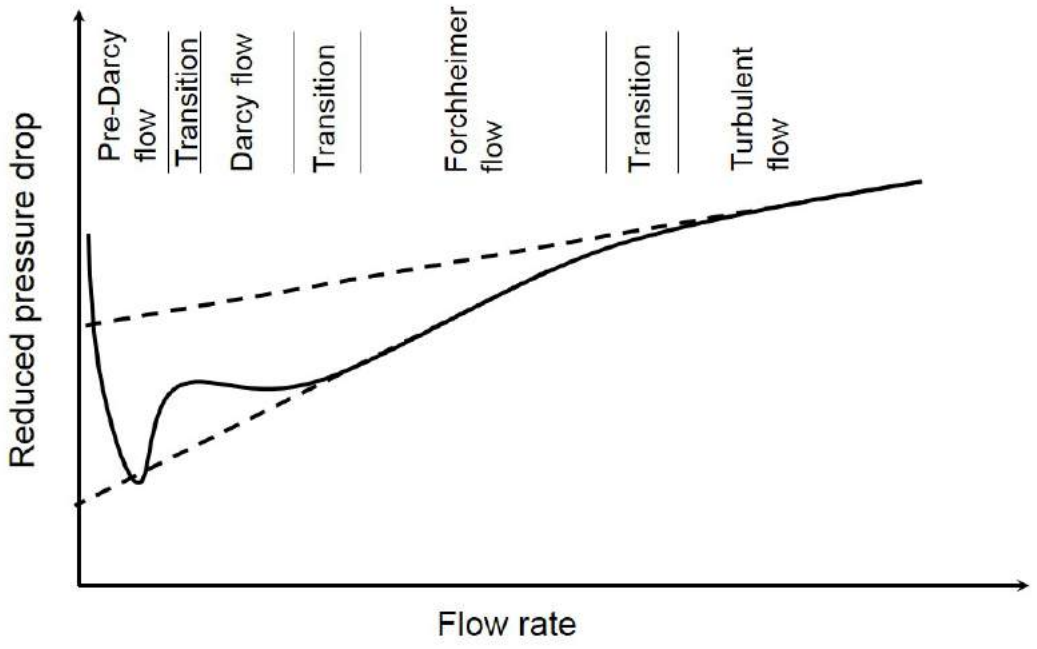

Figure 2.9: Schematic drawing of flow regimes for fluid flow through porous media. (Kececioglu & Jiang 1994).

2.3.2.1 The pre-Darcy regime

The pre-Darcy regime is only observed at very low velocity. The experimental data in this regime are very scarce due to the difficulty of measuring the ultra low pressure and velocity. The pre-Darcy flow regime was identified in the experiment conducted by Kececioglu & Jiang (1994). In this regime, the pressure drop has a non-linear relationship with velocity. Some researchers attributed this to the electro-osmotic and capillary-osmotic forces occurring in the porous media (Polubarinova-Koch 2015).

2.3.2.2 The Darcy regime

Darcy flow also only exists at low velocity and the range sometimes is narrower than the pre-Darcy regime. In this regime, the pressure drop increases linearly with in-

creasing velocity because viscous drag solely contributes to the pressure drop. The relationship between pressure drop and velocity can be described by the Darcy's law (Eq. 2.1). The inertial force, which is casued by the interaction between fluid flow and pore walls, is so small compared to the viscous force that it can be neglected. The study by Dybbs & Edwards (1984) showed that the velocity distribution in the Darcy flow regime is determined by viscous forces and the local geometry. In addition, they found that the boundary layers begin to develop near the surface of the pores when the flow gets into the transition range.

2.3.2.3 The Forchheimer regime

The Forchheimer regime ranges much broader compared to the former two regimes. Although the flow remains steady in the Forchheimer regime, the pressure drop starts to increase non-linearly with increasing velocity because of the influence from the inertial force. The relationship between pressure drop and velocity can be described by the Forchheimer-extended Darcy equation (Eq. 2.2). The boundary layers which developed in the transition range become more pronounced and an "inertial core" appears. The developing of these "core" flows outside the boundary layers is the reason for the increase of inertial force. As velocity increases, the "core" flows enlarge in size and their influence becomes more and more significant on the overall flow. Kinetic energy degradation begins due to the strong interactions between flow and solid walls (e.g., pore constriction and change of flow direction). Therefore, the flow energy dissipation becomes the sum of the viscous and inertial drags.

2.3.2.4 The turbulent regime

As velocity keeps increasing, the flow becomes unsteady and chaotic, getting into the turbulent regime, and the boundary effects become stronger. Vortices and eddies developed from the the near wall region move to the non-near wall region and disturb the entire flow region. The relationship between the pressure drop and the velocity can still be characterized by the Forchheimer-extended Darcy equation (Eq. 2.2), but with different parameters (permeability and drag coefficient). As velocity keeps increasing, inertial force becomes stronger and stronger, and dominates the flow field.

2.3.3 Effects of fluid and structure factors on porous flow

The structural characteristics of the porous media greatly influence the porous flow behaviour, such as the critical Reynolds number of regimes, the pressure drop and even the velocity field distribution. Effects of porosity, particle size, pore shape and flow property on the fluid flow dynamics within the porous structure are reviewed separately.

2.3.3.1 Porosity

The porosity of a porous medium, by definition, is a geometrical property that measures the fluid storage capacity of the porous structure. The greater the porosity, the more pores and less solid barrier are present within the structure, allowing the fluid to flow more freely. Porosity is one of the most significant factors affecting the porous flow behaviour. However, research on the effect of porosity on porous flow is insufficient due to the difficulty in controlling the porosity of traditional porous

media.

2.3.3.2 Particle size and shape

Due to limitation of manufacture processes, many porous media studied by previous researchers were packed beds. Factors such as particle size, shape and material type can affect the fluid flow dynamics within the porous structure.

Soni et al. (1978) performed a series of water flow tests through sands and glass beads with Reynolds number varying from 3.2 $\times 10^{-4}$ to 2.6. Three distinct flow regimes, namely prelinear, linear and postlinear, were found in their experiment. Fand et al. (1987) experimentally studied the flow of fluids through packed beds composed of spheres of uniform diameter and packed beds composed of spheres having different diameters. They found that the bounds of Darcy flow are consistent for both packed beds. In addition, the resistance to flow in both the Forchheimer and turbulent regimes can be characterized by adopting different values of a and b in Ergun equation. Comiti et al. (2000) studied the Darcy flow regime for Newtonian and non-Newtonian fluid flows in packed beds with different particles (spheres, cylinders, plates and polyhedorns). They correlated the friction factor with Reynolds number according to the Ergun equation (Eq. 2.4) and found very different a and b values. Li & Ma (2011) conducted experiments studying the characteristics of frictional pressure drops of fluid flow in packed beds with non-spherical particles, trying to examine the applicability of the Ergun equation. The results show that the Ergun equation is applicable to all the tested beds if the effective particle diameter used in the equation is chosen as the equivalent diameter of the particles.

2.3.3.3 Fluid flow property

Besides the effects of structural characteristics, the property of fluid flow also influences the dynamics of porous flow. Mishra et al. (1975) studied the flow behaviour of Newtonian and non-Newtonian fluids flowing through packed and extended beds. The investigation covered the range of Reynolds number from 10^{-3} to 10^{3}. They presented their experimental results in terms of Reynolds number-friction plot and found that Ergun's equation correlated the data of both the Newtonian and non-Newtonian fluids well. Pamuk & Özdemir (2012) experimentally studied oscillatory and steady flows of water through two different porous media consisting of mono-sized stainless steel balls and showed that for the same range of Reynolds number, the permeability and form drag coefficient of oscillating flows are higher than those of steady flows.

2.3.4 Flow visualization in porous media

Flow visualization is another effective method for measuring fluid flow behaviour. The most often used flow visualization techniques include laser doppler velocimetry (LDV), magnetic resonance imaging (MRI), confocal microscopy, particle tracking velocimetry (PTV) and particle image velocimetry (PIV). These methods make it possible to see how fluid moves through porous media and to measure its velocity in pore scale.

LDV sends a monochromatic laser beam toward the target flow and collects the reflected signals from the seeded solid particles. According to the Doppler effect, the change in wavelength of the reflected radiation is a function of the targeted object's relative velocity. Thus, the velocity of the object can be obtained by measuring the

change in wavelength of the reflected laser light, which is normally done by forming an interference fringe pattern by superimposing the original and reflected signals (Durst 1980).

MRI uses the phenomenon that arises when nuclei with non-zero spin quantum numbers are placed in a strong magnetic field. These nuclei will establish a small magnetisation. If this magnetisation is then excited using a radiofrequency pulse, the magnetisation will rotate and hence induce a current in the radiofrequency coil. This current is measured and can be used to determine how fast the target is moving, where it is, and more (Huettel et al. 2004).

PIV is a non-intrusive whole-flow-field technique providing instantaneous velocity vector measurements in a cross-section of a flow. The target fluid is seeded with particles which are generally assumed to faithfully follow the flow. It is done by taking two images shortly after one another and calculating the distance individual particles traveled within this time. The displacement field is determined from the motion of the seeding particles between the two images. The velocity field is obtained by dividing the displacement field by the known time separation. The technique is applicable to a range of liquid and gaseous flows (Raffel et al. 2018).

PTV shares the same principle with PIV. In contrast to PIV, in which the displacement is determined by a small group of particles, PTV tracks the trajectories of individual particles in three-dimensional space. Therefore, particle identification and determination of its position in space is a very important step in PTV. This is only possible if the particle density is not too high (Dracos 2013).

LDV was one of the earlies techniques used to measure the interstitial velocity within macro-porous media. Johnston et al. (1975) used LDV to measure the velocity in a packed bed of plexiglas spheres of diameter 1.27 cm. The fluid velocity measurements were successfully made in the interstitial regions of the model porous medium, and the applicability of the LDV to the study of flow in porous media was demonstrated. In 1989, using LDV technique, Yarlagadda & Yoganathan (1989) measured the three-dimensional, steady flow velocity components of a viscous, incompressible, Newtonian fluid in a model porous medium constructed from 3 mm glass rods. They studied the viscous drag, inertial flow fields and eddy losses in the porous media, and found that fluid mixing was absent although the fluid followed a tortuous path. The non-Darcy flow regime was not reached due to the high viscous drag coefficient. One of the drawbacks of LDV is that it is a single point measurement system and it is difficult to capture the spatial and temporal variations of velocity field inside the porous media.

MRI is another non-intrusive flow measurement technique used for probing velocity field within porous structures. Sederman et al. (1997) studied the structure-flow correlations within the interparticle space of a packed bed of glass beads using MRI technique. They found that velocity enhancement at the walls of the bed is greater in the shorter, more ordered, packed bed. They also obtained a three-dimensional volume image of the packed bed. Baumann & Werth (2005) used MRI to evaluate the effect of heterogeneous grain packing on colloid transport in flows through columns. The columns were built with fine particles in the core and coarse particles in the shell. The results showed that the velocity in the shell is higher than that in the core region.

Confocal microscopy was used by several researchers to visualize the fluid flow in

porous materials. This technique is great for characterizing the three-dimensional geometry of the microstructure and detect the interfaces of two or multiple phase flows. Fredrich (1999) used this technique in his experiments to statistically reconstruct and characterize the microgeometry of several porous geologic and engineering materials. Datta et al. (2013) used confocal microscopy to directly visualize the spatial fluctuations in fluid flow through a three-dimensional porous medium, and demonstrated that the flow is not randomly distributed in the porous medium.

PTV and PIV have also been used by researchers to quantify pore scale velocity distributions in porous media. Saleh et al. (1992), Rashidi et al. (1996), Hassan & Dominguez-Ontiveros (2008) and Huang, Huang, Capart & Chen (2008) have obtained two-dimensional or three-dimensional velocity distributions in pore scale. PIV has been considered to be the one of the most effective measurement technique for investigating flow behaviour in a dynamic fluid field under laminar and turbulent flow conditions in recent years.

All the measurements mentioned above are carried out on macroporous media. Recently, micro-PIV (μ-PIV) has made it possible to quantify fluid velocity in microfluidic devices with spatial resolutions in the order of tens of microns (Santiago et al. 1998, Meinhart et al. 1999). Zerai et al. (2005) applied μ-PIV to square cross-section throats of widths of 200 μm, 600 μm and 1000 μm, and obtained the two-dimensional streamline pattern as well as the velocity field. Their experiment gave an insight of fluid behaviour in a complex porous matrix. Sen et al. (2012) packed micro-glass spheres of size 200 μm inside a glass micromodel, with a typical pore size of $10-50$ μm. They studied velocity fields at different spatial locations of different pore structures and found that the statistical distribution of the velocity field agreed well with

the available numerical and experimental results pertaining to macroporous media.

2.4 Thermal properties of porous metals

Thermal transport, including conduction and convection, in porous metal is often of particular significance when they are used in thermal management devices. Studying thermal properties of porous metals is important for designing the next-generation heat exchangers.

2.4.1 Applications of porous metals in heat transfer

One of the most common and promising applications of porous metals is heat exchanger. With the rapid development of modern technology, the demand for heat transfer performance has increased in recent years. Traditional heat exchangers, such as fin structures, are becoming more and more difficult to cope with new challenges. For example, in some high performance electronic chips such as computer processors, the nominal heat flux can be up to 500 - 1000 KW/m^2 and there is no doubt that much higher demand will be made in the future (Bastawros & Evans 1997).

Open-cell porous metals in combination with fluid flow, can be used as heat exchangers to improve the convective heat transfer in industrial processes, such as in power stations, combustion systems and for cooling turbine blades or electronic devices (Mahdi et al. 2015). Porous metals are a promising alternative for compact heat exchangers due to their surface area density, excellent thermal conductivity and good fluid flow permeability.

Fig. 2.10 shows an example of aluminium foam being used as passive heat sink for LED lamps (García-Moreno 2016). The heat generated by the high power density LED lamps can be dispersed to the metal foam through conduction and taken away efficiently by the air through convection.

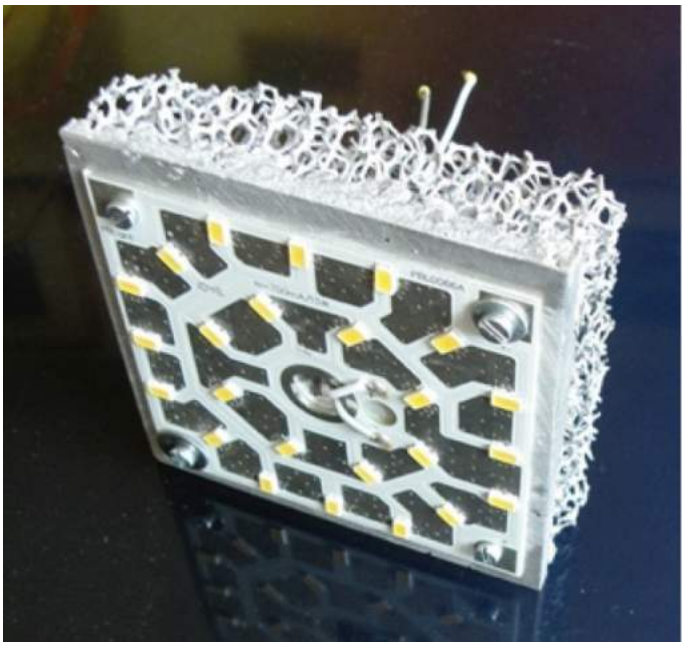

Figure 2.10: Passive thermal cooling of LED lamps by Al-foam.

Many experimental studies have been conducted to investigate the applicability of porous metals as heat exchangers. Ejlali et al. (2009) numerically investigated the fluid flow and heat transfer of an air-cooled metal foam heat exchanger under a high speed laminar jet confined by two parallel walls. It is observed that the heat removal rate can be greatly improved at almost no excess cost. Boomsma & Poulikakos (2002) proved that compressed Al foams not only performed well in heat transfer enhancement, but also made a significant improvement in efficiency over several commercially available heat exchangers which operated under identical conditions. The

metal foam heat exchangers decreased the thermal resistance by nearly half when compared to currently used heat exchangers.

The factors that greatly influence the heat transfer performance of porous metal heat exchangers were reviewed by Hutter et al. (2011). It was reported that the convective heat transfer performance of the metal foam system is affected significantly by the coolant properties (e.g., heat capacity or thermal conductivity). Similarly, the heat transfer performance is also influenced by the properties of the foam material (e.g., thermal conductivity and mechanical properties). Apart from the thermal and mechanical properties, factors such as corrosion resistance and high temperature capability also need to be considered. The heat transfer performance is also affected by the structure of the foam because porosity, pore size and surface area have the greatest influences on the effective thermal conductivity, convective heat transfer and fluid flow properties.

2.4.2 Mechanisms of heat transfer in porous metal

The high thermal conductivity of metals means good thermal conduction through the solid matrix in porous metals. Heat conduction through a matrix fully saturated with fluid (e.g., porous metals in air) depends on the structure of the matrix and the thermal conductivity of each phase. The large surface area to volume of porous metals provides an excellent condition for heat convection. For open-cell porous metals, enhanced flow mixing due to turbulence and tortuous channels also improves heat convection in porous metals. The heat transfer in a porous metal can have four contributions: conduction through the solid phase, conduction through the liquid

phase, convection through the liquid phase and radiation.

Conduction through the solid phase is believed to be the most dominant form of heat transfer in porous metals (Ashby et al. 2000). The effective thermal conductivity (ETC) of the porous metal, therefore, depends significantly on the porosity or the fraction of metal in the porous metal. In addition, the structure of the solid matrix and the bonding quality of the sintered necks in a sintered matrix also affect the heat transfer performance of the porous metal.

The contribution of conduction through liquid phase in pores is very limited in porous metals. In most cases, the coolant used in porous metals is either water or air. The thermal conductivities of copper and aluminium are thousands of times of that of these coolants. Therefore, compared to the solid phase, the contribution of the liquid phase through conduction is negligible.

Convection occurs because of the alternating motion of the hot and cold fluid caused by local density difference of the fluid. The motion of the fluid in a porous metal is important for heat transfer performance because it determines the heat transfer efficiency from the solid matrix to the fluid. There are two types of convection in porous metals: free and forced convection. In free convection, fluid motion is caused by buoyancy force within the fluid. Forced convection occurs only when there is external pressure difference applied across the porous metal.

Heat transfer by radiation is strongly dependent on the temperature. According to the experiments conducted by Zhao, Lu & Hodson (2004), radiation only contributes to heat transport at very high temperatures (200-500^{0}C) in porous media, and its

contribution is negligible at lower temperatures ($< 200^0$C).

2.4.3 Thermal conductivity of porous metals

The effective thermal conductivity (ETC) of porous metal is one of the most important parameters when it is used as heat exchanger. The value of ETC depends on many factors such as thermal conductivity of the solid and liquid phases, porous structure, heat radiation and motion state of the liquid phase.

2.4.3.1 Effect of material on effective thermal conductivity

Numerous experiments have been conducted to investigate the thermal conductivity of porous metals, especially for packed beds (porosity: 0.3 - 0.5) and aluminium foams (porosity > 0.9). Both analytical and empirical correlations have been made to predicate the ETC of these porous materials (Progelhof & Throne 1975, Russell 1935, Maxwell 1881, Progelhof et al. 1976, Collishaw & Evans 1994). One of the drawbacks of these models is that only three parameters were considered, i.e. the thermal conductivity of the bulk metal used in the solid matrix, the thermal conductivity of the liquid phase and the porosity.

Table 2.2: Various empirical models proposed to correlate the effective thermal conductivity and porosity of porous media.

Name	Model	References
Series-Parallel	$\lambda_{eff} = \lambda_s \left(1 - \epsilon^{2/3}\right) + \frac{\lambda_s \epsilon^{2/3}}{\lambda_f + (\lambda_s - \lambda_f)\epsilon^{1/3}}$	Leach (1993).
Parallel-Series	$\lambda_{eff} = \lambda_s \frac{\lambda_s - (\lambda_s - \lambda_f)\epsilon^{2/3}}{\lambda_s - (\lambda_s - \lambda_f)(\epsilon^{2/3} - \epsilon)}$	Leach (1993)
Maxwell	$\lambda_{eff} = \lambda_s \left[\frac{\lambda_f + 2\lambda_s + 2\epsilon(\lambda_f - \lambda_s)}{\lambda_f + 2\lambda_s - \epsilon(\lambda_f - \lambda_s)}\right]$	Maxwell (1881).
Russell	$\lambda_{eff} = \lambda_f \left[\frac{\epsilon^{2/3} + \lambda_s/\lambda_f(1 - \epsilon^{2/3})}{\epsilon^{2/3} - \epsilon + \lambda_s/\lambda_f(1 + \epsilon - \epsilon^{2/3})}\right]$	Russell (1935).
Bruggemann	$1 - \epsilon = \left[\frac{\lambda_f - \lambda_{eff}}{\lambda_f - \lambda_s}\right] \left(\frac{\lambda_s}{\lambda_{eff}}\right)^{1/3}$	Bruggeman (1935).
Progelhoff	$\lambda_{eff} = \lambda_f \left[1 + \frac{\lambda_s}{\lambda_f}(1 - \epsilon)^n\right]$	Progelhof & Throne (1975).
Power law	$\lambda_{eff} = \lambda_s (1 - \epsilon)^n$	Progelhof & Throne (1975).

Table 2.2 lists seven of the most referred correlations in the literature. Both the Series-Parallel (Leach 1993) and the Parallel-Series models simplify the porous structure to a cubical geometry. The Series-Parallel model combines the vertical cell walls and the gas phase in series to give a two phase system, and then combines the system with the horizontal cells walls. The Parallel-Series model uses a reversed order to calculate the thermal conductivity. Obviously, both models have significantly overestimated the thermal conductivity of the porous copper samples. The Russell model analyses the thermal conductivity of a solid matrix with cubic or spherical cells arranged in line. The pores are assumed to have a uniform cell-wall thickness with struts ignored. To make the model more general, Maxwell (1881) assumed that the spheres of one phase are randomly dispersed in a second phase. Subsequently, Bruggeman (1935) developed an expression for a composite with particles of spherical shape dispersed in a continuous matrix. Progelhoff model(Progelhof & Throne 1975) and power law model (Ashby et al. 2000) are empirical correlations based on polymeric and metallic foams respectively, and n is a fitting parameter. The difference is that the thermal conductivity of both phases are considered in the former model, while the latter model considered the contribution of the solid phase only (or the phase with the higher thermal conductivity). The power law model can be viewed as a special case of the Progelhoff model, where the solid-to-fluid conductivity ratio is so high that the contribution of fluid phase can be neglected. The power law model suggests a value of n in the range of 1.65 to 1.85, while the Progelhoff model recommends a n of 1.55.

Recently, Boomsma & Poulikakos (2001) compared the contributions of air and water to the ETC of a fluid-foam system, recognized the predominant role of the solid phase in heat transfer even for high porosity foams, and developed a geometrical

model (Fig. 2.11) based on the idealized three-dimensional basic tetrakaidecahedron geometry of aluminium foam. However, none of the models offers a reliable predication for ETC for all types of porous metals. This is because apart from the thermal conductivity of the solid and liquid phases, porosity, pore shape, pore size, temperature and natural convection also contribute to the ETC.

2.4.3.2 Effect of pore size on effective thermal conductivity

The effect of pore size on ETC is relatively weak. Bhattacharya et al. (2002), Paek et al. (2000), and Calmidi & Mahajan (1999) studied the pore size effects with various foams. They found that there is no systematic dependence of ETC on pore size. For foams with porosities of the order of 0.9 or higher and uniformly distributed pores, the effect of pore size on the ETC is negligible under ambient temperature.

2.4.3.3 Effect of temperature on effective thermal conductivity

Temperature affects the ETC mainly because of the rise of solid conductivity with temperature and the influence of heat radiation. One needs to note that the temperature effect discussed here is high temperature ($> 200^0$C) effect. Zhao, Lu & Hodson (2004), Zhao, Lu, Hodson & Jackson (2004) studied the temperature dependence of ETC in metal foams and found that the value of ETC at 500^0C can be three times of that at room temperature (25^0C). They also pointed out that at high temperatures, the rise of pure solid conduction is very mild, while the heat radiation may dominate the heat transport.

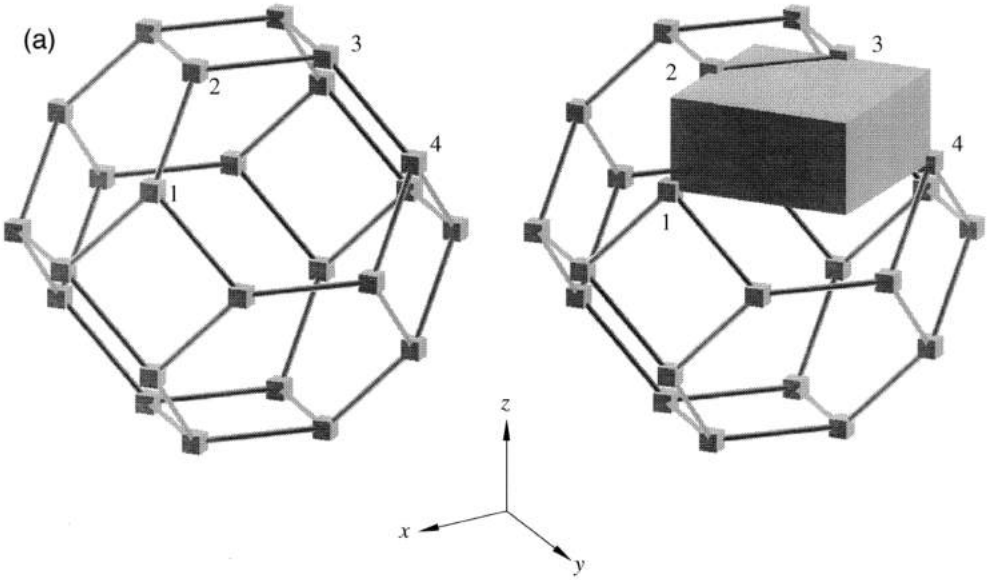

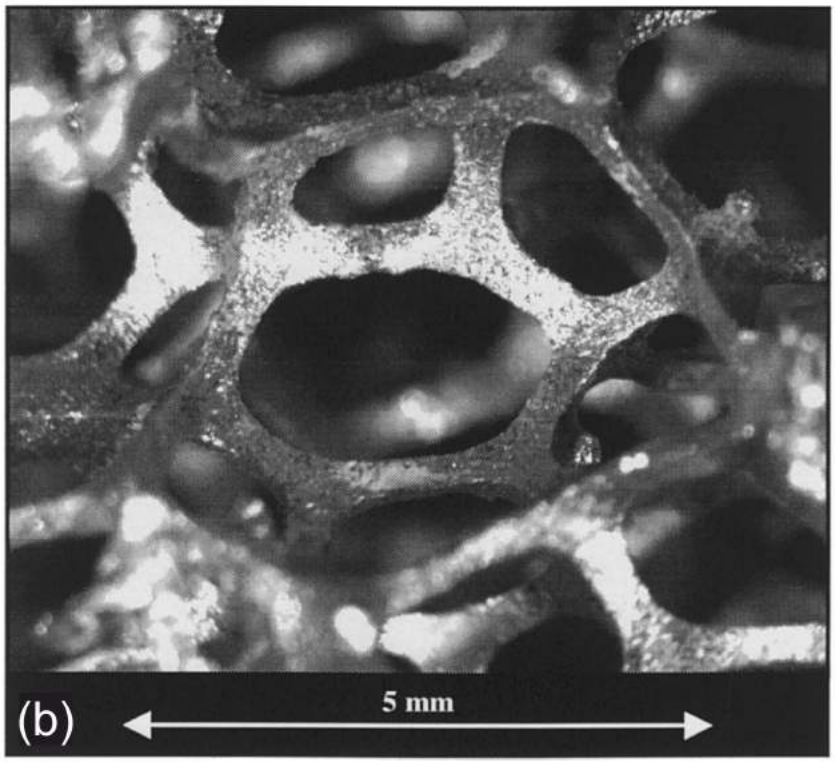

Figure 2.11: (a) The tetrakaidecahedron model with cylindrical ligaments and cubic nodes. The unit cell is shown on the right as a solid block located in a single tetrakaidecahedron cell. (b) Single tetrakaidecahedron cell in an aluminium foam. (Boomsma & Poulikakos 2001).

2.4.3.4 Effect of natural convection on effective thermal conductivity

The contribution of natural convection to ETC was discussed by Valenzuela & Glicksman (1983). They suggested that natural convection is negligible when the pore diameter is below a critical size (3-10 mm). Experiments by Skochdopole (1961) show that a 4 mm diameter is the limit for air-filled foams. Recently, numerical methods have been used by many researchers (Seta et al. 2006, Braga & De Lemos 2005, Merrikh & Lage 2005, Liu & He 2017) to study convective heat transfer in a representative elementary volume of metallic foams. The simulation work offered an insight that convection happens in a much larger dimension than the pore scale. Zhao, Lu, Hodson & Jackson (2004), Zhao, Lu & Hodson (2005), Dyga & Płaczek (2015) experimentally studied convection in high porosity (> 0.93) aluminium foams. They found that natural convection accounts for up to 50% of the ETC at ambient temperature. However, overall, data regarding the contribution of natural convection to ETC is still limited.

2.4.4 Natural convection in porous metals

When the temperature of the saturating fluid phase in a porous medium is not uniform, flow induced by the buoyancy effect may occur (Bear & Corapcioglu 2012). Commonly called free or natural convective movements, these flows depend on density differences due to temperature gradients and boundary conditions. Generally speaking, convective movements which tend to homogenize the whole fluid volume where they take place have two main effects: produce a non-uniform temperature distribution characterized by hot and cold zones and increase the overall heat transfer.

Natural convection is widely used in daily life and high-tech equipment to enhance heat exchange. Convective heat transfer can be improved either by increase the surface area for convection or enhance the heat transfer coefficient. Some researchers use fin structures to increase convection surface area, such as tree-shaped pin fins (Almogbel & Bejan 2000), channel with square pin fins (Şara et al. 2001), plate with pin fins (Huang, Sheu & Wang 2008), rectangular interrupted fins (Ahmadi et al. 2014), and even hybrid fins (Effendi & Kim 2017). Other researchers use corrugated or grooved surface to enhance the heat transfer coefficient (Ali & Ramadhyani 1992, Ali & Hanaoka 2002, Navaei et al. 2015). However, complex internal or external structures mean complex machining and high costs. In addition, one has to balance the other factors, such as flow resistance, when designing a specific structure in order to obtain the optimum heat transfer performance.

Recently, with the development of powder metallurgy techniques, porous metals, motivated by their large surface area, become an alternative structure to extend the surface area. Open-cell metal foams are considered a potential heat exchanger substitute (Calmidi & Mahajan 2000, Bhattacharya & Mahajan 2002) due to their attractive properties, such as high surface area, high thermal conductivity and low density (Thewsey & Zhao 2008, Xiao & Zhao 2013, Diao et al. 2015, 2017).

2.4.4.1 Research progress on natural convection in porous metals

Natural convection in both low porosity and high porosity metal foams has been studied for a long time (Lee et al. 2017, Achenbach 1995). The high flow resistance of low porosity metal foams (0.3 - 0.5) has limited their applications as heat exchang-

ers under natural convection. Metal foams with high porosity are more suitable as heat exchangers under natural convection. Natural convection in high porosity metal foams has been studied both experimentally and numerically.

The most important and interesting case is that a horizontal layer of porous media uniformly heated from below. This case, the porous medium analog of the Reyleigh-Benard problem, was first treated by Horton & Rogers Jr (1945) and independently by Lapwood (1948). Fig. 2.12 shows the schematic of the Horton-Rogers-Lapwood problem. A Cartesian frame with the z axis vertically upward. The layer is confined by boundaries at $z = 0$ and $z = H$, the lower boundary being at uniform temperature $T_0 + \Delta T$ and the upper boundary at temperature T_0. Thus a layer of thickness H and an imposed adverse temperature gradient $\Delta T/H$ is obtained. The medium is supposed to be homogeneous and isotropic, that Darcy's law is valid, and that the Oberbeck-Boussinesq approximation is applicable. Other assumptions includes local thermal equilibrium, negligible heating from viscous dissipation, negligible radiative effects. Then the conservation equations are

$$\nabla \cdot \mathbf{v} = 0 \tag{2.7}$$

$$c_a \rho_0 \frac{\partial v}{\partial t} = -\nabla P - \frac{\mu}{K}\mathbf{v} + \rho_f \mathbf{g} \tag{2.8}$$

$$(\rho c)_m \frac{\partial T}{\partial t} + (\rho c_p)_f \mathbf{v} \cdot \nabla T = \lambda \nabla^2 T \tag{2.9}$$

$$\rho_f = \rho_0[1 - \beta(T - T_0)] \tag{2.10}$$

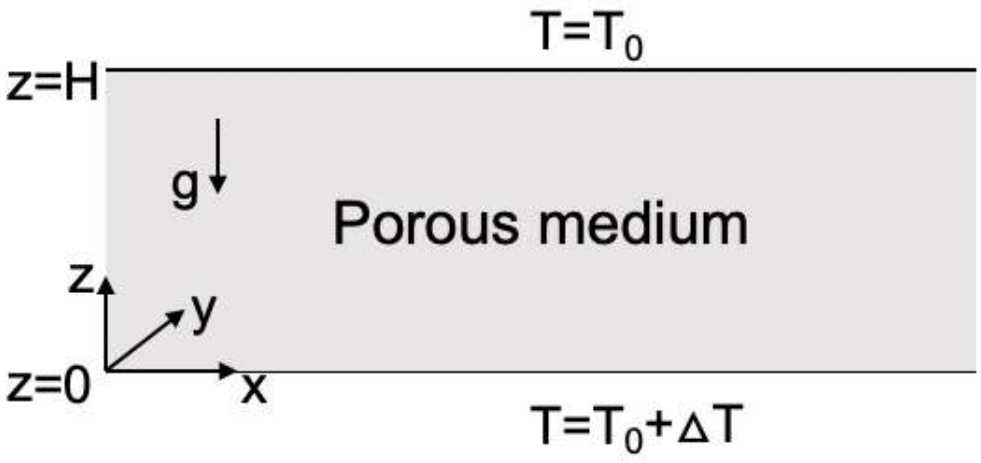

Figure 2.12: The Horton-Rogers-Lapwood problem: infinite horizontal porous layer heated from below.

where $\mathbf{v}$ is the seepage velocity, P is the pressure, μ the dynamic viscosity, K the permeability, c the specific heat, c_a the acceleration coefficient, c_p the specific heat at constant pressure, ρ_0 the reference density, ρ_f the density of the fluid, λ the overall effective thermal conductivity, and β the thermal volume expansion coefficient.

A lot of analysis have been made based on the above fundamental equation. The solution of the equations at small perturbation (linear stability and weak non-linear analysis) has been made (Nield et al. 2006). Other researchers studied the effects of local thermal nonequilibrium (Khashan et al. 2005), non-Darcy, dispersionm viscous dissipation (Magyari & Rees 2006), and non-Boussinesq on convection(Nield 1996). The correlations between heat transfer coefficient and temperature difference have been proposed (Nield et al. 2006). Heat flow in the Darcy flow limit scales as

$$Nu \sim \frac{1}{40} Ra \tag{2.11}$$

In contrast the heat transfer rate in the Forchheimer flow limit scale as

$$Nu \sim Ra^{1/2} \tag{2.12}$$

where Nu is Nusselt number and Ra is Rayleigh number. The most often used form in engineering field is $Nu = C_T Ra^n$, where C_T and n are correlation parameters (Incropera et al. 2007).

Various factors including pore size, porosity, foam height and orientation have been experimentally explored. Bhattacharya & Mahajan (2006) experimentally investigated the buoyancy-induced convection in aluminium foams of different pore sizes (5, 10, 20, and 40 pores per inch, PPI) and porosities (0.89-0.96). The result showed that compared to a heated surface, the heat transfer coefficient in metal foam heat sinks is five to six times higher. They also found that the heat transfer performance decreases with increasing porosity and pore size. Hetsroni et al. (2008) experimentally investigated the natural convection heat transfer in metal foam strips, with internal heat generation. It was found that the foam enhanced the heat transfer performance up to 18 - 20 times relative to a flat plate of the same overall dimensions. In their experiment, the 20 PPI foam performed better than the 40 PPI foam. Zhao, Lu & Hodson (2005) conducted a combined experimental and numerical study on natural convection in open−cell metal foams which were heated from below. They found that natural convection is significant in the Al foams, accounting for up to 50% of the ETC. Further numerical studies indicated that natural convection is promoted by a higher permeability.

2.4.5 Forced convection in porous metals

For the flow parallel to a flat surface that borders the fluid-saturated porous medium. The porous medium is heated from below. With reference to the two-dimensional geometry defined in Fig. 2.13. The equations governing the conservation of mass, momentum (Darcy flow), and energy in the flow region of thickness(Nield et al. 2006) δT :

$$\frac{\partial u}{\partial x} + \frac{\partial v}{\partial y} = 0 \tag{2.13}$$

$$u = -\frac{K}{\mu}\frac{\partial P}{\partial x}, v = -\frac{K}{\mu}\frac{\partial P}{\partial y} \tag{2.14}$$

$$u\frac{\partial T}{\partial x} + v\frac{\partial T}{\partial y} = \alpha_m \frac{\partial^2 T}{\partial y^2} \tag{2.15}$$

where α_m is the thermal diffusivity of the porous medium. The fundamental question in forced convection engineering is to determine the relationship between the heat transfer rate and flow rate or temperature difference. The relationships in the plane wall with prescribed temperature and constant heat flux have been studied by Afifi & Berbish (1999), Magyari et al. (2001) and Ramirez & Saez (1990), Ling & Dybbs (1992), respectively. At high flow rate where the Darcy's law is invalid, Nakayama & Ebinuma (1990), Lai & Kulacki (1989) studied the effects of inertial and thermal dispersion. A lot of researchers includes Vafai & Tien (1989), Jiang et al. (1998), Jiang (1999), Moghari (2008) studied the local thermal nonequilibrium in porous medium forced convection with a two-temperature model.

Under forced convection, the fluid is forced to flow through the porous metal by

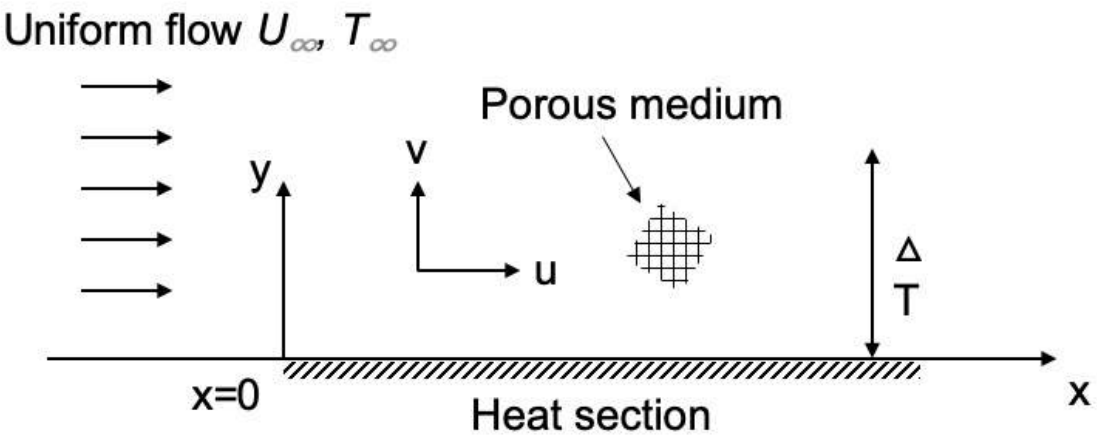

Figure 2.13: Parallel flow through a porous medium with heated from below.

an external source such as fans and pumps. There are two stages involved in the transfer of heat from a heat source to a coolant flowing in a porous metal attached to the heat source. These are heat conduction in the metal matrix and heat convection between the metal matrix and the coolant. The second stage (heat convection) is greatly affected by the surface area and flow condition within the porous metal. As reviewed in the last section, open cell porous metals show great potential as heat exchangers under natural convection due to their large specific surface area and good thermal conductivity (Ashby et al. 2000, Thewsey & Zhao 2008), so do they under forced convection.

Forced convection can significantly enhance heat transfer, especially when natural convection does not meet cooling requirements. Understanding the fluid flow hydrodynamics and heat transfer performance of porous metals under forced convection is of great significance for the development of new generation heat exchanger devices.

Experimental and analytical investigations on heat convection in porous media have

been carried out. Comparison of forced convective heat transfer performance between metal foams and several commercially available heat exchangers was made by Mahjoob & Vafai (2008). Metal foams provide substantially more heat transfer surface area and more boundary layer disruption, which significantly promote heat convection. Dai et al. (2012) compared an open-cell foam heat exchanger with a convectional flat-tube louver-fin heat exchanger. They found that under the same input power and heat transfer rate, the metal foam heat exchanger can be significantly smaller in volume and lighter in weight over a wide range of design space.

2.4.5.1 Correlations of Nusselt number and Reynolds number

For porous metals, the pores are usually in micron scale and the tortuous channels can enhance mixing greatly. The local temperature difference is so small that its influence on fluid property is negligible. Wakao & Funazkri (1978), inspired by the mass transfer correlation in packed bed, correlated Nusselt number and Reynolds number without accounting for the influence of viscosity difference. The correlation was in the form of

$$Nu = 2 + 11Re^{0.6}Pr^{1/3} \tag{2.16}$$

The above equation was is valid on two conditions: the particles in the packed bed are all active and the number of particle layers in the packed bed is greater than two. This correlation has been compared with available experimental data in literature. It showed that at low Reynolds numbers (Re $<$ 100) it underestimated the experimental data, but at high Reynolds number, it represented the experimental data well.

More recently, Hwang & Chao (1994) studied the heat transfer of sintered bronze

beads with different bead sizes. The measurements covered the data in both thermal entrance and thermally fully developed regions. It was found that smaller particles could effectively reduce the thermal entrance length. In their study, the heat transfer between the solid and the fluid phase was fitted well by a relation of the form

$$Nu = C_T Re^n \tag{2.17}$$

where C_t and n are correlation parameters. The values of C_t and n were found to be different below and above the Reynolds number of 100.

Further discussion based on dimensional analysis can be done for the above equation (Bertola & Cafaro 2005, Incropera et al. 2007). It helps to increase the understanding of the intermediate asymptotic behaviours of fluid flow and isolate the effects of different physical mechanisms. The scale dependent character of physical quantities allows one to unfold dimensional groups inside dimensionless numbers; for instance, for the Reynolds number, it can be written as

$$Re = \frac{[U][D]}{[\nu]} = \frac{[L]^2[T]^{-1}}{[l]^2[t]^{-1}} \tag{2.18}$$

where U is velocity, D is pore diameter, ν is kinetic viscosity, L and l are macro-length and micro-length, T and t are macro-time and micro-time.

when a univocal scale-dependent character cannot be determined a priori, which happens whenever a quantity depends simultaneously on two independent physical mechanisms having different scales, one can use a equation of $[L]^\zeta[l]^{1-\zeta}$ and $[T]^\zeta[t]^{1-\zeta}$ to identify micro- and macro-components. Therefore, the Nusselt number can be

expressed as

$$Nu = \frac{[L]^{1+\zeta}[l]^{-(1+\zeta)}}{[T]^{\tau}[t]^{-\tau}} \tag{2.19}$$

Combining equations 2.17, 2.18 and 2.19, and imposing dimensional homogeneity of micro- and macro-components, one find that for forced convective flows

$$n = \frac{1}{2}(1+\zeta) = \tau \tag{2.20}$$

Thus, the exponent of Nusselt number, which is usually determined empirically, is related to the weights of macro-quantities, that is, to numbers expressing the relevance of macro-quantities in convection. This is useful when distinguish laminar from turbulent flow. Laminar flows are dominated by diffusion processes, so that micro-quantities are prevailing and one can write the following inequalities

$$\zeta < 1-\zeta, \tau < 1-\zeta. \tag{2.21}$$

Substituting equation 2.20 into these inequalities yields $n < 0.5$. On the other hand, the importance of macro-quantities is greater in turbulent flows, which are dominated by inertia, so that

$$\zeta > 1-\zeta, \tau > 1-\zeta. \tag{2.22}$$

This determines a lower bound for the exponent $n > 0.75$. The bounds on the values of exponent n calculated by means of scale-size analysis are perfectly consistent with the well-known heat- and mass-transfer empirical correlations reported in standard heat transfer books (Incropera et al. 2007, Kreith et al. 2012).

However, there are more flow regimes in porous structure and the flow behaves more complex than that in a open pipe flow. The above conclusions need to be compared

with experimental results. In addition, the porous media involved in the previous studies are largely limited to packed beds and granular porous media with porosities in the range of $0.3 - 0.5$ (Fand et al. 1987, Kececioglu & Jiang 1994). Very little research has been conducted on the effect of flow behaviour (laminar, transitional and turbulent) on forced convective heat transfer in porous metals manufactured by the space holder methods, which have a porosity range of 0.5 - 0.8. Consequently, further investigations are necessary to achieve a better understanding of flow hydrodynamic, forced convective heat transfer performance and their relations in metal foams.

2.5 Summary

Open-cell porous metals are an potential alternatives to traditional heat exchangers due to their high surface area, high thermal conductivity and light weight. Commercial processes for producing porous metals such as metal gas injection, investment casting, metal deposition and gas-metal eutectic solidification are generally costly and inefficient. LCS process based on space holder method is an efficient and low cost method for producing open-cell porous metals with controllable porosity, pore size and pore shape.

The heat transfer properties, such as heat transfer coefficient and thermal conductivity, of the porous metal and the fluid flow behaviour within it need to be considered when a porous metal is used in thermal appliances. Although studies have been conducted on heat transfer performance and flow behaviour in porous media, previous studies are only focused on the packed bed (porosity < 0.4) and Al foam (porosity $>$

0.90), and the pore size is on the order of millimetres. Therefore, understanding the heat transfer performance and flow behaviour in a pore medium with porosity range of 0.5 - 0.9 is necessary. In addition, heat transfer performance of porous metals and the flow behaviour within it have never been studied simultaneously, so the effect of the flow behaviour on the heat transfer performance is unclear.

Chapter 3

Experimental Methods

3.1 Preparation of porous samples

The fabrication processes for four porous materials, namely porous copper, porous glass, sintered copper and sintered glass, are described in this section. For the porous copper samples, potassium carbonate was used as the pore agent and the LCS process was applied. For the porous glass samples, sodium chloride was used as the pore agent and the Sintering Dissolution Process (SDP) was applied. Sintered copper and sintered glass were fabricated by directly sintering copper spheres and glass spheres together.

3.1.1 Preparation of porous copper samples

The LCS process involves three basic steps: mixing, compaction and sintering (Zhao & Sun 2001, Zhao, Fung, Zhang & Zhang 2005). Figure 3.1 schematically presents the fabrication procedure used for manufacturing the porous copper samples. The details of each step are described separately below.

The LCS process uses K_2CO_3 powder as the pore agent, which can be eliminated by decomposition. The relatively high melting temperature of K_2CO_3 (890^oC) makes it possible to sinter copper at a high temperature, ensuring strong bonding between the copper particles before the pore agent is decomposed. The porous copper samples manufactured by the LCS process have porosity ranging from 0.5 to 0.85, pore size ranges of 250 - 425 μm, 425 - 710 μm, 710 - 1000 μm and 1000 - 1500 μm, and different pore shapes.

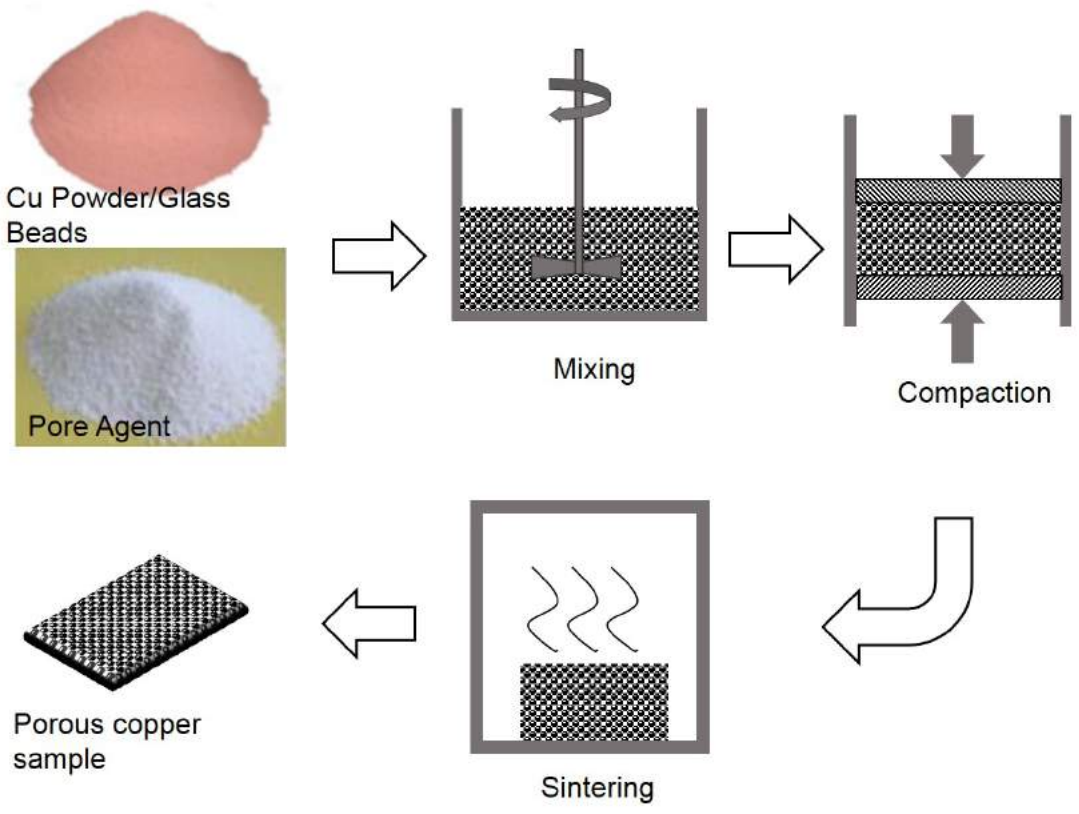

Figure 3.1: Schematic showing stages involved in the fabrication of porous samples.

3.1.1.1 Raw materials

The raw materials used for making the porous copper samples were a copper powder and a potassium carbonate powder. A copper powder (Ecka Granules UK Ltd) with a mean particle diameter of 75 μm and purify of 99.5% was used. Food grade potassium carbonate granules (EE Ltd, Australia), with particle size ranges of 250 - 450μm, 450 - 710μm, 710 - 1000μm and 1000 - 1500μm, and purity of 99% were used as the pore agent. Potassium carbonate with irregular shape and particle size range of 425-710 μm was also used to make the porous copper samples. Fig. 3.2 shows typical optical micrographs of the copper particles, spherical and irregular potassium carbonate particles used in the present study. The final pore size and pore shape within the porous copper samples are determined by the pore agent.

3.1.1.2 Mixing and compaction

The pore agent and the copper powder were mixed at a pre-specified volume ratio according to the target porosity. The masses of the copper powder (M_{Cu}) and the potassium carbonate powder (M_{Agent}) needed for the porous copper sample were determined by the following equations:

$$M_{Cu} = (1 - \varepsilon) V m \rho_{Cu} \tag{3.1}$$

$$M_{Agent} = \varepsilon V m \rho_{Agent} \tag{3.2}$$

where ρ_{Cu} is the density of pure copper, ρ_{Agent} is the density of the pore agent, ε is the target porosity and V is the target volume of the porous sample. Since the spaces

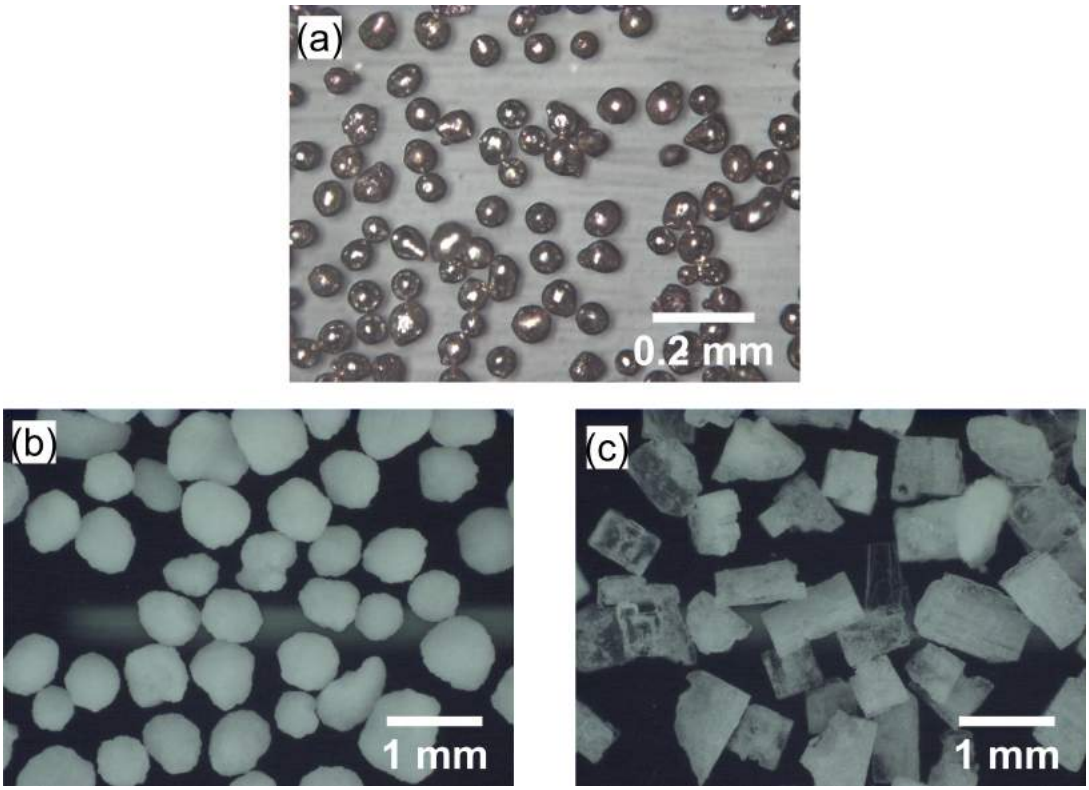

Figure 3.2: Optical micrographs of (a) copper particles, (b) spherical potassium carbonate particles (425-710 μm) and (c) irregular potassium carbonate particles (425-710 μm).

between the copper particles in the copper/pore agent mixture were ignored in the calculations, the quantities of copper and pore agent were slightly more than those actual needed, and the final sample was slightly larger than the designed volume. As a result, the final porosity of the porous copper sample was slightly higher than the target porosity. The lower the porosity, the greater the difference. However, the differences were negligible for the samples used in this study.

The weighted copper and pore agent powders were poured into a glass beaker and a small amount of ethanol was added as a binder. The mixture was then mixed using a glass stirring rod until the pore agent particles were covered with a layer of copper

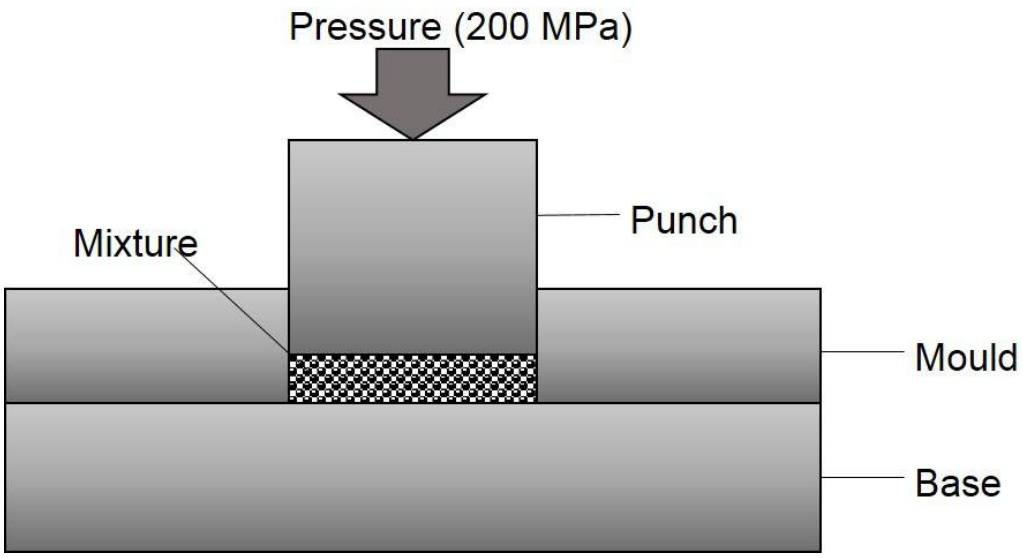

Figure 3.3: Schematic of the compaction step in fabricating porous copper preforms in a mould.

particles. At last, the mixture was compressed to a cuboid shape in a steel mould under a pressure of 200 MPa for approximately ten seconds by a hydraulic press (Moore Hydraulix press, UK). Fig. 3.3 shows schematically the compaction step in making porous copper preforms in a mould. The compact was removed from the mould and placed in a desiccator with silica gel to prevent the potassium carbonate from adsorbing moisture.

3.1.1.3 Sintering and shaping

A VTS vacuum furnace was used for the sintering process. The green compacts were placed on a stainless steel plate with a piece of alumina paper separating the samples and the plate. In order to prevent the the samples form oxidization, the heating of the furnace started after the chamber pressure was evacuated to below 10^{-1} Pa. A typical sintering procedure is shown schematically in Fig. 3.4. The furnace was

first heated to 200^oC and kept at this temperature for 30 minutes to evaporate the ethanol and water in the preforms. The preforms were pre-sintered at 800^oC for 30 minutes to prevent the copper particles from collapsing during sintering. This sintering temperature was selected such that the particles of potassium carbonate, which has a melting temperature of 891^oC, remained in the solid state. In order to remove the carbonate and achieve strong bonding between copper particles, the performs were further sintered at 950^oC for 2 hours. In the second sintering stage, the potassium carbonate decomposed completely, resulting in open-cell porous copper samples with fixed porosities and pore sizes. Figure 3.5 shows typical porous copper samples produced after sintering.

All the sintered samples were cut into a required shape and dimensions by electrical discharge machining (EDM). The dimension of the samples were 55 mm $\times$ 20 mm $\times$ 15 mm, 30 mm $\times$ 30 mm $\times$ 10 mm and 30 mm $\times$ 20 mm $\times$ 5 mm for the thermal conductivity, natural convection and forced convection measurements, respectively.

3.1.2 Preparation of sintered copper samples

Sintered copper samples with different copper particle sizes were manufactured for thermal conductivity measurements. The manufacture process for the sintered copper was the same as that used for the porous copper except that no pore agent was used. Six types of copper powder with particle size ranges of 10 - 20 μm, 20 - 45 μm, 45 - 70 μm, 75 - 90 μm, 100 - 250 μm and 710 - 1000 μm were used. All the copper powders have a high purify of 99.5% and spherical particles. These copper were also supplied by Ecka Granules UK Ltd.

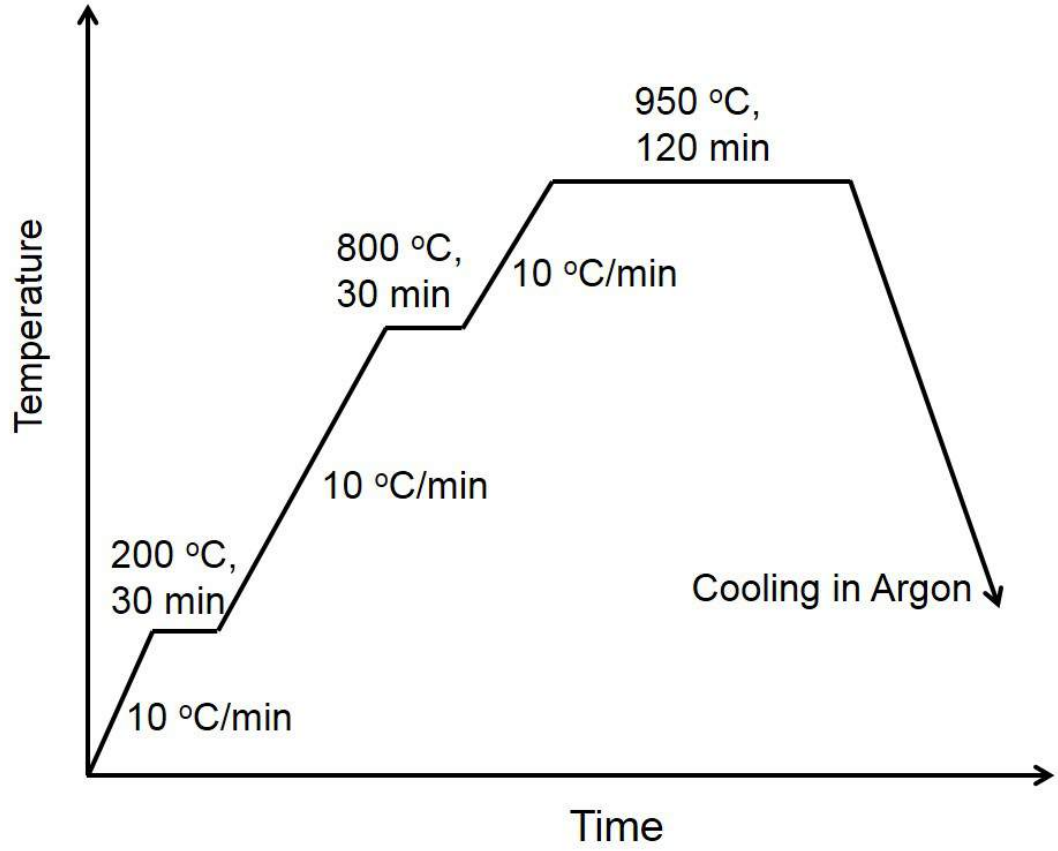

Figure 3.4: Schematic diagram of sintering procedure.

The weighted copper powder was poured into the mould directly and carefully shaked to ensure that the particles were packed as tightly as possible. The powder was then compacted by a punch under a pressure of 200 MPa for ten seconds by a hydraulic press (Moore Hydraulix press, UK). The compact was removed from the mould and placed on a tray for subsequent sintering. The same sintering procedure as used for the porous copper samples, as shown in Fig. 3.4, was used. The sintered copper samples were cut into a rectangular shape with dimensions of 55 mm $\times$ 20 mm $\times$ 15 mm.

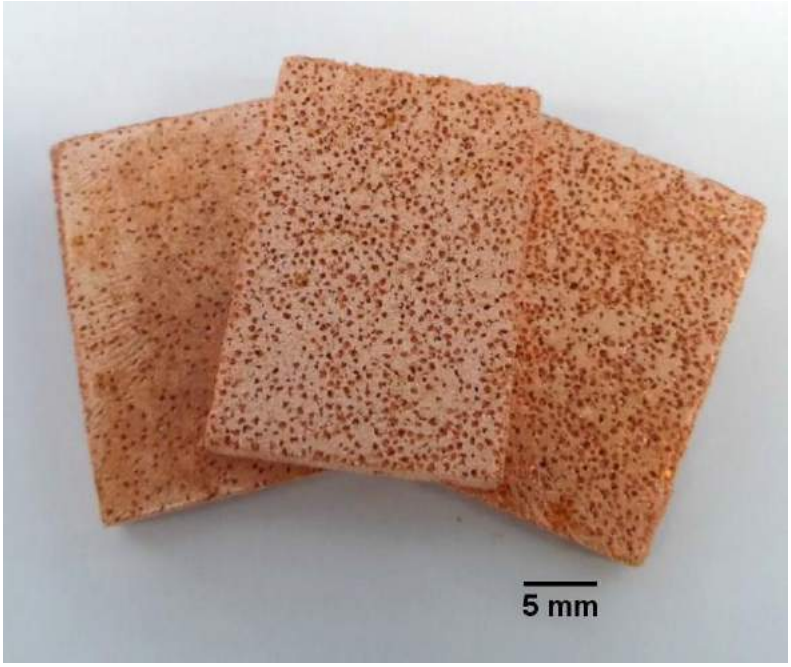

Figure 3.5: Typical porous copper samples produced after sintering using the LCS process.

3.1.3 Preparation of porous glass samples

Porous glass samples with spherical and irregular pores were fabricated by the SDP process (Zhao & Sun 2001). The SDP process is similar to the LCS process, except for a different pore agent and a different way to remove pore agent. Four porous glass samples with spherical pores having porosities of 0.72 0.77, 0.78 and 0.81, and five porous glass samples with irregular pores having porosities of 0.67, 0.69, 0.73, 0.77 and 0.83 were manufactured, respectively.

3.1.3.1 Raw materials

The raw materials used for fabricating the porous glass samples were glass and sodium chloride powders. The glass powder was supplied by Richard Baker Har-

rision Ltd, UK, and has a particle size range of 30 - 50 μm. The sodium chloride powder was bought from TESCO store (UK Ltd) and it is food grade salt. Fig. 3.6(a) shows the typical optical micrographs of the glass, spherical and irregular sodium chloride powders. The particles in the glass powder are not 100% spherical and some irregular particles are present. Fortunately, these irregular glass particles tend to become spherical at high temperature due to surface tension. There are a small number of non-spherical and cracked particles in the spherical sodium chloride powder. Both the spherical and irregular sodium chloride powder has a particle size range of 425-710 μm. The average particle size was used as the characteristic length in all calculations.

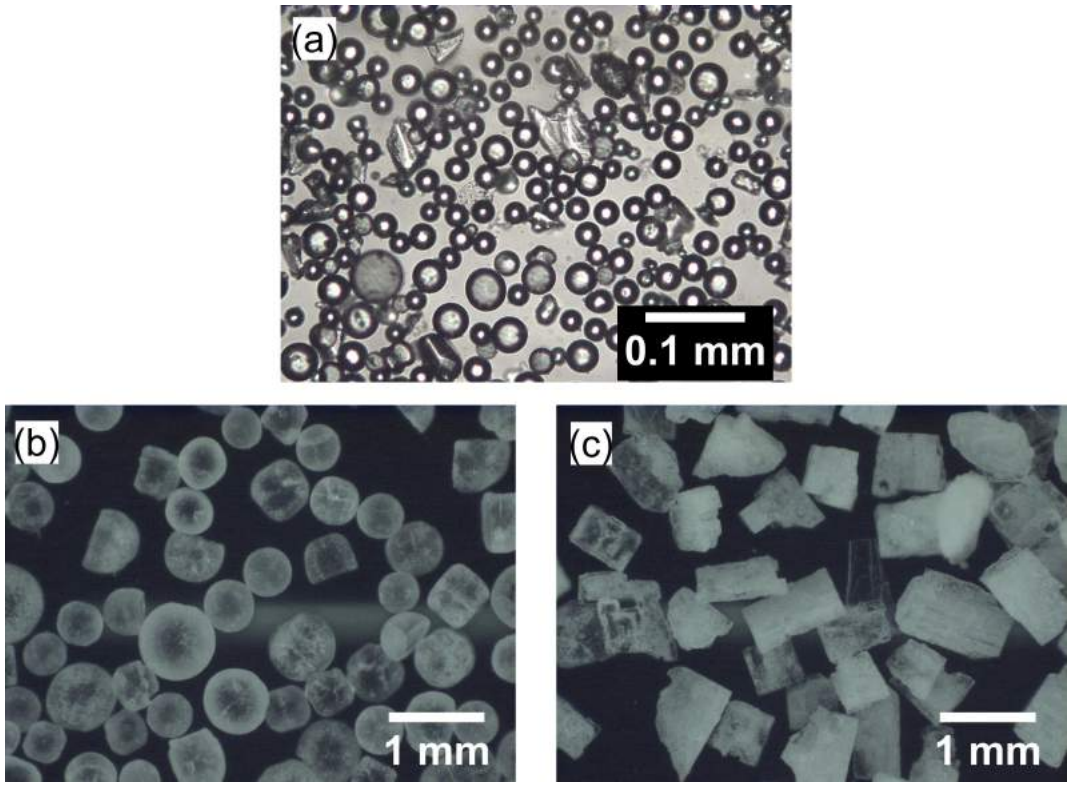

Figure 3.6: Optical micrographs of (a) glass powder, (b) spherical sodium chloride powder and (c) irregular sodium chloride powder.

3.1.3.2 Mixing and sintering

The SDP process is similar to the LCS process, except for a different pore agent and a different way to remove pore agent, so only a brief description is made in this section. The glass powder powder was mixed with the sodium chloride at a prespecified volume ratio according to the target porosity and then compacted in a rectangular mould with two specially machined glass slides at the top and bottom, respectively. Unlike in the fabrication of porous copper samples, the mixture of the glass powder and sodium chloride powder could not be pressed at a high pressure because they are too brittle. Therefore, the mixture was slightly shaked and pressed manually so that the particles tightly packed together.

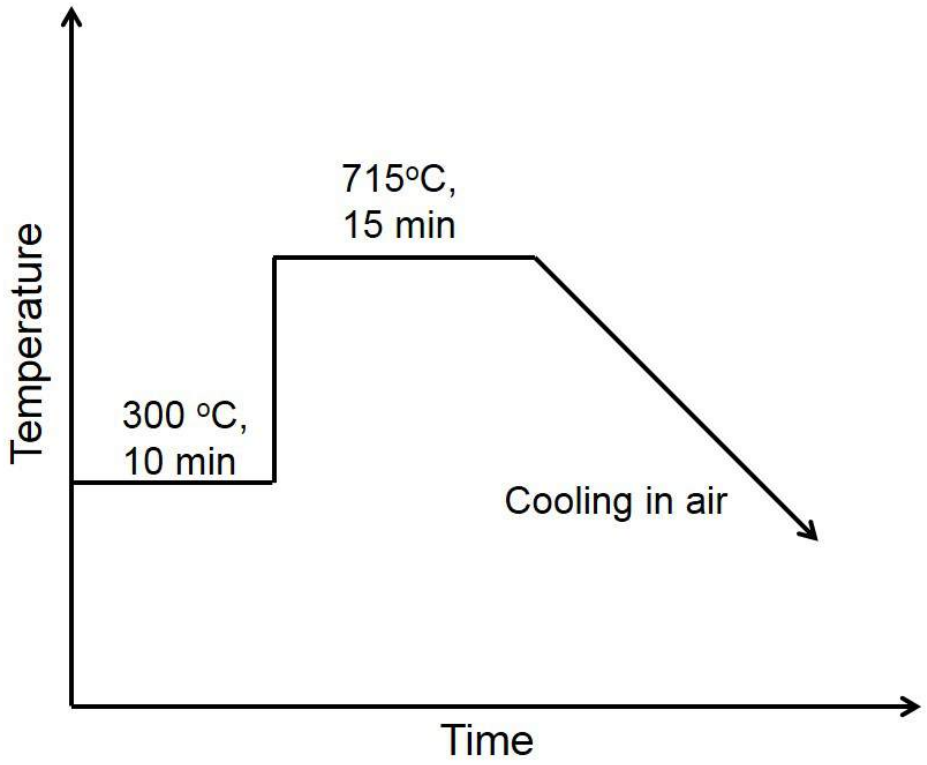

Figure 3.7: Schematic diagram of sintering procedure for porous glass samples.

Fig. 3.7 shows a schematic diagram of the sintering process for the porous glass samples. The preform was first preheated in a low temperature (200 - 300^{o}C) furnace for 10 minutes and then moved rapidly to another furnace at 715^{o}C, and sintered for 15 minutes. Preheating was performed to avoid fracture of the glass particles and the glass slides due to rapid changes in temperature. The sample was gradually cooled to room temperature after sintering for the same reason. Finally, the sample was removed from the mould and the sodium chloride was rinsed away in water. Fig. 3.8 shows the typical porous glass samples produced by the SDP process. The dimensions of the porous glass samples are 25 mm $\times$ 26 mm $\times$ 3.5 mm (thickness of glass slides included).

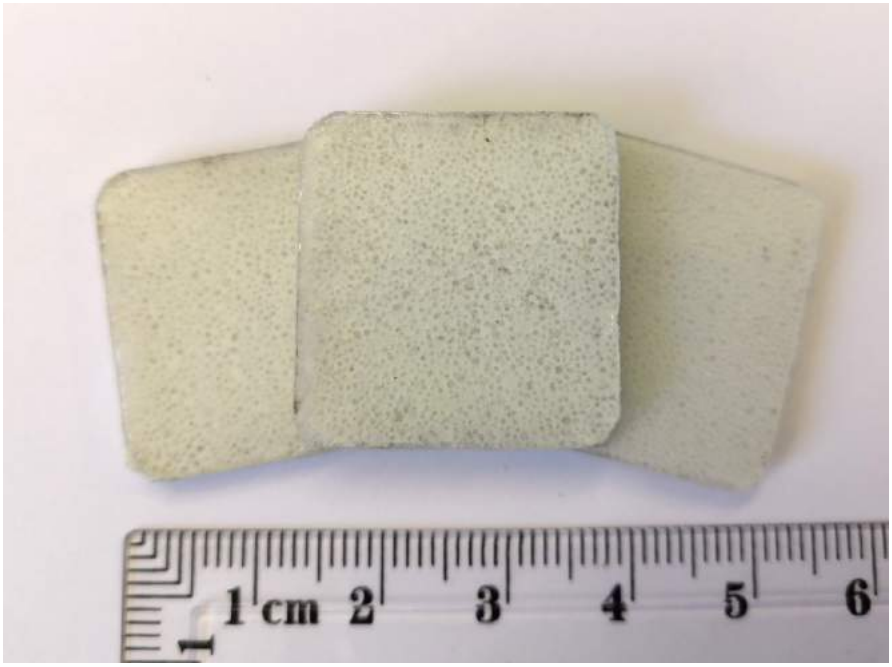

Figure 3.8: Typical porous glass samples produced by the SDP process.

3.1.4 Preparation of sintered glass samples

Three types of glass powders (Boud Minerals Ltd, UK) with diameter ranges of 100 - 200 μm, 300 - 500 μm and 500 - 900 μm were used to fabricate sintered glass samples. The corresponding mean diameters of the glass spheres are 170, 430, and 710 μm, respectively. The mean diameter of the glass powder was taken as Sauter mean diameter (Scala 2013), which was determined from the mean volume equivalent diameter and surface equivalent diameter. Specifically, the mean diameter of the glass powder was obtained by

$$D_m = \frac{\sum_{i=1}^{k} n_i D_i^3}{\sum_{i=1}^{k} n_i D_i^2} \tag{3.3}$$

where n_i is the quantity of the particles with a diameter of D_i, and k is the number of particles with different diameters.

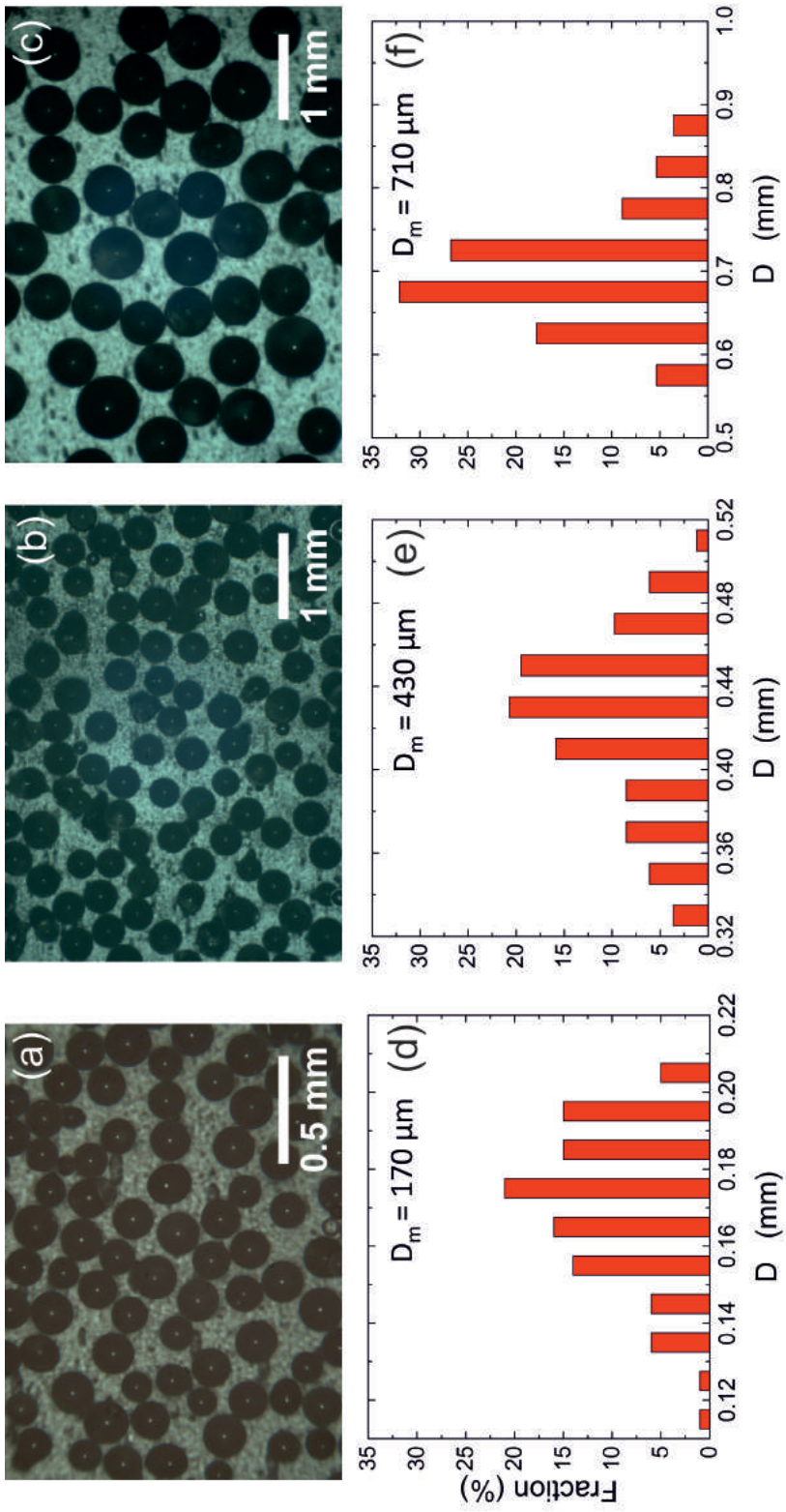

Figure 3.9: Microscope image and diameter distribution of glass spheres with diameter range of (a) and (d) 100-200 μm, (b) and (e) 300-500 μm, and (c) and (f) 500-900μm.

Fig. 3.9 shows the micrographs and particle size distributions of the glass spheres. The particle size distributions were obtained by taking pictures of the glass spheres by an optical microscope and then measuring the diameter of each sphere using the software Image J. The mean diameter of each glass powder was used to characterise the powder in this study.

The sintered glass samples were fabricated by the same process used for fabricating the porous glass samples, except no pore agent was used. The weighted glass spheres were poured into the mould with a glass slide at the bottom. The mould was then shaked manually to ensure that all spheres were tightly packed. Finally, another piece of glass slide was placed on the top and pressed carefully. The preform was then sintered following the same process as shown in Fig. 3.7. The as-fabricated sintered glass samples with particle mean diameters of 170 μm, 430 μm and 710 μm had porosities of 34%, 37% and 40% and were designated as PB170, PB430 and PB710 respectively.

3.1.5 Summary of samples and their characteristics

Table 3.1 lists all the samples manufactured and investigated in this study. The "SG" and "IG" series porous glass samples (spherical and irregular pores) and sintered glass samples were used for pressure drop and flow visualization measurements. The "SCT" series porous copper samples (spherical pores) and sintered copper samples were used for thermal conductivity measurements. The " SCN" series porous copper samples (spherical pores) were used for natural convection study. The"IC" series porous copper samples (irregular pores) were used for pressure drop and forced

convection investigations.

Table 3.1: List of samples investigated in this study.

Sample type	Sample name	Particle size (μm)	Pore size (μm)	Porosity
Porous glass	SG72	30-50	425-710	0.72
with	SG77	30-50	425-710	0.77
spherical	SG78	30-50	425-710	0.78
pores	SG81	30-50	425-710	0.81
	IG67	30-50	425-710	0.67
Porous glass	IG69	30-50	425-710	0.69
with irregular	IG73	30-50	425-710	0.73
pores	IG77	30-50	425-710	0.77
	IG83	30-50	425-710	0.83
	G170	150-250	-	0.34
Sintered glass	G430	250-425	-	0.34
	G710	425-850	-	0.40
	SCT2001	75	250-425	0.62
	SCT2002	75	250-425	0.63
	SCT2003	75	250-425	0.69
	SCT2004	75	250-425	0.73
	SCT2005	75	250-425	0.76
	SCT4001	75	425-710	0.59
	SCT4002	75	425-710	0.63
	SCT4003	75	425-710	0.66
	SCT4004	75	425-710	0.70
Porous copper with spherical				

	SCT4005	75	425-710	0.74
	SCT4006	75	425-710	0.77
	SCT4007	75	425-710	0.80
	SCT7001	75	710-1000	0.59
	SCT7002	75	710-1000	0.66
	SCT7003	75	710-1000	0.69
	SCT7004	75	710-1000	0.73
	SCT7005	75	710-1000	0.80
	SCT1001	75	1000-1500	0.60
	SCT1002	75	1000-1500	0.63
	SCT1003	75	1000-1500	0.70
	SCT1004	75	1000-1500	0.75
	SCT1005	75	1000-1500	0.78
	SCN2001	75	250-425	0.65
	SCN2002	75	250-425	0.70
	SCN2003	75	250-425	0.75
	SCN2004	75	250-425	0.79
	SCN2005	75	250-425	0.82
	SCN4001	75	425-710	0.66
	SCN4002	75	425-710	0.71
	SCN4003	75	425-710	0.77
	SCN4004	75	425-710	0.81
Porous	SCN4005	75	425-710	0.85
copper with	SCN7001	75	710-1000	0.66
spherical	SCN7002	75	710-1000	0.70
pores				

	SCN7003	75	710-1000	0.76
	SCN7004	75	710-1000	0.80
	SCN7005	75	710-1000	0.85
	SCN1001	75	1000-1500	0.67
	SCN1002	75	1000-1500	0.71
	SCN1003	75	1000-1500	0.76
	SCN1004	75	1000-1500	0.82
	SCN1005	75	1000-1500	0.83
Porous copper with irregular pores	IC64	75	425-710	0.64
	IC66	75	425-710	0.66
	IC71	75	425-710	0.71
	IC75	75	425-710	0.75
	IC78	75	425-710	0.78
Sintered copper	C1	10-20	-	0.12
	C2	20-45	-	0.13
	C3	45-70	-	0.12
	C4	75-90	-	0.16
	C5	45-90	-	0.15
	C6	710-1000	-	0.13

The porous structure of the samples was analysed using an Nikon optical microscope and a scanning electron microscope (SEM, JEOL-JSM-6610). The porosity of each sample was obtained by measuring its density. The mass of the sample was obtained by an electronic balance and the dimensions (length, width and height) of the sample were measured by a calliper for five times at different positions to obtain a mean

value. The porosity (ϵ) was calculated by:

$$\epsilon = 1 - \frac{M}{Vm\rho_{pure}} \tag{3.4}$$

where M and Vm are the mass and volume of the porous sample, respectively, and ρ_{pure} is the density of pure copper or glass.

3.2 Flow visualization in porous glass

The experimental methodologies of determining the velocity field within micro pores and measuring the pressure drop across the porous media are described in this section. The details of the flow rig, flow system and the μ-PIV system are provided. The method of measuring the pressure drop is explained. The selection of working fluid, image acquisition, pre and post processing are described in details.

3.2.1 Definition of Reynolds number

The Reynolds number was defined as $Re = \rho V D_d/\mu$, where ρ is the density of water, V_d is Darcian velocity, D is characteristic length of the sample and μ is dynamic viscosity of water. For porous copper and porous glass samples, the mean diameter of the pores was used as the characteristic length. For the sintered glass and sintered copper samples, the mean diameter of the particles was used as the characteristic length.

3.2.2 experimental setup

Fig. 3.10 shows the experimental system used for velocity field and pressure drop measurements in the porous glass samples. It mainly includes fluid flow feeding, pressure measurement, mass flow rate measurement and image acquisition (μ - PIV system) parts. The working fluid was either pumped by a syringe pump (Harvard Apparatus, PHD ULTRA, not included in the graph) or driven by pressurized air from the pressure vessel. At low velocity, the fluid was driven by the syringe pump because it can control the flow rate from 122.2 nl/min to 126.9 ml/min very precisely. At high velocity, the fluid was driven by pressurized air and a mass balance was used to measure the mass flow rate.

Validyne differential pressure transducers (Validyne Engineering, US) with different ranges were employed to measure the pressure drop across the porous medium. The mass flow rate was measured by a balance directly connected to a computer, which collected the weight data automatically. The weight data was collected every 2 seconds and the final flow rate was determined by averaging all the flow rates in each measurement.

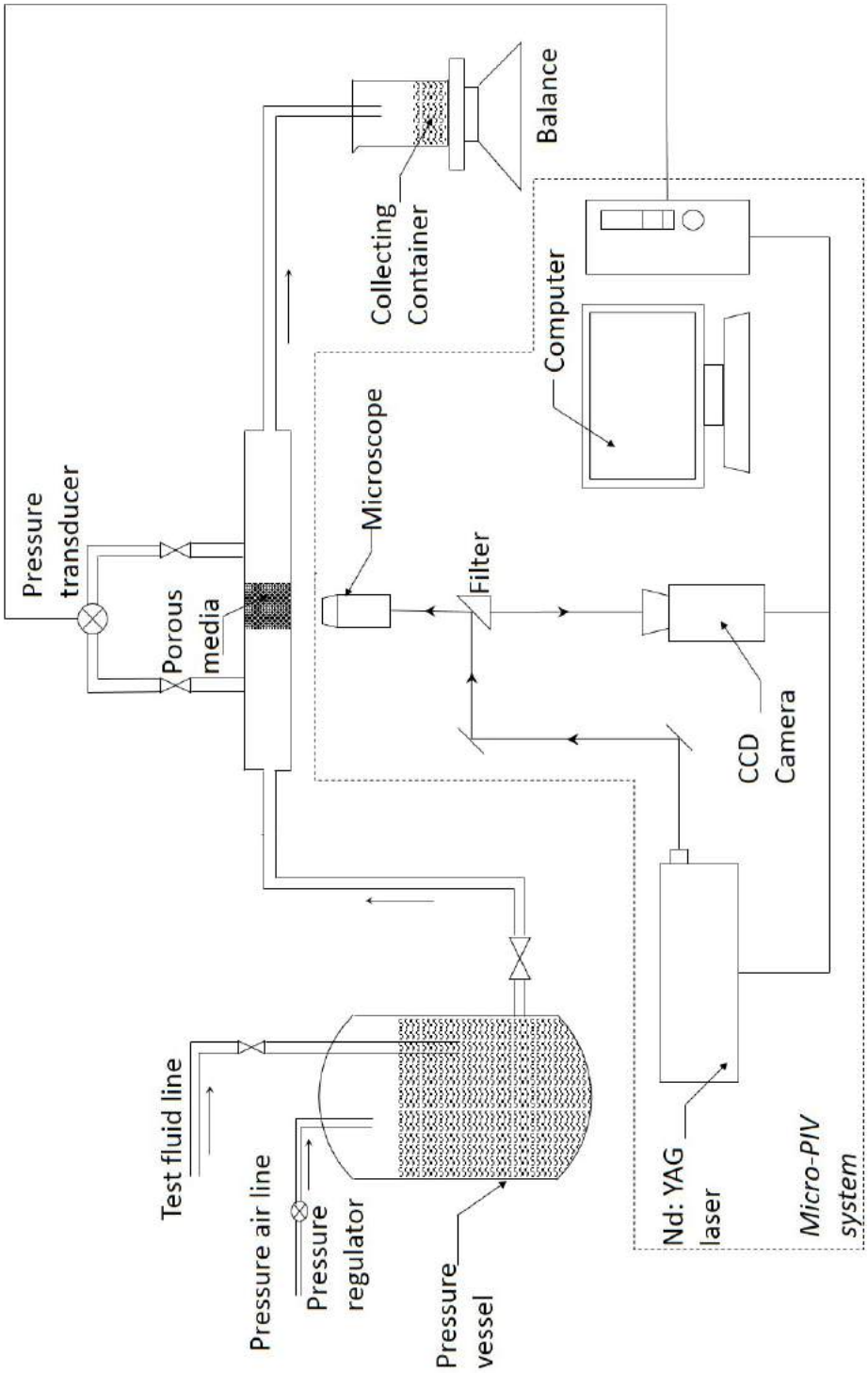

Figure 3.10: Schematic drawing of the flow system and μ - PIV system.

The refractive index of the porous medium after being sintered was roughly determined by saturated the porous medium into solutions with different refractive index and check the transparency of the sample. Mixtures of methyl salicylate (1.526) and dimethyl (1.479) sulfoxide with refractive index from 1.48 to 1.52 at a step of 0.01 were prepared. Saturate the porous medium into different mixtures and check the transparency of the combination under microscope. The refractive index of the most transparent combination was regarded as the refractive index of the porous medium. This refractive index was used as a reference value for the preparation of other solutions.

Both organic and inorganic solutions matching the refractive index of the porous medium (around 1.51) for an optimal view were tested but found not working well in the current setup. Organic solutions such as a mixture of methyl salicylate and dimethyl sulfoxide, with a volume ratio of 7:3, and a mixture of benzyl alcohol (1.54) and ethanol (1.36), with a volume ratio of 17:3, matched the refractive index very well. However, the organic solutions softened and destroyed all the polyvinyl chloride components (flow rig, pipes, and pressure vessel) and reacted with the fluorescent particles, removing their fluorescence so they could no longer be detected by the camera under laser excitation. Inorganic solutions, e.g., sodium iodide (1.51, 40^{o}C, saturated solution) and zinc iodide (1.33 - 1.62) (Bai & Katz 2014) also matched the refractive index well, but iodine precipitated gradually from the solution in air and the solution slowly turned to yellow, significantly affecting the image quality. In addition, iodide is quite expensive compared with the other candidates.

Hence, water was used as the working fluid despite the difference in refractive index compared to the glass (1.33 and 1.512 for water and glass, respectively). 1% fluo-

rescent particles with a diameter of 1 μm (in liquid suspension form, supplied by Thermo Fisher scientific) was added to deionized water to trace the flow path.

3.2.3 Flow rig and pressure vessel

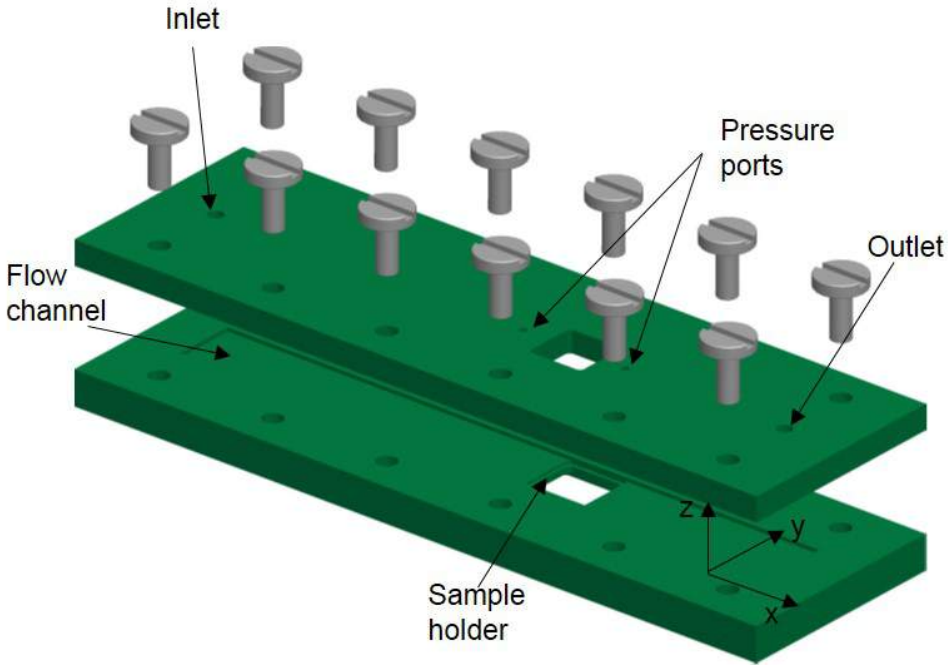

Figure 3.11: The exploded view of the sample holder (test rig).

A special test rig, as shown in Fig. 3.11, was designed in order to create a flow of fluid through the tiny porous glass samples. The rig is made of polyvinyl chloride for easy machining and light weight when put on the microscope platform. The rig consists of a top part and a bottom part. A rectangular channel with internal dimensions of 250 mm $\times$ 25 mm $\times$ 1.5 mm was machined in the bottom part. A hole with the same size of the sample was drilled on the bottom part to ensure that the light from the bottom can be received by the camera. Steps were machined on both top and bottom parts at the hole edges to hold the sample and at the same time,

to offset the thickness of the glass slide. Two ports located 10 mm away from the sample were drilled on both sides of the sample and were connected with a pressure transducer each through pipes. The inlet is 145 mm (96 times of the height of the channel) away from the porous sample to ensure that the flow is fully developed before reaching the porous medium (Han 1960, Goldstein & Kreid 1967).

When loading the sample, the sample was first placed on the hole steps on the bottom part, and the gap between the glass slide and the substrate was filled with silicon gel. The top part was then carefully secured with bolts to ensure that the channel was enclosed and there was no leakage. The gap between the top glass slide and the top part was also filled with silicon gel. The rig was left for 12 hours before using to allow the silicon gel to dry completely.

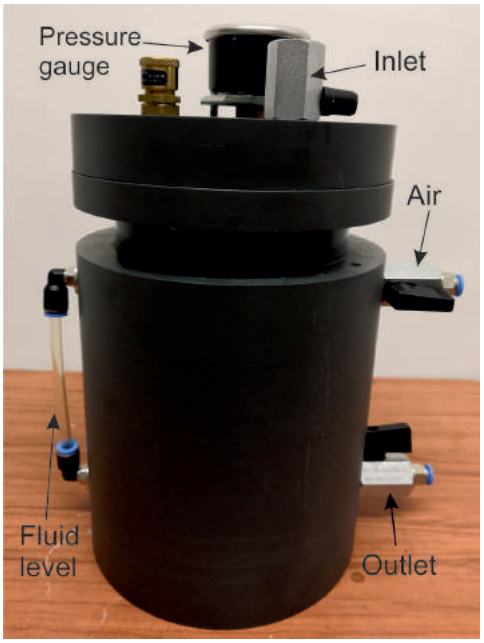

Figure 3.12: The pressurized vessel used for driving fluid flow.

A pressure vessel was designed and used to drive fluid flow through the channel and

the porous glass sample at high velocity. Fig. 3.12 shows a picture of the pressure vessel. The pressure vessel is made of polyvinyl chloride and has a capacity of 1.5 liter. The pressure vessel consists of three ports: an inlet at top for filling working fluid, an outlet at bottom connected to the inlet port of the sample holder (Fig. 3.11) and a connector for connecting to pressurized air. The pressure vessel has a pressure gauge and a fluid level indicator to show the the pressure and the fluid level in the vessel. The pressure within the vessel was controlled in the range of 0.4 bar to 0.8 bar depending on the porosity of the sample and the flow rate.

3.2.4 μ-PIV and image acquisition

The main components of the μ - PIV system (Dantec Dynamics) are shown in Fig. 3.13. A Nd:YAG laser with a wavelength of 532 nm was used for illumination. A microscope (Leica Microsystems Ltd.) with adjustable objectives was used to observe the flow behaviour. During experiment, the fluorescent particles emit light with a wavelength of 612 nm when exited by the laser. This long wavelength light from the particles reaches the camera, while the short wavelength light from the remaining parts is filtered out. A CCD camera (FlowSence series, Dantec Dynamics) mounted on the microscope, which has a resolution of 1600 $\times$ 1200 pixels, was used to collect the images.

Three microscopic objectives, with magnification of 10 $\times$, 20 $\times$ and 40 $\times$ were used for different samples. These objectives give total magnifications of 100 $\times$, 200 $\times$ and 400 $\times$. The field of view of these objectives are 2.16 mm $\times$ 1.62 mm, 1.08 mm $\times$ 0.81 mm and 0.54 mm $\times$ 0.40 mm, respectively. They have depths of field of 8 μm,

3.7 μm and 1 μm respectively, which are effective to exclude the particles in adjacent layers.

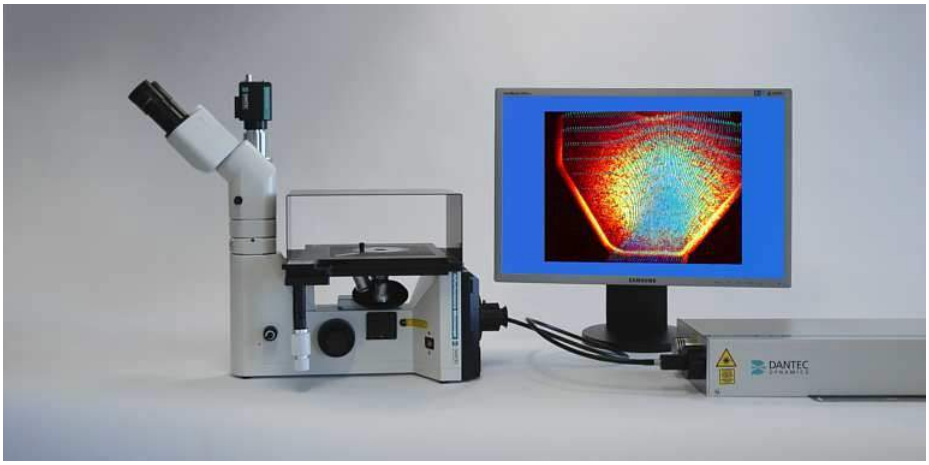

Figure 3.13: Dantec Dynamics μ-PIV system.

Before each measurement, pure water was driven through the flow system at a high flow rate (> 5 g/s) to ensure that all the trapped air bubbles were expelled. The reason for using pure water to expel air is to prevent fluorescent particles from stacking in the porous medium, which affects the image quality in the following experiment. The flow rate studied ranges approximately from 0.001 g/s to 10 g/s, depending on the porosity of the sample.

For each sample at every chosen Reynolds number, 300 pairs of frames, at a frequency of 8 frame pairs per second, in the $x - y$ plane and fixed z position, were obtained. For flow at very low Reynolds numbers, the single frame mode was used to acquire images because under the double frame mode even the maximum time interval is still too short for the flow to move a far enough distance. Under the single frame mode, the time interval between each frame can range from one-tenth of a second to several seconds. In the cross correlations, the adjacent two single frames

are treated as a frame pair. For flow at high Reynolds numbers, the standard double frame mode was used. Under this mode, the time interval between two frames plays a very important role in the PIV measurements. A short interval means a small displacement of particles between two frames, which will magnify the displacement error and thus the velocity error. However, a large time interval may result in particles flowing out of the interrogation area, leading to totally wrong correlations in subsequent cross correlations. In the present experiment, the time interval range from 15 to 15000 μs depending on the flow rate.

3.2.5 Image processing

The image processing includes pre-processing, vector field calculation and post-processing. The pre-processing involves removing the background and enhancing the signal to noise ratio so that the fluorescent tracing particles can be clearly distinguished from the background. The vector field calculation aims to convert the position information on the pre-processed image to velocity vectors. Post-processing mainly includes plotting velocity filed map, velocity fluctuation calculation and statistical analysis.

The commercial software DynamicStudio (Dantec Dynamics) was used for image pre-processing. Fig. 3.14(a) shows a typical raw image collect from μ-PIV. The glass sphere powder with the average diameter of 710 μm and the fluorescent particles of 1 μm are present. The glass spheres are still visible due to the red light reflection from the nearby fluorescent particles. This is an inherent problem of flowing through porous media: the background fluorescent signals get reflected in the

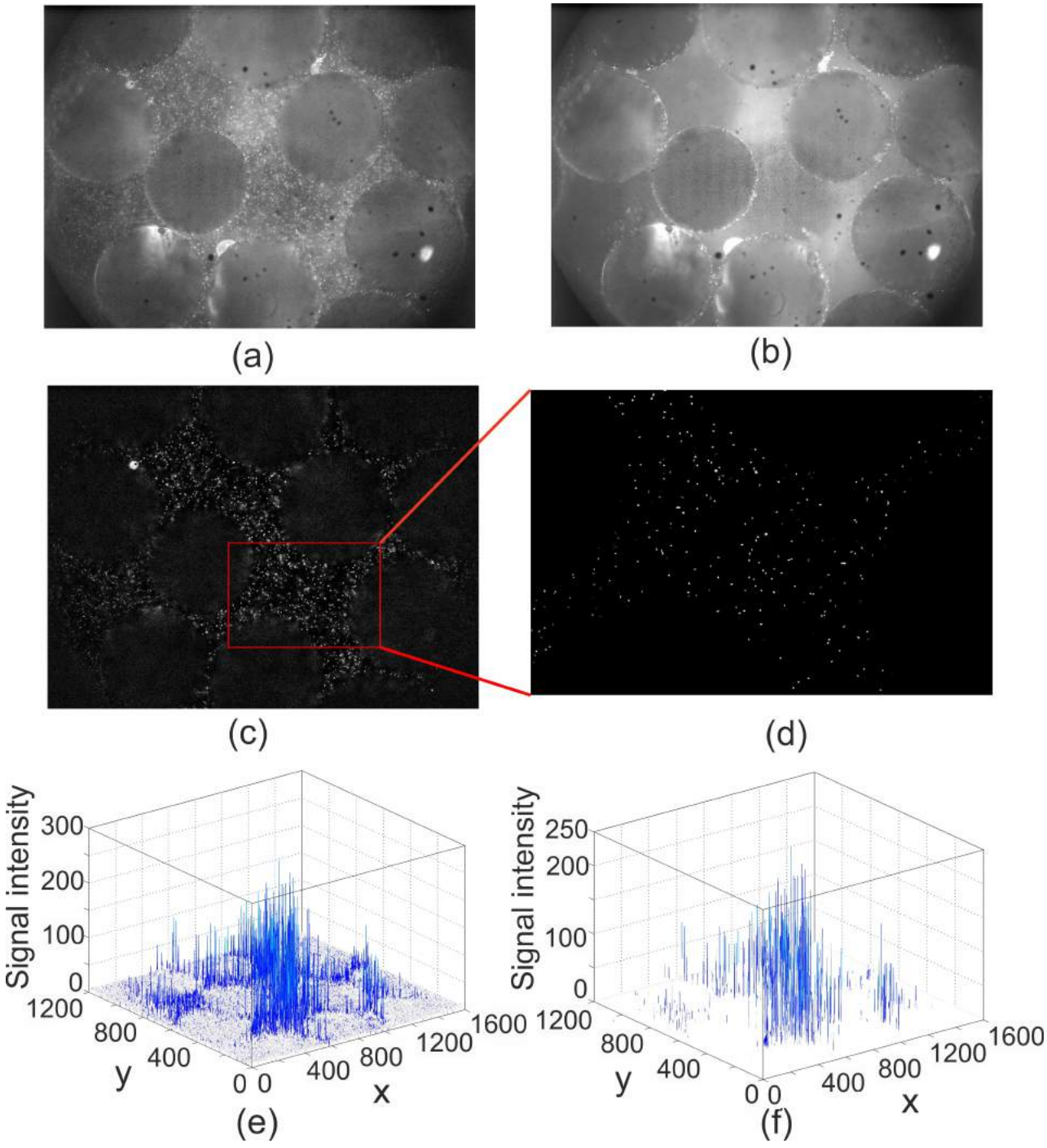

Figure 3.14: Image pre-processing steps used to enhance the signal noise ratio. (a) Raw image, (b) background (mean image), (c) the background is removed, (d) a constant value is subtracted, (e) signal intensity of image (c), (f) signal intensity after substracting a constant value.

glass sphere which creates a lot of background noise, making it harder to identify the tracing particles compared to a simple macro channel experiment. One of the major challenges was therefore to remove the background and to enhance the signal to noise ratio.

The first step in pre-processing is obtaining the background image of the local structure. It was obtained by averaging the 300 pairs of double frames, as shown in Fig. 3.14(b). Ideally, there should be no fluorescent particles in the background image as they are moving with fluid flow. In reality, however, some of the fluorescent particles tend to stick on the surface of the glass spheres and keep unmoved. This makes the glass surface brighter than other regions. The noise intensity in the glass surface area is thus higher due to more reflections. Although the background has been subtracted from the raw image, as shown in Fig. 3.14(c), the light from the reflection in the glass spheres region and the unfocused particles in the adjacent layers still makes the background quite bright.

Fig. 3.14(e) displays the signal intensity distribution of Fig. 3.14(c). Pixels with a value of zero on image have been set to white when they were plotted on the signal intensity chart. Pixels with a positive value were set to be blue, and the height of the peak indicates the intensity of the local signal. The blue dots and short peaks, which mainly located in the glass sphere regions, were believed to be noise.

Typically, the intensity value of the noise is less than 15 and the intensity of the fluorescent particles ranges from 20 to hundreds. Therefore, a constant intensity value was subtracted from all the pixels on the image in order to remove the noise. Any pixel having an intensity value less than zero was set to zero. The choice of

the intensity value was dependent on the intensity of the signal and the noise. This process also reduces the signal intensity and the signal intensity can be strengthened by multiplying a reasonable constant value if the signal intensity is too weak to be detected by the software after subtracting (Sen et al. 2012). Fig. 3.14(d) shows the fluorescent particle distribution after subtracting a constant value and Fig. 3.14(f) shows the corresponding signal intensity distribution. Obviously, the noise in the glass sphere region disappeared and the signal to noise ratio is much better in the flow region.

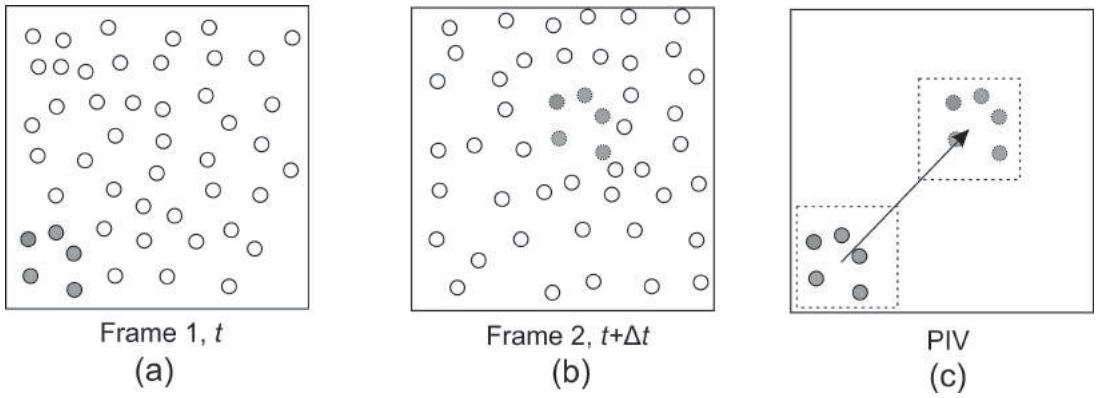

Figure 3.15: A schematic view of a frame pair for cross correlation. (a) Particle distribution at time t in the first frame, (b) particle distribution at time $t + \Delta t$ in the second frame, and (c) cross correlation of the interrogation area.

The velocity vector field was calculated based on the pre-processed images. It was calculated using the DynamicStudio software by cross correlating the frame pairs. The frames were first subdivided into small interrogation areas (IA), each 32 pixels $\times$ 32 pixels. The size of the IA can be varied according to the flow rate. However, using too small an IA window can result in a particle moving out of the interrogation window and costs more time for calculation, while using too large an IA window can reduce magnitude and reduce accuracy. Fig .3.15 shows a schematic diagram of how

velocity is calculated. If the images are collected in the double frame mode, frame 1 and frame 2 represent the first and second images in the frame pair. Otherwise, in the single frame mode, the time series images need to be first redistributed into double frames, e.g., the first and the second images as a pair, the second and third images as a pair, and so on. For each IA window, there is 50% overlap with the adjacent IA windows to avoid ignoring the small displacements. The displacement of the IA window is detected by the software, combined with the known time difference between the two frames, and the velocity is calculated.

Post-processing mainly refers to velocity field analysis such as statistical analysis of the velocity components, velocity profile analysis across specific line, velocity fluctuation analysis and so on. The calculated velocity vectors were exported to files first and then all the above post-processing was done in Matlab and Origin.

3.3 Pressure drop through porous glass samples

The pressure drop over the porous media was measured by a differential pressure transducer (Model DP15, Validyne Engineering, US). The transducer has a sandwich structure with a diaphragm in the middle. The diaphragm, which is changeable, determines the measuring range of the transducer. Three diaphragms, DP3-26, DP3-34 and DP3-42, with working ranges of 3.5 kPa, 22 kPa and 140 kPa, respectively, were used to achieve a more accurate pressure measurements. The accuracy of the pressure transducer is +/- 0.2% of the full scale.

3.3.1 Calibration of pressure transducer

Figure 3.16: The calibration system for the pressure transducer.

The transducer needs to be calibrated each time the diaphragm is replaced or the transducer is reassembled. The calibration procedure is to find the standard relationship between the pressure and the voltage. Fig. 3.16 show the system used for the calibration of the pressure transducer. It consists of a pressure control box which gives an of accurate pressure value, a data logger (U12 series, LabJack, US) and a computer (not shown in the diagram) with software LJStreamM (LabJack, US) to communicate with the data logger.

The pressure box is connected to pressurized air through a controllable valve that adjusts the pressure supplied to the pressure box. Before calibration, the high pressure side of the transducer was connected to the pressure box and the main valve was opened and closed several times so that the pressure fluctuated between zero and full scale to seat the diaphragm completely. During calibration, the pressure was

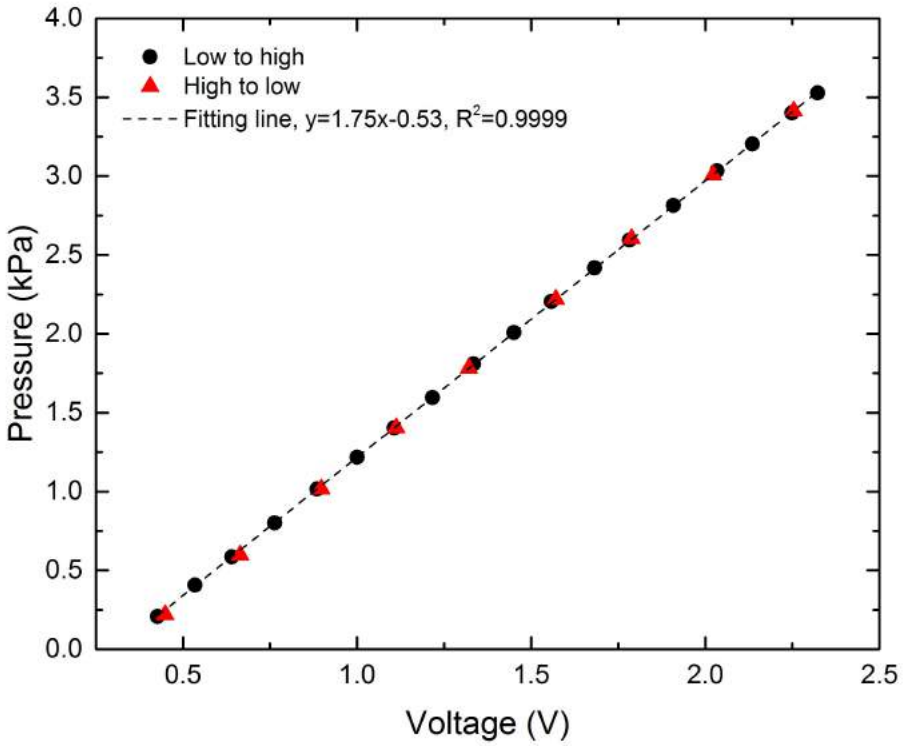

Figure 3.17: A typical pressure transducer calibration graph (diaphragm model DP3-26).

adjusted from 0 to the upper limit at a reasonable step, and the voltage from the software and the pressure value from the pressure control box were recorded simultaneously. The calibration was repeated by reversely adjusting the pressure, i.e., from the upper limit to 0, to ensure that there was no hysteresis in the pressure-voltage diaphragm. A linear relation between pressure and voltage was obtained and this relation was used to determine the pressure drop over the porous media in experiment. Fig. 3.17 shows a typical calibrated pressure-voltage relation.

3.3.2 Measurement procedure

The pressure drop over the porous glass samples was measured in the test rig shown in Fig. 3.11. The pressure transducer was connected to the pressure ports on the test rig according to the schematic diagram shown in Fig. 3.10, in the same way as in the calibration, i.e., the high pressure side of the transducer was connected to the upstream port and the low pressure side was connected to the downstream port.

The air bubbles trapped in the pressure transducer and the porous sample were expelled out before each measurement. In expelling the air out from the transducer, the outlet was closed and one of the bleed screws on the pressure transducer was removed to allow the fluid to flow out until no air bubbles were visible. The operation was repeated for the other bleed screws. Before expelling the air out from the porous sample, the connection from the pressure port to the pressure transducer was shut off to protect the diaphragm from being damaged. Then the main valve was opened and closed at a high flow rate for several times to drive out the air bubbles trapped in the sample.

For each sample, the flow rate was varied from low to high at a reasonable step by a fine valve. At each flow rate, the fluid first flowed for about 60 seconds to achieve a steady state. The corresponding voltage was then recorded by the software at a frequency of 100 Hz for about 60 seconds. The fluid mass was recorded simultaneously every 2 seconds by the computer. The mean voltage was used to determine the pressure drop according the pressure-voltage relation obtained from the calibration. The volumetric flow rate was calculated from the mass flow rate.

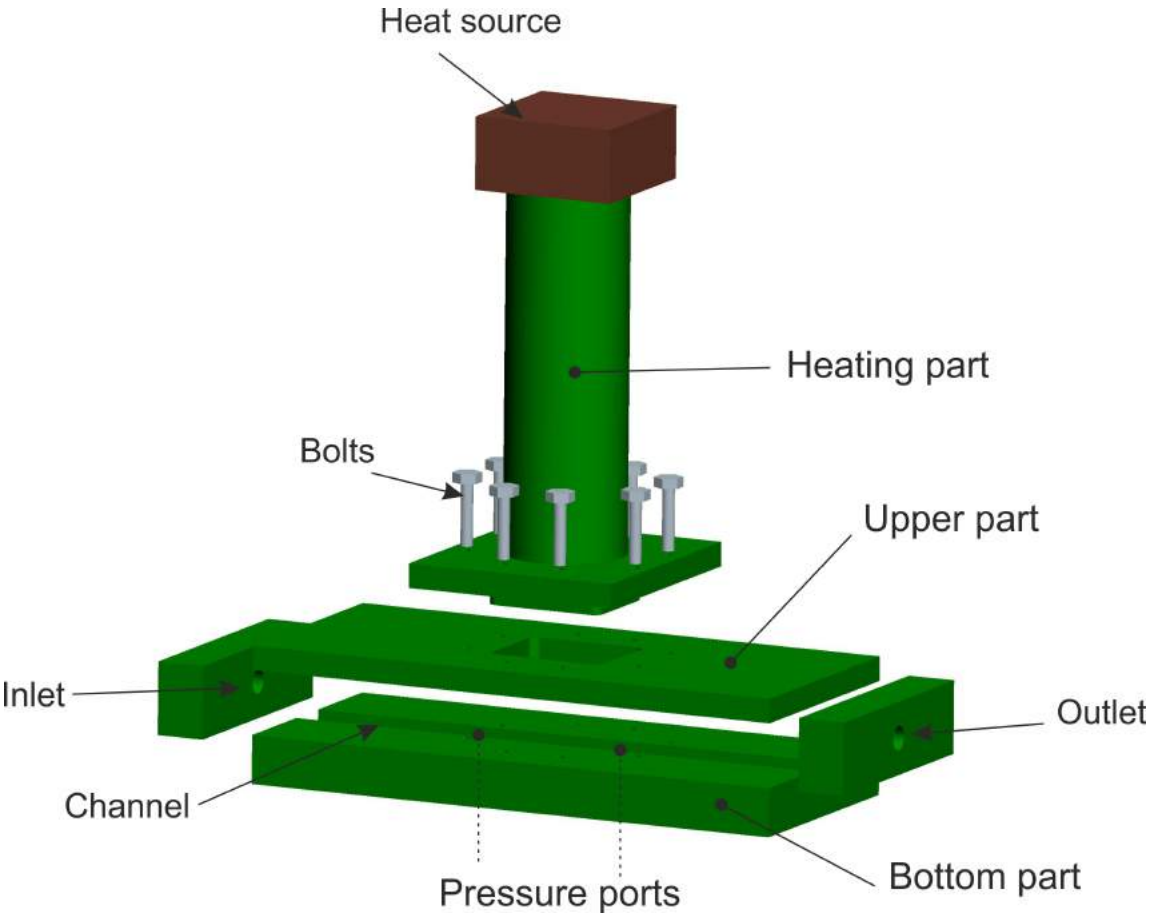

Figure 3.18: Rig for pressure drop and heat transfer measurements for porous copper samples.

3.4 Pressure drop through porous copper samples

3.4.1 Measurement system

Fig. 3.18 shows the rig for the pressure drop measurement for the porous copper samples. It consists of 5 parts, namely inlet, outlet, upper part, bottom part and heating part. A rectangular channel, with dimensions of 230 mm × 20 mm × 5 mm, was machined on the bottom part. Two holes (pressure ports), located 50 mm apart was drilled in the channel for connecting the pressure transducer though pipes. A rectangular window was machined on the upper part for fitting the heating

part and replacing samples. The four parts (inlet, outlet, upper and bottom) were glued together to avoid leakage. After loading the sample in the channel through the window, the heating part was mounted on top by 8 bolts. The heating part is used for heat transfer measurements and does not function in the pressure drop measurement. The heating part, a pure copper bar with same cross section as the sample, was used to transfer heat from the heat source to the porous copper samples. A jig (not shown) was used to ensure that the copper bar was in tight contact with the porous sample.

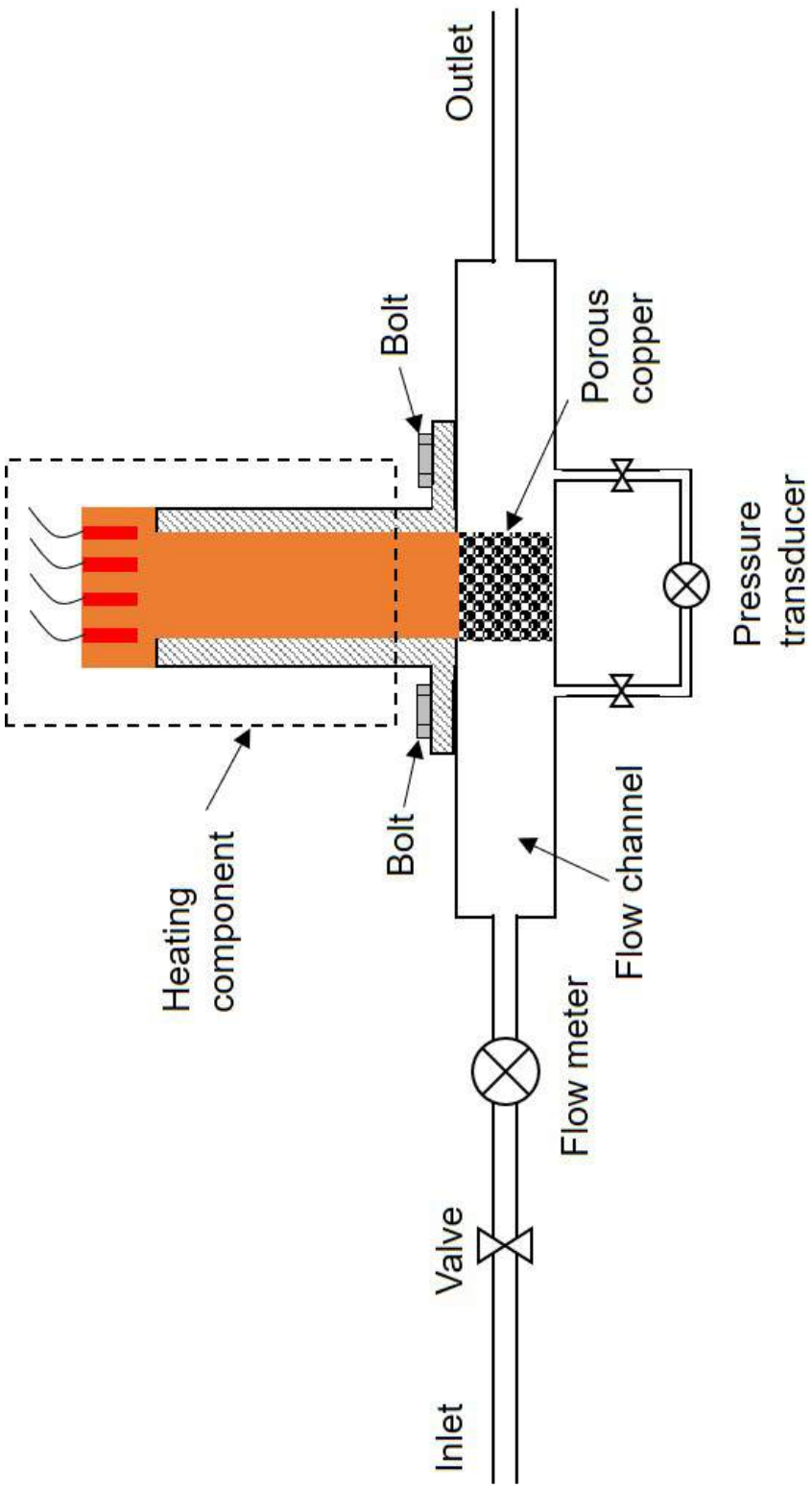

Figure 3.19: Schematic drawing flow system for pressure drop test in porous copper. Note that the heating section is used for convection testing and does not work during pressure drop measurements.

Fig. 3.19 shows a schematic of the system used to measure the pressure drop of the porous copper samples. The sample holding rig is connected to a water tap through a pipe with a fine valve and a flow meter. During the measurement, water was driven into the channel by pressure, passing through the porous copper. Two volume flow meters with different ranges were used to obtain a more accurate reading. One flow meter has a range of 0 - 1500 ml/min, with a minimum scale of 30 ml/min and the other has a range of 0 - 4000 ml/min, with a minimum scale of 200 ml/min. A digital balance (not shown) was also used to obtain an accurate flow rate.

3.4.2 measurement procedure

The procedure for measuring the pressure drop over the porous copper samples is similar to that used for the porous glass samples. The same procedure as for the porous glass samples was applied to expel the air in pressure transducers and porous copper samples.

For each sample, the flow rate was varied from low to high in steps of 50 and 200 ml/min in the flow rate ranges of 50 - 1000 and 1000 - 3000 ml/min, respectively. For each flow rate, 60 seconds was allowed for the flow to reach a steady state before recording the pressure data. The pressure recording lasted about 60 seconds at a sampling rate of 100 Hz and the mean value was used. The volumetric flow rate was calculated from the mass flow rate.

3.5 Thermal conductivity

3.5.1 Measurements of thermal conductivity

The measurement of thermal conductivity of moderate to good conductors can be carried out under steady-state conditions using a longitudinal heat-flow technique. It offers greater flexibility in that the materials having a wide range of conductivity values can be investigated by selecting the correct specimen size. The basis for this method lies in Fourier's law that the heat flux of a one-dimensional steady state problem can be expressed as (Kaviany 2012):

$$J = \lambda A \frac{\Delta T}{\Delta L} \tag{3.5}$$

where J is heat flow, λ is the thermal conductivity of the material, A is the cross-sectional area of the conductor and $\Delta T/\Delta L$ is the temperature gradient.

A method reported by Corsan (1984) determines the heat flow by measuring the temperature difference in a pure copper comparator with known thermal conductivity. Assuming that the porous copper specimen and the comparator are perfectly contacted and ignoring the heat loss at the other surfaces of the comparator and the specimen, the heat flow is a constant throughout the porous specimen and the solid comparator. As the cross-sectional area is the same between the comparator and the porous specimen, the thermal conductivity of the porous copper, λ_p is given by:

$$\lambda_p = \lambda_{Cu} \frac{(\Delta T/\Delta L)_{Cu}}{(\Delta T/\Delta L)_p} \tag{3.6}$$

where λ_{Cu} is the thermal conductivity of the solid copper comparator, given by the

manufacturer as 391 W/mK, $(\Delta T/\Delta L)_{Cu}$ is the temperature gradient in the solid copper comparator and $(\Delta T/\Delta L)_p$ is the temperature gradient in the porous sample.

3.5.2 Experimental apparatus

Fig. 3.21 shows the main components of the measurement system and the details of the measurement section. The system includes a measurement section and various support systems. A power supplier was used to supply power and control the temperature. A vacuum chamber was used when the thermal conductivity was measured under a vacuum condition. The data logging system was located in the vacuum chamber and connected to a computer through a cable. The cooling system is located outside of the vacuum chamber and a copper bar was used to dissipate the heat.

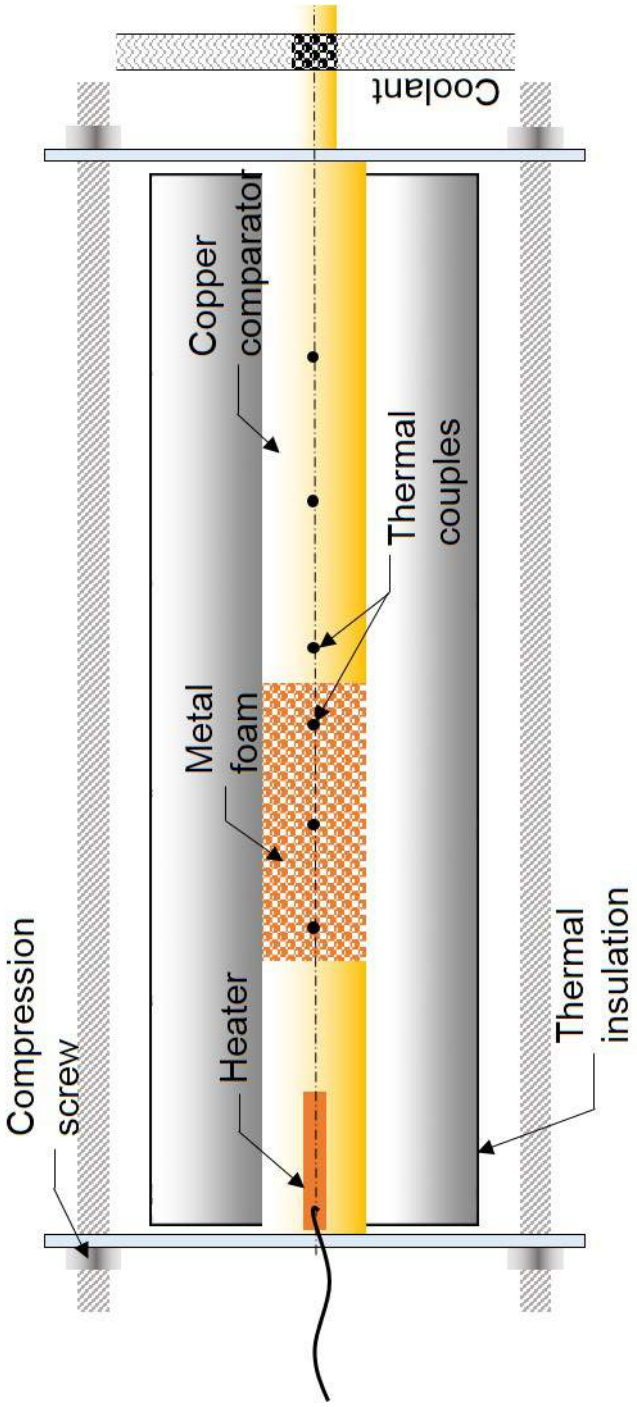

Figure 3.20: Schematic diagrams of (a) the main components of the measurement system and (b) the details of the sample section.

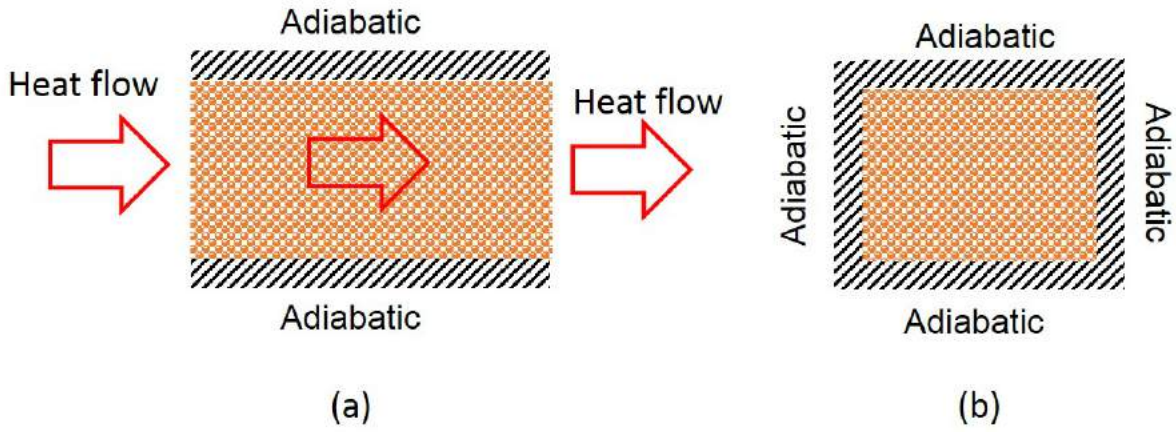

Figure 3.21: Boundary condition of the sample at thermal conductivity measurement. (a) Front view and (b) left view.

A solid copper bar embedded with a cartridge heater in the centre was used as the heat source. The heater power was controlled by a variac so that a reasonable temperature difference across the sample can be achieved for different porous copper samples. The porous copper sample was clamped onto the bottom of the copper bar. Another solid copper bar with the same cross-sectional area was used as the comparator and was clamped onto the other end of the porous copper sample. In order to remove the heat conducted through the sample and the comparator and to obtain steady state temperature gradients, the end of the comparator was immersed in circulating cold water. The porous copper sample used in the present experiment have a rectangular geometry, with a dimension of 55 mm $\times$ 20 mm $\times$ 15 mm. Thermally conductive grease with conductivity of 3.6 W/mK (supplied by Chemtronics, USA) was applied to the heater/sample and sample/comparator interfaces to reduce the contact resistance.

Three holes with a diameter of 1 mm were drilled with depth of 10 mm at specific locations along the length of the comparator and the porous sample. Each hole had a

T-type thermalcouple inserted to measure the temperature during heat conduction. All the thermal couples, with a accuracy of 0.5 ^0C, were linked directly to a data acquisition unit (resolution: 0.01 ^0C, TC-08, Pico Technology, UK). The conduction system was housed in a grooved PTFE block (thickness of 10mm), which was then wrapped tightly by 50 mm polyethylene foam. A clamp was used to hold the heater, sample and comparator firmly together to ensure a good contact at the interfaces.

To study the contribution of fluid to the effective thermal conductivity, the measurements were conducted under vacuum condition (pure sample system), saturated in water (sample-water system) and under ambient pressure (sample-air system). In the case of the sample-water system, it was difficult to fill all the pores with water under the normal ambient pressure, especially the pores at the ends or corners of the passage, due to the small size of the pores. This problem was overcome by immersing the sample in water and placing them in a vacuum chamber. The trapped air was pumped out completely and all the air was replaced by water in the sample. Once the water filled the porous copper sample, the sample was removed and placed in the measurement channel. Water remained in the pores due to the capillary effect. Finally, the gap around the sample was sealed to avoid evaporation.

3.5.3 Measurement procedure

The sample was first placed in the PTFE channel and the heater/sample/comparator assembly was secured as described in the last section. The heat cartridge was then switched on. The temperatures at the different locations were measured after the steady state was reached (approximately 45 minutes, depending on the relative den-

sity of the sample). In the present measurements, the temperature difference between the hot and cold ends of the sample was maintained at about 20^0C. The steady state temperature (temperature changes $< 0.1^0C$ in 10 minutes) was recorded by the data acquisition unit.

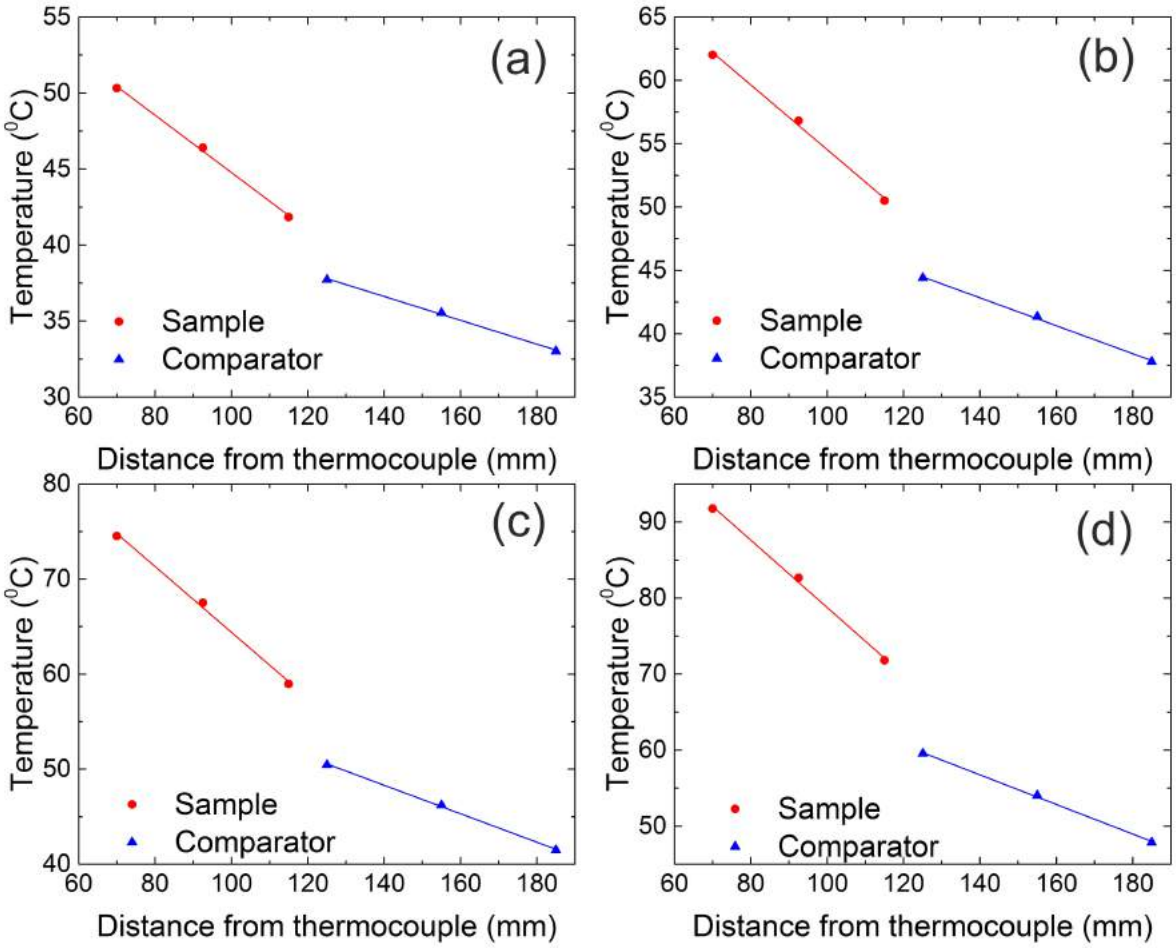

Figure 3.22: Temperature gradients in the Al alloy (6082) sample and the comparator under various heat powers: (a) 23 W, (b) 30 W, (c) 44 W and (d) 52 W.

The apparatus was assessed with three standard metal bars, made of pure copper, aluminium alloy (6082) and mild steel. They have thermal conductivity reference ranges of 390 - 398 W/mK, 165 - 175 W/mK and 43 - 55 W/mK, respectively.

Fig. 3.22 shows the temperature gradients in the Al alloy (6082) and the pure copper comparator in steady-state condition under various heat powers. The change of temperature gradient between the Al sample and the Cu comparator is clearly visible. The thermal conductivity values of the Al samples calculated according to the Eq. 3.6 are 162.6 W/mK, 168.5 W/mK, 169.3 W/mK and 171.6 W/mK for 23 W, 30 W, 44 W and 52 W powers, respectively. The maximum deviation is about 5%, showing that the effect of heat flux on thermal conductivity is negligible in the experiment.

Fig. 3.23 compares the experimental results with theoretical values of thermal conductivity for pure copper, Al alloy and mild steel under various heat powers. For the pure copper sample, the experimental results are lower than the theoretical value. Only at the heat power of 44 W the experimental value was very close to the theoretical value. For the Al alloy and mild steel samples, the experimental results fall within the reference value ranges. The thermal conductivity of the porous copper samples in the present study is less than 200 W/mK. Therefore, this setup is accurate enough for the measurements.

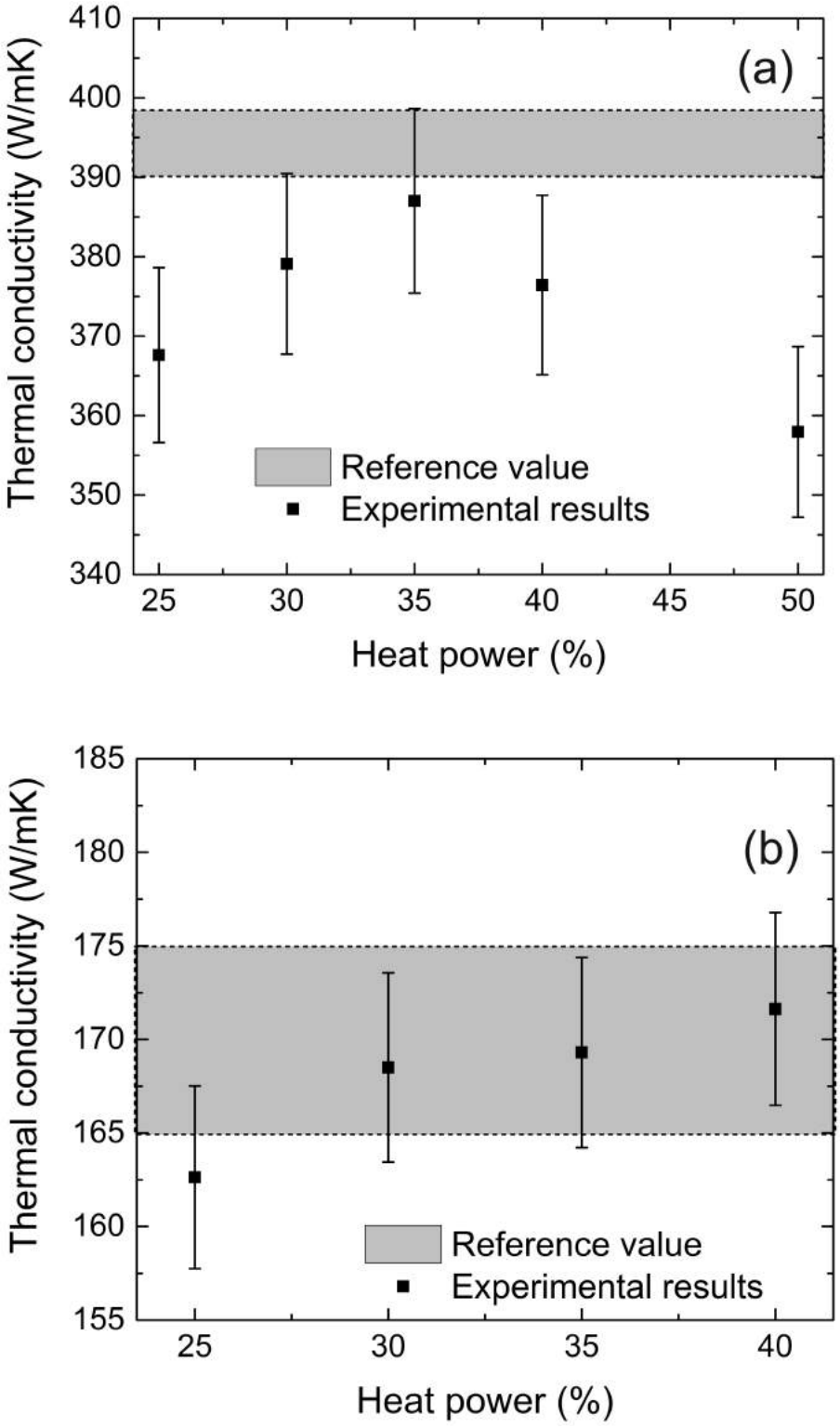

Figure 3.23: Comparison of the experimental and reference values of thermal conductivity under various heat powers for (a) pure copper, (b) Al alloy (6082), and (c) mild steel. (to be continued)

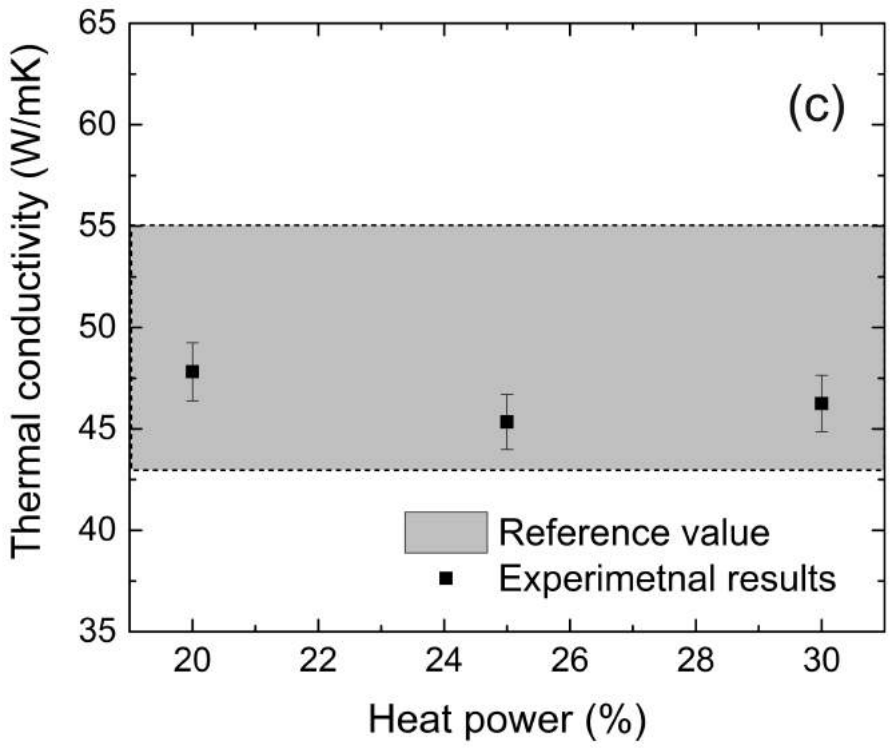

Figure 3.23: (continued) Comparison of the experimental and reference values of thermal conductivity under various heat powers for (a) pure copper, (b) Al alloy (6082), and (c) mild steel.

3.6 Natural convective heat transfer coefficient

3.6.1 Experimental apparatus

Fig. 3.24 shows schematically the heating assembly and thermal insulation used in the present experiment. The insulation part consisted of two polyurethane foams (thermal conductivity 0.036 W/mK) joined together by two acrylic frames by four screws in the corners. The dimensions of the whole insulation block are 160 mm × 160 mm × 80 mm. A rectangular hole with dimensions of 30 mm × 30 mm × 12 mm was drilled in the centre of the upper part of the insulation block to accommodate the heating component. The heating component consisted of a silicone rubber heating pad (Omega, UK) and a thermal buffer made of pure copper. The silicone

rubber heating pad was attached to the lower surface of the thermal buffer using a layer of thermally conductive grease. The grease was spread on the entire surface of the heat pad so as to provide a uniform heat flux to the copper buffer. A tiny notch was cut in the middle of the upper surface of the copper buffer to embed a T-type thermocouple. This thermocouple was used to measure the temperature of the porous copper sample. The upper surface was then flattened with a layer of thermal grease before sticking the porous sample on to it. The thermal grease was employed to enhance the thermal coupling by eliminating the air gap between the sample and the copper buffer. T-type thermocouples were employed on the other surfaces of the foam block to monitor the heat loss from the insulation foam.

3.6.2 Measurement procedure and calculation

The heating and insulation assembly was kept confined into an enclosed environment of 1.2 m $\times$ 0.8 m $\times$1 m to minimise the effect of ambient temperature fluctuation and to ensure that the sample was cooled by natural convection only. The ambient temperature in the enclosed space was monitored by two T-type thermocouples located far away from the sample to avoid any influence of the hot air from the sample. The heat power was varied from 0.3 to 2.5 W by adjusting the voltage input, resulting in five temperature differences, from 10 K to 50 K. At each temperature difference, the temperatures and the input voltage were recorded. The system normally took about 60 minutes to reach a steady state (temperature fluctuation $< 0.1^0C$ in 10 minutes). All the thermocouples, with a accuracy of 0.5^0C, were linked directly to a data acquisition system.

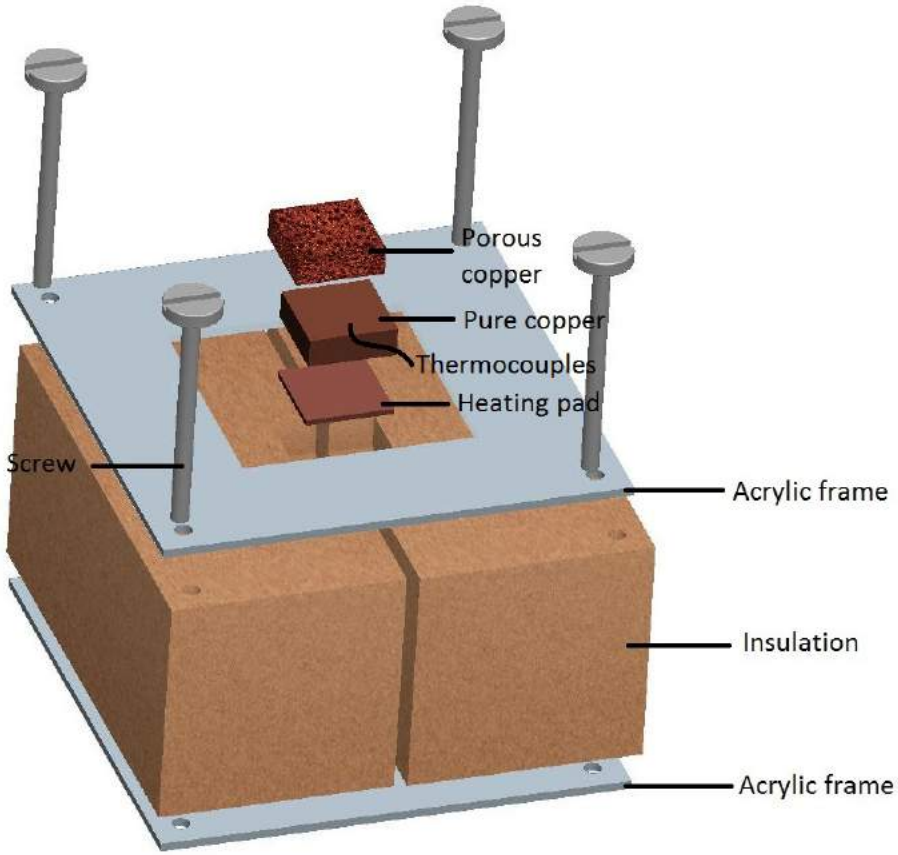

Figure 3.24: Schematic of heating and thermal insulation assembly.

The heating assembly was positioned either horizontally or vertically in order to investigate the influence of sample orientation on natural convection. Fig. 3.25 schematically shows the orientation of the sample and the behaviour of the surrounding flow. The horizontally positioned sample was heated from the bottom, while the vertically positioned sample was heated from the side surface.

Ignoring the heat loss from the insulation foam surface, the natural convective heat

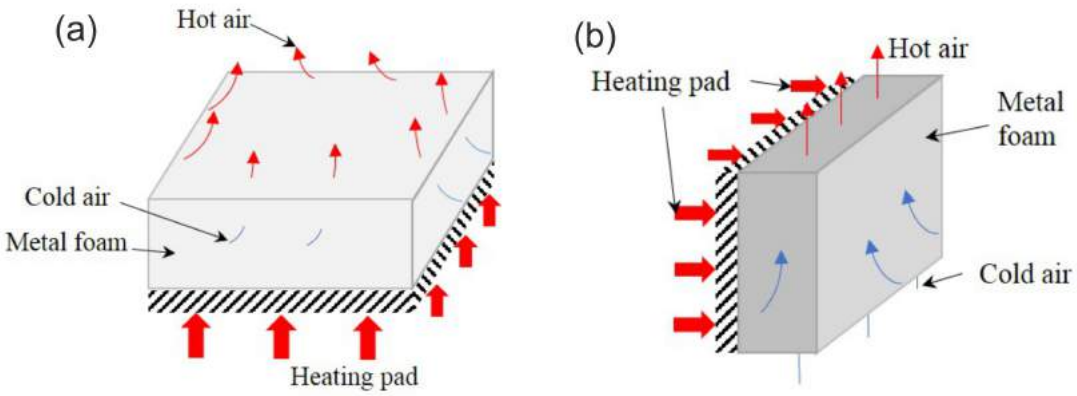

Figure 3.25: Schematics showing flow behaviour near the porous copper sample at (a) horizontal (heating from the bottom surface) and (b) vertical (heating from the left surface) orientations.

transfer coefficient of the porous copper sample was defined as

$$h_n = \frac{J}{A\Delta T} = \frac{J_{in}}{A(T_p - T_{amb})} \tag{3.7}$$

where A is the heated area of the porous copper sample, T_p and T_{amb} are temperatures of the sample and ambient environment respectively, J_{in} is the input power.

3.7 Forced convective heat transfer coefficient

The forced convective heat transfer performance of the porous copper samples with various porosities in different flow regimes was investigated. In forced convection experiment, the coolant (water) was forced through the sample attached to a heating source and the heat transfer coefficient was measured. The flow rate ranged from 0.05 g/s to 75 g/s in order to cover as many flow regimes as possible.

3.7.1 Experimental apparatus

Fig. 3.26(a) shows schematically the system used to measure the forced convective heat transfer coefficient of the porous copper samples. The experimental apparatus consists of a sample section and various supporting systems such as heater control, flow control, flow meter and data logger. The heater control system supplies electric power to the heater, which can be varied by adjusting the voltage input. The maximum pressure that the flow control system can provide is 400 kPa. A very fine valve, combined with a volume flow meter was used to control the flow rate. To obtain a more accurate result of the flow rate, the mass flow rate was measured again by a balance. The temperature signals were recorded by the logging system.

The rig used for forced convective heat transfer coefficient measurements is the same one used for the pressure drop measurements as shown in Fig. 3.18, so only the heating part is narrated in this section. For convenience, a schematic diagram of the sample section is shown again in Fig. 3.26(b). The sample, with dimensions of 30 mm $\times$ 20 mm $\times$ 5 mm, was placed in the rectangular channel which has the same cross-sectional area as the sample. A pure copper bar was used to supply a heat flux from the heater block to the sample. The heater block is made of a pure copper block embedded with 5 cartridge heaters. Using a copper bar avoided direct contact between the very hot heater block and the sample and also provided an accurate measurement of heat flux taken away by the coolant. The heater block, copper bar and the sample were clamped together by a jig, after a thermally conductive grease with a thermal conductivity of 3.6 W/mK was applied to the heater block/copper bar and copper bar/sample interfaces to enhance heat conduction. The copper bar was wrapped up by a thermal insulation material to reduce heat loss.

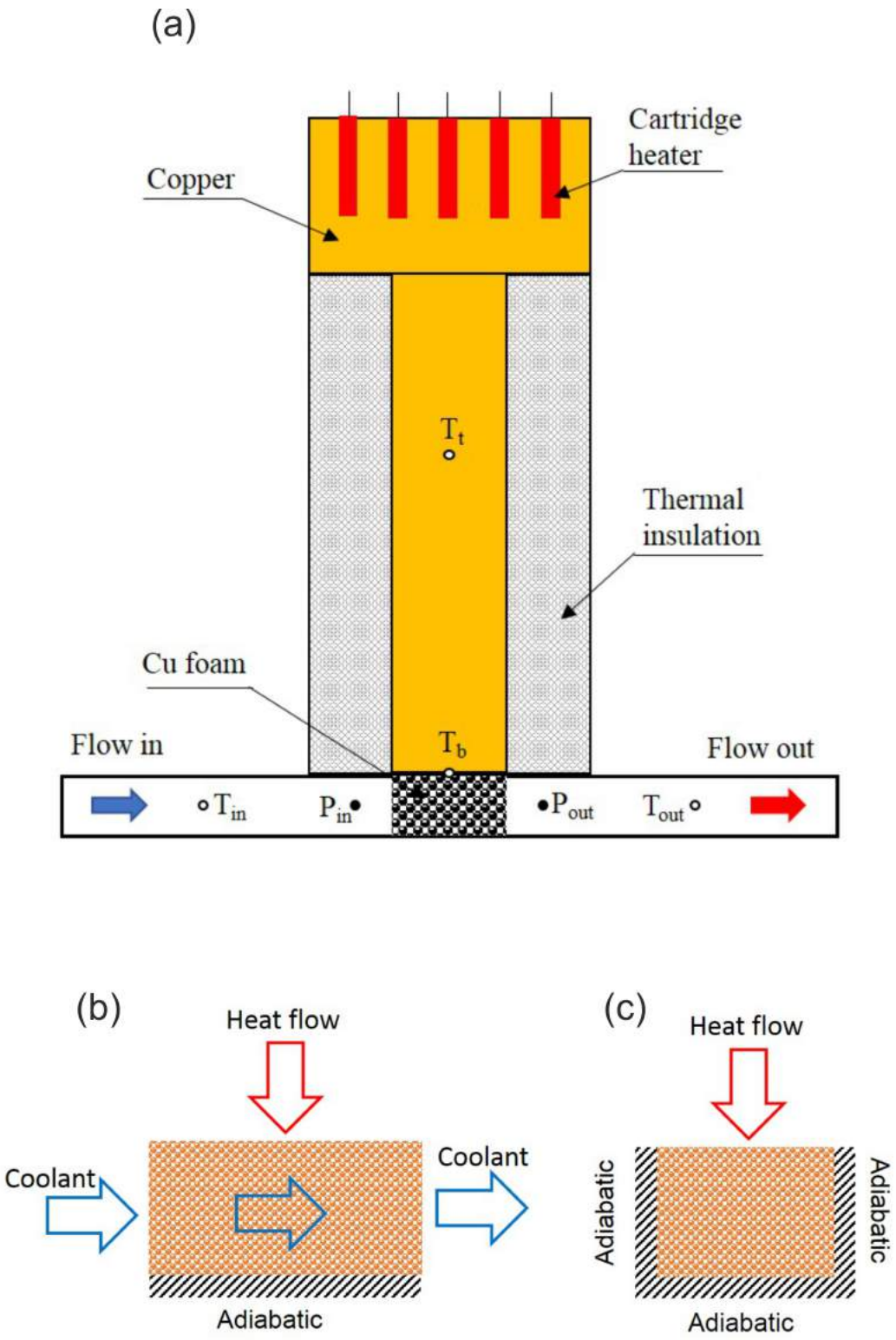

Figure 3.26: Schematic diagrams of (a) the design of the sample section, (b) boundary condition setup from front view and (c) left view.

K - type thermocouples were used to measure the temperature differences across the sample and across the copper bar. A thermocouple was fixed in the hole drilled in the top part of the copper bar, labelled as T_t, and another one was located at the centre of the interface between the copper bar and the sample, labelled as T_b. The distance between T_t and T_b is 80 mm. Two thermocouples were fixed in the internal wall of the channel to measure the temperatures of the inlet and outlet part of the flow. The thermocouples were made flat with the wall surface flat to minimise the disturbance of the thermocouples to the flow. A distance greater than (> 40 mm) between the outlet thermocouple and the sample was chosen so that the fluid mixed completely and the temperature of the fluid distributed uniformly after exiting the sample.

3.7.2 Measurement procedure and calculations

Before each measurement, the largest flow rate was applied for several minutes to remove any air bubbles entrapped in the porous copper sample. The power input was set to 70 V in the present study to obtain a reasonable temperature gradient. The flow rate was adjusted from small to large at a step of 50 ml/min.Approximately 30 - 45 minutes was allowed to achieve a steady state (temperature fluctuation within 0.1 ^0C in 10 minutes) when the flow rate was altered. All the signals were collected by the data logger and recorded by the computer.

The heat flux conducted from the heater to the sample through the copper bar can

be calculated by

$$J = \lambda_{Cu} A \frac{(T_t - T_b)}{d} \tag{3.8}$$

where λ_{Cu} is the thermal conductivity of pure copper, A is the cross-sectional area of the copper bar, and d is the distance between T_t and T_b. Ignoring the heat loss from the copper bar, the heat through the copper bar is equal to the heat taken away by water. The overall heat transfer coefficient of the cooling system, comprising the porous copper sample and the water flow, is determined by

$$h_f = \frac{J}{A(T_b - T_{in})} \tag{3.9}$$

where T_{in} is the water temperature at the inlet.

3.8 Error and uncertainty

3.8.1 Mean value and standard deviation

A finite set of values for any physical parameters measured in this thesis was obtained by repeating measurements under the same conditions. The mean value (X) for n measurements is:

$$X = \frac{1}{n} \sum_{i=1}^{n} x_i \tag{3.10}$$

and the standard deviation was calculated by:

$$\frac{\delta x}{X} = \frac{\sqrt{\sum_i (x_i - X)^2/(n-1)}}{X} \times 100\% \tag{3.11}$$

The length, width, height, thickness and weight of the porous samples were measured

at least three times. The standard deviations were less than 0.25%. The thermal conductivity and heat transfer coefficient were also measured at least three times under the same experimental conditions and the standard deviations were 2.8% and 2.4%, respectively.

3.8.2 Experimental uncertainty

When several independent variables (x_i) are used in a function Φ,

$$\Phi = x_i^a x_2^b \cdots x_N^n \tag{3.12}$$

the uncertainty can be expressed by:

$$\frac{\delta\Phi}{\Phi} = \sqrt{(a\frac{\Delta x_1}{x_1})^2 + (b\frac{\Delta x_2}{x_2})^2 + \cdots + (n\frac{\Delta x_N}{x_N})^2} \tag{3.13}$$

For example, the uncertainty of the porosity measurements in this study is due to errors in the measurements of mass of glass slide, mass of porous sample and dimensions of the sample. According to the method of Coleman & Steele (2018), the uncertainty of the porosity defined in this study can be calculated as:

$$\frac{\sigma\epsilon}{\epsilon} = \sqrt{\left(\frac{\sigma m_{slides}}{m_{sample} - m_{slides}}\right)^2 + \left(\frac{\sigma m_{sample}}{m_{sample} - m_{slides}}\right)^2 + \left(\frac{\sigma l}{l}\right)^2 + \left(\frac{\sigma w}{w}\right)^2 + \left(\frac{\sigma h}{h}\right)^2} \tag{3.14}$$

The errors associated with the balance and the calliper, provided by the manufacturer, are 0.01g and 0.01mm. The typical values of the slide mass and sample mass were about 2.8 g and 4 g, resulting in an error of 0.83% for each of them. The external dimensions of the samples are 26 mm $\times$ 25 mm $\times$ 3.5 mm, resulting errors in

length, width and height of 0.03%, 0.04% and 0.28%, respectively. With each factor considered, the total error of porosity was estimated to be 1.21%.

In this thesis, the systematic and mechanical errors of the facilities and the standard errors of length, width, thickness and weight measurements were considered for uncertainty analysis. These uncertainties are summarized in table 3.2.

Table 3.2: Uncertainties of parameters measured in this thesis.

Parameter	Uncertainty
Porosity	$< 1.21\%$
Thermal conductivity	$< 5.1\%$
Heat transfer coefficient	$< 6.1\%$
Reynolds number	$< 5.2\%$

The measurement uncertainty associated with the μ-PIV measuremnts was calculated according to the method outlined by Meinhart et al. (1999). For a magnification greater than unity, the diameter of the diffraction-limited point spread function, in the image plane, is given by

$$d_s = 2.44 M_a \frac{\lambda}{2N_A} \tag{3.15}$$

where M_a is the magnification of the microscope, λ is the wavelength of the light and NA is the numerical aperture of the lens. For the 40$\times$ objective lens with N_A = 0.6, d_s is about 43.2 μm.

The effective particle diameter d_e, i.e., the size of the particle appearing on the CCD

chip, can be evaluated as 58.8 μm using the following equation

$$d_e = \sqrt{M^2 d_p^2 + d_s^2} \tag{3.16}$$

where d_p is the diameter of fluorescent particle (1 μm provided by supplier). Given the CCD pixel size of 7.4 μm, this means that the particles to be resolved are more than the minimum 3 - 4 pixels required for the location of the particle image correlation peak to within one tenth of the particle image diameter (Meinhart et al. 1999). The measurement uncertainty is yielded by $\sigma_x = d_e/10M$. The uncertainties in the x and y directions are assumed to be the same, and the uncertainty in one direction was estimated to be 0.208 μm. For a typical displacement of a particle between two frames, e.g. at velocity of 0.57mm/s and a time interval of 5000 μs, the percentage error was evaluated to be 5.2%.

3.9 Summary

Porous copper and porous glass samples were manufactured using either the Lost Carbonate Sintering process or the Sintering and Dissolution process. Sintered copper and sintered glass samples were also manufactured by sintering. Pressure drop in these porous media was measured in purpose-designed apparatuses. μ-PIV was used to measure the velocity field in the porous glass and sintered glass samples. The thermal conductivity, natural convective and forced convective heat transfer coefficients of the porous copper samples were measured.

Chapter 4

Flow behaviour in porous media

In this chapter, the results of the characterization of the flow behaviour in four different porous media are presented. The four porous media are sintered glass, porous glass with spherical pores, porous glass with irregular pores and porous copper with irregular pores. Both pressure drop and μ-PIV measurements were conducted in the three types of porous glass samples. Only pressure drop measurements was conducted in the porous copper samples. The experiment results are presented separately for each porous medium and then compared with each other in the last section.

4.1 Flow characteristics in sintered glass

4.1.1 Structural properties

Fig. 4.1 shows a typical optical micrograph of the sintered glass sample with a glass sphere size of 300 - 500 μm. The spherical shape of the glass spheres remains intact after sintering and the sintered necks (black circles) are small compared to the sphere size. Fig. 4.1 also shows that the glass spheres are not in the densest packing as

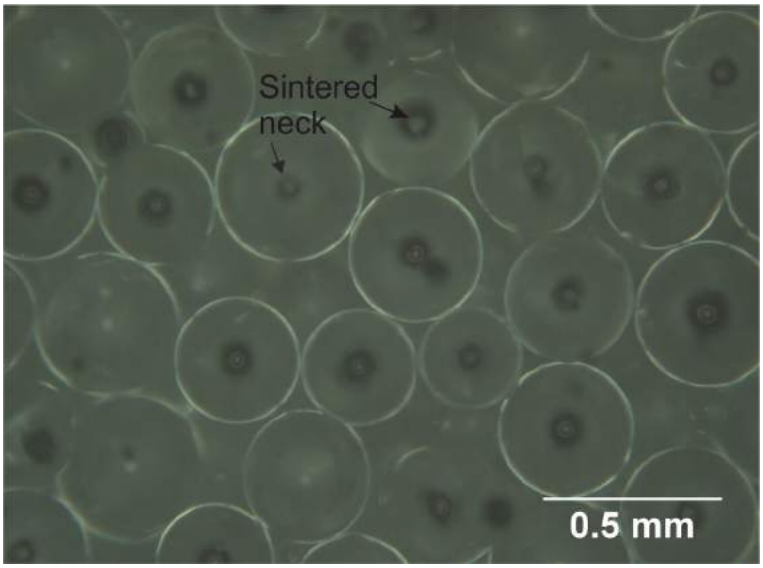

Figure 4.1: Optical micrograph of sintered glass with particle size of 300 - 500 μm.

some large pores are present.

Table 4.1 lists the structural characteristics of the three sintered glass samples. The aspect ratio is defined as the ratio between the height of the sample and the diameter of the glass spheres. Low aspect ratio means that the walls can influence the porosity of the sample because of the large voids in the near wall region (Patil & Liburdy 2013). Samples G170 and G430 have approximately the same porosity, while sample G710 has a higher porosity because of the significant influence from the low aspect ratio.

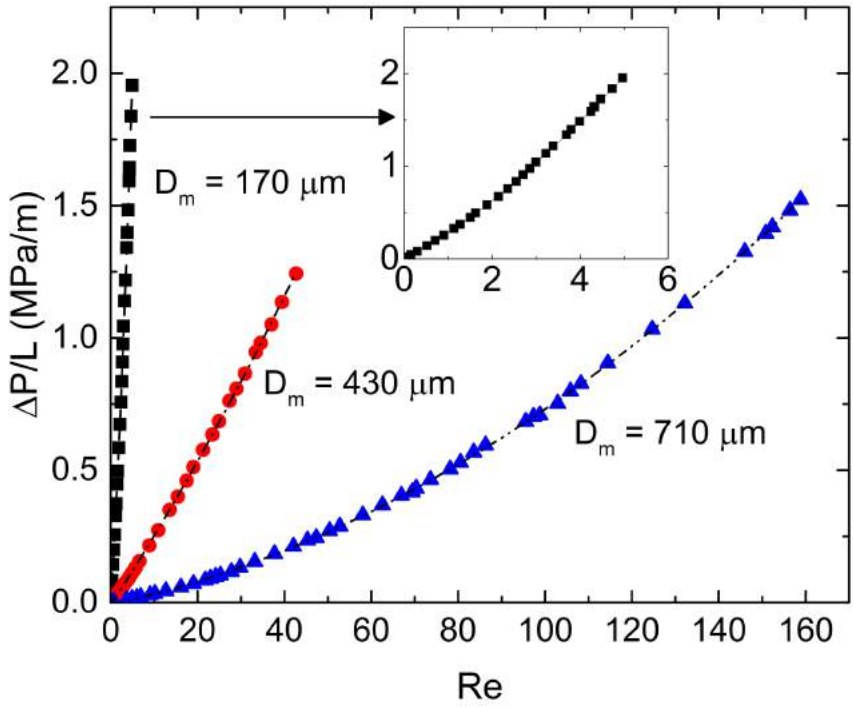

Figure 4.2: Relationship between the pressure drop per unit length across the sintered glass with different particle sizes with Reynolds number .

Table 4.1: Characteristics of the sintered glass used in the present study.

Sample	Sphere diameter (μm)	Mean diameter (μm)	Porosity	Aspect ratio	PIV magnification
G170	100 - 200	170	0.34	8.52	400 ×
G430	300 - 500	430	0.34	3.48	200 ×
G710	500 - 900	710	0.40	2.11	100 ×

4.1.2 Pressure drop

Fig. 4.2 shows the plots of pressure drop versus Reynolds number for the three sintered glass samples. Theses typical pressure drops plots shows that pressure drop increases with Reynolds number. However, it is difficult to identify the Darcy regime or the Forchheimer regime in this plot. Fig. 4.2 shows that sphere size has a great influence on pressure drop. For example, although sample G170 and G430 have a similar porosity, the pressure drop in G170 is nearly ten times of that in G430 for a given Re. This is because the smaller the particle size, the larger the internal surface area in sintered glass sample, which can result in additional flow resistance.

4.1.3 Flow regimes

The Forchheimer-extended Darcy equation (eq. 2.6) can be expressed in terms of the relationship between reduced pressure drop and Reynolds number and rewritten as follows:

$$-\frac{\Delta P}{LV} = \frac{\mu}{K} + \frac{\mu C}{D} Re \tag{4.1}$$

Flow regime can be identified by observing the slope change of the plot, i.e. the value of C. The four flow regimes, pre-Darcy, Darcy, Forchheimer and turbulent, correspond to $C < 0$, $C = 0$, $C > 0$ (higher magnitude) and $C > 0$ (lower magnitude). Fig. **??** shows the plots of the reduced pressure drop versus Reynolds number. Five different flow regimes can be identified: (i) pre-Darcy, (ii) Darcy, (iii) Forchheimer, (iv) transition to turbulent and (v) turbulent.

In the pre-Darcy regime, the increase in fluid velocity can be greater than that ex-

pected from the increase in pressure drop. The nature of the flow in pre-Darcy regime is not clearly understood due to experimental difficulties in accurately measuring the ultra small flow rates and the associated pressure drops. Some models (Polubarinova-Koch 2015, Lu et al. 2018) have been developed to explain the phenomena in the pre-Darcy regime. Among these models, the interactions between the medium and the fluid attracted the most attention. Polubarinova-Koch (2015) pointed out that water has a polar molecule which tends to orient itself in an electrostatic field. Static water molecules can become oriented around surfaces, forming a quasicrystalline structure that effectively narrows the pores or completely occludes them. As an increasing pressure drop is applied to the water in the porous medium, the weak intermolecular bonds are progressively overcome. In effect, the network of flow channels in the medium becomes a function of fluid velocity. The permeability of the medium increases with fluid velocity until the quasicrystalline water structures are all broken down and Darcy linearity is obtained. Because the behavior of water bound to pore walls by electrostatic force might be considered to be non-Newtonian, some researchers (Fand et al. 1987, Swartzendruber 1962) attributed the existence of pre-Darcy flow to non-Newtonian behavior of fluids.

The Darcy regime exists only at low flow rates and spans a narrow flow rate range. Since pressure drop in this regime is only produced by the viscous force from the inner surfaces of the solid phase, therefore, it is believed that the characteristics of the flow in this regime reflects the actual geometry of the internal morphology of the porous medium.

The two non-linear post-Darcy regimes, are the Forchheimer regime and the turbulent flow regime. In these two regimes, in addition to the viscous forces that are

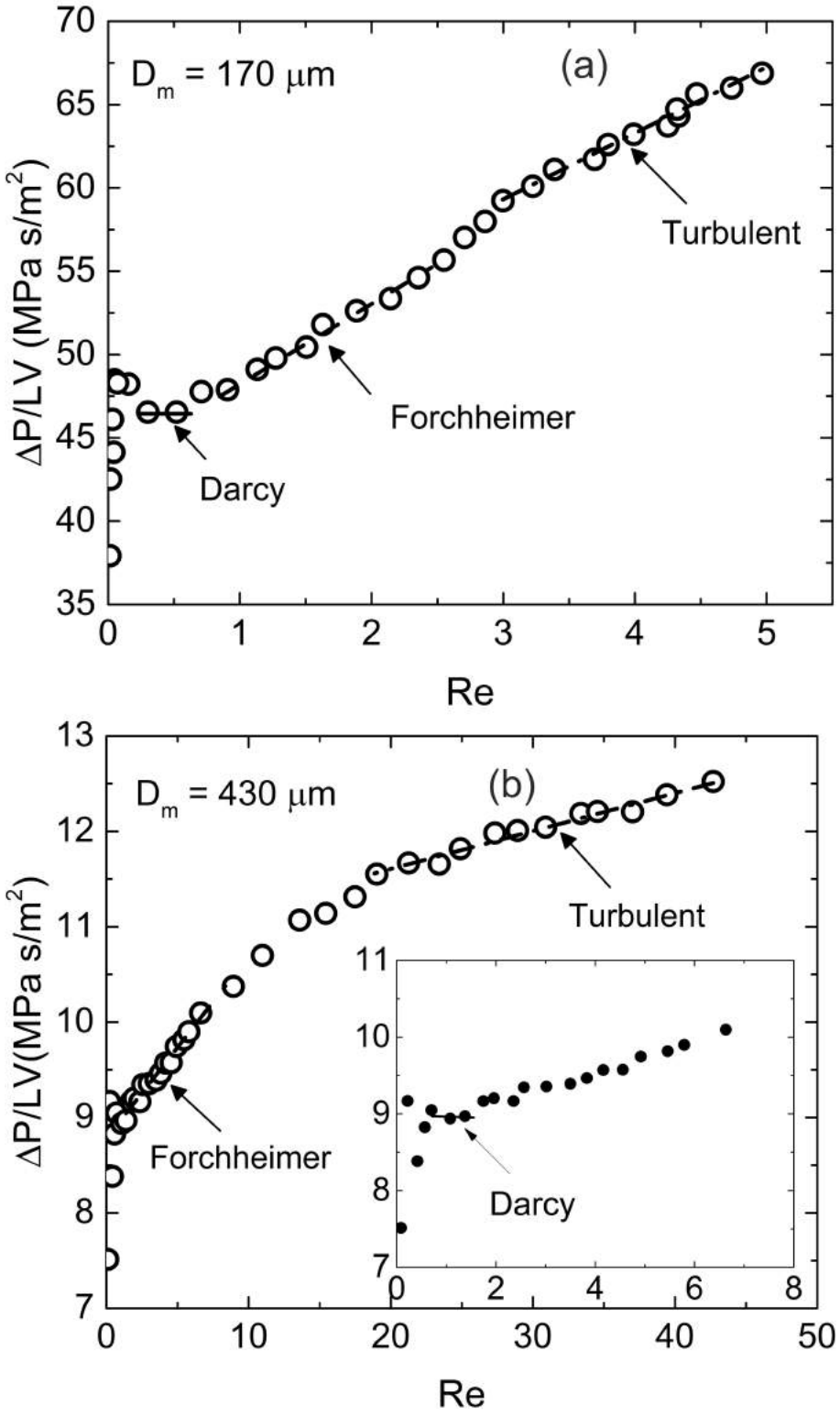

Figure 4.3: Reduced pressure drop versus Reynolds number for (a) $D_m = 170$ μm (G170), (b) $D_m = 430$ μm (G430) and (c) $D_m = 710$ μm (G710). The insets in (b) and (c) are the magnification in the low Reynolds number range. (to be continued)

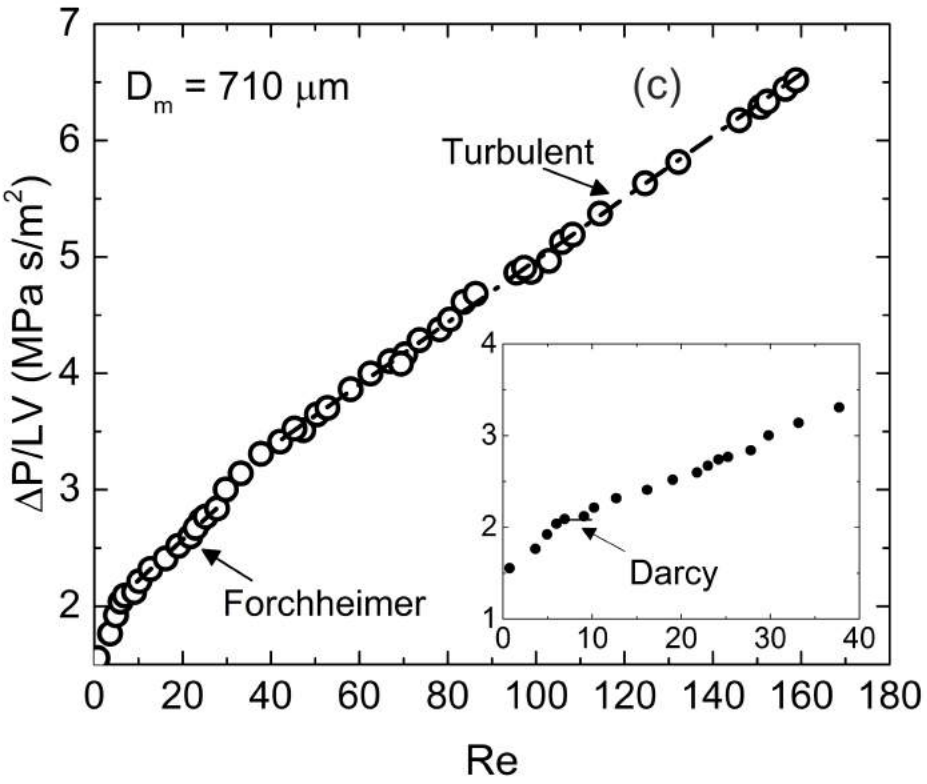

Figure 4.3: (continued) Reduced pressure drop versus Reynolds number for (a) D_m = 170 μm (G170), (b) D_m = 430 μm (G430) and (c) D_m = 710 μm (G710). The insets in (b) and (c) are the magnification in the low Reynolds number range.

solely responsible for Darcy flow, the inertial force and turbulence effects begin to play an important role. The near-wall layers developed in the Darcy regime become more and more pronounced (Dybbs & Edwards 1984). Inertial cores developed in the near-wall layers due to the uneven channel wall, and the movement of these inertial cores from near-wall layers to non-near-wall layers cause a nonlinear relationship between pressure drop and flow rate. It should be noted that the pressure drop-Reynolds number relationship in Forchheimer regime and turbulent regime in packed beds can be described by the Forhcheimer-extended Darcy equation, but with different parameter values (permeability and form drag coefficient).

4.1.4 Effect of sphere size

Fig. 4.4 plots the critical Reynolds number for the onset of each flow regime as a function of sphere size of the sintered glass. The onset Reynolds numbers for the transition to Darcy, transition to Forchheimer, Forchheimer, transition to turbulent, turbulent are designated as Re_D, Re_{TF}, Re_F, Re_{TT} and Re_T, respectively. The Reynolds number ranges of the flow regimes are therefore: pre-Darcy ($Re < Re_D$), Darcy ($Re_D < Re < Re_{TF}$), transition to Forchherimer ($Re_{TF} < Re < Re_F$), Forchheimer ($Re_F < Re < Re_{TT}$), transition to turbulent ($Re_{TT} < Re < Re_T$) and turbulent ($Re > Re_T$). Fig. 4.4 shows that the sphere size of the sintered glass has a significant effect on the onset and range of the flow regimes. The onset Re for each regime increases with sphere size and the range for each regime becomes wider with increasing porosity, especially markedly for the Forchheimer regime.

The flow regime bounds obtained from Fig. **??** and some available literature results are listed in table 4.2. The flow regime boundaries in terms of average sphere diameter based Reynolds number and permeability based Reynolds number are shown. The permeability based Reynolds number is defined as $Re' = \rho V_i \sqrt{K/\epsilon}/\mu$, where V_i is the interstitial velocity, equal to the Darcian velocity divided by porosity, K is the permeability and ϵ is porosity. The study conducted by Fand et al. (1987) found that the"simple media" (packed beds with single size glass spheres) and "complex media" (packed bed with mixed size spheres) have identical flow regime bounds. However, a similar study conducted by Kececioglu & Jiang (1994) found that the regime bounds are different for packed beds with different sphere sizes in terms of sphere size based Reynolds number, but they are identical in terms of permeability based Reynolds number. In the current study, the regime bounds identified in terms of either of the

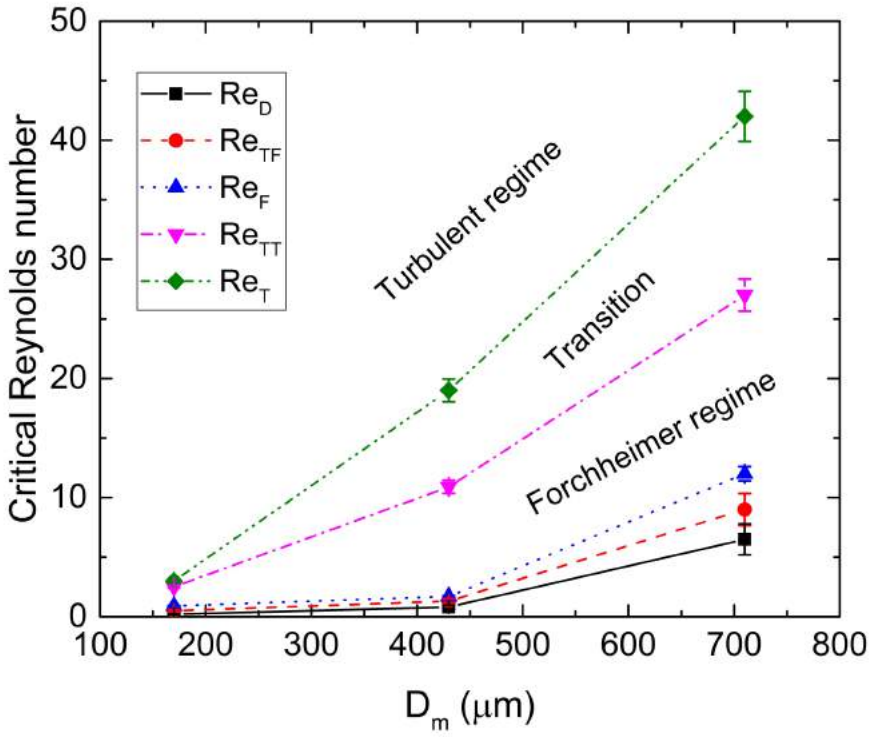

Figure 4.4: Relationship between flow regime boundary and sphere size of the sintered glass.

Reynolds numbers are different. The glass spheres used in the present study are in the microscale, so the sintered glass contains more internal surface area than the macro packed beds. The finer channels produced by micro spheres are less tortuous (Diao et al. 2017), but may have a large flow resistance. Furthermore, packed beds made from spheres with a wide diameter range have a more complex structure than that made from uniform particles.

Table 4.2: Flow regime boundaries of current and previous studies.

	Material	Pre-Darcy	Darcy	Forchheimer	Turbulent
Current study	G170	Re<0.2	0.2<Re< 0.5	0.9<Re<2.5	3.0<Re
		Re'<0.03	0.03<Re'<0.07	0.12<Re'<0.34	0.40<Re'
	G430	Re<0.7	0.8<Re<1.3	1.7<Re<10.9	19<Re
		Re'<0.08	0.09<Re'<0.16	0.20<Re'<1.27	2.22<Re'
	G710	Re<6.0	6.5<Re<9.0	12<Re<27	42<Re
		Re'<0.76	0.8<Re'<1.2	1.5<Re'<3.5	5.4<Re'
Fand et al. (1987)	Packed spheres	NA	Re<2.3	5.0<Re<80	120<Re
			Re'<0.26	0.57<Re'<9.00	13.5<Re'
Kececioglu & Jiang (1994)	3-mm spheres	Re<0.3	0.3<Re<0.7	1.6<Re<10	13<Re
		Re'<0.062	0.062<Re'<0.120	0.34<Re'<2.30	3.4<Re'
	6-mm spheres	Re<0.6	0.6<Re<1.0	3.0<Re <21	25<Re
		Re'<0.062	0.062<Re'<0.120	0.34<Re' <2.30	3.4<Re'

4.1.5 Permeability and form drag coefficient

The values of the permeability and form drag coefficient were obtained by fitting the Forchheimer-extended Darcy equation (Eq. 2.2) to the plots in Fig. 4.2 or **??**. There are two methods to do this (Boomsma & Poulikakos 2002): one method fits the pressure-drop data points from each separate regime without including the transition points; the second method uses a larger flow velocity range which encompasses all the data from the pre-Darcy regime to the turbulent regime. The pre-Darcy and Darcy regimes are excluded when calculating the drag coefficient for all regimes. The calculated permeability and form drag coefficient values are listed in table 4.3.

Table 4.3: Permeability (K $\times$ 10^{-10} m^2) and drag coefficient (C $\times$ 10^4 m^{-1}) of sintered glass samples at various flow regimes.

Sample	Darcy		Forchheimer			Turbulent			All regimes		
	K	R^2	K	C	R^2	K	C	R^2	K	C	R^2
G170	0.21	0.99	0.228	77.7	0.99	0.21	66.4	0.99	0.224	78.5	0.99
G430	1.05	0.99	1.10	6.45	0.99	0.92	1.60	0.99	0.96	2.29	0.99
G710	4.80	0.99	5.30	2.35	0.99	4.28	1.78	0.99	4.45	1.83	0.99

Fig. 4.5 shows the relationship between permeability and sphere size. It shows that increasing sphere size leads to a dramatic increase in permeability. This is because increasing particle size leads to a lower fluid resistance since there is less inner solid surfaces in the sintered glass. Furthermore, the pores in the sintered glass samples with large spheres are larger than those in the small sphere samples. Therefore, the permeability of sintered glass increases with increasing sphere size.

The experimental values of permeability are compared with the values predicated

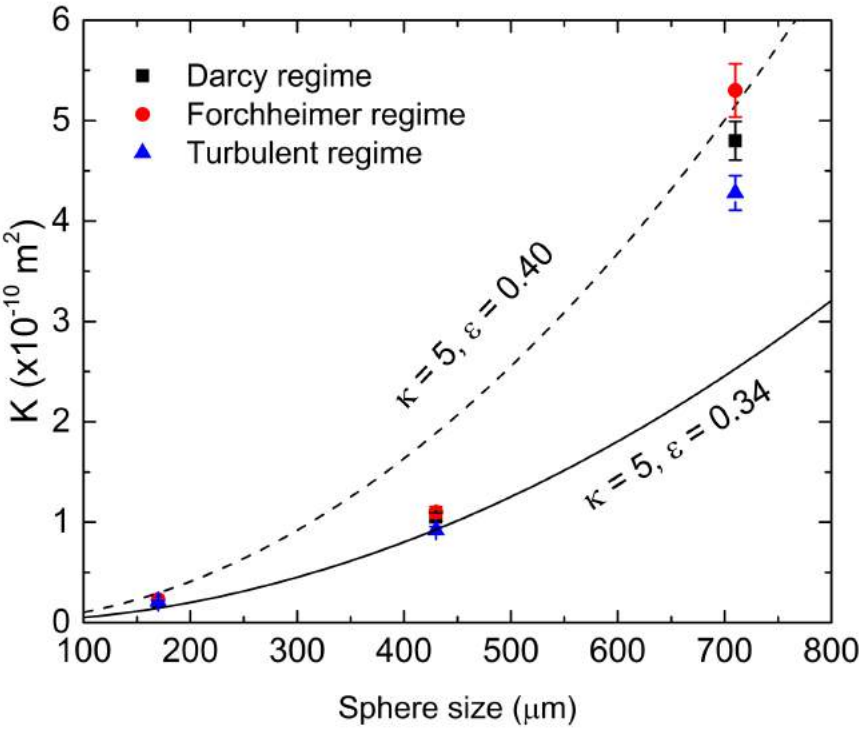

Figure 4.5: Variation of permeability with sphere size. The solid and dash lines represent the permeability predicated from Eq. 4.2.

from the semi-empirical expression proposed by Kececioglu & Jiang (1994):

$$K = \frac{\epsilon^3}{s_v^2 \kappa (1-\epsilon)^2} = \frac{D_g^2 \epsilon^3}{36\kappa(1-\epsilon)^2} \tag{4.2}$$

where ϵ is the porosity, s_v is the surface area per unit volume of the particles and κ is an experimentally determined dimensionless constant known as Kozeny-Carman constant, the value of which was recommended as 5 for smooth spherical particles by Macdonald et al. (Macdonald et al. 1979).

Fig. 4.5 shows that the experimental and the calculated permeability values agreed very well. It also shows the significant effect of porosity on permeability. Comparing the solid and dash lines, which represent the permeability of sintered glass with

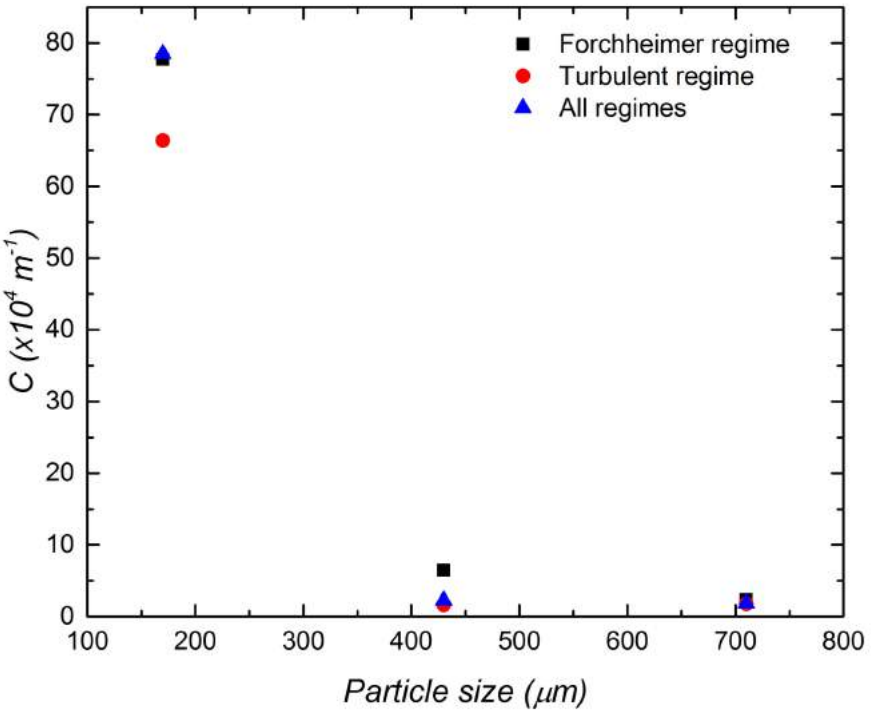

Figure 4.6: Variation of form drag coefficient with particle size.

porosities of 0.34 and 0.41 respectively, indicates that the larger the particle size, the stronger the effect of porosity on permeability.

The relationship between form drag coefficient and sphere size of the sintered glass is plotted in Fig. 4.6. The form drag coefficient decreases sharply with increasing particle size as shown in the figure. Previous studies (Dybbs & Edwards 1984) reported that the form drag force are caused mainly by the motion of inertial cores from the near wall region, where they are developed, to the non-near wall region. The quantity of interstices between particles in sintered glass sample with small sphere is much more than that with large spheres. The likelihood in developing more inertial cores is higher in sintered glass samples with small spheres. Therefore the form drag coefficient is much higher in sintered glass samples with small spheres.

4.1.6 Micro-PIV measurement

The velocities measured by μ-PIV are presented using a Cartesian right-hand coordinate with x = streamwise, y = lateral, z = bed normal, and the corresponding velocity components are denoted by u, v and w. The local velocity magnitude is $U = \sqrt{u^2 + v^2}$ and the time-averaged local velocity magnitude is represented by $\bar{U}$.

4.1.6.1 Instantaneous velocity distribution

Fig. 4.7 shows four local structures and the corresponding instantaneous velocity distributions in the Darcy regime at a specific Reynolds number. R1 and R4 were taken from samples G170 and G710 respectively, and R2 and R3 were taken from sample G430. All of these regions were located around the middle between the entrance and the exit of the sintered glass sample.

R1 shows a flow between two spheres having different diameters. Most of the fluid flows through the relatively wide channel at the bottom, resulting in a very asymmetric flow pattern around the two spheres. R2 shows an impinging channel flow where a high velocity flow impinges onto a solid sphere, resulting in a stagnation region and a nearly symmetric flow pattern around the sphere. R3 shows a flow across a junction of size $\sim$ D_m where fluid enters the junction through four inlets and exits through two outlets. There is a glass sphere just below the focus plane in this junction area as shown in Fig. 4.7(e). R4 shows a typical repeating jet-like flow with high velocity flow entering into the voids from a small gap. The development of flow from Darcy regime to turbulent regime and the velocity fluctuations in these

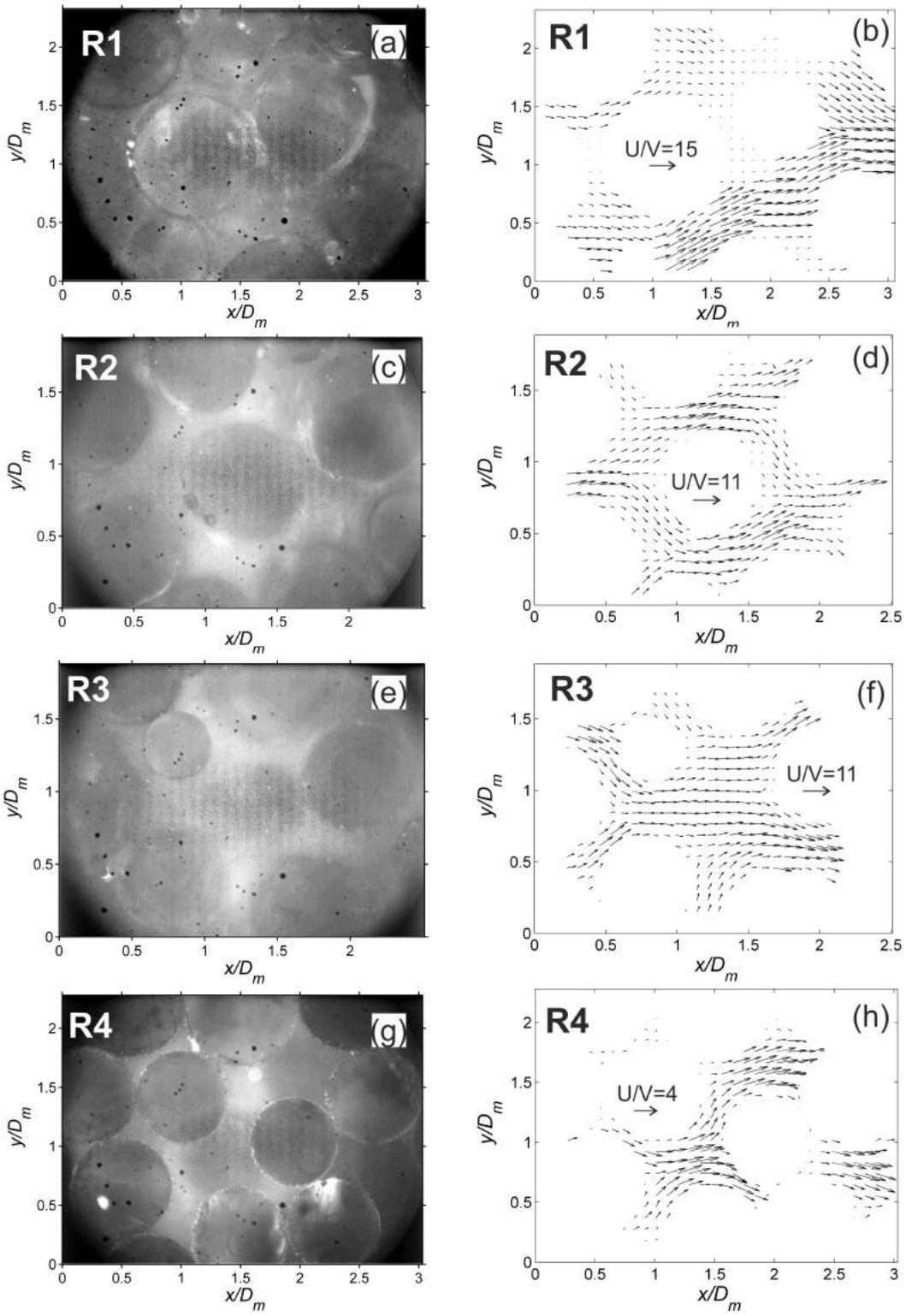

Figure 4.7: Local structure of sample (a) $D_m = 170$ μm, (c) $D_m = 430$ μm (region I), (e) $D_m = 430$ μm (region II) and (g) $D_m = 710$ μm, and (b), (d), (f) and (h) are corresponding instantaneous velocity distributions at Re of 0.39, 1.1, 1.1 and 6.9, respectively. These four regions are designated as R1, R2, R3 and R4, respectively.

areas are discussed in following sections.

4.1.6.2 Time-averaged velocity distribution

The time-averaged velocity distribution from the pre-Darcy to the turbulent regime in each region was studied to gain an insight into the details of the flow behaviours in the sintered glass samples. The time-averaged velocity distribution in different regimes is similar in regions of R1, R2 and R3, so the flow velocity distributions are presented briefly. The time-averaged velocity distribution in different regimes is very different in region R4, so the velocity distribution is presented in details.

Fig. 4.8 shows the contour plots of time-averaged velocity distribution at a specific Re and velocity profile along a reference line at various Re values for R1, R2, and R3. It is note that the ends of the reference lines are not located on the fluid/solid interface, but they are located in the fluid field and there is a small distance from the solid wall. The contour plots of velocity distribution are similar at different Reynolds numbers for these three regions and therefore only one is presented for each region. The color in the contour plots indicates the velocity magnitude and the arrow indicates the local flow direction. The solid glass spheres was set as white as only noise exists in these regions.

Fig. 4.8 shows that the local structures of R1 and R2 and the velocity profiles along the reference lines of AB and CD are similar, but the velocity distribution at the pore scale (contour plots) is different. The velocity is asymmetrically distributed in R1 and symmetrically distributed in R2. The velocity profiles along the lines show a parabolic shape at all Re values for these two regions and both skew downward (to

B at Re = 4.7 in R1 and D at Re = 40 in R2) after entering the turbulent regime. In R3, velocity magnitude decreases near the E and F regions and increases in the middle region when flow transits from the Darcy-Forchheimer regime (Re = 0.2, 3) to the turbulent regime (Re = 19, 40). The velocity profile shows a parabolic shape in some areas even in this complex region, as displayed by the fitting lines in Fig. 4.8(f).

Fig. 4.9 shows the development of velocity distribution with Reynolds number (flow regimes) at the pore scale in R4. We focus mainly on the lower left part of the flow field, which has been marked with two inlets (inlet 1 and inlet 2), two outlets (outlet 1 and outlet 2) and a reference line GH in the junction. The velocity profile along the reference line of GH is shown in Fig. 4.10.

Fig. 4.9 shows that the velocity distribution is similar before reaching turbulent regime (Re = 5, 26), but is different in the turbulent regime (Re = 57, 140). In the pre-Darcy regime (Re = 5), velocity magnitudes in the two inlets are similar, but the velocity magnitude in outlet 2 is higher than that in outlet 1. This is probably because the flow direction in outlet 2 is more aligned to the bulk velocity and thus less tortuous and energy-consuming than outlet 1. The velocity profile along line GH has a parabolic shape. In the Forchheimer regime (Re = 26), there is an area near inlet 2 (marked by a red circle) where the velocity decreased to zero. This is caused by the vortices after the glass sphere near inlet 1. The velocity magnitude in outlet 2 becomes higher compared to that in the pre-Darcy regime and the overall flow in the junction area skews toward the wall in the H side, which can also be seen from the velocity profile along GH in Fig. 4.10. In addition, the velocity profile in the junction center also shows that the velocity magnitude is uniform, like a plug flow.

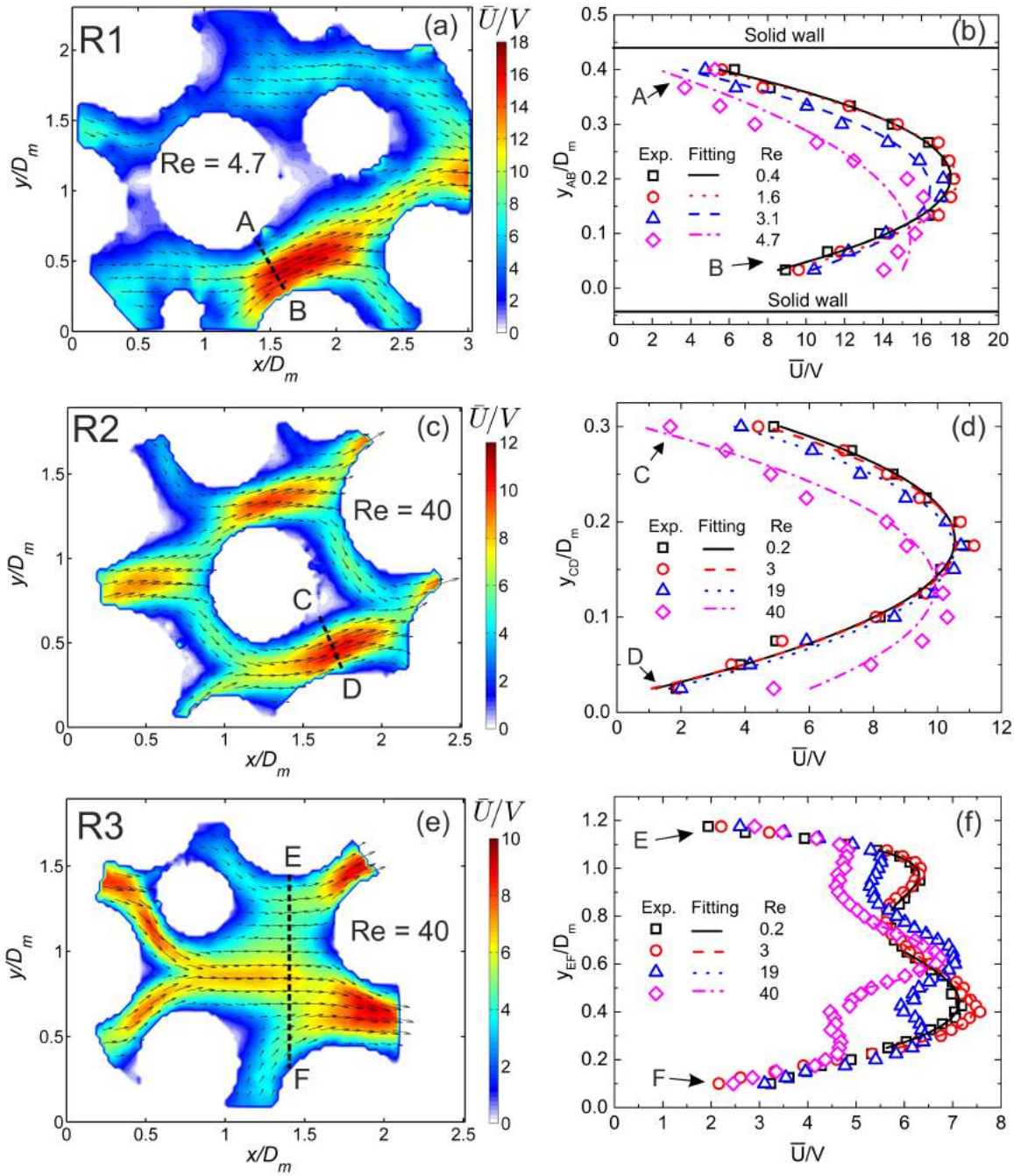

Figure 4.8: Time-averaged velocity distributions in sample (a) $D_m = 170\ \mu$m (R1), (c) $D_m = 430\ \mu$m (R2) and (e) $D_m = 430\ \mu$m (R3), and (b), (d) and (f) are corresponding velocity profiles at different Re values along the reference lines of AB, CD and EF. The colour in contour plots represents the magnitude of the velocity, and the arrow represents the velocity direction.

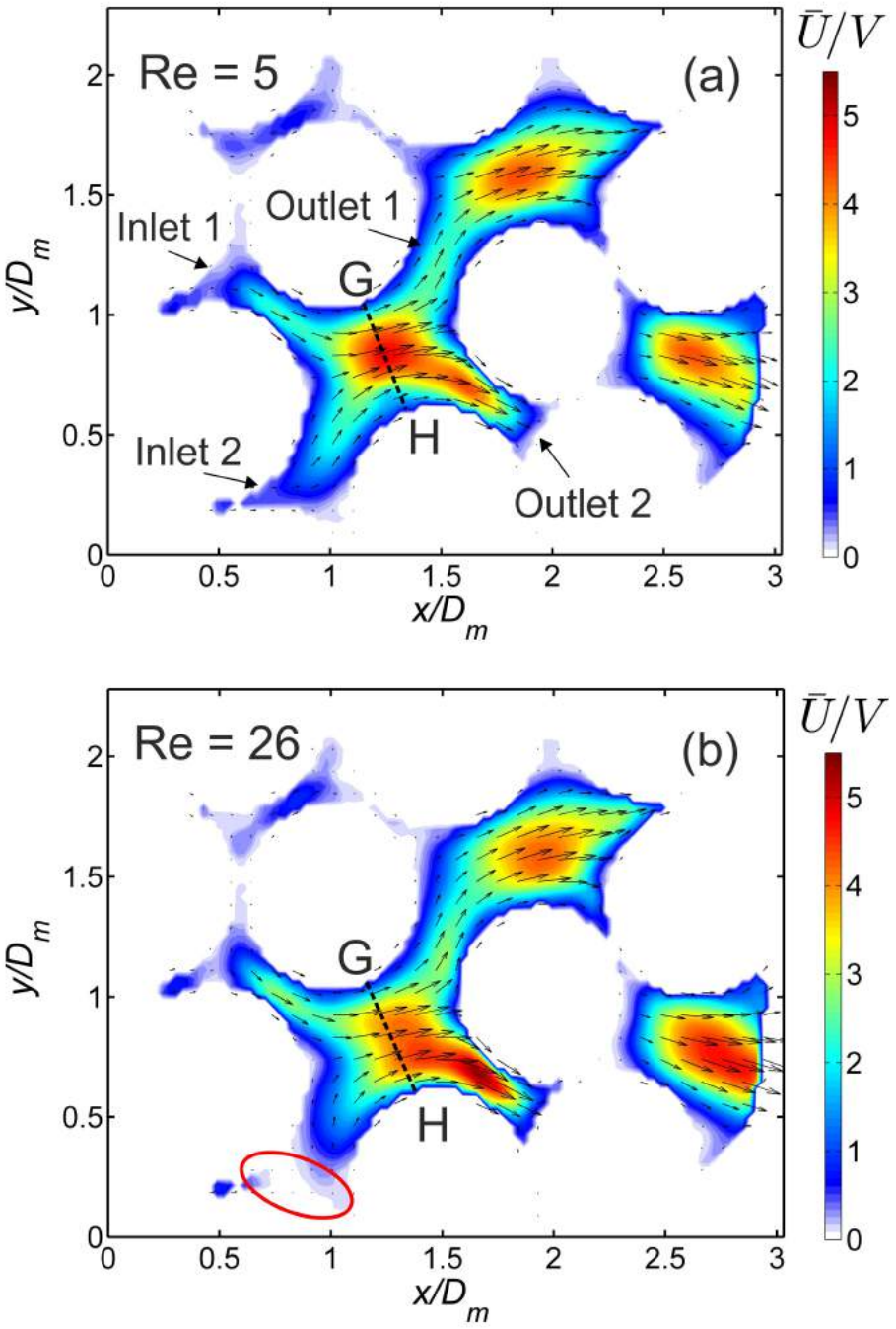

Figure 4.9: Time-averaged velocity distribution in sample $D_m = 710\ \mu m$ (R4) in (a) pre-Darcy regime, (b) Forchheimer regime, (c) and (d) turbulent regime. The colour represents the magnitude of the velocity, and the arrow represents the velocity direction. (to be continued)

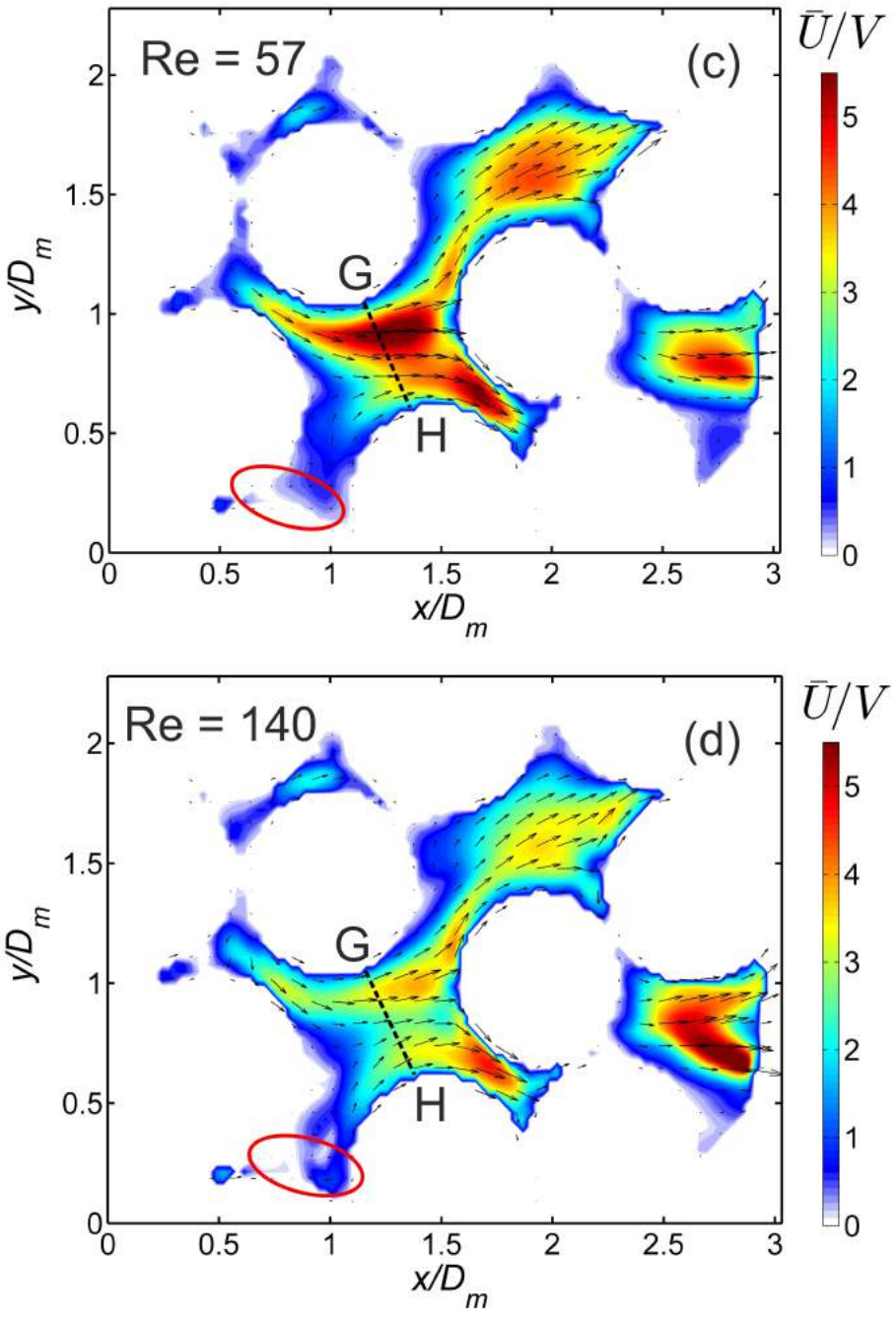

Figure 4.9: (continued) Time-averaged velocity distribution in sample $D_m = 710\ \mu m$ (R4) in (a) pre-Darcy regime, (b) Forchheimer regime, (c) and (d) turbulent regime. The colour represents the magnitude of the velocity, and the arrow represents the velocity direction.

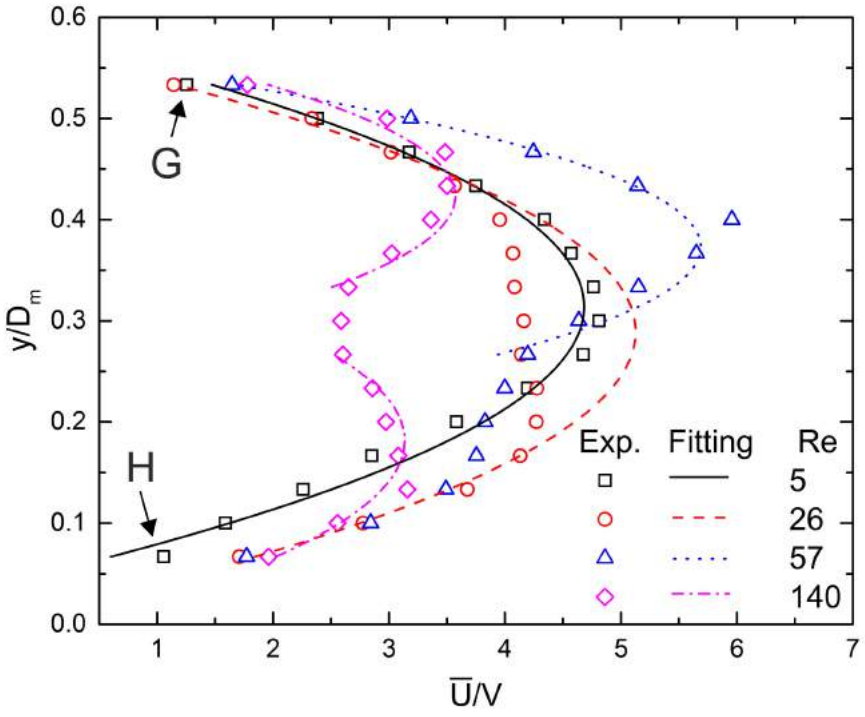

Figure 4.10: Velocity profile at different Reynolds numbers along the reference line GH in Fig. 4.9.

The velocity distribution in the turbulent regime (Re = 57, 140) differs from the previous regimes and the velocity distribution changes significantly with Reynolds number. The velocity development in the turbulent regime can be divided into three phases: initial phase, transition phase and stable phase. In the initial phase (Re = 57), two tributaries form in the junction area: one tends to flow out from outlet 1 with a relatively higher velocity magnitude and the other tends to flow out from outlet 2 with a relatively lower velocity magnitude. The velocity profile along the line GH in Fig. 4.10 (Re = 57) shows this asymmetrical feature and the velocity profile near point G still shows a parabolic shape. In addition, the velocity magnitudes in inlet 1 and outlet 1 increase compared to those in the previous regimes. The transition phase is in the Reynolds number range of 57 to 140. In this phase, the velocity near point G decreases gradually until reaching another state where the

velocity magnitude is comparable to that in the junction area. In the stable phase (Re = 140), the velocity is distributed more uniformly and a recirculation is observed near the inlet 2 area (red circle). The velocity profile along line GH in Fig. 4.10 shows that the flow splits quite evenly between outlets 1 and 2.

4.1.6.3 Statistical analysis of velocity magnitude

A statistical analysis on the time-averaged velocity field at different Re in regions R1, R2, R3 and R4 is conducted. The probability distribution of the Darcian velocity normalized longitudinal (u) and transverse (v) velocity components is shown in Fig. 4.11. Overall, the longitudinal velocity component shows a strong skewness towards the positive or downstream direction and the transverse velocity shows a symmetrical distribution about $v/V = 0$, which is consistent with previous reportsPatil & Liburdy (2013), Datta et al. (2013), Sen et al. (2012). Due to the large surface area in porous structure, the velocity magnitudes in the near wall region dominates the flow, and therefore the velocity in the non-near wall region only account for a small part of the flow field. This is agree with the pdf distribution of the longitudinal velocity component in which the velocity magnitude corresponding to the peak is located near the solid wall in the contour map, e.g. the peak of R2 is $u/V = 2$ and this value is located in the near wall region in Fig.fig:TimeAveragedVelocityMapG170430(c).

There are also differences between these regions in spite of a similar pdf distribution. In R1, both the pdf of u/V and v/V at different Reynolds numbers is seen to collapse to a single curve. This is because the velocity distribution ($\bar{U}/V$) at the pore scale does not change with Re. In R2, velocity magnitude becomes more uniform in the turbulent regime (Re = 40), so the pdf curve of u/V component becomes

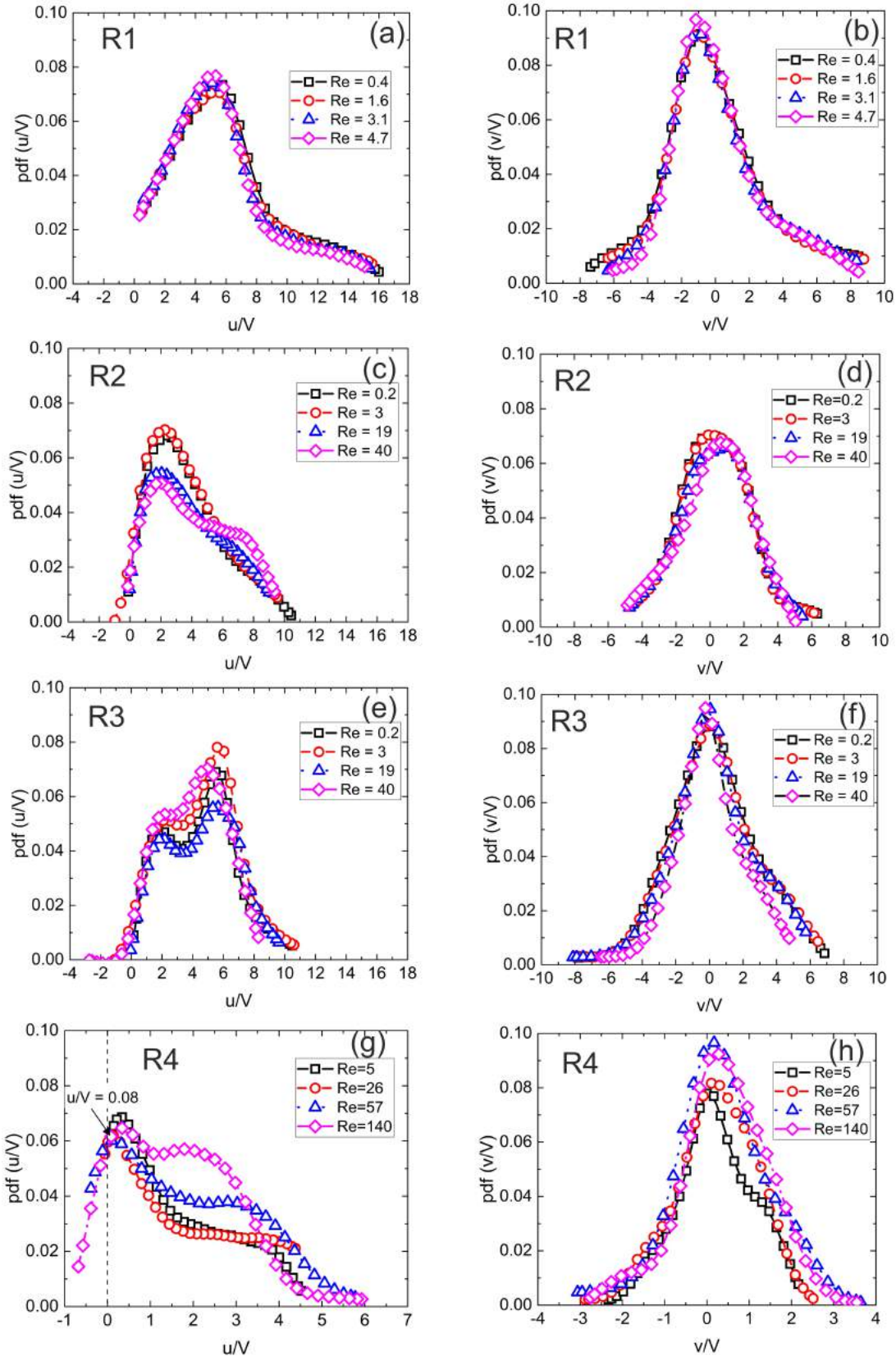

Figure 4.11: (a), (c), (e) and (g) show probability density function (pdf) of u/V for R1, R2, R3 and R4, and (b), (d), (f) and (h) are the corresponding pdf of v/V.

flatter. In R3, there are two peaks in the pdf of u/V. The first peak ($u/V = 1.5$) and the second peak ($u/V = 6$) corresponding to the velocity magnitudes located at the near wall region and the central region, respectively. In R4, the near zero peak ($u/V = 0.08$) means that at Re = 5 and 26 (before reaching turbulent regime), the velocity in the near wall region and the velocity in the y direction predominate the flow field as the velocity in these two regions produce a very small u component. The pdf curve of (u/V) becomes flatter in turbulent regime (Re = 140), indicating the velocity becomes more uniform at the pores scale in the field of view (see Fig. 4.9(d)).

Negative longitudinal velocities in R4 are observed when the Reynolds number is beyond 26, which means some fluid is moving in reversed direction or recirculation, opposite to the bulk flow direction. A recirculation region is observed in the velocity contour map of R4 in Fig. 4.9 (marked with red circles). Negative values of the longitudinal velocity component are also found by Maier et al. (1998) using Lattice-Boltzmann simulations and by Kutsovsky et al. (1996) using nuclear magnetic resonance imaging to study flow through packed beds. Their findings that the negative tails decrease as the Reynolds number decreases, is consistent with our results.

4.1.7 Velocity fluctuation at the pore scale

The velocity fluctuation intensity in the sintered glass samples was studied to better understand the flow behaviour at the pore scale. In arriving at these results, the local mean velocity components were subtracted from each velocity record. The longitudinal velocity fluctuation and the local velocity fluctuation were normalized by the

Darcian velocity and the local time-averaged velocity respectively. The longitudinal velocity fluctuation is defined as $\sqrt{u'^2}/V$ and the local velocity fluctuation intensity is defined as $U' = \sqrt{u'^2 + v'^2}/\bar{U}$, where u' and v' are fluctuations of the velocity components. The velocity fluctuation intensity at the pore scale can be compared by longitudinal velocity fluctuation. Whether the flow is laminar or turbulent can be determined by checking the value of the local velocity fluctuation, i.e., $U' \sim 0$ for laminar flow and $U' \geq 0.1$ for turbulent flow. Due to the limitation of experimental conditions such as strong light reflection and low contrast at high magnifications, some wrong velocity vectors in some frames make it difficult for a fluctuation analysis in regions of R1, R2 and R3 . Therefore, only velocity fluctuation in R4 is presented in this section.

4.1.7.1 Longitudinal velocity fluctuation

Fig. 4.12 shows the Darcian velocity normalized longitudinal velocity fluctuation in R4. Overall, the longitudinal velocity fluctuation increases as Re increases, especially after entering the turbulent regime, and the fluctuation is unevenly distributed at the pore scale. The longitudinal velocity fluctuation distribution in the pre-Darcy (Re = 5) and Forchheimer (Re = 26) regimes is nearly identical i.e., the strong fluctuation is in the near wall region, with the same fluctuation intensity. The fluctuation becomes stronger in the near wall region in the turbulent regime (Re = 57, 140) and the strong velocity fluctuation has already spread to the non-near wall region. If a line is drawn between point P and Q, it can be found that the strong fluctuation is mainly in the GPQ area, which is produced by the flow from inlet 1. Fig. 4.12 also shows that the fluctuation intensity in the rectangle (marked in the figure) is very strong in the turbulent regime (Re = 140), It can be inferred that this is due to the

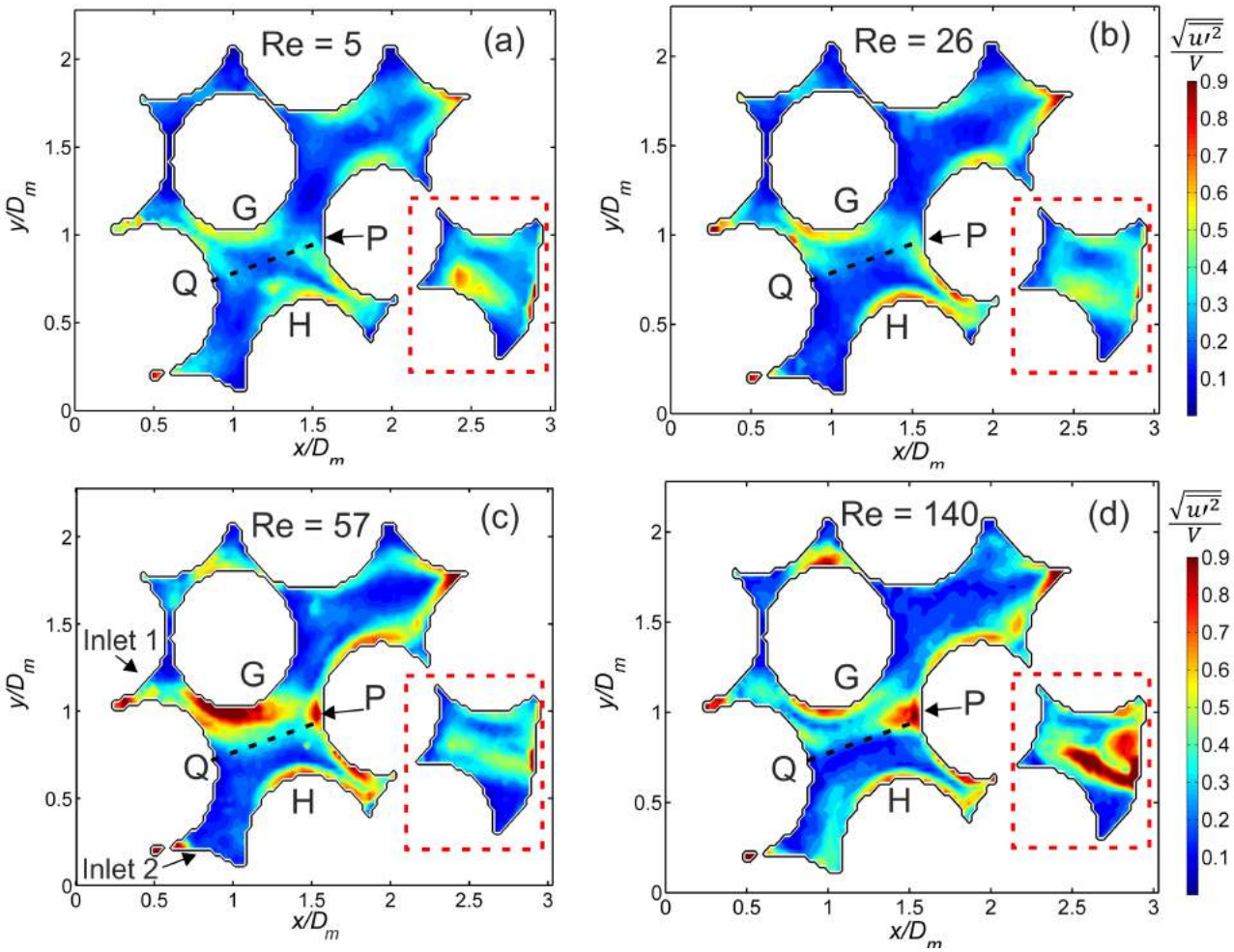

Figure 4.12: Contour plots of Darcian velocity normalized longitudinal velocity fluctuation in the region R4 at (a) Re = 5, (b) Re = 26, (c) Re = 57 and (d) Re = 140.

flow from the z direction because there is no entry to this area in the focal plane. In addition, the very thin layer with strong velocity fluctuation near point H is believed to be caused by the high uncertainty of PIV in the surface of the solid bed. The high fluctuation in point P means that the position of stagnation point changes with time and this is explained by the instantaneous velocity map in Fig. 4.13.

Fig. 4.13 shows the instantaneous velocity distribution of the junction area (sur-

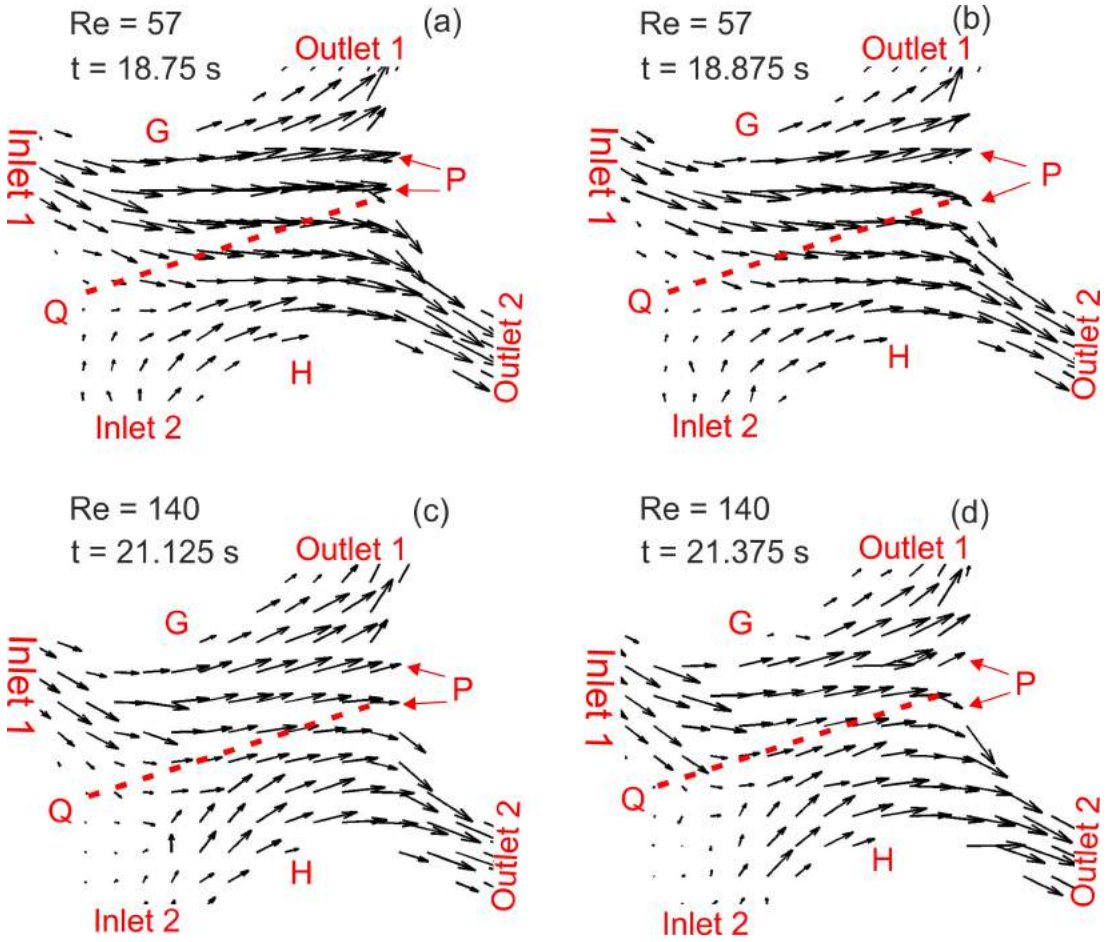

Figure 4.13: Instantaneous velocity map near point P shown in Fig. 4.12 at (a) - (b) Re = 57 and (c) - (d) Re = 140 at different times.

rounded by points G, H, P and Q) in Fig. 4.12 at different times in the turbulent regime (Re = 57 and 140). It can be seen that the two velocity vectors are parallel at point P at t = 18.75 s and split to two directions at t = 18.875 s, Re = 57. The same flow behaviour was observed at Re = 140. Another phenomenon at Re = 140 is that the velocity vector in inlet 2 region increase quickly from zero to a mean value, meaning the flow is mainly from z direction. These fluid flow turns smooth to outlet 2, producing a weak fluctuation in the HPQ area. However, the fluid from inlet 1 keeps in the focal plane and part of it turns sharply to outlet 1, producing a strong fluctuation in the GPQ area.

4.1.7.2 Local velocity fluctuation

Fig. 4.14 shows the local velocity fluctuation normalized by the local time-averaged velocity magnitude in R4 at Re = 26 and 140. The solid spheres were set to white and the edges of the solid spheres were drawn as black line for a better view. The flow regions with abnormal fluctuation intensity were also set to white as there is only noise in these areas. The determination of the noise level is semi-empirical, In our case, the time-averaged local velocity magnitude in those areas was set as the threshold. Therefore, the region with local velocity magnitude less than the threshold is treated as noise and set to white.

Fig. 4.14 shows that the velocity fluctuation intensity, especially in the non-near wall region, increases significantly from the Forchheimer regime (Re = 26) to the turbulent regime (Re = 140). The fluctuation intensity in the near wall region is very high in both the Forchheimer and turbulent regimes. This is caused by two reasons: (1) the μ-PIV uncertainty near the surface of solid spheres is high and (2) the velocity magnitude near the surface of solid spheres is extremely low. In the non-near wall region, the velocity fluctuation intensity is close to 0.05 in the Forchherimer regime and greater than 0.1 in the turbulent regime. Fig. 4.15 plots velocity fluctuation magnitude along the line GH in Fig. 4.14 at various Reynolds numbers. It can be seen that the thickness of the near wall layer is about $0.1D_m$ and the velocity fluctuation is abnormally high in this layer. In the central region, velocity fluctuation stays at a low level before reaching turbulent regime and fluctuating around 0.1 in the turbulent regime.

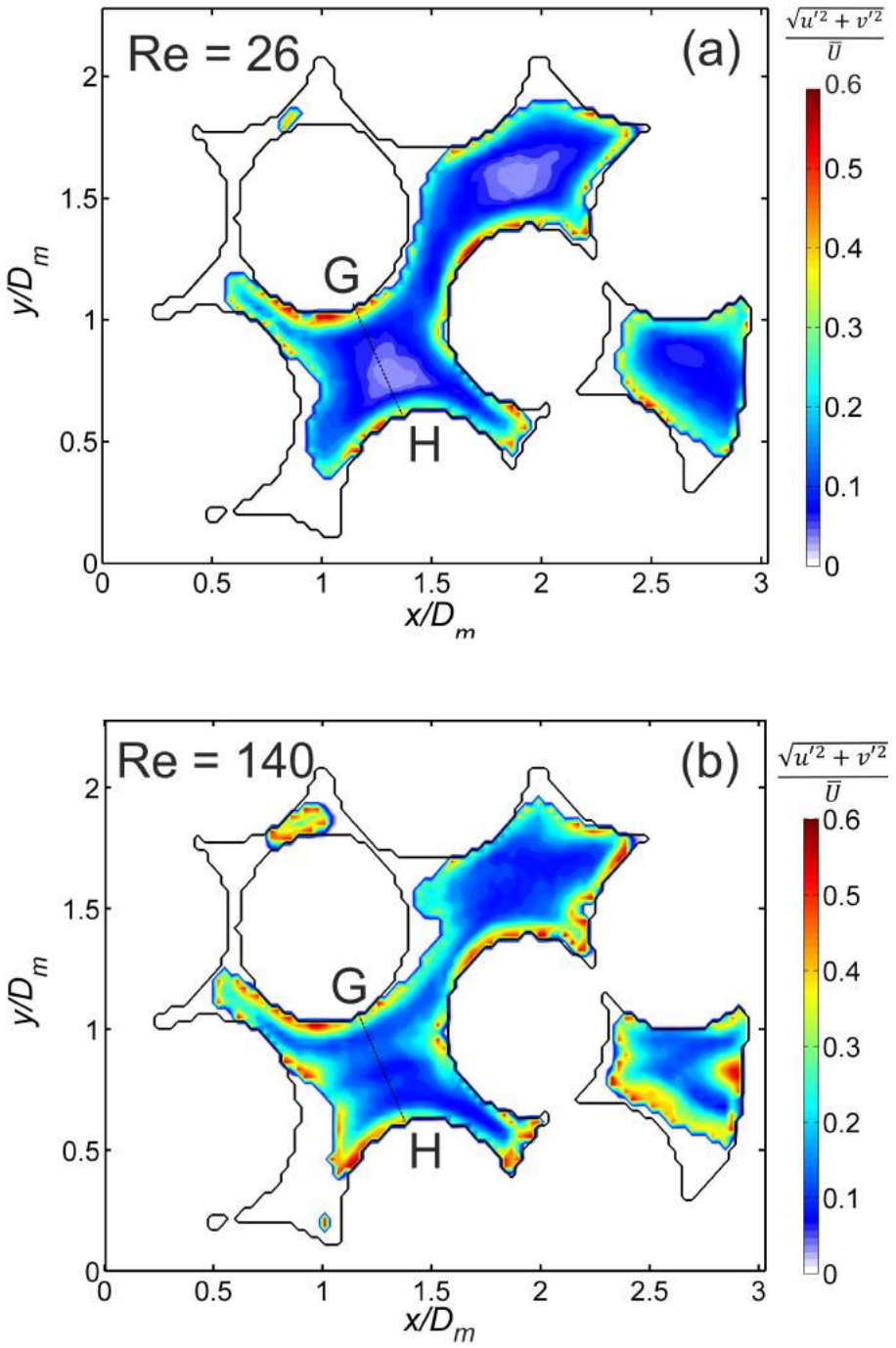

Figure 4.14: Contour plots of local velocity fluctuation normalized by the local time-averaged velocity magnitude in the (a) Forchheimer regime (Re = 26) and (b) turbulent regime (Re = 140). The solid spheres and high noise areas are set to white.

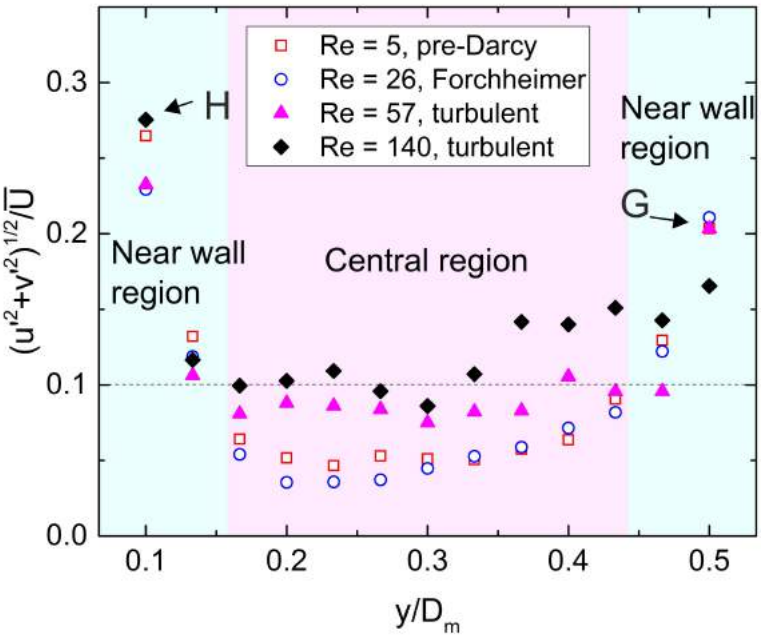

Figure 4.15: The time-averaged velocity magnitude normalized fluctuation intensity distribution along line GH in Fig. 4.14 at various Reynolds numbers. The near wall region and the central region are marked with different colours.

The transition regime between laminar and turbulent flow can be obtained by examining the variation of the fluctuation intensity with Re. Fig. 4.16 shows the variation of globally averaged velocity fluctuation with Re in region R4. The value was calculated by averaging the time-averaged velocity magnitude local velocity fluctuation over a line or the whole 2D region, represented as $[(u'^2 + v'^2)^{1/2}/\bar{U}]$. The reduced pressure drop $(\Delta P/LV)$ - Re was also presented in the same plot (left - hand y axis) to compare the critical Reynolds numbers obtained from these two methods. Different flow regimes are marked with different colours according to the reduced pressure drop plots. Fig. 4.16 shows that the transition regime obtained from the pressured drop measurement agrees well with that obtained from the μ-PIV measurement. It demonstrates that the flow in the pre-Darcy, Darcy and Forchheimer regimes is laminar because the velocity fluctuation remains at a nearly fixed, low value before the

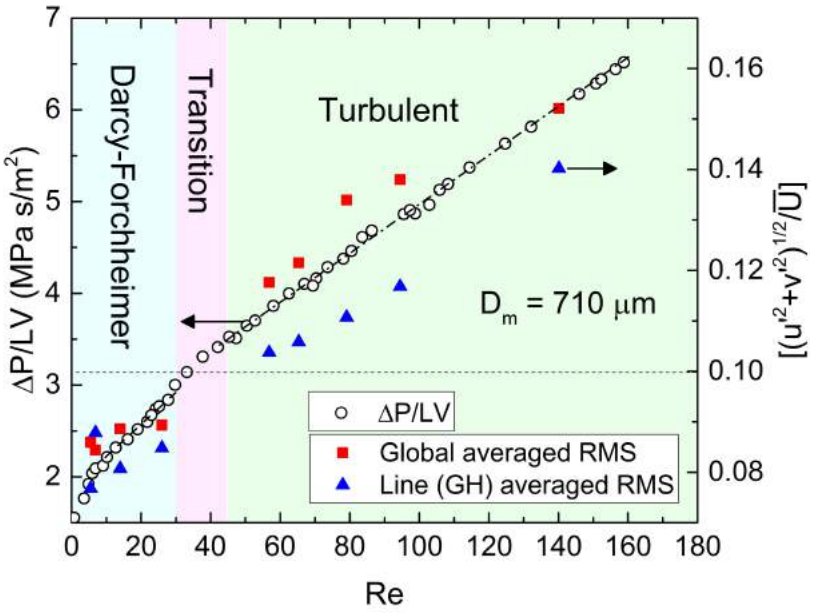

Figure 4.16: Global averaged velocity fluctuation (right - hand y axis) and reduced pressure drop (left - hand y axis) versus Reynolds number in R4. Flow regimes are marked with different colours.

transition regime, and increases dramatically after the transition regime.

4.2 Flow characteristics in the porous glass with spherical pores

4.2.1 Structural properties

Table 4.4 lists the information of the fabrication parameters, including masses of NaCl powder and glass powder, along with the target and final porosities of the 4 porous glass samples with spherical pores. The actual porosity is different from the target porosity due to interparticle voids and densification of the glass powder during sintering. The actual porosity is determined by the volume fraction of the

NaCl particles and the final interparticle voids. In practice, it is approximately the volume percentage of the NaCl plus ≈ 7%.

Table 4.4: Details of porou glass with spherical pores.

Samples	NaCl (g)	Glass beads (g)	Target Porosity	Actual porosity	PIV magnification
SG72	1.3155	0.8068	0.65	0.72	100 ×
SG77	1.4167	0.6915	0.70	0.77	100 ×
SG78	1.4167	0.6915	0.70	0.78	100 ×
SG81	1.5179	0.5762	0.75	0.81	100 ×

Fig. 4.17(a) shows a typical pore structure of the porous glass samples, obtained by scanning electron microscopy. The large pores are negative replicas of the sodium chloride particles and are largely spherical. They are all interconnected to form an open cell network. The cell walls are formed by the sintered glass particles and are therefore quite rough. It can also be seen that the spherical shape of glass particles still remain after sintering. Fig. 4.17(b) and (c) show the top view and side view of the porous sample. The top view illustrates the spherical pores distributing uniformly in the sample and side view shows the typical sandwich structure of the sample.

4.2.2 Pressure drop

Fig. 4.18 shows the relationship between pressure drop and Reynolds number for porous glass with spherical pores. The pressure drop shows a typical quadratic

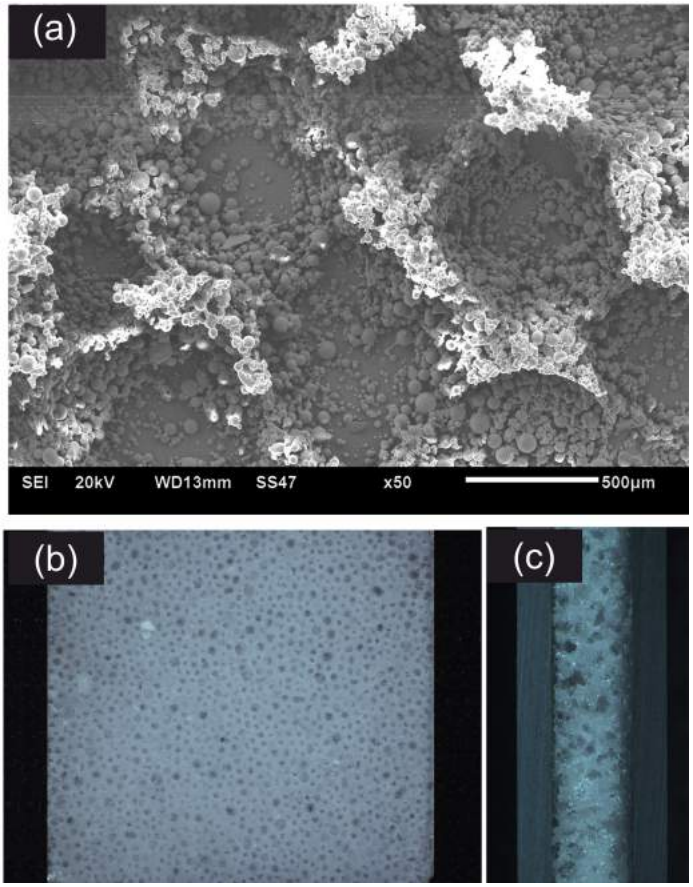

Figure 4.17: (a) Microstructure of porous glass under scanning electron microscope. (b) Top view and (c) side view of the porous glass sample.

relationship with Re, with the quadratic curve fitting the data well with a high correlation factor. The normalized pressure drop of SG72 is more than double that of SG77 and SG78 for a given Re, implying great dependence of pressure drop on porosity.

4.2.3 Flow regimes

Flow regimes can be distinguished by slope changes of the $\Delta P/LV$ - Re plots showed in Fig. 4.19. Table 4.5 lists the flow regime boundaries obtained from the figures.

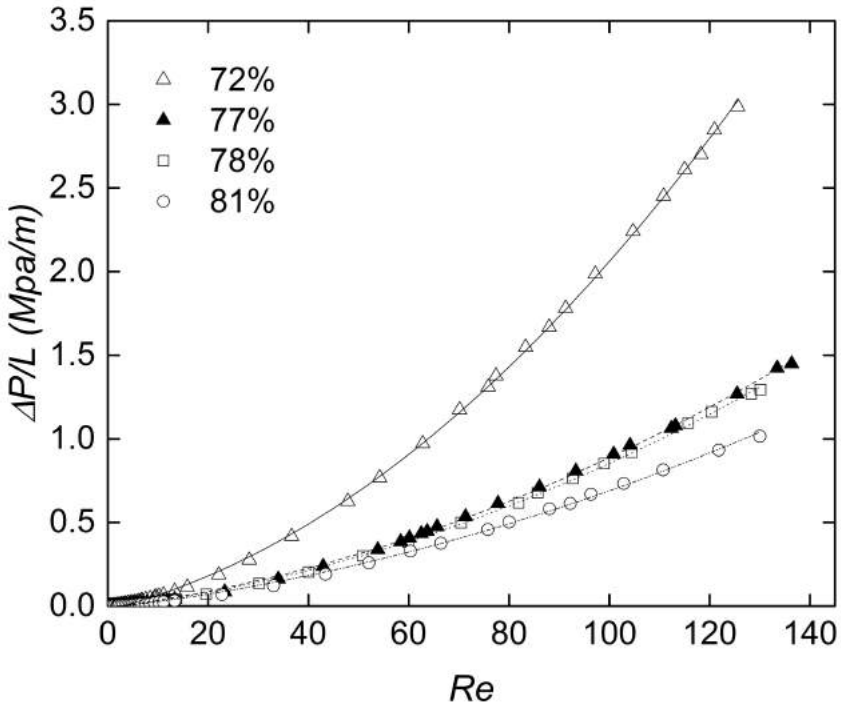

Figure 4.18: Pressure drop versus Reynolds number in porous glass with spherical pores.

Results on porous metal from several previous studies are also listed in the table for comparison. The literature on the fluid flow in metal foams show different flow regime boundaries. Boomsma & Poulikakos (2002) provided the pore size based transition Reynolds number between the Darcy and Forchheimer flow regimes, which is quite high compared with the present results, probably due to its high porosity and different structure.

The regimes boundaries identified are also different from that identified in the sintered glass samples, because they have a completely different internal structure and porosity distribution. We would therefore expect different results for porous samples with the same porosity but produced using different techniques as they would have different pore morphologies. However, two samples produced in the same way, with

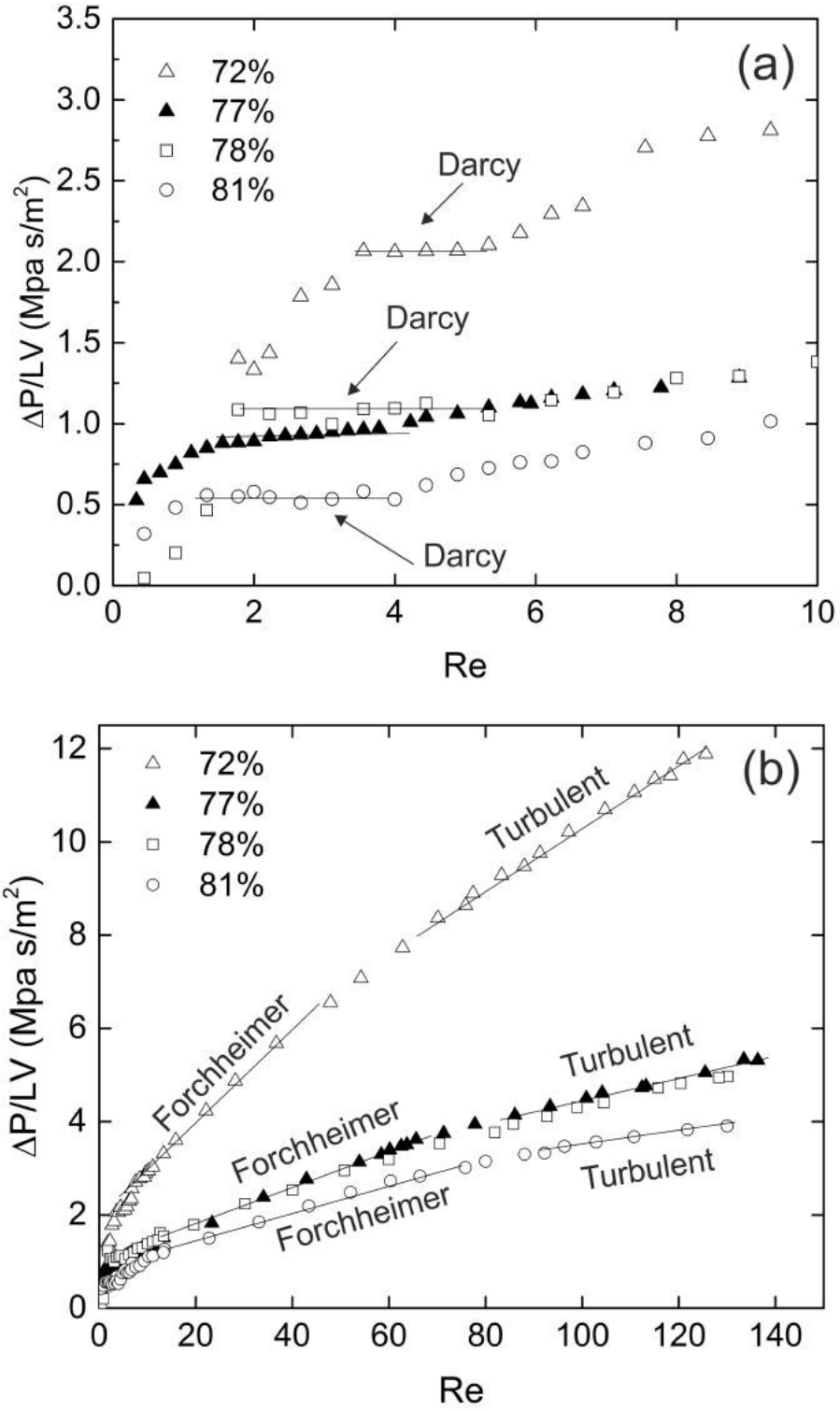

Figure 4.19: Reduced pressure drop versus Reynolds number: (a) pre-Darcy and Darcy regimes and (b) all flow regimes. (a) is an enlarged plot of (b) at low Re.

the same porosity, are expected to give similar results if the pore morphology is reproducible. This is evidenced by samples SG77 and SG78, which have very similar porosities and give very similar results.

Table 4.5: Flow regime boundaries of porous glass with spherical pores. (PPI-pores per inch)

	Sample	pre-Darcy	Darcy	Forchheimer	Turbulent
Current study	SG72 (0.72)	$Re < 3.50$	$3.50 < Re < 4.8$	$6.8 < Re < 47$	$62 < Re$
		$Re' < 0.20$	$0.20 < Re' < 0.28$	$0.39 < Re' < 2.73$	$3.58 < Re'$
	SG77 (0.77)	$Re < 1.72$	$1.72 < Re < 4.5$	$8.8 < Re < 65$	$71 < Re$
		$Re' < 0.11$	$0.11 < Re' < 0.31$	$0.61 < Re' < 4.52$	$4.91 < Re'$
	SG78 (0.78)	$Re < 1.55$	$1.55 < Re < 3.7$	$10.0 < Re < 70$	$70 < Re$
		$Re' < 0.10$	$0.10 < Re' < 0.27$	$0.73 < Re' < 5.12$	$5.12 < Re'$
	SG81 (0.81)	$Re < 1.34$	$1.34 < Re < 2.7$	$11.1 < Re < 75$	$88 < Re$
		$Re' < 0.09$	$0.09 < Re' < 0.19$	$0.79 < Re' < 5.38$	$6.27 < Re'$
Boomsma et al.	10 PPI (0.92)	NA	$Re < 725$	$725 < Re$	NA
(Boomsma &	20 PPI (0.92)	NA	$Re < 412$	$412 < Re$	NA
Poulikakos 2002)	40 PPI (0.93)	NA	$Re < 177$	$177 < Re$	NA

Fig. 4.20 plots the relationship between flow regime boundaries and porosity of porous glass with spherical pores. It shows that the onset Re for each flow regime boundary increases linearly with porosity, except that Re_D and Re_{TF} decrease slightly with porosity. In addition, the range of the Forchheimer regime is much wider than that for the sintered glass samples.

4.2.4 Permeability and form drag coefficient

Table 4.6 lists the permeability and form drag coefficient values of porous glass with spherical pores. The values were calculated by two different methods (Boomsma & Poulikakos 2002) based on data from each flow regime or from all regimes. The variations of permeability and form drag coefficient against porosity in each and all flow regimes are plotted in Figs. 4.21 and 4.22.

Table 4.6: Permeability (K $\times$ 10^{-10} m^2) and form drag coefficient (C $\times$ 10^4 m^{-1}) of porous glass with spherical pores in various flow regimes.

Sample	Darcy		Forchheimer			Turbulent			All regimes		
	K	R^2	K	C	R^2	K	C	R^2	K	C	R^2
SG72	5.40	0.99	4.04	4.25	0.99	2.60	3.32	0.99	3.04	3.50	0.99
SG77	8.7	0.99	7.1	1.94	0.99	4.76	1.29	0.99	5.39	1.39	0.99
SG78	9.69	0.99	8.11	1.64	0.99	5.30	1.20	0.99	6.15	1.32	0.99
SG81	16.3	0.99	11.92	1.35	0.99	7.02	0.75	0.99	8.74	0.93	0.99

Figure 4.21 shows that porosity has a significant effect on the permeability. Increasing porosity leads to lower fluid flow resistance since there is a lower fraction of solid matrix and thus less internal surface area. Furthermore, the likelihood of the pores

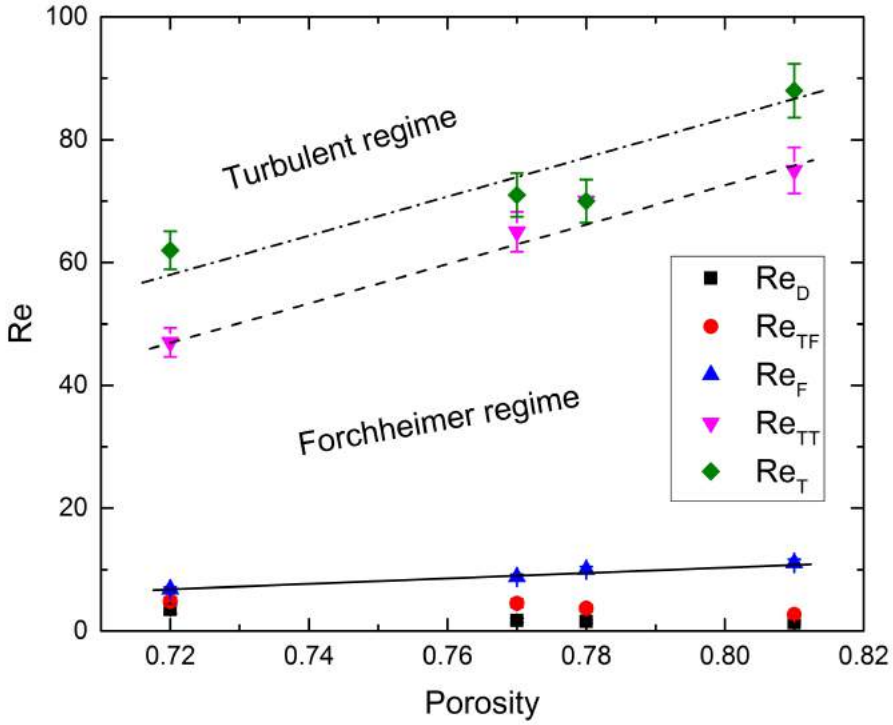

Figure 4.20: Relationship between flow regime boundaries and porosity in porous glass with spherical pores.

being connected to each other is higher in samples with a high porosity than in low porosity samples. Therefore, the permeability of the porous medium increases with increasing porosity.

It is also found that the permeability of the porous glass decreases from Darcy to Forchheimer and then to turbulent regime. The highest permeability occurs in the Darcy flow regime, while the lowest permeability occurs in the turbulent regime for all the samples. The larger permeability in the Darcy flow regime is likely because of the weak effect from the near-wall layers and low energy dissipation in the flow. In the non-Darcy flow regime, the inertial drag force effect and kinetic energy degradation resulting from pore walls and sharp changes of flow direction lead to the decrease of mass transfer efficiency.

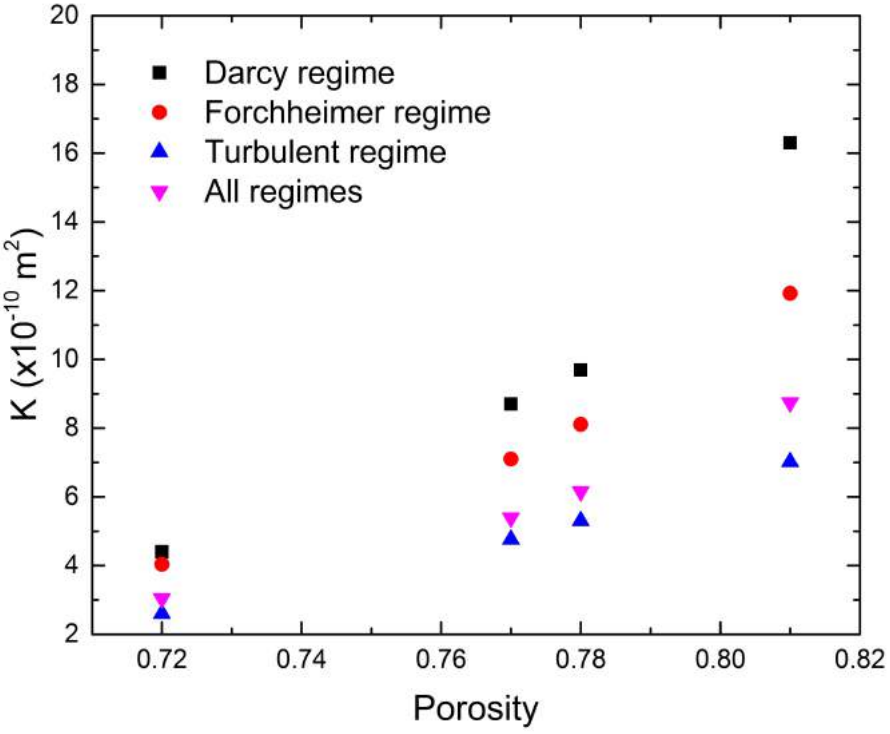

Figure 4.21: Variation of permeability with porosity in porous glass with spherical pores.

Fig. 4.22 shows that form drag coefficient decreases with increasing porosity. Increasing porosity reduces the quantity of corners, edges and turns where the inertial cores develop. The interaction between fluid flow and solid walls becomes weak in high porosity samples because of less solid walls. As a consequence, the form drag coefficient decreases as porosity increases. The value of form drag coefficient calculated from the Forchheimer regime is larger than that calculated from the turbulent regime. What causes the decrease of form drag coefficient from the Forchheimer regime to the turbulent regime is still unclear.

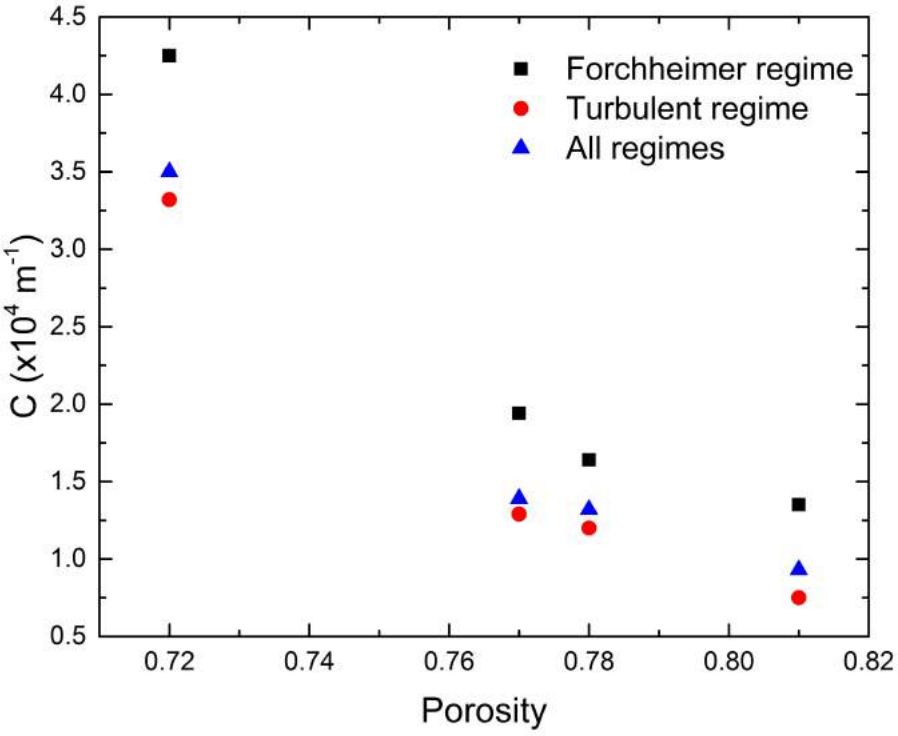

Figure 4.22: Variation of form drag coefficient with porosity in porous glass with spherical pores.

4.2.5 Micro-PIV measurements

In order to gain an insight into the flow behaviours in the porous glass with spherical pores, the velocity fields from the pre-Darcy regime to the turbulent regime in individual pores are studied. Although each sample and region has unique properties, the flow through different samples behaves similarly and shows a similar trend. Only one sample, SG72, is therefore taken as an example for detailed visual analysis, while the statistics for all samples tested are presented.

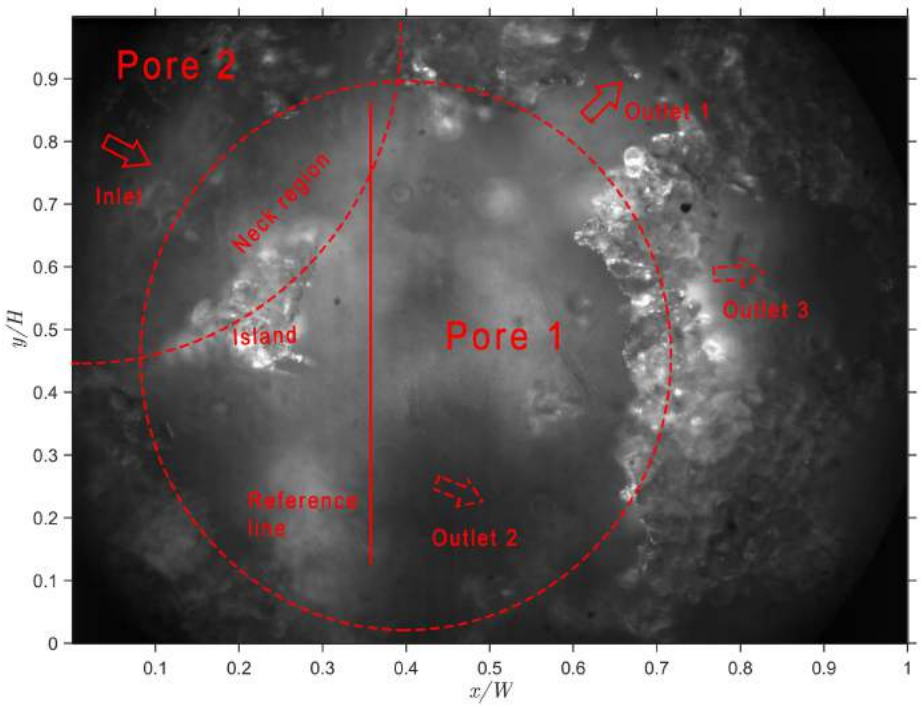

Figure 4.23: Local pore structure in sample SG72.

4.2.5.1 Local porous structure

Fig. 4.23 shows the local porous structure with fluid passing through, with W and H representing the width and height of the field of view. The structure consists of a main pore (pore 1) in the center and another pore (pore 2) in the upper left corner, and a narrow neck region formed due to the overlap of the two pores. The neck region plays a crucial role in connecting neighboring pores and thus forming an open channel network to let fluid pass through from one pore to another. An irregular island protrudes into the neck region, narrowing the flow channel again.

For this given local structure, theoretically flow can get into pore 1 from the inlet, and exit from three outlets. Outlet 1 is located in the focus plane, forming an acute angle with the streamwise direction (x direction). Outlet 2 is located deeper than

the focus plane in the z direction, forming an apparent right angle with the streamwise direction, and the fluid has to move perpendicularly to the mean flow direction in order to flow out through this outlet. Outlet 3 is a complicated path with three acute angle turns. Some parts of outlet 3 are in the focus plane and some parts are not. Therefore, the flow needs to move downward first, passing through the solid bridge and then move upward to the focus plane again to exit through this outlet. Some other outlets or inlets may exist besides these mentioned above due to the complex structure. To capture the main features, the geometry is characterized in this simplified manner.

4.2.5.2 Time-averaged velocity distribution

A reference line perpendicular to the x direction has been drawn across the pore and the time-averaged velocity profiles at various Reynolds numbers along the line are plotted in Fig. 4.24. The contour plots of the time-averaged velocity at the pore scale are shown in Fig. 4.25. The color indicates the magnitude of velocity and the arrow indicates the direction of local velocity. The solid matrix is shown as white in the contour plots as only noise exists in this region. For this particular structure, the main flow is divided into two subflows by the island as shown in the contour plots. Accordingly, the flow is divided into three regions, region 1, region 2 and region 3 for convenience of description. In theory, the velocity should decrease from the center of a pore to zero at the near-wall region because of the friction effect from the pore wall (no slip condition). However, in reality, the PIV measurement error at the near-wall region is high because when fluid passes along the wall, the fluorescent particles tend to stick on the surface of the rough wall, resulting in a very bright fringe, making it very difficult to precisely trace the path of the particles.

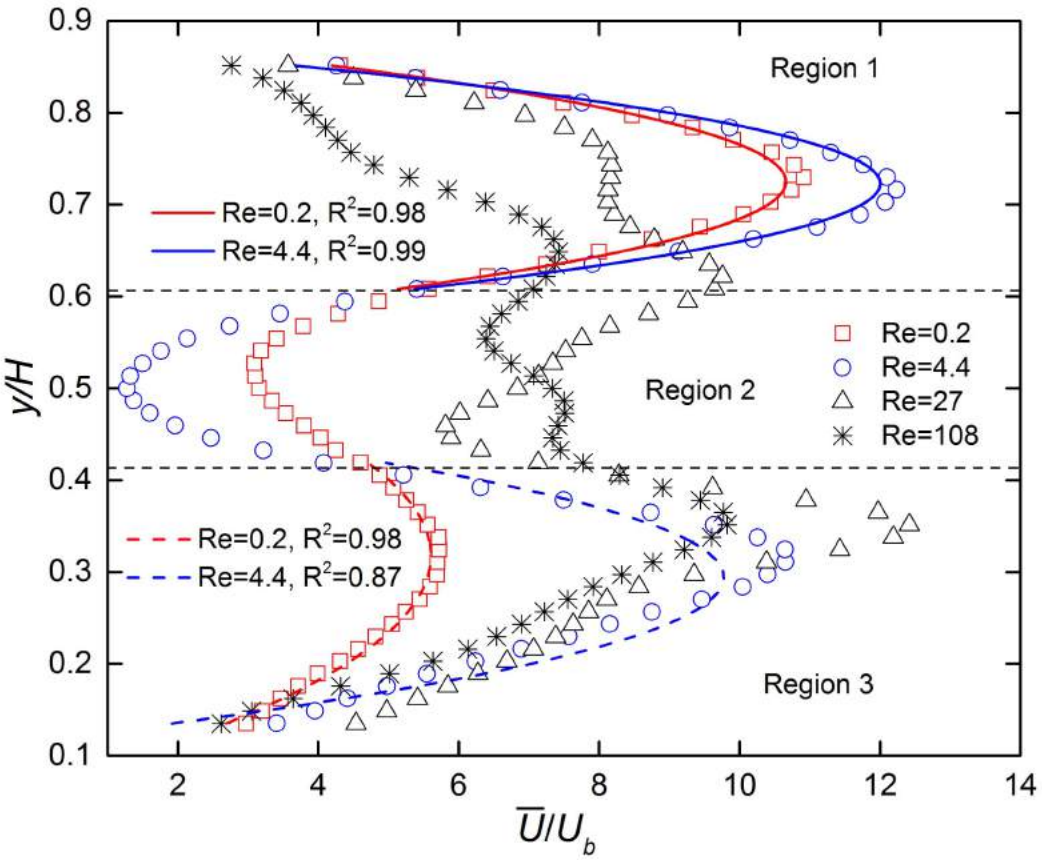

Figure 4.24: Velocity profile at various Reynolds numbers along the refreence line in Fig. 4.23.

• **Flow behaviour in the Pre-Darcy regime**

In the pre-Darcy regime (Re = 0.2), the maximum velocity magnitude in region 1 is about twice that of region 3 as shown in Fig. 4.24. The vector map in Fig. 4.25(a) shows that all the fluid tends to exit pore 1 through outlet 1 and even the flow in region 3 moves toward outlet 1. The velocity profile along the reference line in region 1 and region 3 at pre-Darcy regime (Re = 0.2) fitted well with a parabolic function, with a very high correlation factor R^2. Apparently, the flow in the pore approximates

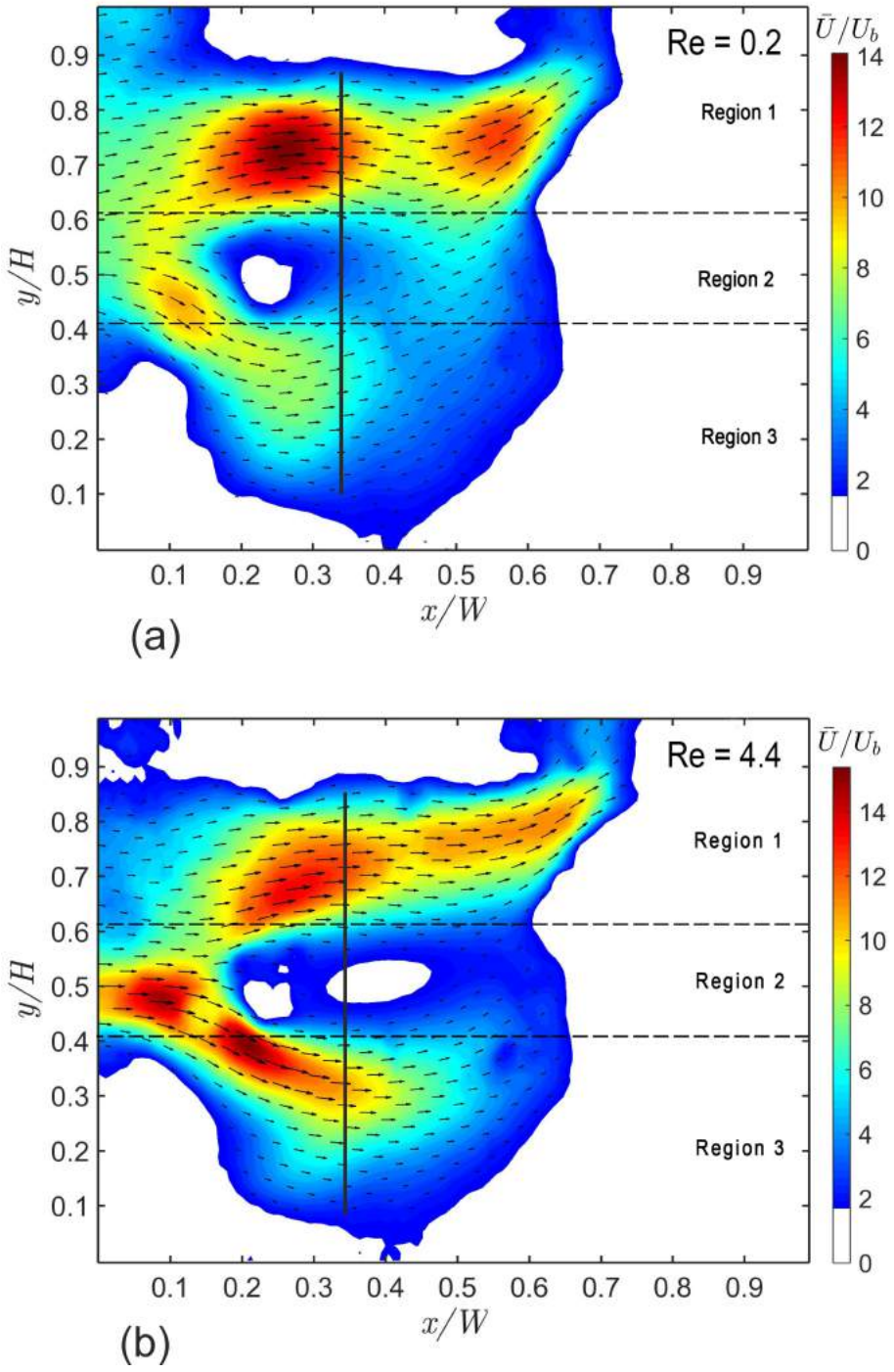

Figure 4.25: Contour plots of velocity distribution in a pore of SG72 at various Reynolds numbers. (a) pre-Darcy flow regime, (b) Darcy flow regime, (c) Forchheimer flow regime and (d) turbulent flow. The color represents the magnitude of the velocity and arrow represents the time-averaged velocity direction. (to be continued)

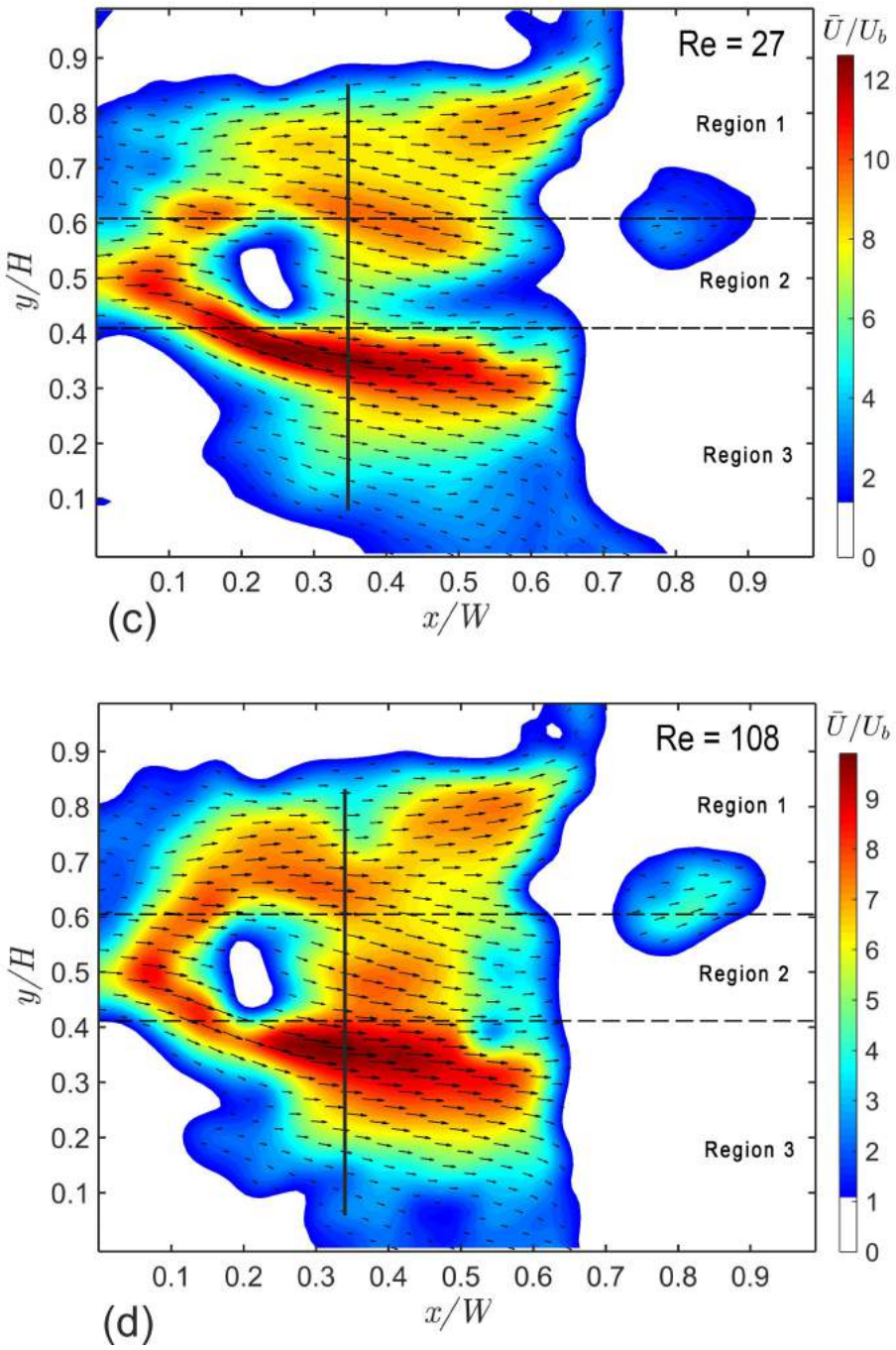

Figure 4.25: (continued) Contour plots of velocity distribution in a pore of SG72 at various Reynolds numbers. (a) pre-Darcy flow regime, (b) Darcy flow regime, (c) Forchheimer flow regime and (d) turbulent flow. The color represents the magnitude of the velocity and arrow represents the time-averaged velocity direction.

a fully developed laminar flow profile in the pre-Darcy regime.

• **Flow behaviour in the Darcy regime**

In the Darcy flow regime (Re = 4.4) at a Reynolds number about 20 times higher, Fig. 4.24 shows that the velocity profile along the reference line in Darcy regime has the same trend with that in pre-Darcy regime. However, there are some differences. Although the normalized velocity has increased in both region 1 and region 3 compared to the pre-Darcy flow, the normalized velocity in region 3 has increased much more with the maximum value becomes comparable with that of region 1. The normalized velocity in region 2 has decreased and is much lower than that in the pre-Darcy regime. This is because less fluid transported from region 3 to outlet 1 and the fluid in region 3 flows out from outlet 2.

The vector map in Fig. 4.25(b) confirms this, because the velocity in region 2 is almost zero (meaning no flow there) and nearly all the vectors in region 3 point in the x direction. Since outlet 2 locates deeper than the focus plane, the fluid has to move in the negative z direction in order to exit from outlet 2. However, when the Reynolds number reaches a certain value, the higher momentum fluid can overcome the resistance in the directions with large angle to the streamwise direction, leading to the velocity component v and w start to increase.

Fig. 4.24 shows that the velocity profile along the reference line in region 1 still fit very well to a parabolic function. However, the data in region 3 deviate from this shape. The deviation can be attributed to the commencement of fluid flow in the z direction, which is not measured by μ-PIV. Despite this change, the flow is still

laminar. Compared with the pre-Darcy regime, channels which have large angles to the streamwise direction become involved in fluid transport in the Darcy regime, and new flow paths are opened.

• Flow behaviour in the Forchheimer regime

In the Forchheimer regime (Re = 27), Fig. 4.24 shows that the normalized velocity in region 3 has increased again and exceeds the velocity in region 1 while the velocity in region 1 has decreased significantly. The velocity profile in both regions is far away from the parabolic fashion.

Fig. 4.25(c) shows that some fluid in region 1 exits from outlet 1 and some exits from outlet 3 and even outlet 2, effectively making the channel wider, all leading to the decrease of the peak velocity in region 1. In region 2, the mean velocity direction is changed completely from the pre-Darcy regime to the Forchheimer regime. The flow direction is from region 3 to outlet 1 (upward) in the pre-Darcy regime, while the flow direction is from region 1 substantially directed towards outlet 2 or outlet 3 (downward) in the Forchheimer regime. The normalized velocity magnitude in region 2 increases from the Darcy regime to the Forchheimer regime also because the fluid in region 1 starts to pass through region 2 and flows out from outlet 3.

• Flow behaviour in the turbulent regime

In the turbulent regime (Re = 108), Fig. 4.24 shows that the velocity profile becomes significantly flatter along the reference line. The velocity magnitude in region 2 becomes comparable to the other two regions. Fig. 4.25(d) shows that the mean

velocity direction becomes more aligned to the x direction than in the other three regimes. All these phenomena may be caused by turbulence, which transports the momentum more efficiently throughout the pore.

4.2.5.3 Velocity fluctuations in pore scale

Fig. 4.26 shows examples of velocity fluctuation in the Forchheimer (Fig. 4.26(a)) and turbulent (Fig. 4.26(b)) flow regimes. In arriving at these results, the local mean velocity components were subtracted from each velocity record respectively. The local velocity fluctuation is defined as $U' = \sqrt{u'^2 + v'^2}/\bar{U}$, where u' and v' are fluctuations of the velocity component. The laminar and turbulent flow can be determined by checking the value of the local velocity fluctuation, i.e., $U' \sim 0$ for laminar flow and $U' \geq 0.1$ for turbulent flow.

In order to improve clarity, the background is set to be white. The fluctuation intensity in most regions of the pore is less than 10% at Re = 27, while the intensity is larger than 15% all over the pore at Re = 108. The contour maps clearly show that the velocity fluctuation intensity decreases gradually from the near-wall region to the pore center. The high fluctuation intensity in the near-wall region can be attributed to two reasons. First, the rough surface of the pore wall intensifies the fluctuating motion of the fluid. Second, as the local mean velocity magnitude ($\bar{U}$) near the wall is quite small due to viscous effect, the fluctuations will appear large when normalized by this low value. In addition, the fluctuation intensity in region 2 is significantly higher than in the other two regions. This is a region that contains the wake of the island identified in Fig. 4.25(a). It is therefore a region where the two streams from regions 1 and 3 are interacting and mixing, leading to this increased

level of fluctuation.

Fluctuation intensities along the reference line in the Forchheimer and turbulent regimes are shown in Fig. 4.26 (c). The figure shows a large difference between the two flow regimes, as the overall intensity at Re = 108 is about three times that of the intensities at Re = 27. The μ-PIV measurement has verified that the flow in the Forchheimer regime is not turbulent, but unsteady laminar flow (vortices appear at fixed positions, and most of the local velocity in the whole vector map changes direction only slightly with time). After the Forchheimer regime, the flow becomes more unsteady and chaotic, qualitatively resembling turbulent flow. Compared to a simple wall-bounded flow, the turbulence intensities in porous media do not show any clearly defined shape, except the high fluctuations near the wall as discussed above. This is due to the extreme complexity of the porous geometry in all three dimensions.

By examining the variation of turbulence intensity with Re, the critical Reynolds number (Re_c) between the laminar and turbulent flows can be obtained. Fig. 4.27 shows the global averaged velocity fluctuation ($\bar{U}'$) versus Reynolds number for porous glass with different porosities. The value was calculated by averaging the local local velocity fluctuation over a line or the whole valid 2D region, represented as $\bar{U}'$. To compare with the critical Reynolds number obtained from pressure measurements, the reduced pressure drop data are also presented in the same plot (right-hand y axis). The trend of reduced pressure drop data in Forchheimer and turbulent flow regimes were fitted respectively, and the intersection region is where the critical point locates. As the transition point cannot be identified as a single point but quite a wide region, a grey band is used to highlight the transition region.

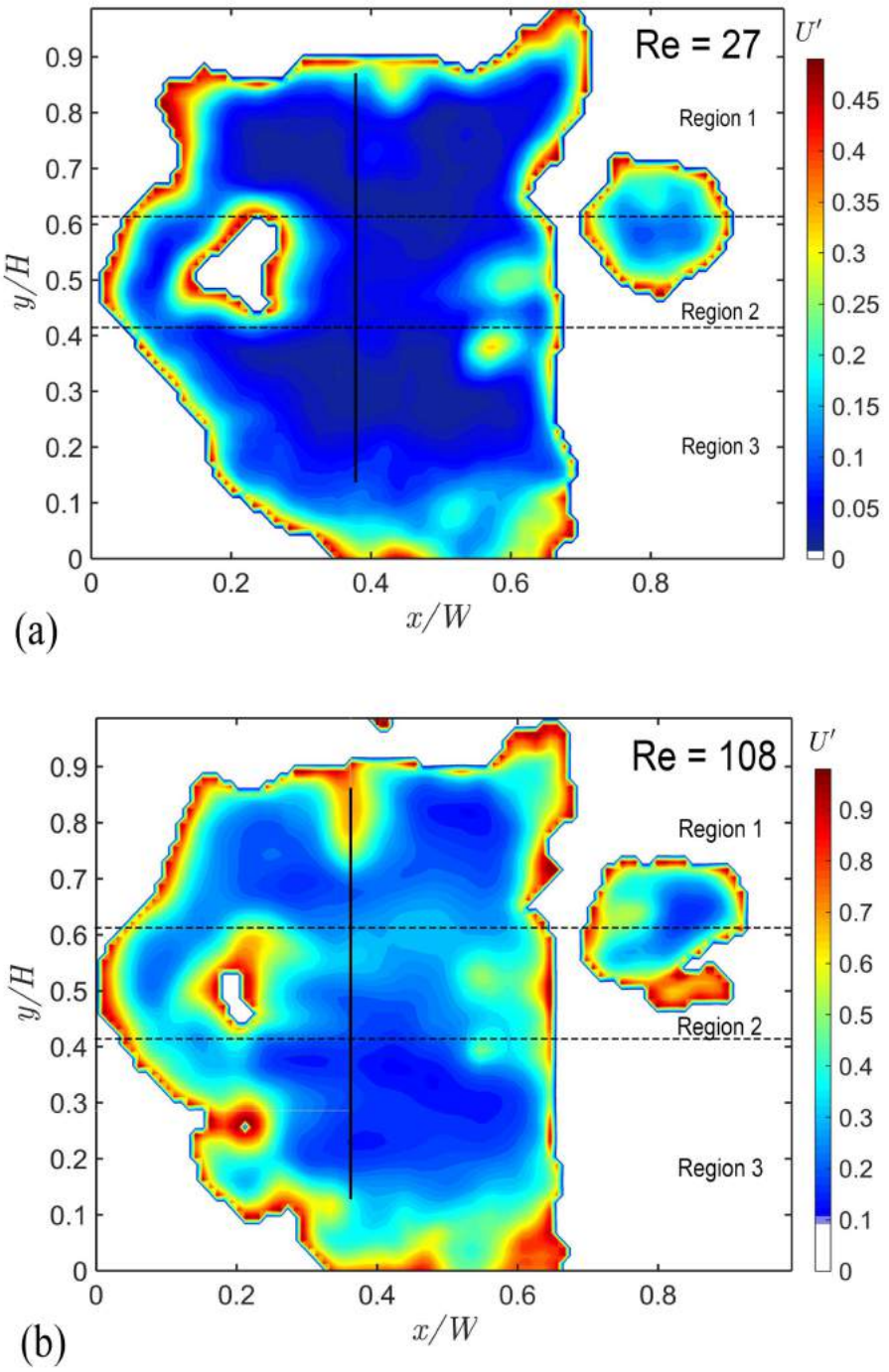

Figure 4.26: Velocity fluctuation intensity in a pore of F72 at different Reynolds numbers. (a) Re = 27 (Forchheimer regime), (b) Re = 108 (turbulent regime), and (c) fluctuation intensity along the reference line. (to be continued)

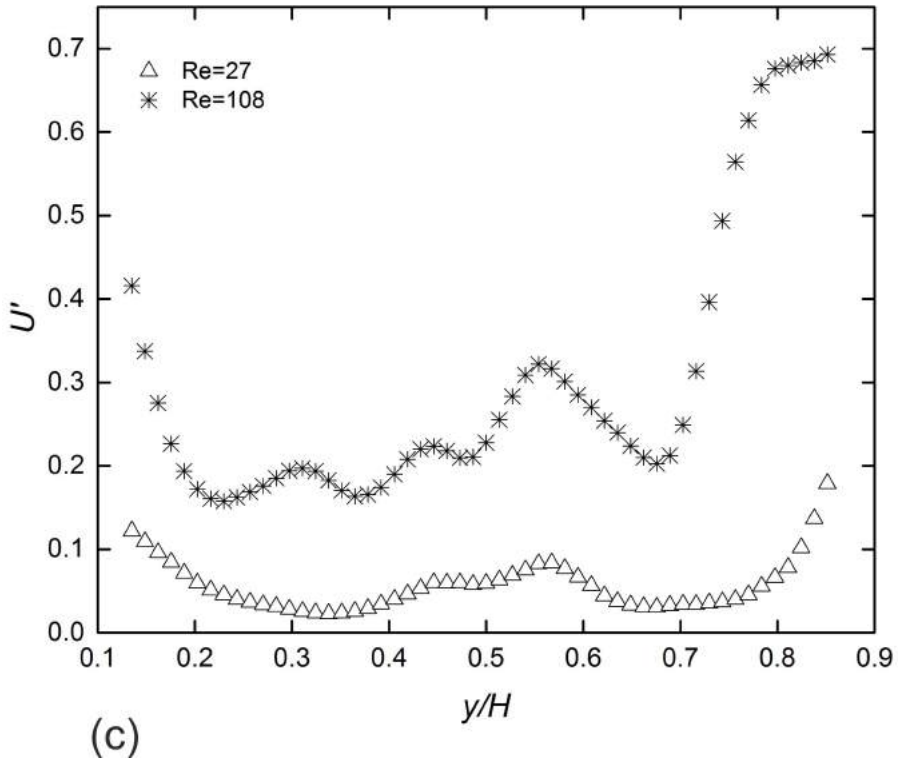

Figure 4.26: (continued) Velocity fluctuation intensity in a pore of F72 at different Reynolds numbers. (a) Re = 27 (Forchheimer regime), (b) Re = 108 (turbulent regime), and (c) fluctuation intensity along the reference line.

The plots show that the critical Reynolds number obtained from pressure drop measurements agrees very well with that obtained in μ-PIV measurements. This critical number identifies the transition from laminar to turbulent flow, because in all samples, the velocity fluctuation keeps at a nearly fixed, low value at Re below Re_c, and increases dramatically at Re just above Re_c. Although there is a similar trend of the turbulence intensity with Re in all samples, the difference in fluctuation intensities is also apparent. For example, the low porosity sample (SG72) shows an overall higher fluctuation level; i.e., when Re = 120, the fluctuation intensity in SG72 is about 0.25, which is two times of that of the other samples.

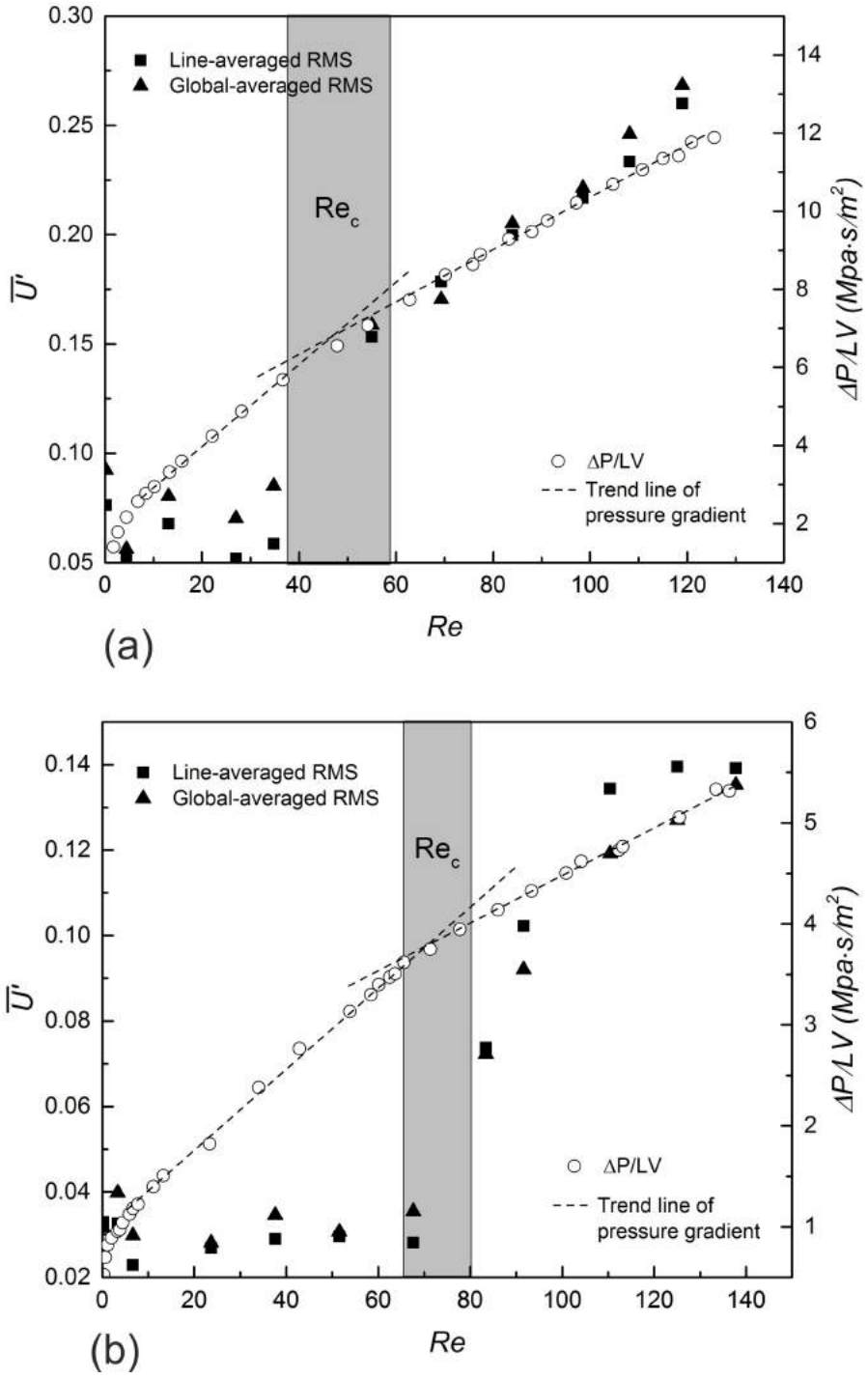

Figure 4.27: Global averaged velocity fluctuation (left-hand y axis) versus Reynolds number for various porosities. Trend lines of reduced pressure drop in Forchheimer and turbulent regimes are drawn with a dashed line for identifying the critical Reynolds number (Re_c). The critical area is filled with grey color. (a) SG72, (b) SG77, (c) SG78 and (d) SG81. (to be continued)

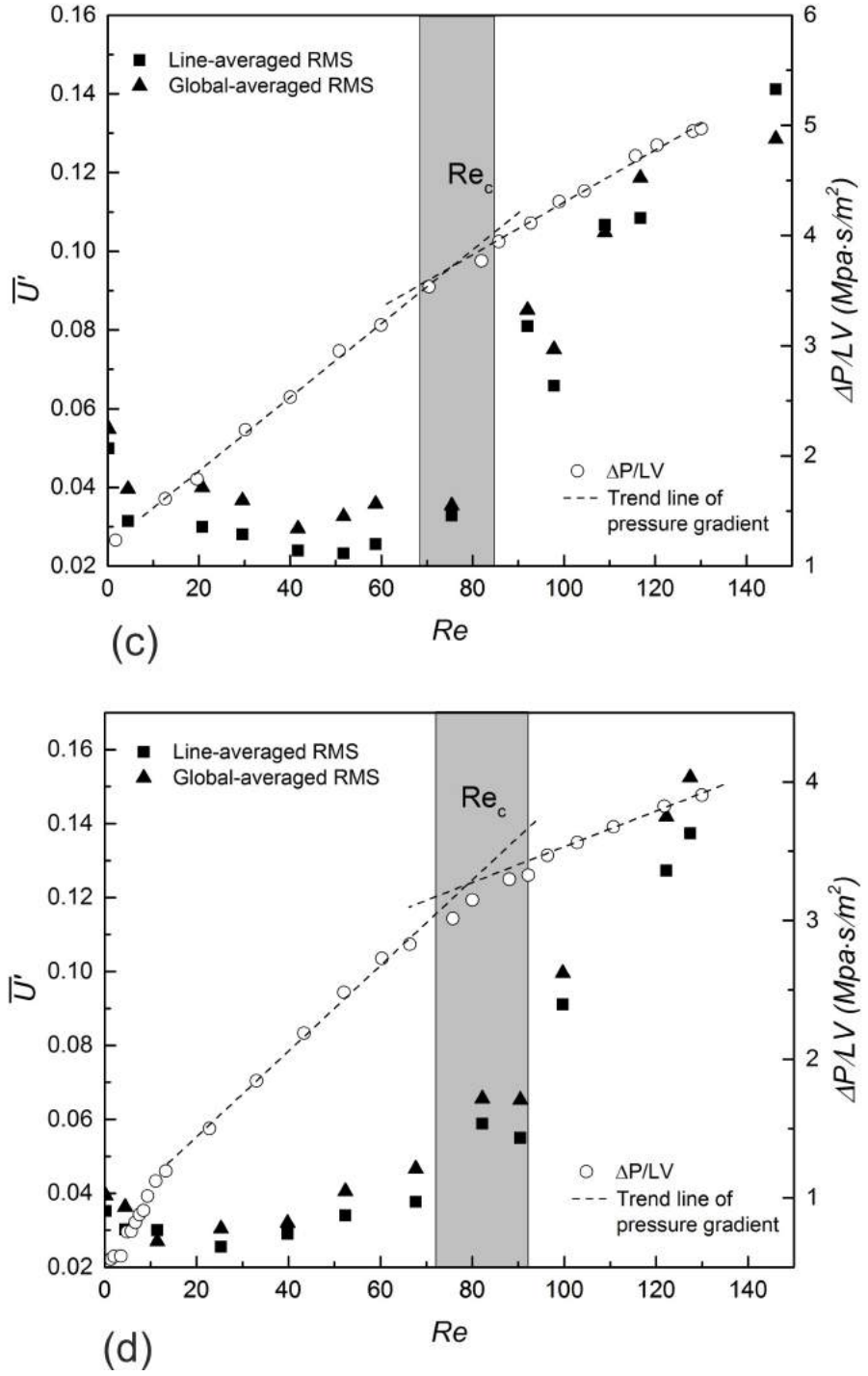

Figure 4.27: (continued) Global averaged velocity fluctuation (left-hand y axis) versus Reynolds number for various porosities. Trend lines of reduced pressure drop in Forchheimer and turbulent regimes are drawn with a dashed line for identifying the critical Reynolds number (Re_c). The critical area is filled with grey color. (a) SG72, (b) SG77, (c) SG78 and (d) SG81.

4.3 Flow characteristics in the porous glass with irregular pores

4.3.1 Structural properties

Fig. 4.28 displays the optical microscope image of porous glass sample with irregular pores. The pores are negative replicas of the sodium chloride particles and therefore have irregular shapes. The connectivity neck between pores is irregular compared to porous glass samples with spherical pores. In addition, there are a lot of sharp protrusions and pits on the solid wall, as marked in Fig. 4.28(b), making the structure more complex than the samples with spherical pores.

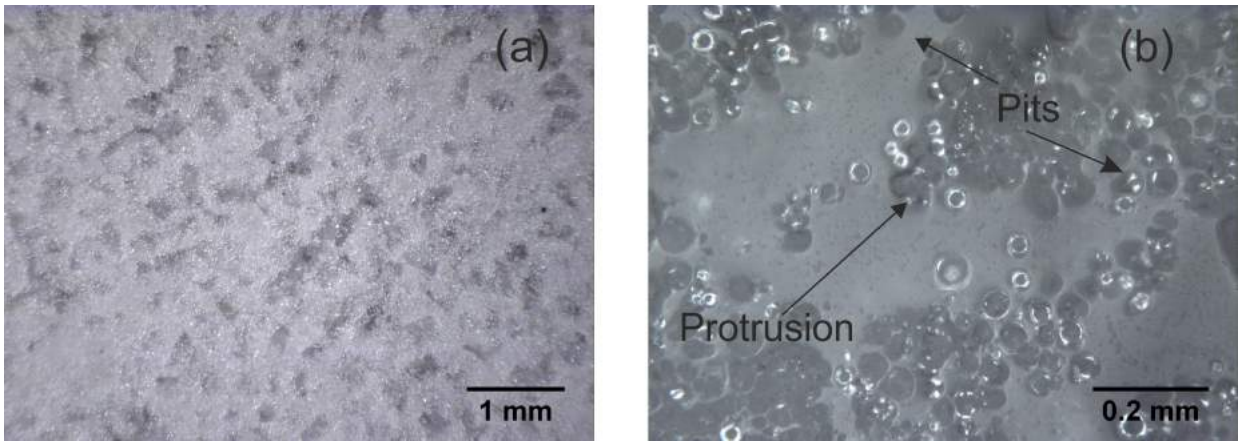

Figure 4.28: Optical microscope images of porous glass with irregular pores. The porosity of the sample is 73%.

Table 4.7: Detailed information of porous galss samples with irregular pores.

Sample	Sodium chloride size (μm)	Equivalent pore size (μm)	Porosity	PIV magnification
IG67	425-710	500	0.67	200×
IG69	425-710	500	0.69	200×
IG73	425-710	500	0.73	100×
IG77	425-710	500	0.77	100×
IG83	425-710	500	0.83	100×

Table 4.7 lists the structural properties of five porous glass samples with irregular pores. The mean equivalent diameter is applied as the characteristic length for calculating Reynolds number. In this study, the equivalent diameter of an irregular particle is defined as the diameter of a spherical particle having the same volume. For the sodium chloride powder used in the present experiment, the mean equivalent diameter is around 500 μm.

4.3.2 Pressure drop

Fig. 4.29 shows the relationship between pressure drop and Reynolds number in porous glass with irregular pores. Similar to the pressure drop in porous glass with spherical pores, the pressure drop in porous glass with irregular pores also shows a typical quadratic relation with Re, with a high correlation factor. The pressure drop also shows a great dependence on porosity. For example, the pressure drop of IG67 is more than ten times that of IG83 for a given Re.

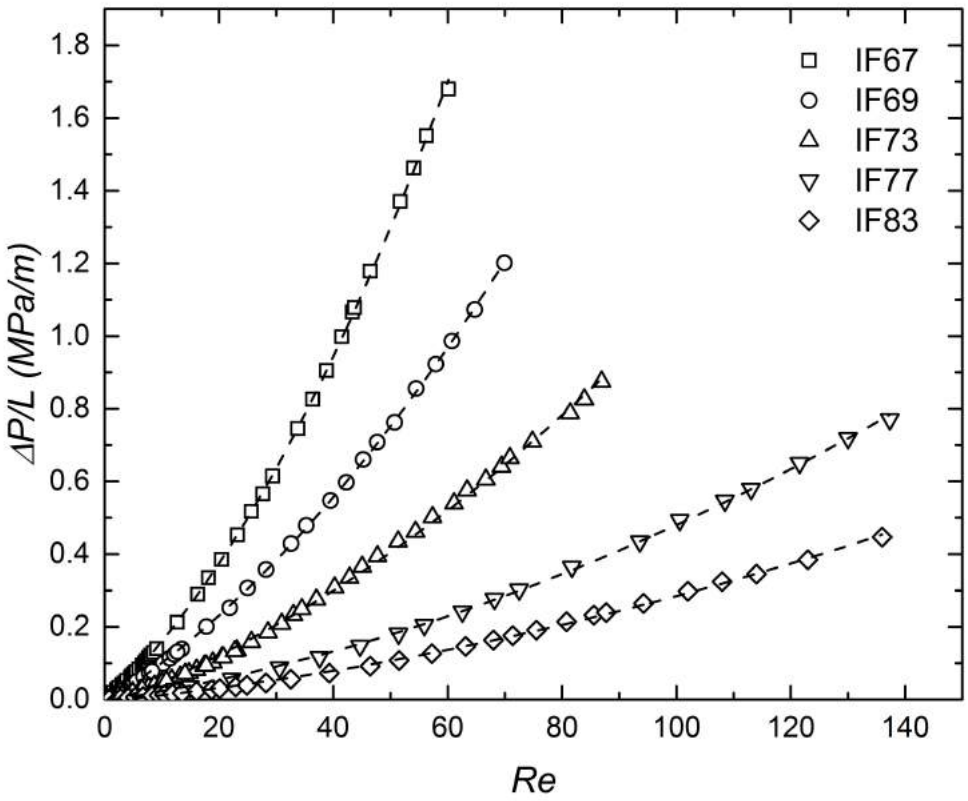

Figure 4.29: Relationship between the pressure drop per unit length versus Reynolds number.

4.3.3 Flow regimes

Fig. 4.30 shows the $\Delta P/LV - Re$ plots of all porous glass samples with irregular pores. Flow regimes can be identified by slope changes of these reduced pressure drop plots. The insets in the figure are the results in low Reynolds number range. Similar to the results in other porous media, four typical regimes are identified from each plot. At extremely low velocity (Re $\lesssim$2), a pre-Darcy regime is identified, as shown in each inset. The Darcy flow regime is identified by its unique flow behaviour. For porous glass with irregular pores, Darcy flow occurs at 2$\lesssim$ Re $\lesssim$6, with the exact range depending on the porosity. Even with the complexity of the irregular pores, Darcy regime exists and the spanning range is comparable to the porous glass with

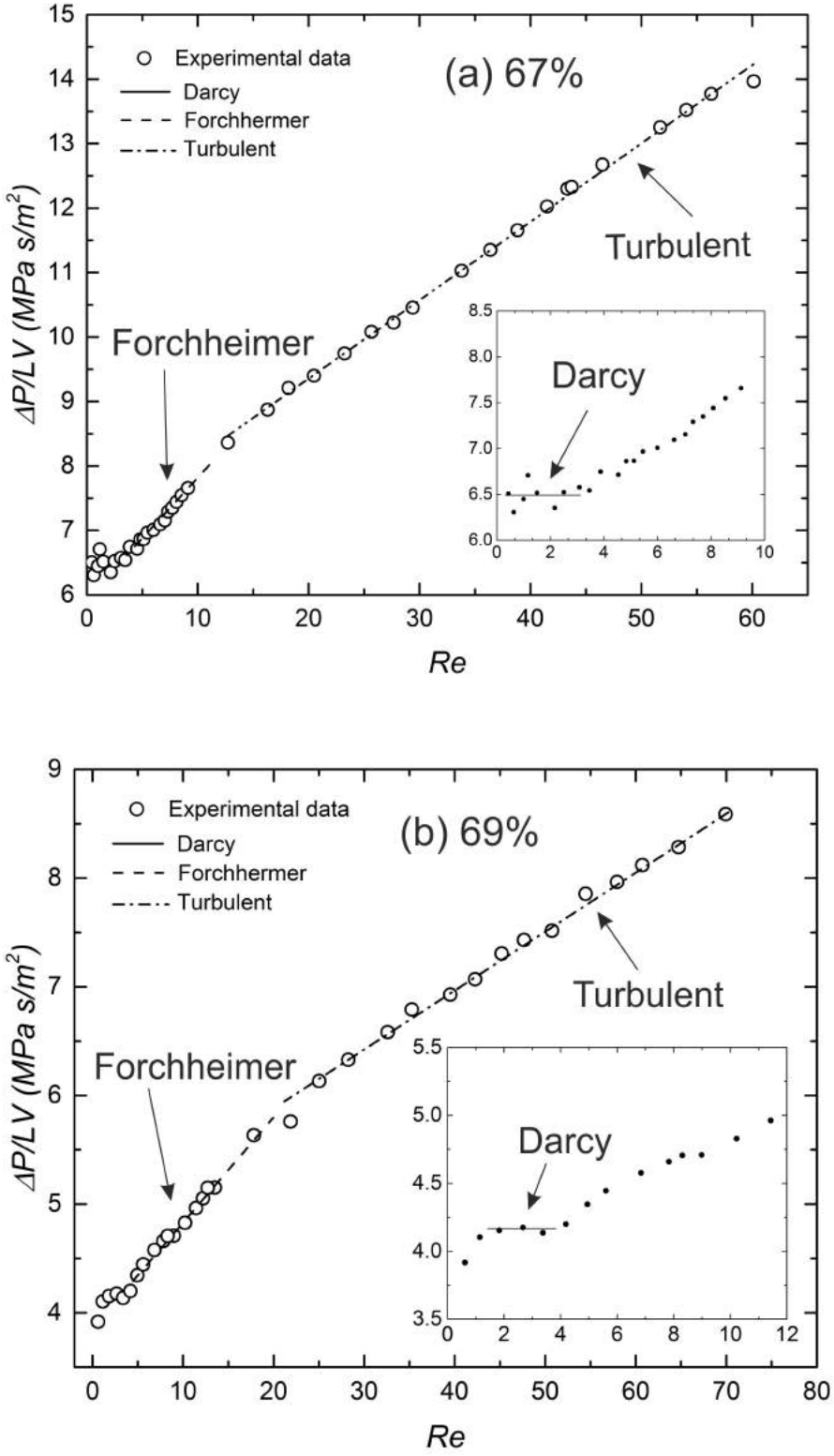

Figure 4.30: Reduced pressure drop versus Reynolds number. The insets are the results in the low Reynolds number range. Porosity: (a) 0.67, (b) 0.69, (c) 0.73, (d) 0.77 and (e) 0.83. (to be continued)

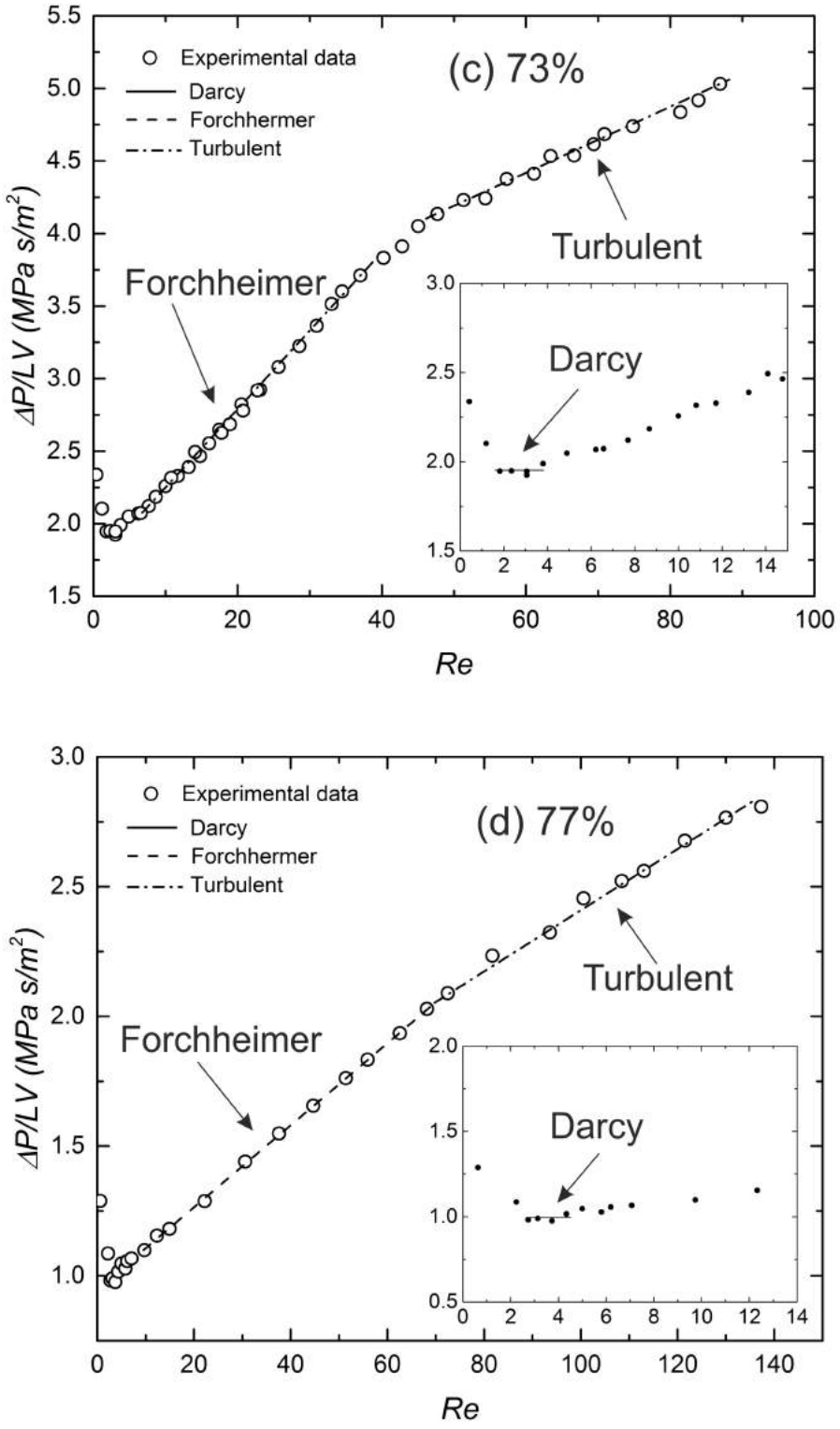

Figure 4.30: (continued) Reduced pressure drop versus Reynolds number. The insets are the results in the low Reynolds number range. Porosity: (a) 0.67, (b) 0.69, (c) 0.73, (d) 0.77 and (e) 0.83.(to be continued)

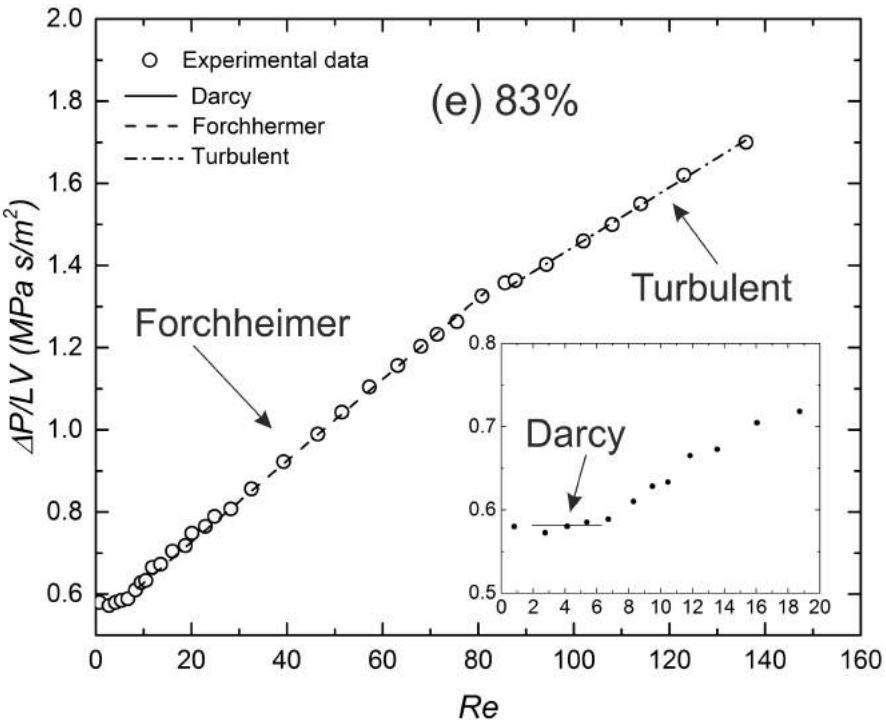

Figure 4.30: (continued) Reduced pressure drop versus Reynolds number. The insets are the results in the low Reynolds number range. Porosity: (a) 0.67, (b) 0.69, (c) 0.73, (d) 0.77 and (e) 0.83.

spherical pores. This implies that the involvement of more sharp edges and corners does not affect the nature of the flow within a porous medium. Forchheimer and turbulent regimes are also observed in the reduced pressure drop plots. The identified flow regime boundaries are listed in table 4.8.

Table 4.8: Flow regime boundaries of porous glass with irregular pores.

Sample	Pre-Darcy	Darcy	Forchheimer	Turbulent
IG67	$Re < 1$	$1 < Re < 3.5$	$4 < Re < 10$	$15 < Re$
	$Re' < 0.04$	$0.04 < Re' < 0.16$	$0.18 < Re' < 0.45$	$0.68 < Re'$
IG69	$Re < 1.5$	$1.5 < Re < 4$	$4 < Re < 20$	$25 < Re$
	$Re' < 0.07$	$0.07 < Re' < 0.20$	$0.20 < Re' < 1.10$	$1.37 < Re'$
IG73	$Re < 1.5$	$1.5 < Re < 4$	$5 < Re < 40$	$45 < Re$
	$Re' < 0.12$	$0.12 < Re' < 0.28$	$0.36 < Re' < 2.90$	$3.25 < Re'$
IG77	$Re < 2.5$	$2.5 < Re < 5$	$8 < Re < 65$	$72 < Re$
	$Re' < 0.23$	$0.23 < Re' < 0.45$	$0.74 < Re' < 5.95$	$6.69 < Re'$
IG83	$Re < 2$	$2 < Re < 6$	$8 < Re < 80$	$90 < Re$
	$Re' < 0.15$	$2 < Re' < 0.65$	$0.87 < Re' < 8.75$	$9.62 < Re'$

Fig. 4.31 shows the relationship between the onset Reynolds number for each regime and porosity in porous glass with irregular pores. Similarly to the porous glass with spherical pore, the onset Reynolds number tends to increase linearly with porosity. The distribution of the regime ranges is similar to the porous glass with spherical pores, where the Forchheimer regime has a wide range, while the transition to turbulent regime is narrow.

4.3.4 Permeability and form drag coefficient

Fitting the Forchheimer-extended Darcy equation to the pressure drop curve in Fig. 4.29, the permeability and form drag coefficient can be obtained. As discussed above, there are two methods calculate them: one method uses the pressure drop data points

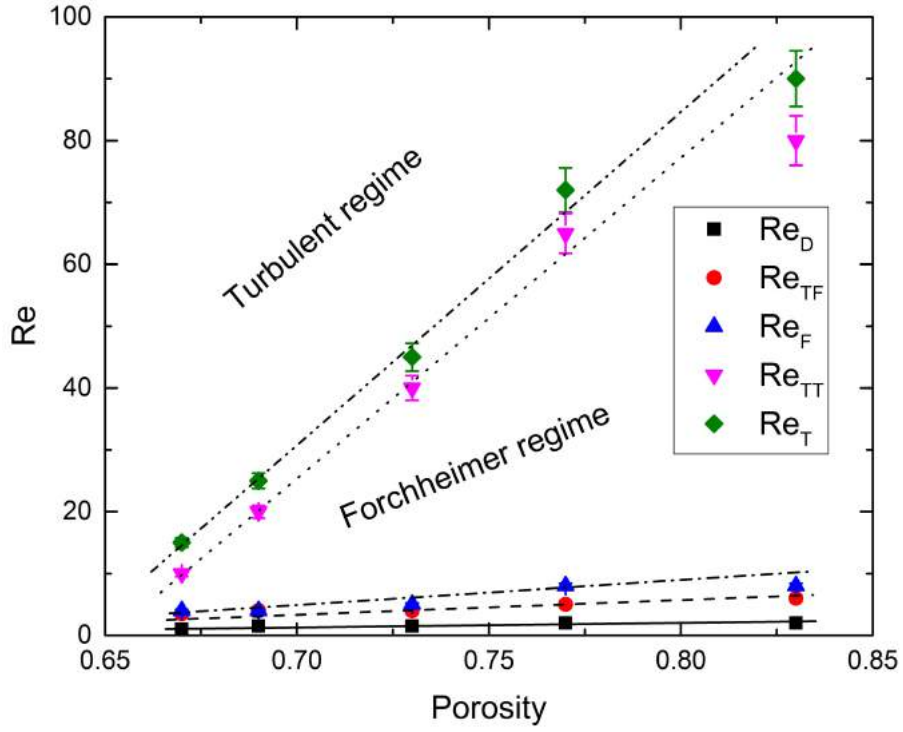

Figure 4.31: Relationship between flow regime boundary and porosity for porous glass with irregular pores.

from each regime without including the transition data; the other uses a larger flow velocity range which encompasses all the data from the pre-Darcy regime to the turbulent regime. The Darcy regime is excluded when calculating the form drag coefficient for all regimes as only viscous force exists in this regime. The calculated values of permeability and drag coefficient are listed in table 4.9.

Table 4.9: Permeability (K $\times 10^{-10}$ m^2) and form drag coefficient (C $\times$ 10^4 m^{-1}) of porous glass with irregular pores at various flow regimes.

Sample	Darcy		Forchheimer			Turbulent			All regimes		
	K	R^2	K	C	R^2	K	C	R^2	K	C	R^2
IG63	1.5	0.99	1.67	8.5	0.99	1.4	5.89	0.99	1.44	6.07	0.99
IG69	2.46	0.99	2.52	4.3	0.99	2.06	2.68	0.99	2.16	2.87	0.99
IG73	5.07	0.99	5.87	2.66	0.99	3.36	1.17	0.99	4.02	1.51	0.99
IG77	8.73	0.99	10.47	0.78	1.00	7.56	0.55	0.99	8.57	0.62	0.99
IG83	16.8	0.99	18.3	0.48	1.00	11.9	0.3	0.99	14.3	0.36	0.99

Fig. 4.32 shows the variation of permeability with porosity in porous glass with irregular pores. Porous glass samples with high porosity have a much higher permeability than low porosity samples. For instance, the permeability of porous glass having a porosity of 0.83 is about 10 times that of the porous glass having a porosity of 0.63. Flow regime also influences the permeability of the porous glass. The Forchheimer regime has the highest permeability and the turbulent regime has the lowest permeability. For example, the value of permeability of sample IG83 in the Forchheimer regime is 18.3 $\times 10^{-10}$ m^2, 40% higher than the permeability in the turbulent regime, 11.9 $\times 10^{-10}$ m^2. The effect of flow regime on permeability is more obvious for samples with high porosities (> 0.72).

Fig. 4.33 shows the effects of porosity and flow regime on form drag coefficient. Increasing porosity leads to decrease of the form drag coefficient because the fraction of solid matrix decreases. The effect of flow regime on form drag coefficient is also significant. The value of form drag coefficient calculated from the Forchheimer

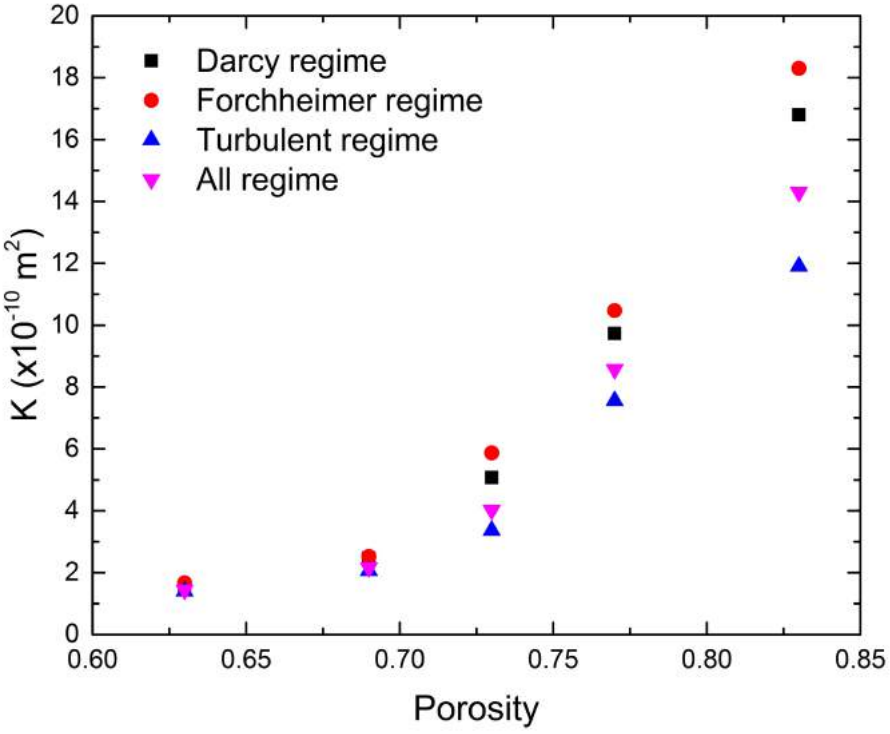

Figure 4.32: Variation of permeabiltiy with porosity in porous glass samples with irregular pores.

regime is much higher than the value calculated from the turbulent regime. The value of form drag coefficient calculated from all regimes is close to the value calculated from the turbulent regime. The effect of flow regime on form drag coefficient is more obvious for samples with low porosities.

4.3.5 Micro-PIV measurements

Fig. 4.34 shows the instantaneous velocity field of five different pore regions obtained from five samples in the Darcy regime. The flow fields are located approximately 250 μm (half of the pore diameter) from the wall to the middle of the pore. As expected, the inner structure of this irregular porous medium is more complex than

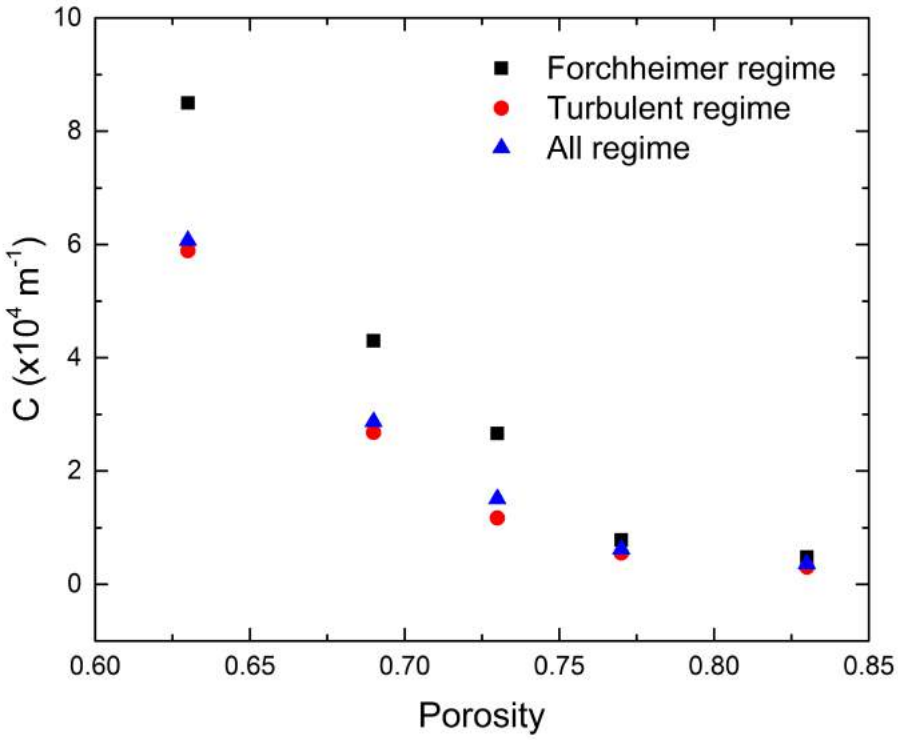

Figure 4.33: Variation of form drag coefficient with porosity in porous glass samples with irregular pores.

the porous glass with spherical pores. Compared to the porous glass with spherical pores, there are more sharp edges and solid protrusions in the path of the flow in porous glass with irregular pores. Although the pore structure is quite complex and different from other, the flow behaviour is similar. For conciseness, only two typical pore structures, IG69 and IG73, shown in Fig. 4.34(b) and (c), are described in details in the following section. However, the statistic results of all samples are presented.

4.3.5.1 Time-averaged velocity distribution in pore scale

• Velocity distribution in sample IG69

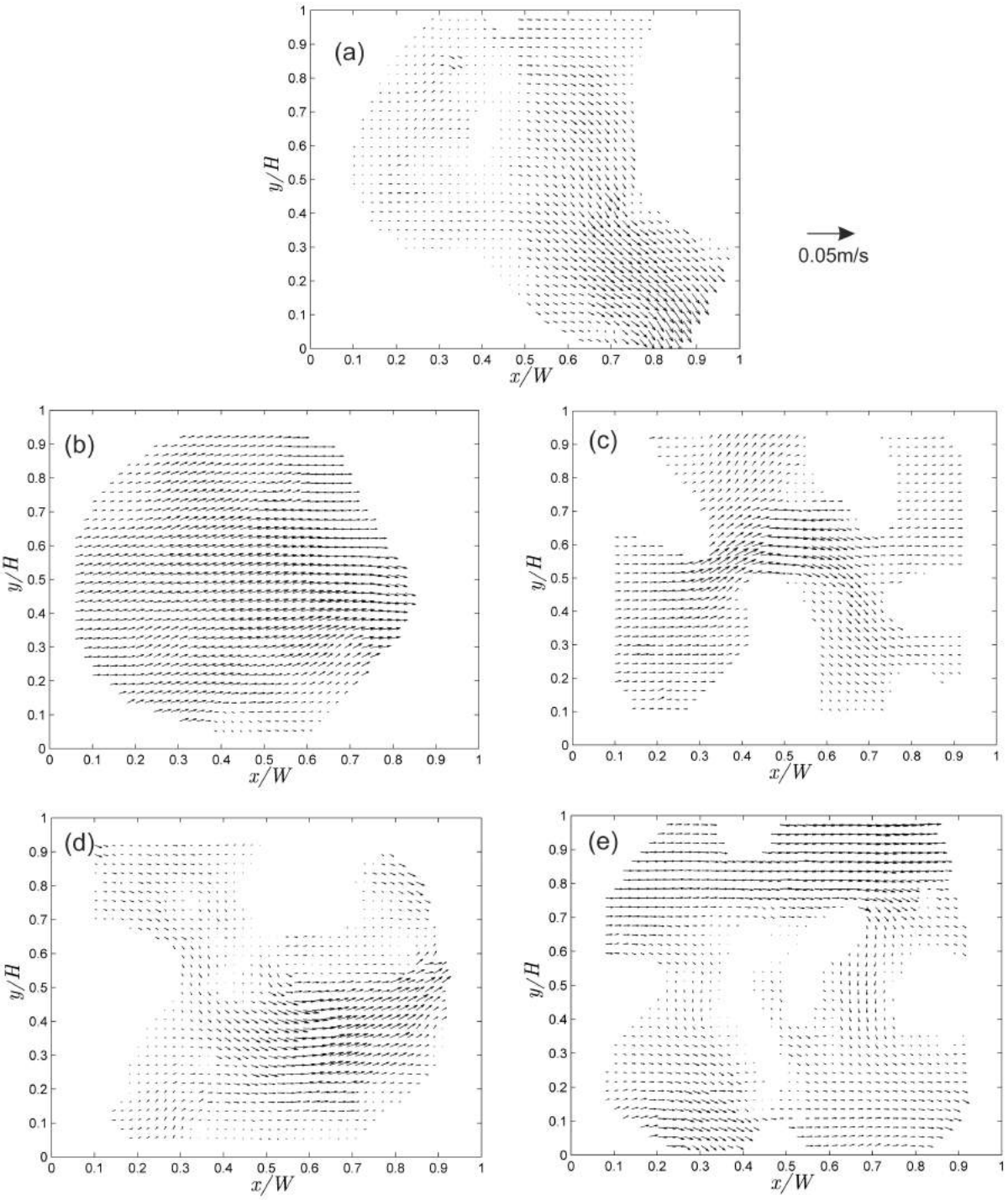

Figure 4.34: Instantaneous velocity map in five pores from different samples in the Darcy regime. Arrow indicates the local flow direction and magnitude and the solid matrix has been set to white for a clearer view. Sample: (a) IG67, (b) IG69, (c) IG73, (d) IG77 and (e) IG83.

Fig. 4.35(a) shows the local structure in sample IG69 with fluid passing through. W and H represent the width and height of the field of view. The pore looks like rectangular in the focus plane. After removing the solid matrix and the near wall region, the flow field becomes spherical. A reference line perpendicular to the bulk flow direction has been drawn in Fig. 4.35(a). The time-averaged velocity magnitude along the line is plotted in Fig. 4.35(b). Contour plots corresponding to the four velocity profiles are plotted in Fig. 4.35(c)-(f). These four contour plots represent of the Darcy, Forchheimer and turbulent regimes.

Fig. 4.35(c)-(d) shows that the flow behaviour in the Darcy and Forchheier regimes are very similar, confirming the results from the pressure measurements. In these two regimes, the velocity is uniformly distributed. Similar to the flow in a pipe, the highest velocity is at the center of the channel and the velocity is gradually decreasing to zero from center to wall due to shear stress from the solid wall. However, in the Forchheimer regime, the layers affected by walls in both the upper and bottom regions are thicker than those in the Darcy regime. Consequently, the main flow stream is squeezed more to the central region. The velocity profile along the reference line, shown in Fig. 4.35(b), reveals the same phenomenon. The velocity profiles fits well with a quadratic function, but less well in the Forchheimer regime. This result is consistent with the hypothesis made by Dybbs & Edwards (1984) that the inertial core developed in the near-wall region starts to move toward the channel center.

In the turbulent regime (Re = 30, 55), the contour plots shows that the velocity magnitude in the bottom part is much higher than that int the upper part. A large momentum spans across the pore in the bulk velocity direction in the bottom

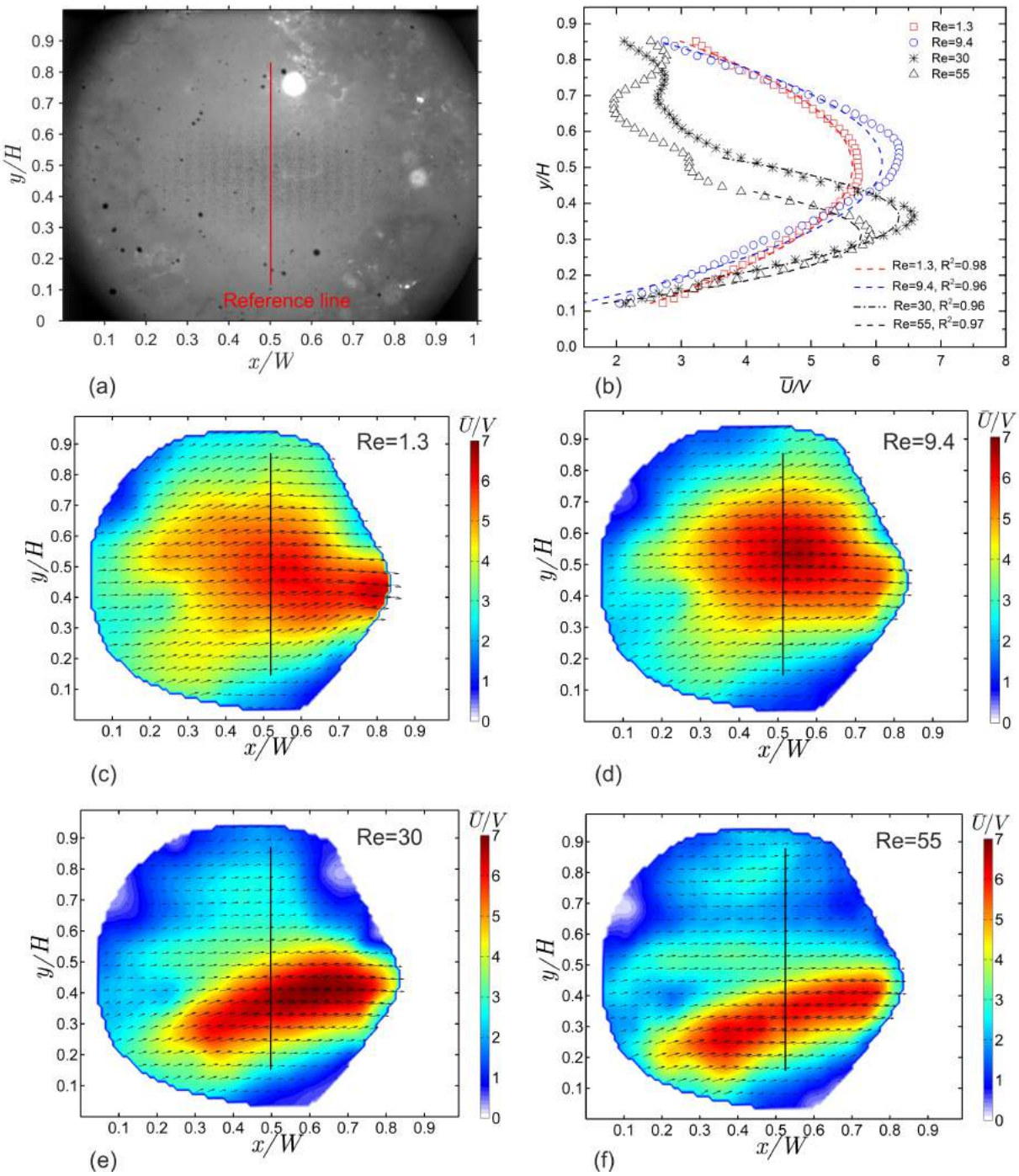

Figure 4.35: Velocity distribution in a pore of IG69 at various Reynolds numbers. The color represents the magnitude of the normalized velocity and arrow represents the velocity direction. The bulk flow velocity is from left to right. (a) Pore structure, (b) velocity profiles along the reference line in (a) in different flow regimes. (c) Darcy regime at Re = 1.3, (d) Forchheimer regime at Re = 9.4, (e) and (f) turbulent regime at Re = 30 and Re = 55.

part. The same feature is found in the velocity profile along the reference line in Fig. 4.35. The velocity profile skews downward in the turbulent regime and the skewness becomes stronger as Reynolds number increases. Another interesting phenomenon is that the velocity data in the bottom part still fit well with a quadratic function. In addition, even in the turbulent regime, the velocity distribution varies with Reynolds number. For example, as Reynolds number increases from 30 to 55, the velocity magnitude decreases in the entire pore. This means the velocity will be increased in somewhere else.

• **Velocity distribution in sample IG73**

Fig. 4.36(a) shows the local structure in sample IG73. A reference line was also drawn for studying the development of velocity profile. This structure is composed of several pores and therefore there are several junctions. This local structure connects to the global structure with four interfaces: one inlet and three outlets, as marked in the figure. The inner wall surface is very uneven in this sample because of the irregular pore shape and high porosity. The fluorescent particles can easily stack in this area, making them very bright spots in the camera, which creates more uncertainty in post processing. Therefore, it is necessary to remove these areas from the data to obtain a clean image.

Contour plots shows that in Darcy (Re = 2) and Forchheimer (Re = 9) regimes, fluid flow shows similar pattern, with fluid entering the geometry through the only inlet (inlet 1) and exiting the three outlets equally, as shown in the Fig. 4.36(c) and (d) (it should be noted that the colorbar scale used in these two graph is different). The velocity profiles in these two regimes along the reference line are also similar. Both profiles follow the quadratic function if points near the wall are excluded. In the

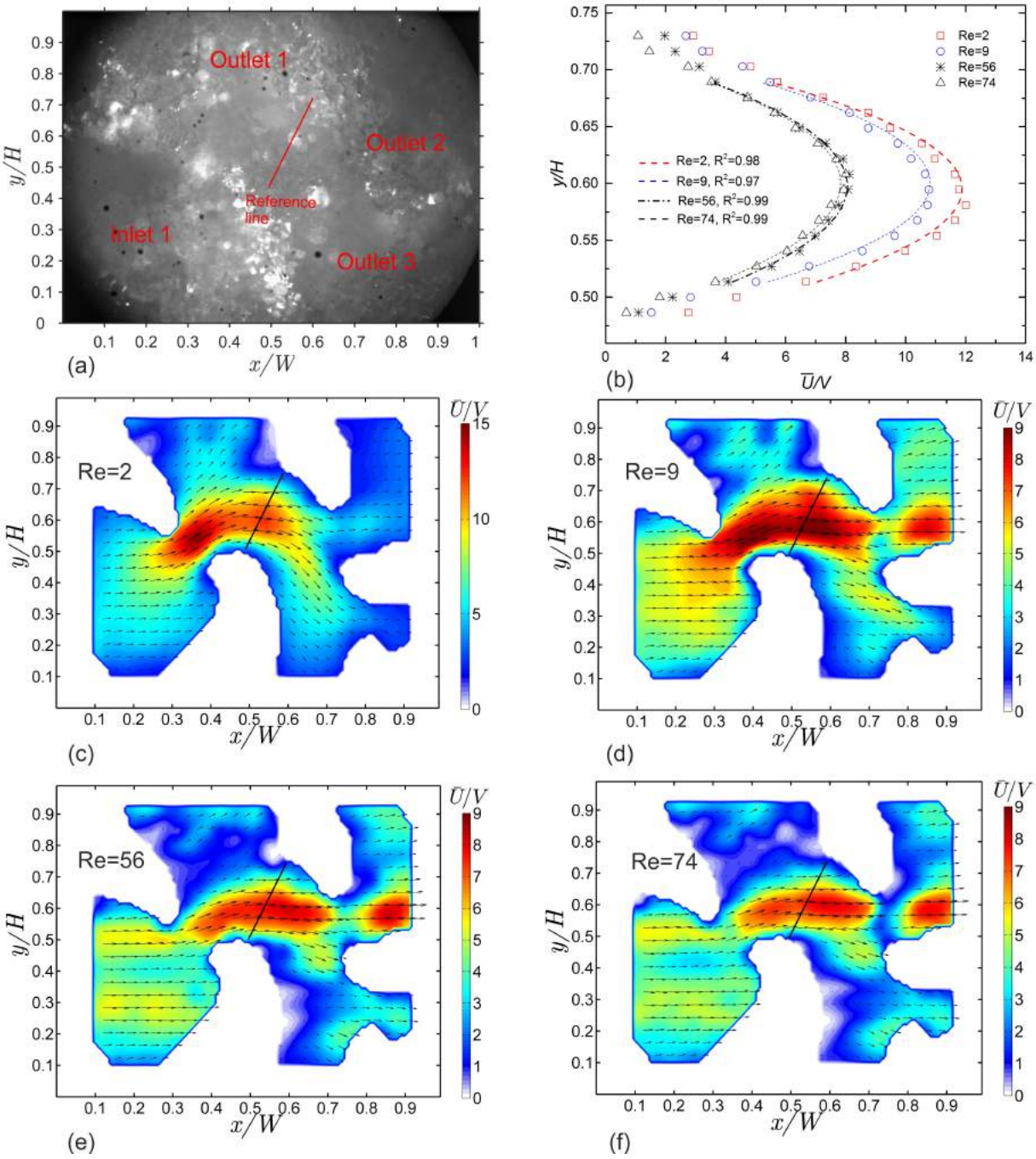

Figure 4.36: Velocity profile in a pore of IG73 at various Reynolds numbers. The color represents the magnitude of the normalized velocity and arrow represents the velocity direction. The bulk flow velocity is from left to right. (a) Pore structure, (b) velocity profile along the reference line in (a) in different flow regimes. (c) Darcy regime at Re = 2, (d) Forchheimer regime at Re = 9, (e) and (f) turbulent regime at Re = 56 and 74. The colorbar used in (c) is different from the rest of the contour plots.

turbulent regime (Re = 56, 74), the fluid transportation efficiency of outlet 1 and outlet 3 is not as high as in the Darcy and Forchheimer regimes. As a consequent, most of the fluid flows out of this geometry mainly through outlet 2. The velocity profile becomes more flatter in the turbulent regime, indicating that the distribution of momentum is more spread and uniform.

• **Comparison of samples IG69 and IG73**

There is similarity and difference between the two pore geometries (IG69 and IG73). The similarity is that the main velocity profile across the pore shows a quadratic function in all flow rate conditions. The velocity profiles along the reference line is nearly the same in the Darcy and Forchheimer regimes, but different in the turbulent regime. The difference is that no obvious skewness is observed in the velocity profile in sample IF73 as Reynolds number increases.

In summary, the disordered geometry in porous media forces each fluid element to follow a tortuous path and travel a total distance larger than the length of the sample. Some channels are longer and some are shorter, so some channels may need higher pressure to pass through than the others. At low flow rates, some narrow and winding channels are seldom involved in fluid transport because the pressure is insufficient to drive flow to overcome the shear stress in these areas. However, at high flow rates, more channels are involved in fluid transportation to accommodate the increased fluid. In other words, different channels may be involved for fluid transport at different flow rates.

4.3.5.2 Velocity fluctuations in pore scale

Figs. 4.37 and 4.38 show the local velocity fluctuation in various flow regimes of sample IG69 and IG73. The calculation procedure of fluctuation is the same as used for porous glass samples with spherical pores. The glass matrix has been removed from the contour plots.

Fig. 4.37 shows that the fluctuations are strong in the near wall region and decrease gradually as the distance from the wall increases. At a low Reynolds number (Re=1.3), shown in Fig. 4.37(a), the strongest fluctuation begins at the junction of fluid and solid within the upstream part (left on the graph). Comparing these contour plots with the pore geometry in Fig. 4.35(a), shows that the fluid flows on the solid bed in the region of $x/W < 0.2$, which explains the strong fluctuation in this area in Darcy regime.

In the near wall region ,there is a thin layer with relative weak fluctuations in the Darcy regime. The fluctuations become slightly stronger when entering the Forchheimer regime. The thickness of the layer does not increase too much. However, the thickness increases sharply after the flow has developed into a turbulent flow. The thickness is also sensitive to the flow rate in the turbulent regime. Another interesting phenomenon is that the velocity fluctuation intensity in the center of the pore remains at a very low level throughout all the flow regimes. As the flow rate increases, the central area is reduced. If the flow rate keeps increasing, this area should finally disappear.

A similar evolution behaviour of velocity fluctuation intensity can be observed in

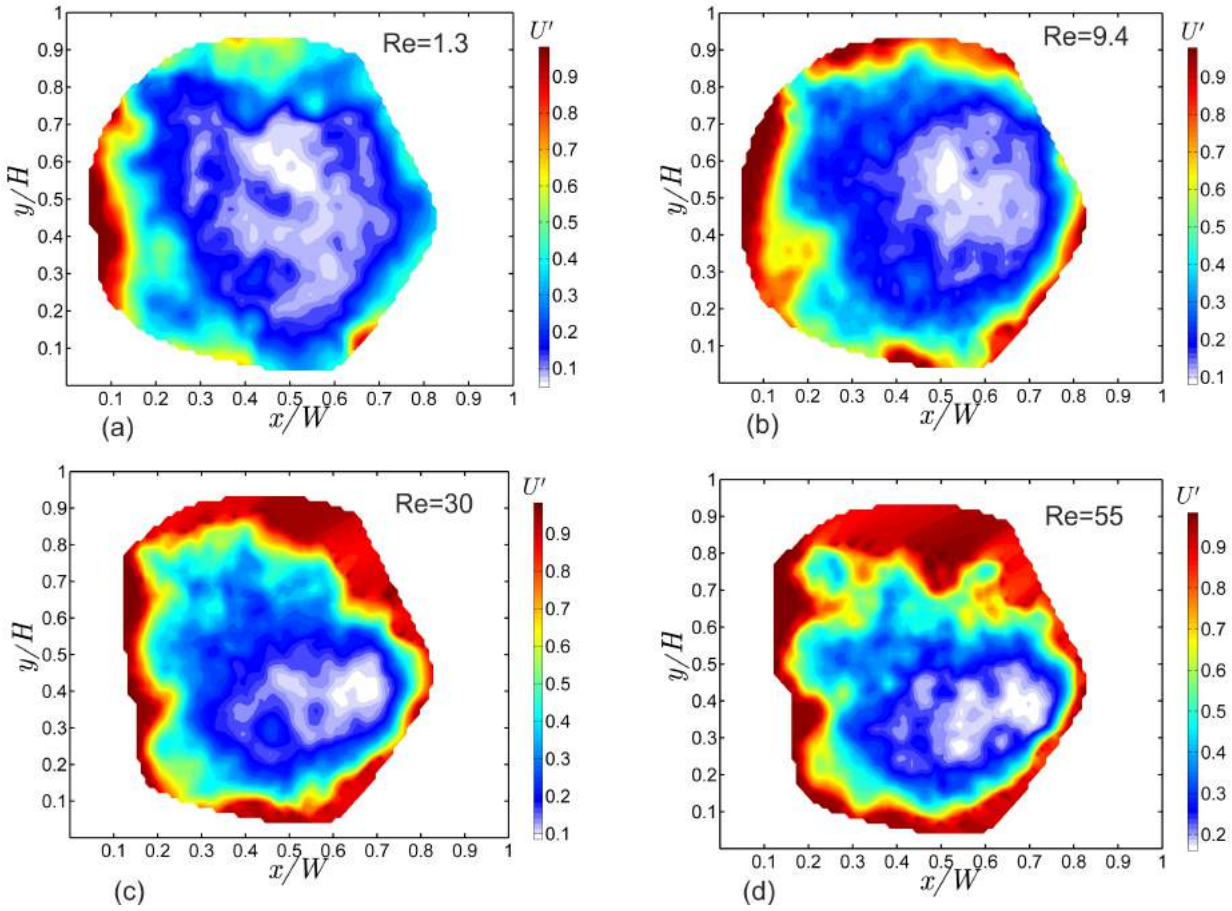

Figure 4.37: Contour plots of velocity fluctuation intensity in a pore of sample IG69 at different Reynolds numbers. (a) Darcy regime at Re = 1.3, (b) Forchheimer regime at Re = 9.4, (c) and (d) turbulent reigme at Re = 30 and 55.

sample IG73, as shown in Fig. 4.38. In the Darcy and Forchheimer regimes, the fluctuation intensity is close to zero through the field of view, except the near wall region. The high fluctuation intensity in these exceptional areas is caused by the normalization of the low local velocity magnitude. In addition, there is no significant difference in the velocity fluctuation intensity between the Darcy and Forchheimer regimes. In the turbulent regime, the thickness of the fluctuating layer near the wall region increases and the fluctuation becomes stronger. The size of the area with low fluctuation also decreases as Reynolds number increases. The extra high fluctuation

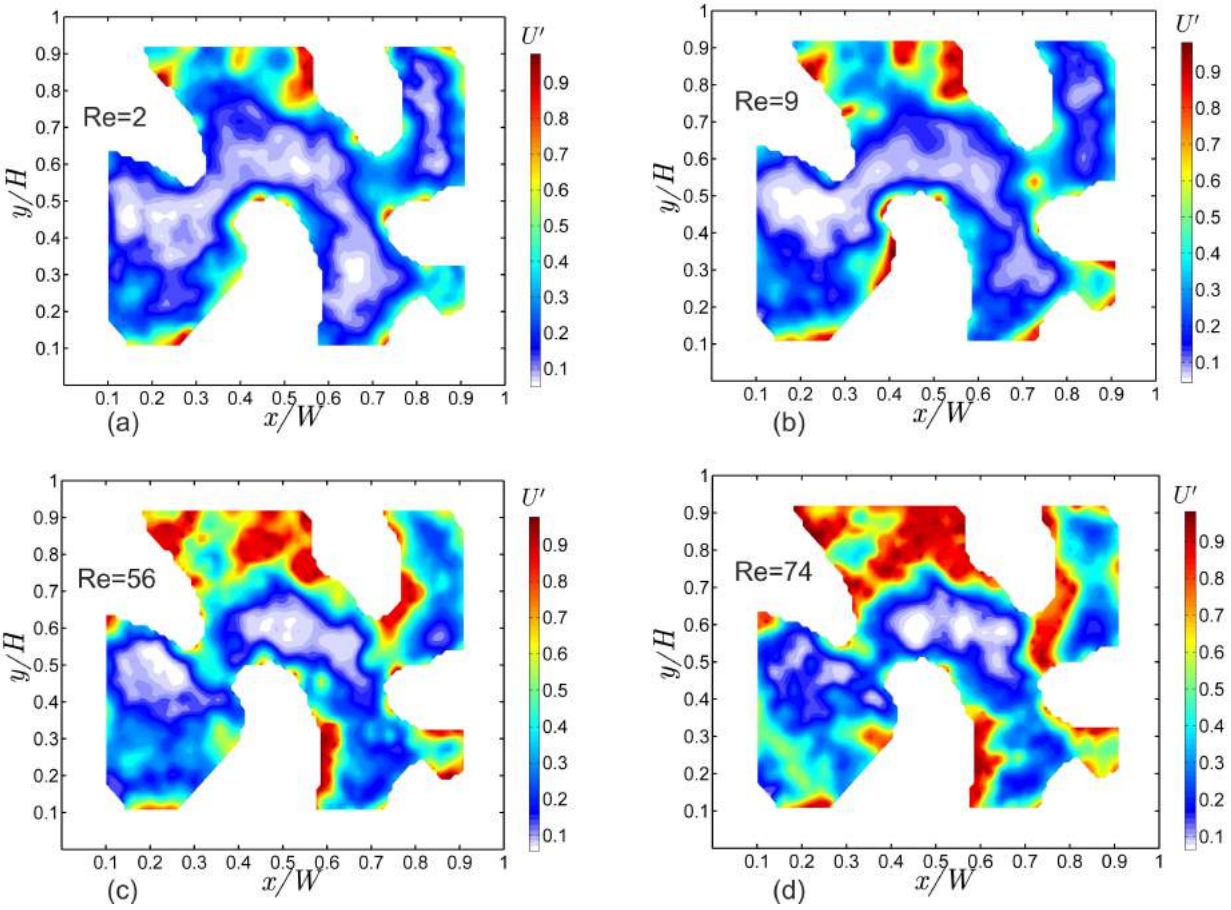

Figure 4.38: Contour plots of velocity fluctuation intensity in a pore of sample IG73 at different Reynolds numbers. (a) Darcy regime at Re = 2, (b) Forchheimer regime at Re = 9, (c) and (d) turbulent regime at Re = 56 and 74.

intensity in the outlet 1 in the turbulent regime is caused by the normalization of a low local velocity magnitudes (see Fig. 4.36).

4.3.5.3 Critical Reynolds number

The critical Reynolds number (Re_c) between the laminar and turbulent flow regimes is obtained by examining the variation of velocity fluctuation intensity with Re, i.e., velocity fluctuation less than 0.1 in laminar flow and larger than 0.1 in turbulent

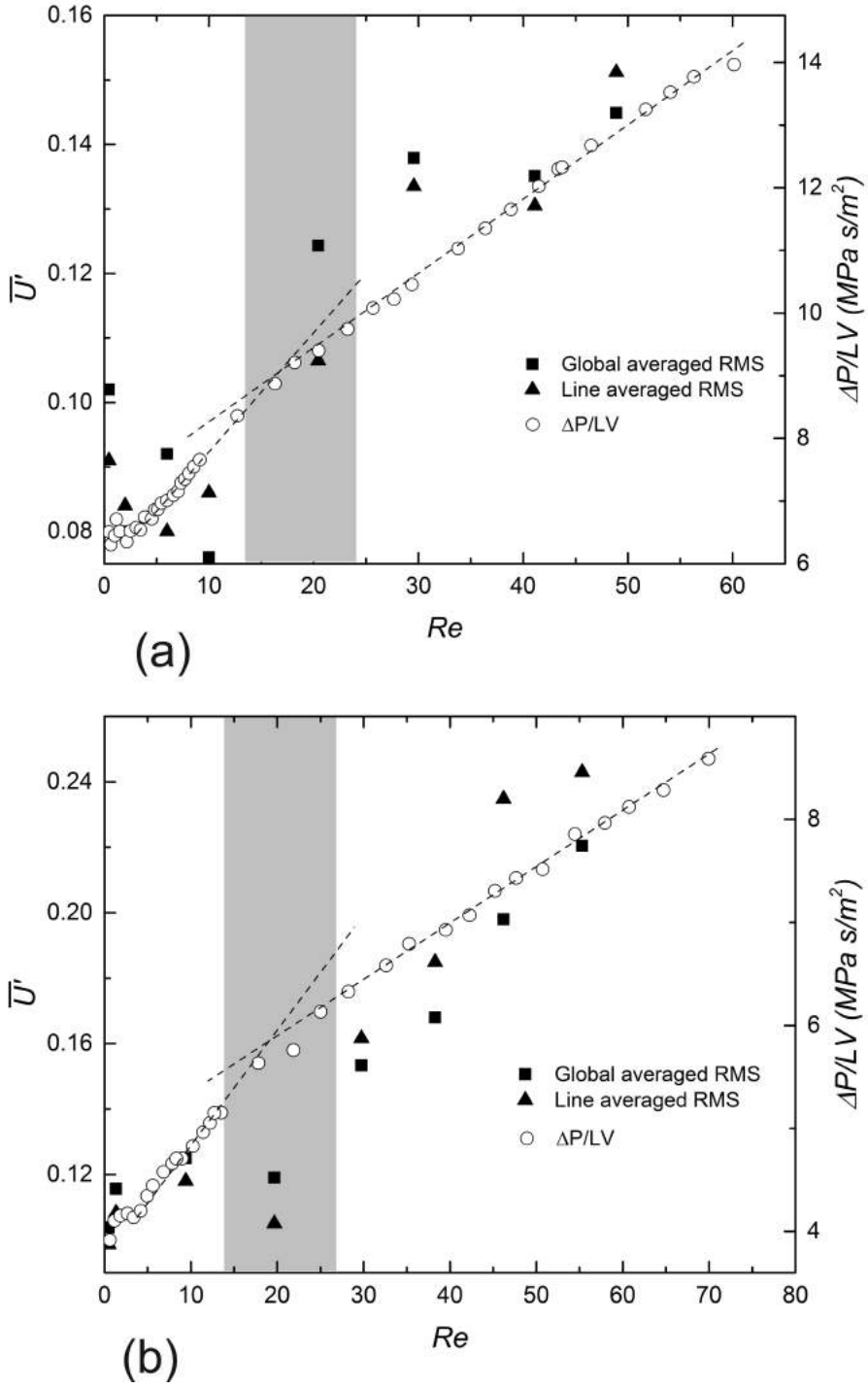

Figure 4.39: Global averaged velocity fluctuation (left-hand y axis) versus Reynolds number for various porosities. Trend lines of pressure drop in the Forchheimer and turbulent regimes are drawn. The location of transition is marked by grey. Sample: (a) IG67, (b) IG69, (c) IG73, (d) IG77 and (e) IG83. (to be continued)

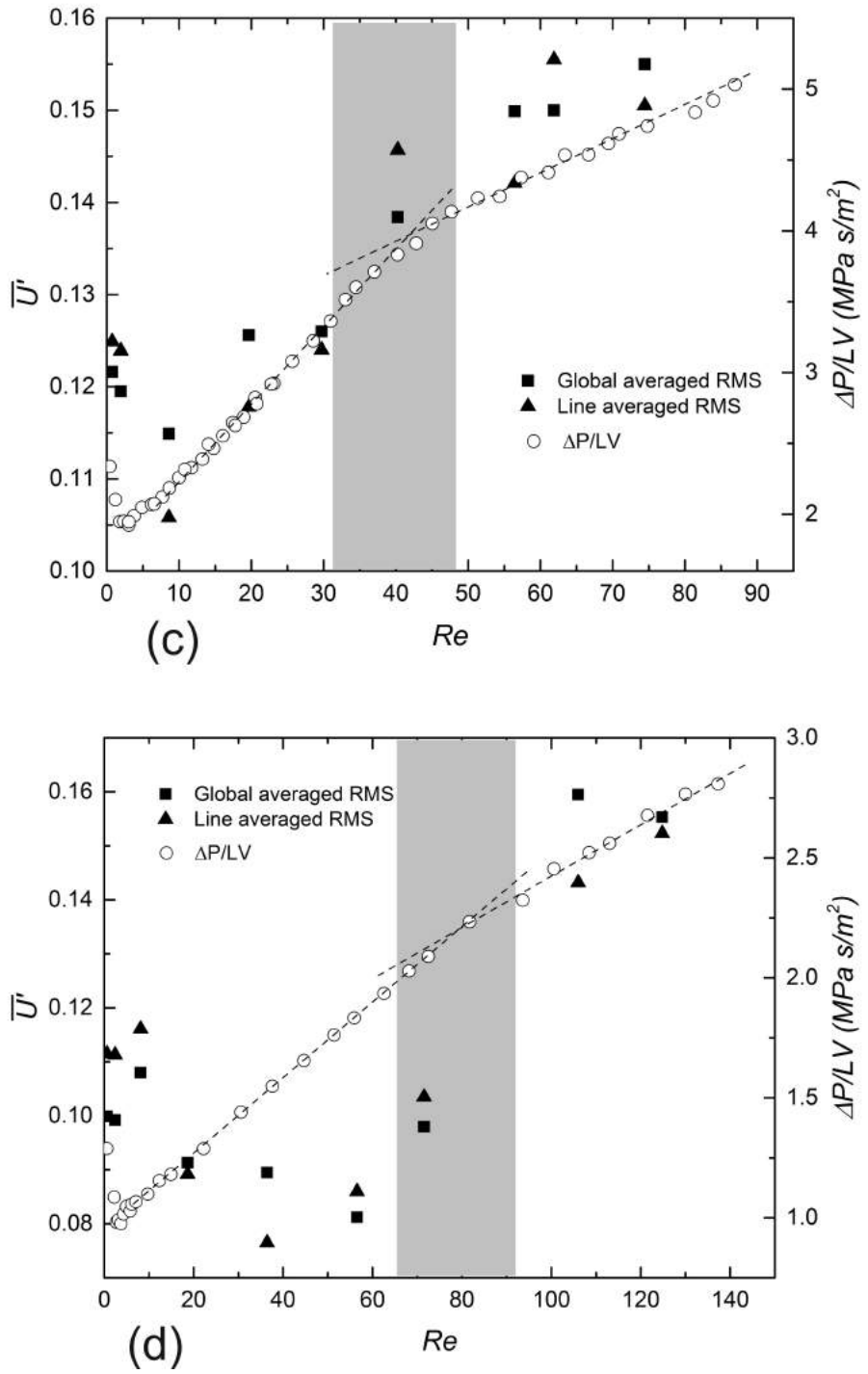

Figure 4.39: (continued) Global averaged velocity fluctuation (left-hand y axis) versus Reynolds number for various porosities. Trend lines of pressure drop in the Forchheirmer and turbulent regimes are drawn. The location of transition is marked by grey. Sample: (a) IG67, (b) IG69, (c) IG73, (d) IG77 and (e) IG83. (to be continued)

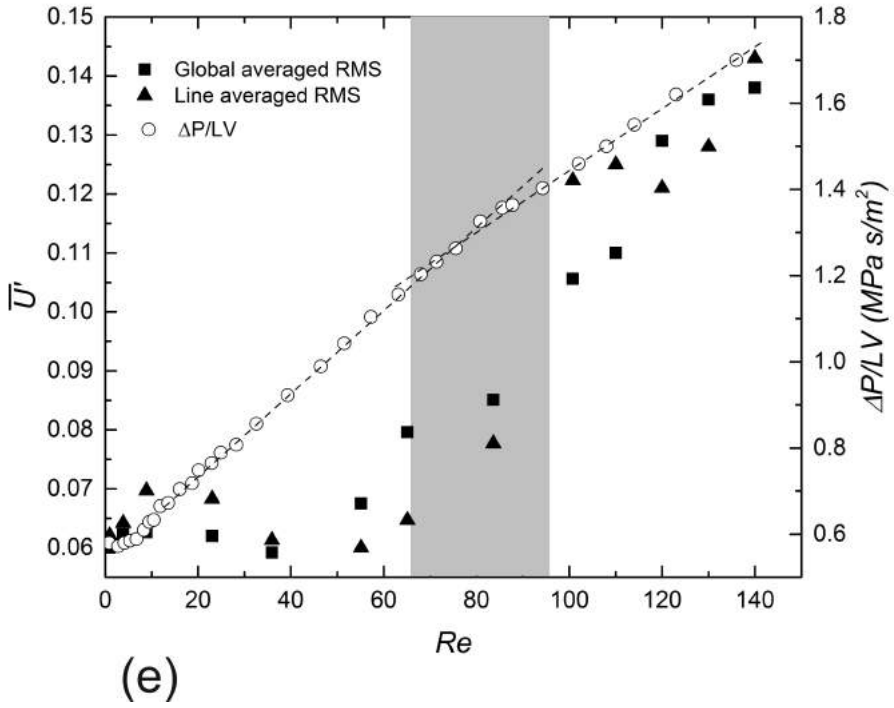

Figure 4.39: (continued) Global averaged velocity fluctuation (left-hand y axis) versus Reynolds number for various porosities. Trend lines of pressure drop in the Forchheimer and turbulent regimes are drawn. The location of transition is marked by grey. Sample: (a) IG67, (b) IG69, (c) IG73, (d) IG77 and (e) IG83.

flow. Fig. 4.39 shows the global averaged velocity fluctuation ($\bar{U}'$) versus Reynolds number for porous glass with irregular pores. The value was calculated by averaging the local velocity fluctuation (U') over the reference line or the whole valid 2D region. The pressure drop data are also presented (right-hand y axis) for comparison. The pressure drop data in the Forchheimer and turbulent regimes are fitted with straight lines and the intersection is where the critical point locates. The transition cannot be identified as a single point but a Re range, so the transition area was highlighted by a grey band. Fig. 4.39 also shows that the grey band corresponds to the sharp increase in the $\bar{U}'$-Re curve. In all samples, the velocity fluctuation remains at a nearly fixed value at Re below Re_c and increases dramatically at Re above Re_c. This critical Reynolds number therefore identifies the transition from laminar to turbu-

lent flow. It should be noted that in some samples, such as samples IG69 and IG73, although below Re_c, the global averaged velocity fluctuation is higher than 0.1 at a Re below Re_c. This may be caused by the data from the near wall regions with exceptional high fluctuation intensity values.

4.4 Flow characteristics in porous copper

The structure, pressure drop, flow regime, permeability and form drag coefficient in five porous copper samples, namely IC64, IC66, IC71, IC75, IC78, with porosities of 0.64, 0.66, 0.71, 0.75 and 0.78, are presented in this section. The detailed information of these samples is listed in table 3.1.

4.4.1 Structural properties

Fig. 4.40 shows the representative microstructure of a typical porous copper sample. The large spherical pores inside the sample represent the spaces previously occupied by potassium carbonate particles. Compared to the porous glass samples, the high pressure compacting process used in manufacturing the porous copper samples has improved the contacts between the metal particles, which benefits the subsequent sintering process. Fig. 4.40(b) shows a typical pore in the porous copper sample. The pore walls are composed of individual sintered copper particles, resulting in a high surface area of the matrix. The copper particles assemble tightly around the pore, forming solid walls. Small holes or interstices between the copper particles are also found. This morphology often appears in the samples with low porosity where the potassium carbonate have less chance to touch each other. Fig. 4.40(c) shows a

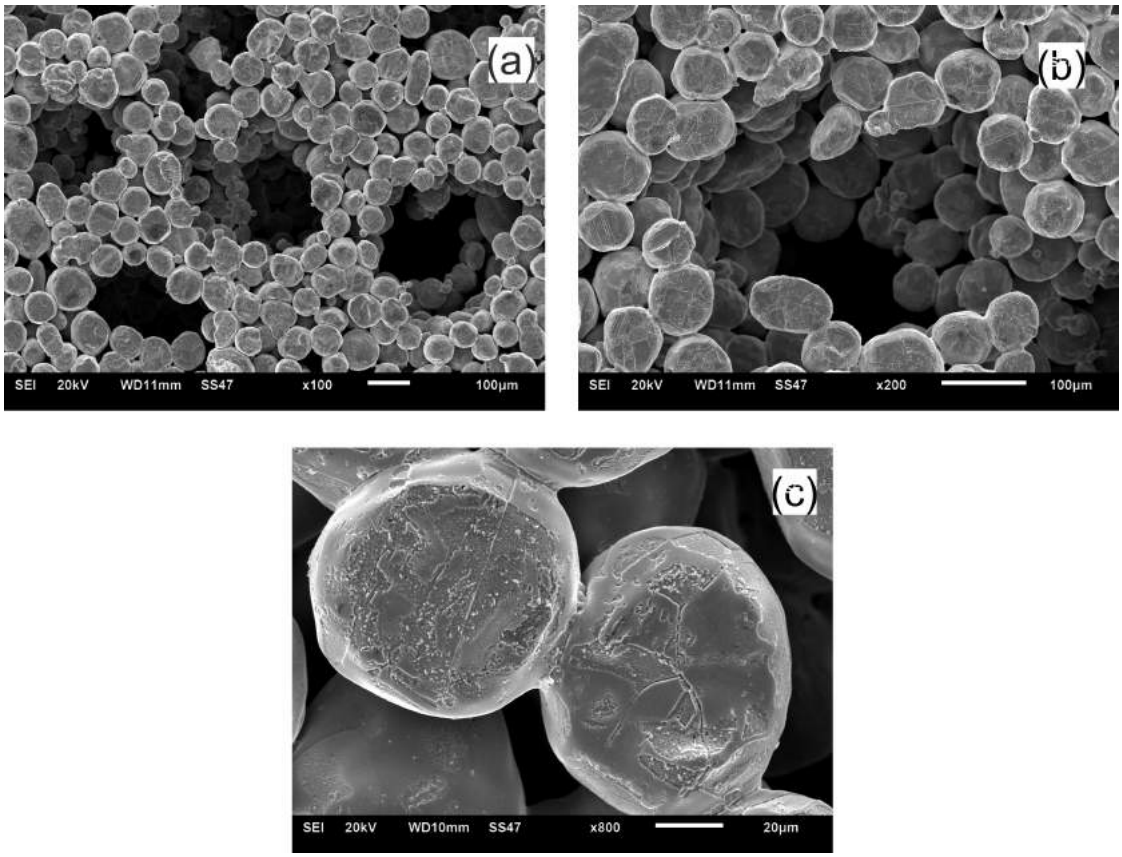

Figure 4.40: SEM micrographs of a LCS copper sample showing representative features.

sintering neck between two copper particles. The diameter of the sintering neck is about half of the particle diameter, providing the strength of the porous metal.

4.4.2 Pressure drop

The relationship between the length-normalised pressure drop and the pore size based Reynolds number for porous copper samples with different porosities is shown in Fig. 4.41. The pressure drop in the porous copper also depends significantly on the porosity of the samples. The pressure drop across the sample increases with a decrease in the porosity due to the increased obstruction of the solid phase to the

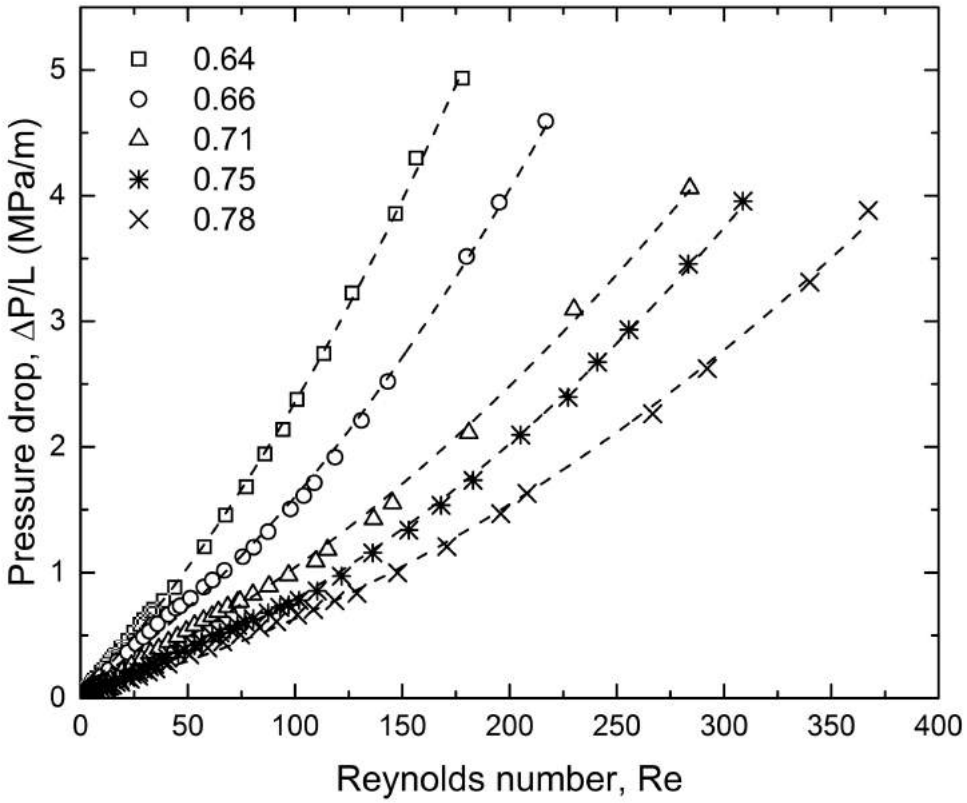

Figure 4.41: Relationship between length-normalised pressure drop and pore size based Reynolds number for porous Cu samples with different porosities.

fluid flow. The relationship between pressure drop and Reynolds number is initially linear at low Reynolds numbers and becomes nonlinear at high Reynolds numbers. However, it is difficult to identify the transition from the linear range to the nonlinear range from the $\Delta P/L - Re$ plots.

4.4.3 Flow regime identification

Fig. 4.42 plots the reduced pressure drop against the Reynolds number for the porous Cu samples with different porosities. Five different flow regimes can be identified: (i) pre-Darcy, (ii) transition to Darcy, (iii) Darcy, (iv) transition to non-Darcy and

(v) non-Darcy regimes. The flow behaviour is similar to the porous glass samples with a similar structure. However, there are several differences between the porous copper and the porous glass samples in terms of flow regimes. The flow in the porous glass samples showed four well-defined flow regimes: pre-Darcy, Darcy, Forchheimer and turbulent. The slope difference between the Forchheimer regime and the turbulent regime in the porous copper samples is quite small. Therefore, these two flow regimes are combined and designated as non-Darcy regime in the current analysis. Fig. 4.42 shows that there are extended transitions from pre-Darcy to Darcy and from Darcy to non-Darcy in the porous copper samples. These transition regimes have a clearly different slope from the neighbouring regimes and they are much wider than the transition regimes observed in the porous glass samples. In addition, the Darcy regime in the porous copper samples occurs at a much lower Reynolds number and spans a much wider range of Reynolds number than in the porous glass samples.

Table. 4.10 lists the flow regime bounds of the porous copper samples. It shows that the flow regime bounds differ significantly among these samples. However, a general trend can be observed that the boundary of each flow regime increases with porosity.

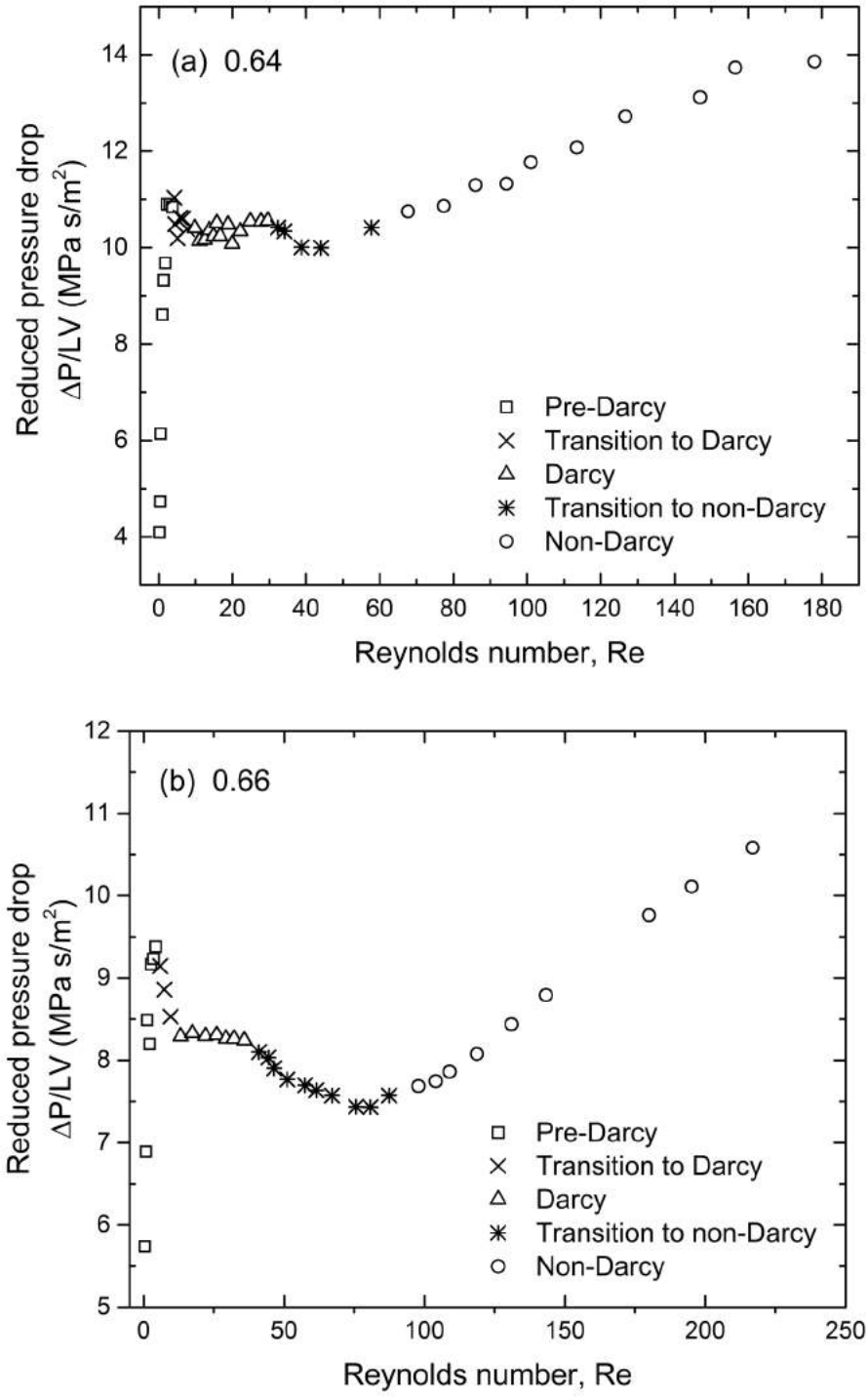

Figure 4.42: Reduced pressure drop versus Reynolds number for porous copper samples with various porosities. Porosity: (a) 0.64, (b) 0.66, (c) 0.71, (d) 0.75 and (e) 0.78. (to be continued)

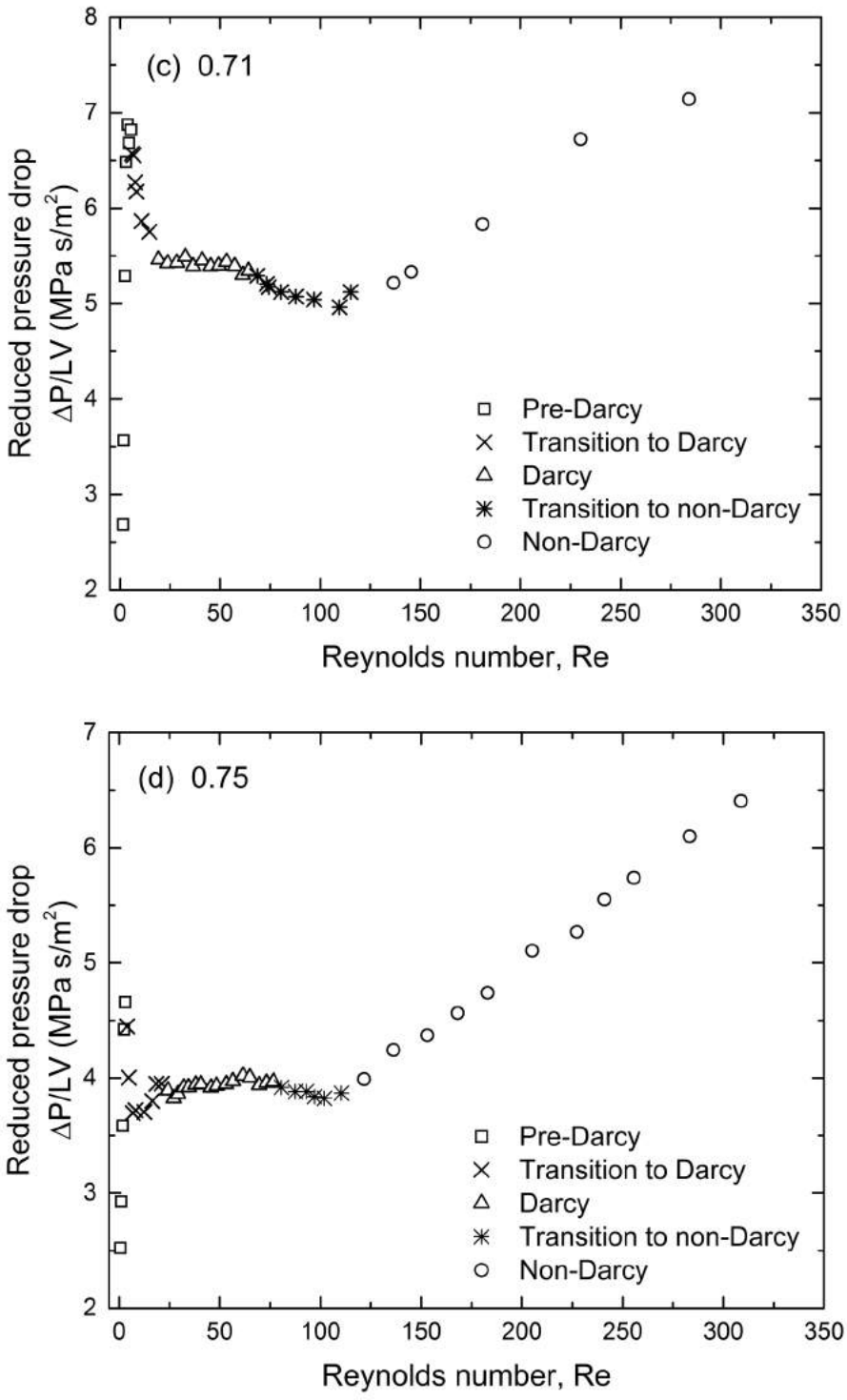

Figure 4.42: (continued) Reduced pressure drop versus Reynolds number for porous copper samples with various porosities. Porosity: (a) 0.64, (b) 0.66, (c) 0.71, (d) 0.75 and (e) 0.78. (to be continued)

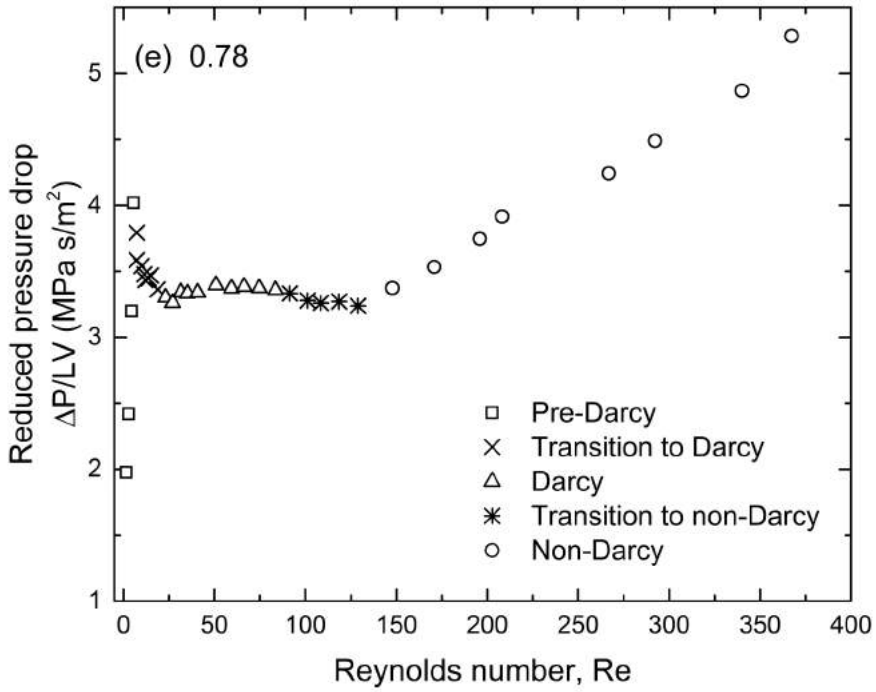

Figure 4.42: (continued) Reduced pressure drop versus Reynolds number for porous copper samples with various porosities. Porosity: (a) 0.64, (b) 0.66, (c) 0.71, (d) 0.75 and (e) 0.78.

Table 4.10: Comparison of flow regime bounds of different porous copper samples.

Sample ID	Materials	Pre-Darcy	Darcy	Non-Darcy
IC64	0.64	Re<4.0	10<Re<30	44<Re
IC66	0.66	Re<5.0	15<Re<35	80<Re
IC71	0.71	Re<5.5	23<Re<65	109<Re
IC75	0.75	Re<5.0	24<Re<80	110<Re
IC78	0.78	Re<5.5	23<Re<85	147<Re

Fig. 4.43 plots the critical Reynolds number for the onset of each flow regime as a function of porosity of the porous Cu samples. The onset Reynolds numbers for

the transition to Darcy, Darcy, transition to non-Darcy and non-Darcy regimes are designated as Re_{TD}, Re_D, Re_{TN} and Re_{ND}, respectively. The Reynolds number ranges of the five flow regimes are therefore: pre-Darcy ($Re < Re_{TD}$), transition to Darcy ($Re_{TD} < Re < Re_D$), Darcy ($Re_D < Re < Re_{TN}$), transition to non-Darcy ($Re_{TN} < Re < Re_{ND}$) and non-Darcy ($Re > Re_{ND}$). Fig. 4.43 shows that the porosity of the porous copper sample has a significant effect on the onset and range of the flow regimes. The onset Re for each regime increases nearly linearly with porosity. For example, non-Darcy flow starts at $Re_{ND} = 65$ in the sample with a porosity of 0.64 and is delayed at a higher onset value of $Re_{ND} = 150$ in the sample with a porosity is 0.78. The Re range for each regime also becomes wider with increasing porosity, especially markedly for the Darcy regime.

4.4.4 Permeability and form drag coefficient

Table 4.11 shows the permeability (K) and form drag coefficient (C) of the porous copper samples, calculated by two approaches: (1) the permeability for the Darcy regime was obtained by fitting the experimental data within the Darcy regime to the Darcy equation (Eq. 2.1), while the permeability and form drag coefficient for the non-Darcy regime were obtained by fitting the experimental data within the non-Darcy regime to the extended Darcy-Forchheimer equation (Eq. 2.2). (2) The permeability and form drag coefficient for all regimes were obtained by fitting all the data to the extended Darcy-Forchheimer equation.

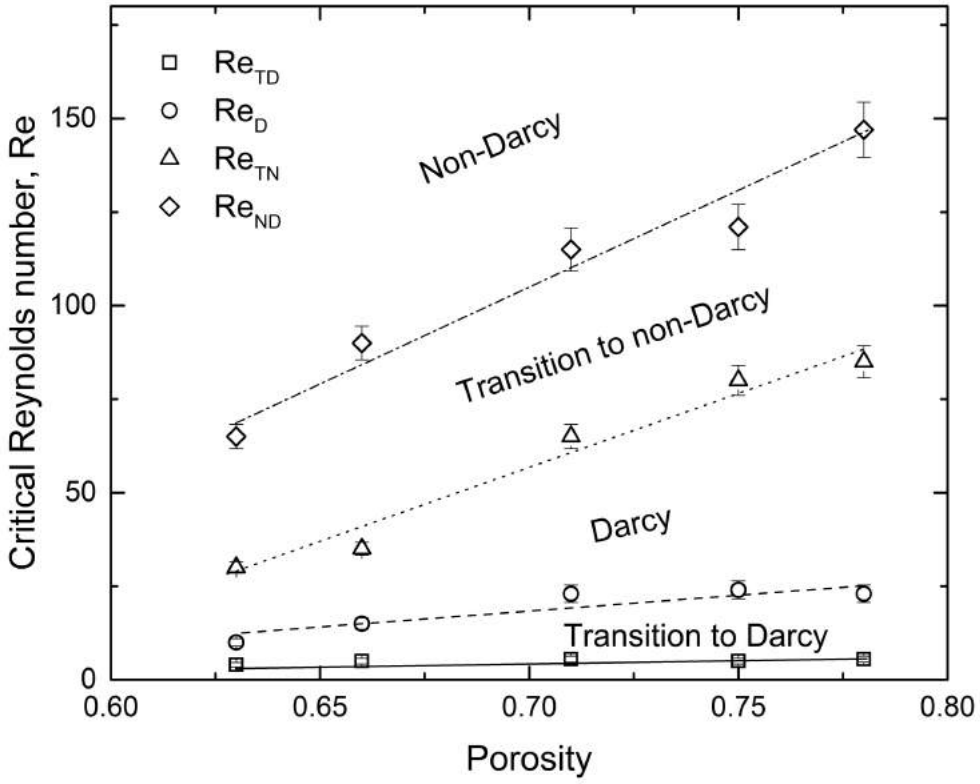

Figure 4.43: Relationship between critical Reynolds numbers and porosity of the porous Cu samples.

Table 4.11: Permeability ($K \times 10^{-10}$ m^2) and form drag coefficient ($C \times 10^4$ m^{-1}) of porous copper at various flow regimes.

Sample	Darcy		Non-Darcy			All regimes		
	K	R^2	K	C	R^2	K	C	R^2
S63	0.96	0.99	1.15	1.5	0.99	1.1	1.38	0.99
S66	1.21	0.99	1.90	1.23	0.99	1.62	0.98	0.99
S71	1.84	0.99	2.66	0.59	0.99	2.33	0.49	0.99
S75	2.53	0.99	4.16	0.63	0.99	3.15	0.43	0.99
S78	2.97	0.99	4.88	0.43	0.99	4.08	0.36	0.99

Table 4.11 shows that the effect of flow behaviour on permeability is significant in LCS porous copper. The value of permeability calculated from non-Darcy regime is greater than the value calculated from the Darcy regime. In other words, non-Darcy regime has a greater ability for mass transport than the Darcy regime.

Fig. 4.44 shows the variations of permeability and form drag coefficient with porosity. It shows that increasing porosity leads to dramatic increase in permeability and dramatic decrease in form drag coefficient. The lower fluid resistance in a sample with a higher porosity is due to the lower fraction of solid matrix impeding the fluid flow and the lower tortuosity (Diao et al. 2017). For the porous copper samples, the permeability in the Darcy regime is approximately one third lower than the permeability in the non-Darcy regime.

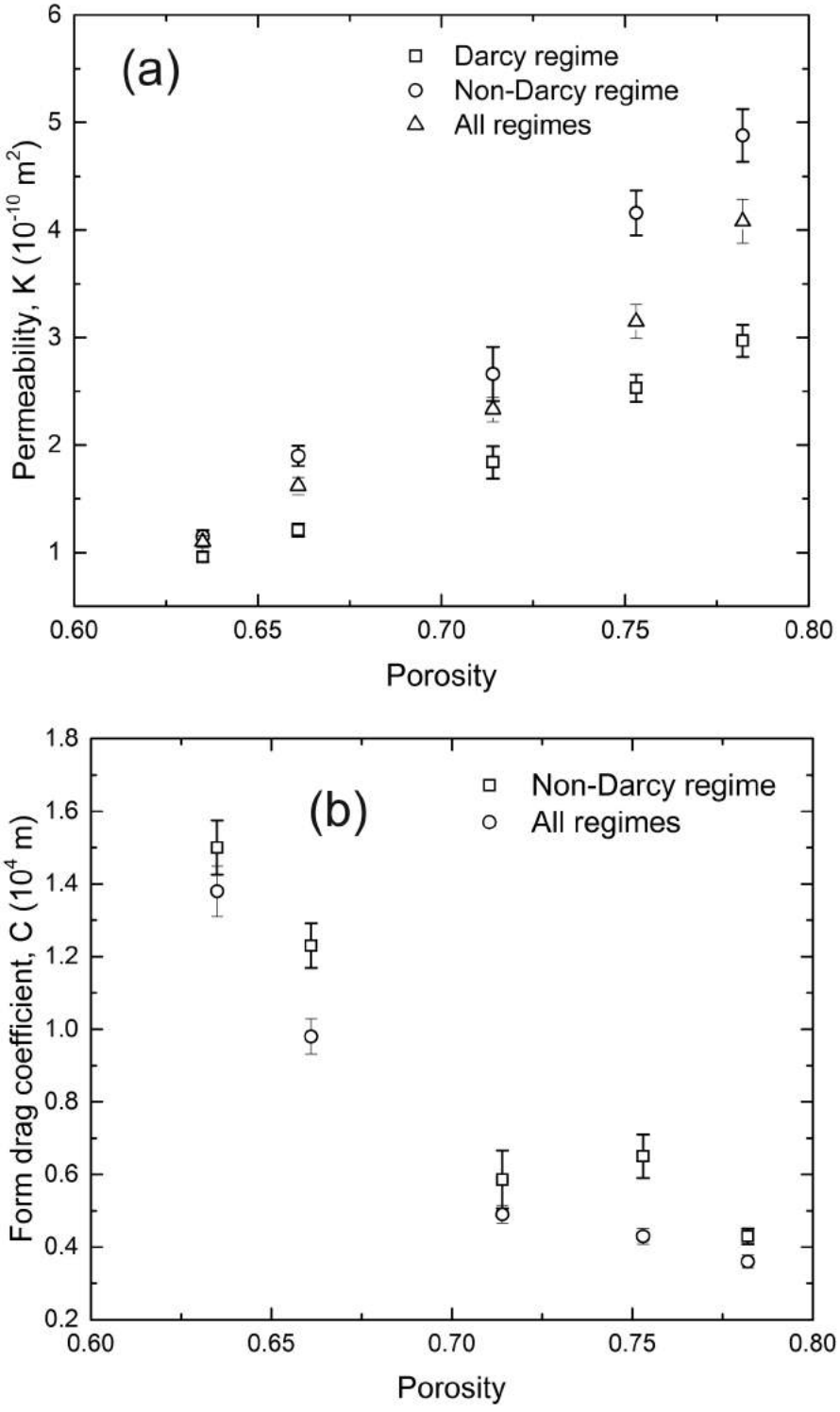

Figure 4.44: Relationships of (a) permeability (K) and (b) form drag coefficient (C) with porosity in porous copper samples.

4.5 Effects of structural properties and flow state on fluid flow

This section compares the results obtained from the four different porous media and discusses the effects of porosity and pore shape on flow regime bounds, permeability, form drag coefficient, friction factor and velocity distribution in pore scale.

4.5.1 Effect of particle size, porosity and pore shape on flow regime bounds

The flow regime boundaries listed in tables 4.2, 4.5, 4.8 and 4.10 show that the critical Reynolds number corresponding to each flow regime bound is different in different porous media. In other words, structural characteristics influence the transition of flow from one state to another.

Particle size has a significant effect on the flow regime bounds in sintered glass samples. As seen from Fig. 4.4, the critical Reynolds number increases with the mean diameter of the sintered glass sample. In other words, turbulent flow develops easily in smaller particle sample than in large particle sample. For example, the flow is turbulent in sample G170 at Re = 5, while the flow is still laminar in sample G710. This is because decreasing particle size results in more channels, junctions and more contraction and expansion structures in sintered glass samples. All these factors can contributes to the onset of turbulent. The width of the Forchheimer regime and the transition range increases as the particle size increases. However, the reasons for causing this is still unclear.

The effect of porosity on the width of flow regime range is different for different porous media. In the sintered glass samples and porous glass samples with spherical pores (Fig. 4.20) and irregular pores (Fig. 4.31), increasing porosity leads to a wider increases Forchheimer regime, but the transition range remains narrow in all samples. In the porous copper samples (Fig. 4.43), as the porosity increases, the range of the Darcy regime becomes wider, while the width of the transition range from the Darcy regime to the non-Darcy regime remains roughly the same.

Fig. 4.45 shows the regime bounds of porous glass samples with spherical and irregular pores. The flow regime bounds located at the low Reynolds number range are shown in Fig. 4.45(b) for a better view. The effect of pore shape on flow regime bounds is not as significant as the effect of porosity, but more complex. For porous glass samples with different pore shapes, the critical Reynolds numbers are similar at some porosities, but differ at other porosities. The slopes of the trend line for Re_{TT} and Re_{T} are greater in porous glass samples with irregular pores. There is no obvious trend between critical Reynolds number and porosity for the regime bounds located at the low Reynolds number range (Re_{D}, Re_{TF} and Re_{F}), due to the high measurement uncertainty at ultra-low pressure drops and flow rates.

Fig. 4.46 compares the flow regime bounds in porous copper and porous glass samples with irregular pores. These two porous media were manufactured by the same process and have a similar structure. However, the critical Reynolds number of porous copper sample is much greater than that of the porous glass sample for a given porosity. This difference could be attributed to two reasons. First, the difference in surface wettability between copper and glass results in a different interaction

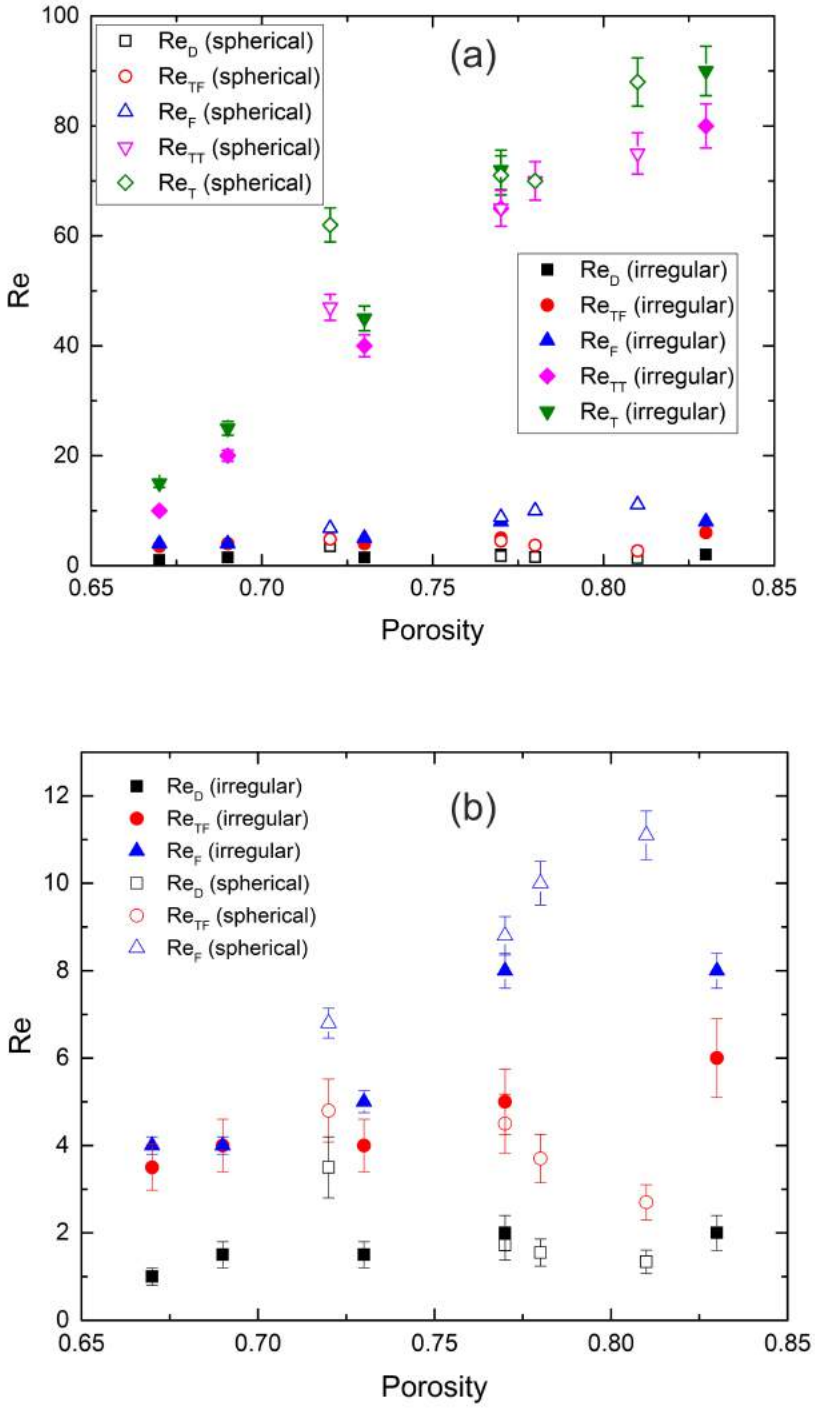

Figure 4.45: Comparison of flow regime bounds between LCS porous glass with spherical and irregular pores. (a) All flow regime bounds, (b) bounds for Darcy and Forchheimer regimes.

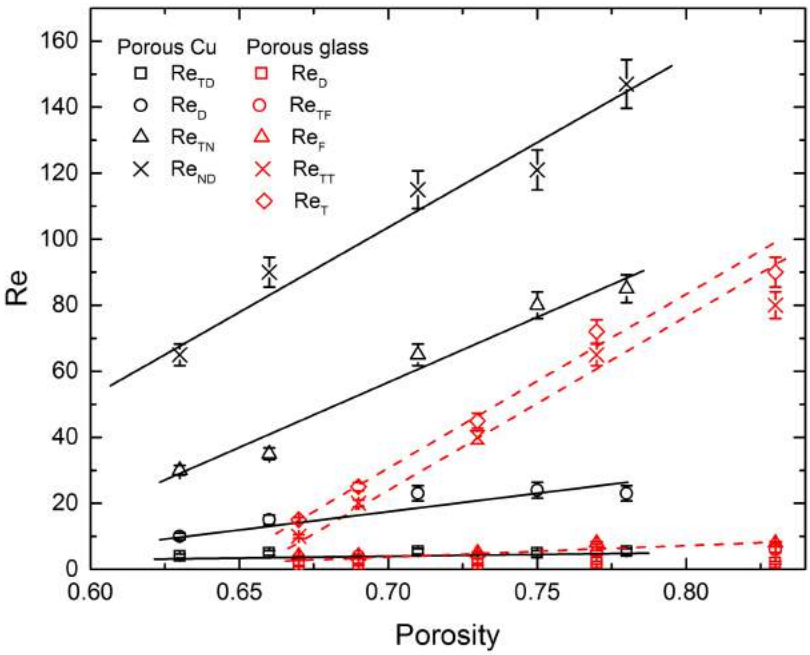

Figure 4.46: Comparison of flow regime bounds between porous copper and porous glass samples with irregular pores.

between the solid wall and the fluid flow. Second, the porous copper was pressed under a higher pressure (200 MPa) during manufacture, while the porous glass was only pressed with hand. As a consequence, the gap between copper particles is much smaller than the gap between glass particles, seen in Figs. 2.7 and 4.17. Therefore, for samples with the same porosity, the pore density (pores produced by the space holder) in porous copper samples is higher than that in porous glass samples.

4.5.2 Effect of structural properties and flow state on permeability and form drag coefficient

The effect of structural characteristics (porosity, pore shape and material) and flow state on permeability and form drag coefficient in porous media are compared. The

permeability and form drag coefficient calculated from different regimes (tables 4.6, 4.9 and 4.11) were plotted against porosity in Figs. 4.47 and 4.48, respectively. Since the Forchheimer regime was not identified in the porous copper samples, the permeability and form drag coefficient obtained from the non-Darcy regime were compared with those of the porous glass samples.

Fig. 4.47 shows the variation of permeability with porosity in different flow regimes. The permeabilities calculated from Darcy, Forchheimer, turbulent (non-Darcy) and all regimes are presented and compared separately. In the Darcy regime, porous glass samples with spherical and irregular pores have nearly identical permeability at a given porosity, while porous copper sample shows smaller permeability (Fig. 4.47(a)). The difference in permeability between porous copper and glass increases with increasing porosity. In the Forchheimer and turbulent regimes, the permeabilities are nearly the same for the three materials when the porosity is less than 0.72. As the porosity increases to above 0.72, the porous glass sample with irregular pores has the largest permeability and the porous copper sample has the lowest permeability. The permeability values calculated from all regimes have same trend as that in the Forchheimer regime, although the values are different.

Fig. 4.48 shows the variation of form drag coefficient with porosity in different flow regimes for different porous media. The effect of porosity on form drag coefficient is the same in all flow regimes. For a given porosity, the porous glass sample with spherical pores has the greatest form drag coefficient, followed by porous glass sample with irregular pores, and the porous copper sample has the lowest value.

In summary, high porosity leads to high permeability and low form drag coefficient.

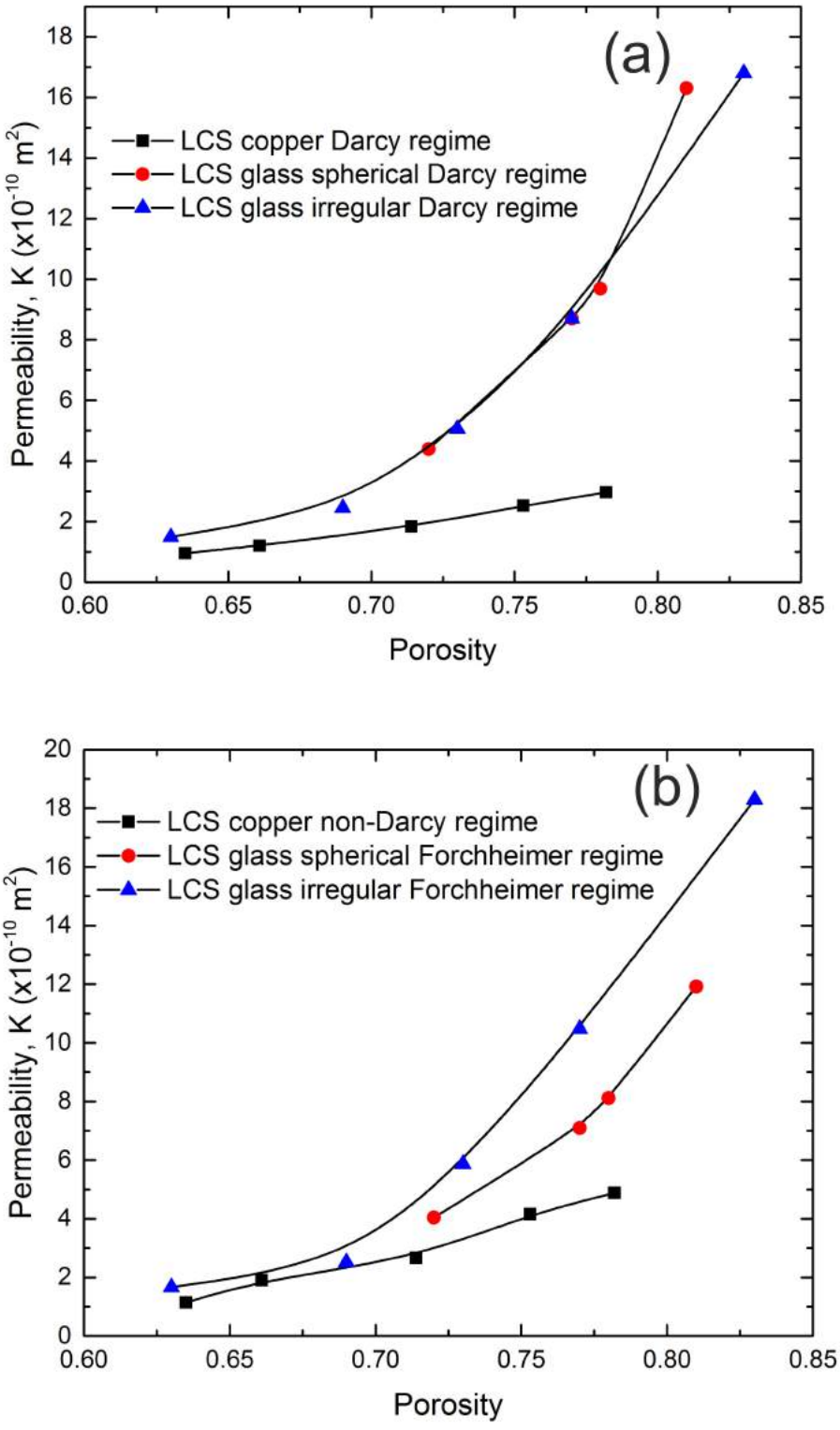

Figure 4.47: Variations of permeabiltiy with porosity in different flow regimes. (a) Darcy regime, (b) Forchheimer regime, (c) turbulent regime and (d) all regimes. (to be continued)

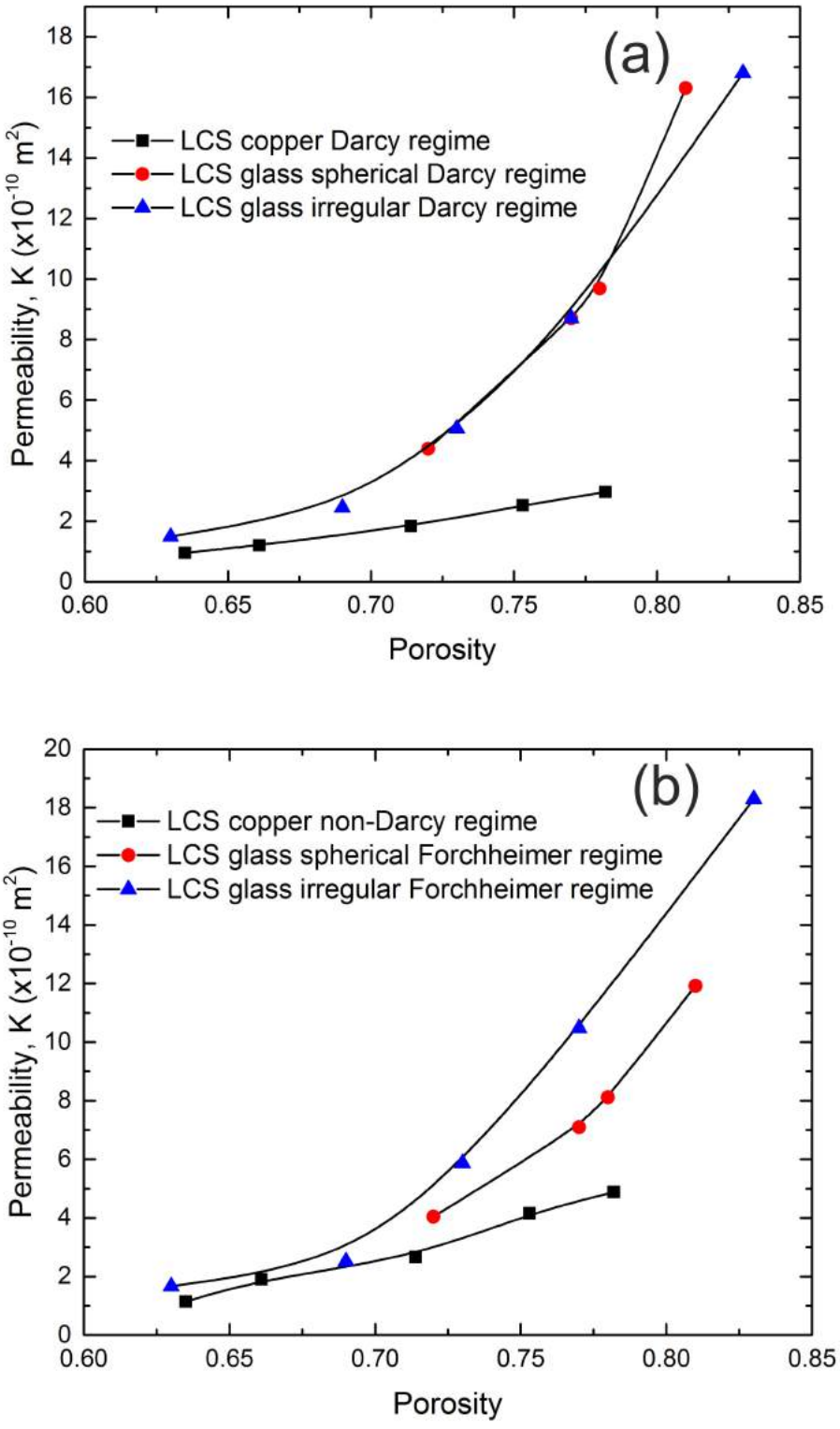

Figure 4.47: (continued) Variations of permeabiltiy with porosity in different flow regimes. (a) Darcy regime, (b) Forchheimer regime, (c) turbulent regime and (d) all regimes.

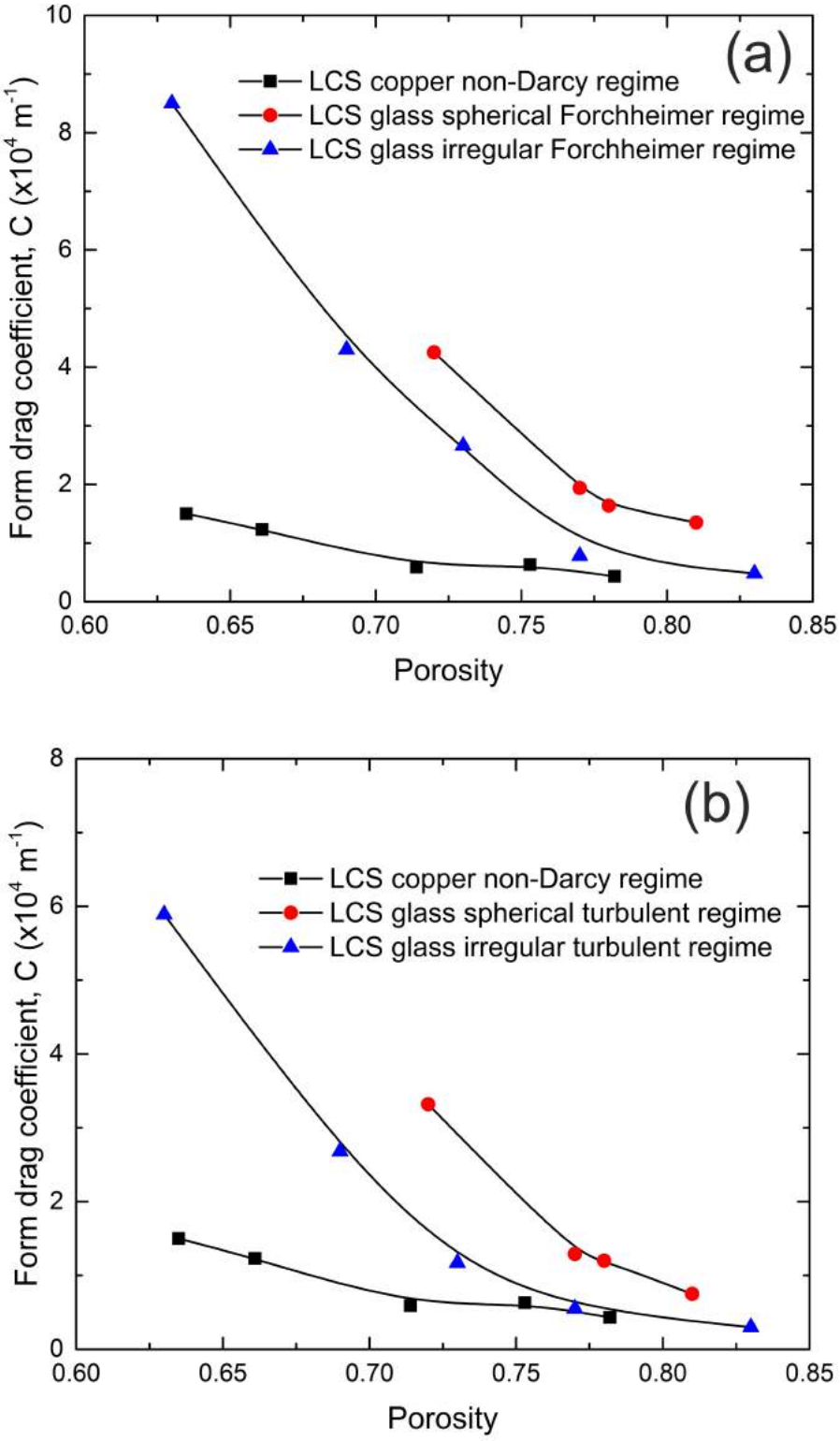

Figure 4.48: Variations of form drag coefficient with porosity in different flow regimes. (a) Forchheimer regime, (b) turbulent regime and (c) all regimes. (to be continued)

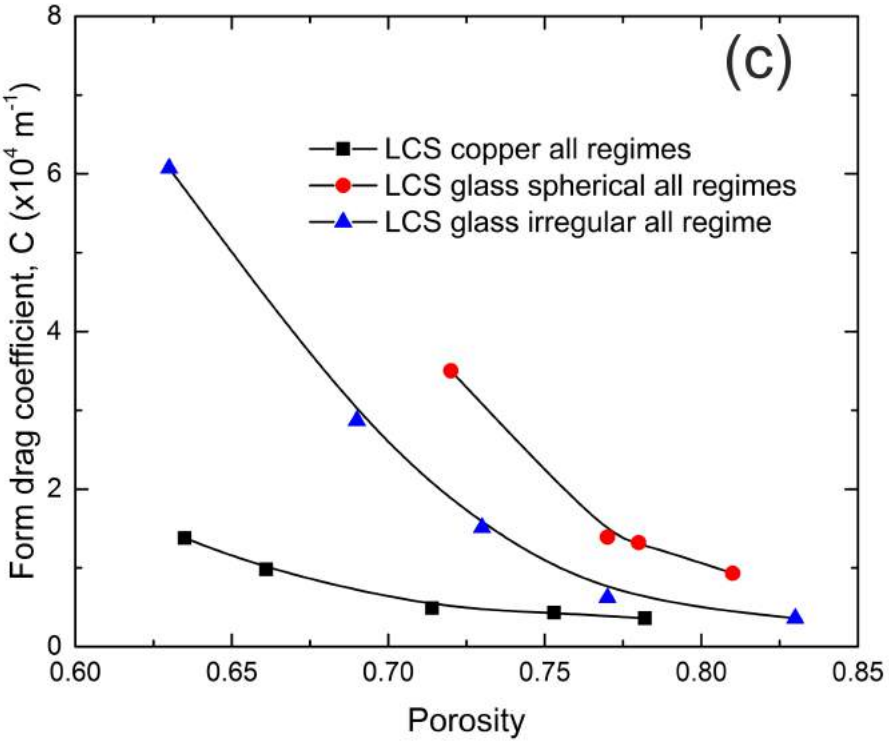

Figure 4.48: (continued) Variations of form drag coefficient with porosity in different flow regimes. (a) Forchheimer regime, (b) turbulent regime and (c) all regimes.

Porous glass has higher permeability and lower form drag coefficient than porous copper probably because of different fraction of secondary pores (spaces between solid particles) duet to different pressures applied during manufacture.

4.5.3 Effect of porosity and pore shape on friction factor

The Forchheimer-extended Darcy equation (Eq. 2.2) can be rewritten In a non-dimensional form as

$$f = \frac{A}{Re} + B \tag{4.3}$$

where $f = \frac{\Delta P}{1/2\rho V^2}\frac{D}{L}$, is defined as the friction factor, $A = 2D^2/K$ and $B = 2CD$. It should be noted that D is mean particle size (D_m) in the sintered glass samples, and mean pore size (D_p) in the porous glass and copper samples. Eq. 4.3 shows that the relationship between friction factor and Reynolds number is very sensitive to Reynolds number. At low Reynolds numbers, the term A/Re can be very large, and Eq. 4.3 becomes $f \approx A/Re$, indicating a linear relationship between friction factor and reciprocal of Reynolds number. At high Reynolds numbers, the term A/Re becomes negligible, and Eq. 4.3 becomes $f \approx B$, indicating a constant friction factor.

Flow regimes can also be identified according to the different relationships between friction factor and Reynolds number. In the Darcy regime, the data should follow the A/Re curve as predicated by the Darcy equation. In the pre-Darcy and non-Darcy regime, the data deviate from the A/Re curve due to the effect of other forces such as inertial force.

The f-Re relationships of the sintered glass, porous glass and porous copper samples are shown in a logarithmic coordinate system in Figs. 4.49 and 4.50. The relationship agrees well with Eq. 4.3: the friction factor is inversely proportional at low Reynolds numbers and deviates from it at high Reynolds numbers.

Fig. 4.49 shows the $f - Re$ relationship in sintered glass samples. The calculated values of A are 2752, 3521 and 2112 for samples G170, G430 and G710, respectively. It can be seen that the effect of mean particle size on friction factor is insignificant before reaching the turbulent flow regime. For fully developed turbulent flow, smaller mean particles correspond to higher friction factor values, according to the trend of the experimental data.

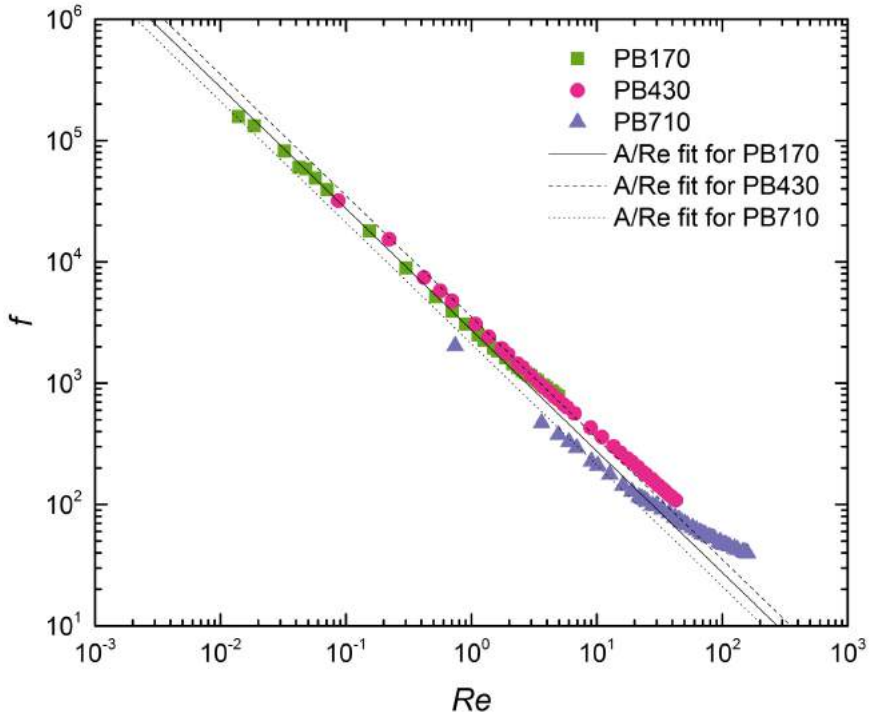

Figure 4.49: Variation of friction factor with Reynolds number in packed bed with different particle sizes.

Fig. 4.50 shows the friction factor as a function of Reynolds number in porous glass samples with spherical and irregular pores and porous copper samples. For a given Reynolds number, porous samples with a lower porosity has a higher friction factor for the three porous media. The effect of porosity on friction factor in porous glass sample is more significant than that in porous copper sample.

The effects of porosity and Reynold number on friction factor have been studied in other porous media (Boomsma & Poulikakos 2002, Vafai & Tien 1981, Dukhan & Patel 2008, Paek et al. 2000, Dukhan 2006, Dukhan et al. 2014). Dukhan et al. (2014) summarized and compared the previous experimental data and found a similar f-Re relationship for different porous media characteristics (material, porosity, pore size

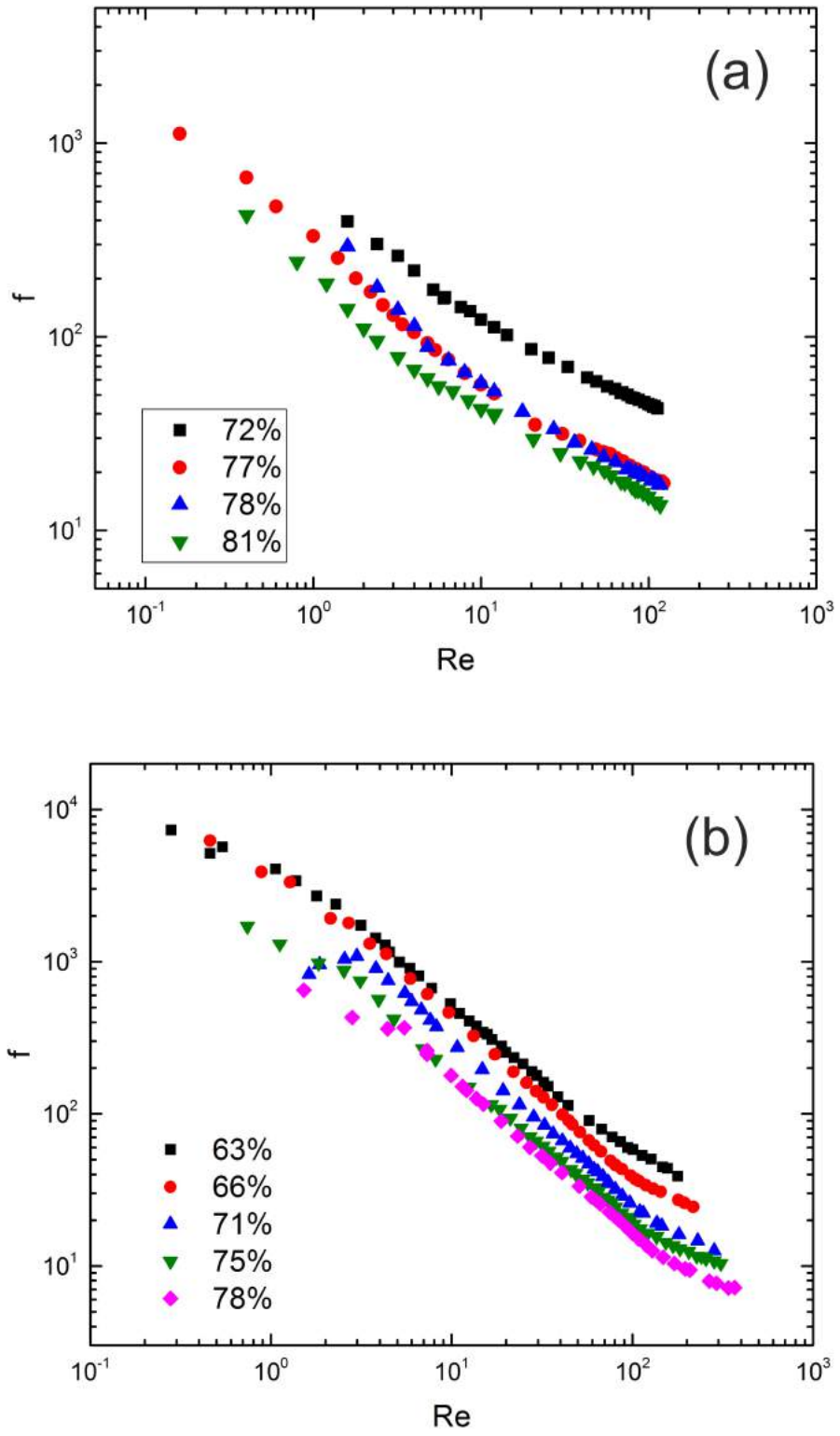

Figure 4.50: Effect of porosity on friction factor in various porous meida. (a) Porous glass sample with spherical pores, (b) porous glass sample with irregular pores and (c) porous copper samples. (to be continued)

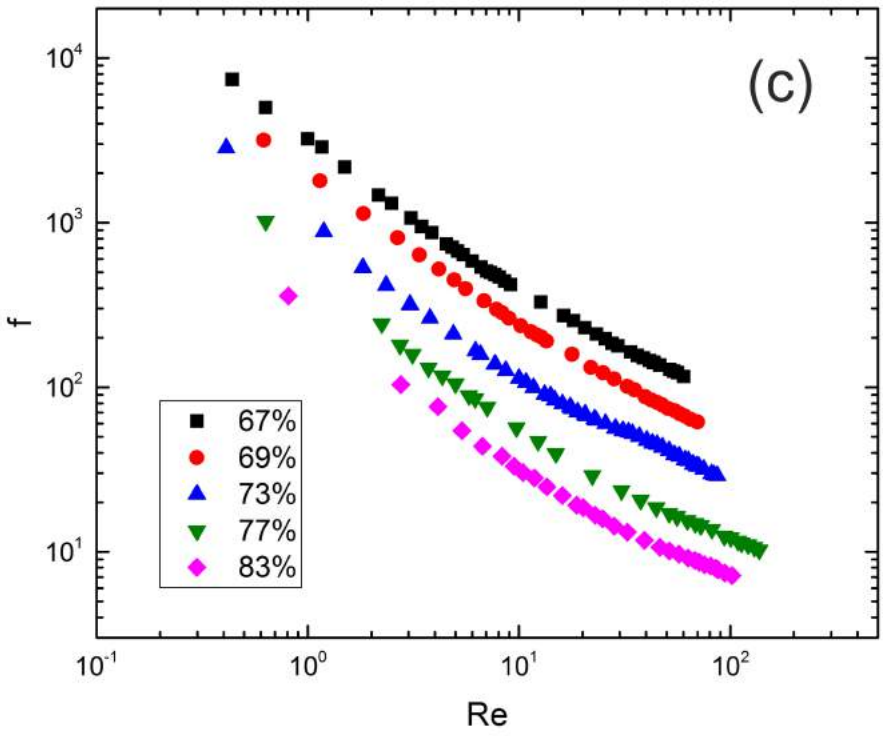

Figure 4.50: (continued) Effect of porosity on friction factor in various porous meida. (a) Porous glass sample with spherical pores, (b) porous glass sample with irregular pores and (c) porous copper samples.

and pore shape) and fluids (water and air). In this comprehensive comparison, the friction factor was found to follow 1/Re for all experimental data. This is because the square root of permeability was used as the characteristic length in calculating Reynolds number, resulting in A = 1 in Eq. 4.3. What should be used as a characteristic length is still being debated. Bonnet et al. (2008) used cell diameter in place of the particle diameter in Ergun equation, while Sedghi-Asl et al. (2014) employed the reciprocal of the surface area density as the characteristic length. Pore size is a physical property of the porous medium, so it is more appropriate than permeability because its value is calculated by fitting experimental data. Therefore, the average pore diameter is used as the characteristic length in the present study.

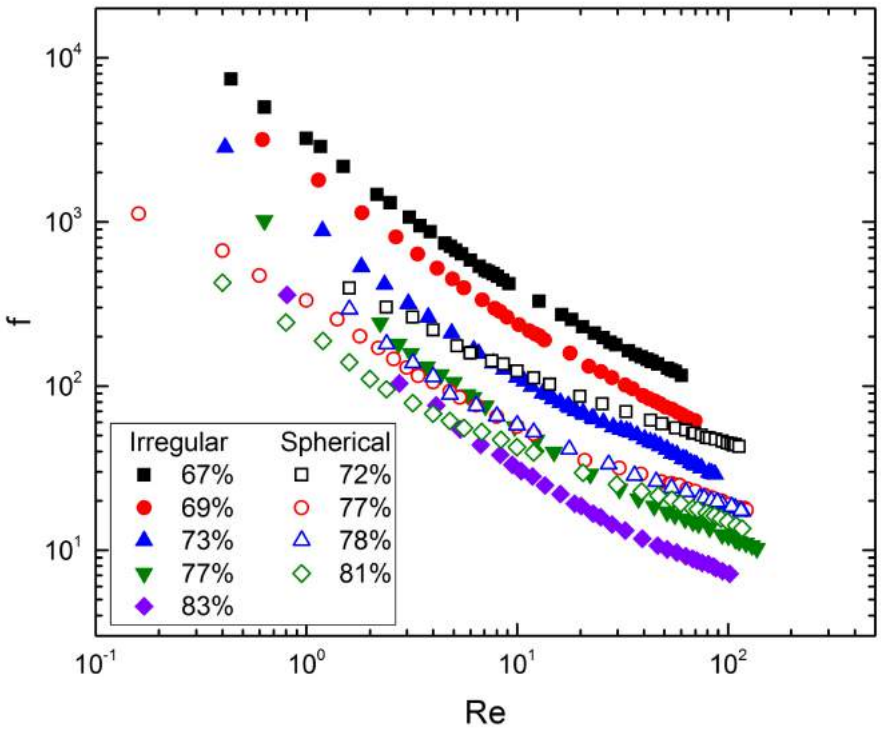

Figure 4.51: Effect of pore shape on friction factor in porous glass samples. The solid and hollow points are the results from the porous glass samples with irregular and spherical pores, respectively.

Fig. 4.51 shows the effect of pore shape on friction factor in porous glass samples. The effect of pore shape on friction factor can be divided into two parts: For a given porosity, the friction factor of the porous glass sample with spherical pores is lower than that with irregular pores at low Reynolds numbers ($\mathrm{Re} \lesssim 10$). At high Reynolds numbers ($\mathrm{Re} \gtrsim 10$), the opposite is true. This is because at low Reynolds numbers, the friction is mainly from viscous force and spherical pores exert less friction than irregular pores. At high Reynolds numbers, the inertial force begins to work and spherical pores have a higher form drag than the irregular pores.

The effect of matrix material on friction factor is shown in Fig. 4.52. On the whole, porous copper has higher friction factors at low Reynolds numbers, but lower fric-

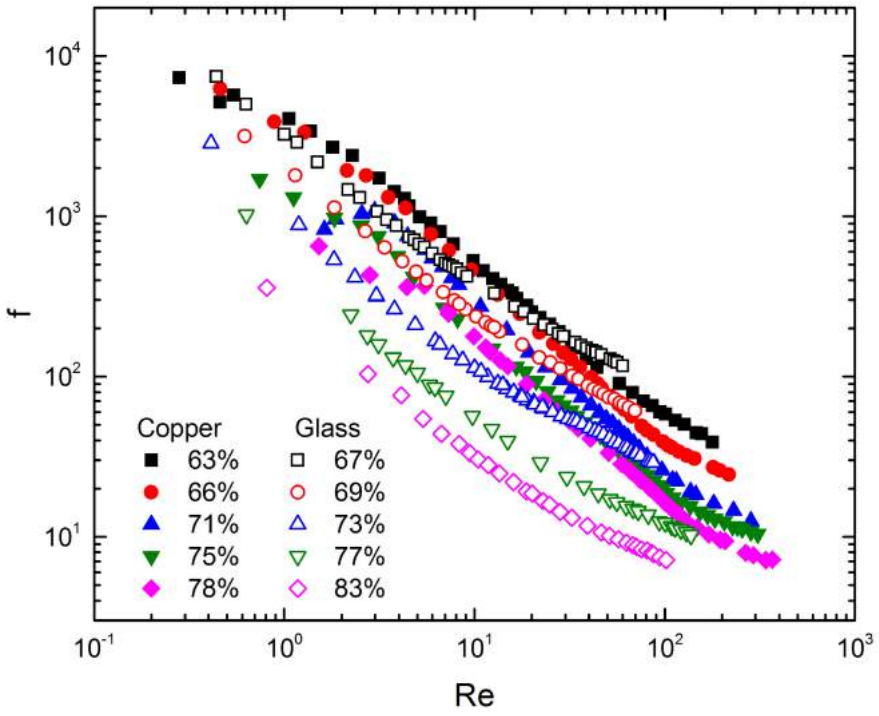

Figure 4.52: Effect of matrix material on friction factor. The solid and hollow points are the results from the porous copper and porous glass samples, respectively.

tion factors at high Reynolds numbers than porous glass. This is consistent with the two facts: (1) copper particle has a rougher surface than glass sphere, which has higher friction resistance at low Reynolds number; (2) porous copper sample have less secondary pores than porous glass samples, which has a lower form drag.

4.6 Summary

The fluid flow hydrodynamics of four types of pore media, sintered glass sample, porous glass sample with spherical and irregular pores, and porous copper sample were investigated. Pressure drop measurements and μ-PIV measurements were conducted on the first three types of porous media, and pressure drop measurements

were conducted on porous copper samples.

It is found that pressure drop increases with Re in all porous media. Pressure drop shows a linear relationship with Re at low Reynolds numbers and a non-linear relationship at high Reynolds numbers. Based on the relationship between reduced pressure drop and Reynolds number, four different flow regimes, pre-Darcy, Darcy, Forchheimer and turbulent, were identified in the sintered glass samples and porous glass samples. Three flow regimes, pre-Darcy, Darcy and non-Darcy, were found in the porous copper samples.

In sintered glass samples, Permeability increases with increasing particle size and form drag coefficient decreases sharply with increasing particle size. In porous glass and porous copper samples, permeability increases and the form drag coefficient decreases with increasing porosity.

The values of permeability and form drag coefficient also depends on which regime they are calculated from in porous media. In porous glass samples, the Darcy and Forchheimer regimes have the highest permeability, while the turbulent regime has the lowest permeability. In porous copper samples, the non-Darcy regime has the highest permeability and the Darcy regime has the lowest permeability. The value of the form drag coefficient in porous glass samples obtained from the Forchheimer regime is larger than that obtained from the turbulent regime. The influence of flow regime on permeability and form drag coefficient in sintered glass samples is not as obvious as that in porous glass and porous copper samples.

In the Darcy regime, the value of friction factor follow the function A/Re, where the

value of A depends on permeability and characteristic length of the sample. In the fully developed turbulent regime, the friction factor tends to be a constant, the value of which is related to form drag coefficient and characteristic length. For a given Reynolds number, the friction factor decreases with increasing porosity. Pore shape and matrix material also affect friction factor.

The μ-PIV measurements revealed the velocity and fluctuation distributions in the pores of porous media. Despite the considerable complexity of the pore space, the velocity profile shows a parabolic shape in the pre-Darcy, Darcy and Forchheimer regimes, and becomes much flatter in the turbulent regime. The velocity profiles in the Darcy and the Forchheimer regimes are similar and different from the velocity profiles in the pre-Darcy and the turbulent regimes.

The flow visualizations obtained from μ-PIV also demonstrated that, as the Reynolds number varies, different channels were involved in transporting fluid in the porous media and the flow path changed significantly. This can explain the fact that different flow regimes have different effective permeabilities due to these changes in the flow paths.

The μ-PIV measurements also quantified the velocity fluctuations characteristic of unsteady flow. The critical Reynolds number at the transition between laminar and turbulent flow can be identified. This compared very well with the critical Re between the Forchheimer and turbulent flow regimes identified from the pressure-drop measurements, confirming the conclusions made by Dybbs and Edwards (Dybbs & Edwards 1984) that both Darcy and Forchheimer are laminar flow.

The statistic analysis of the velocity components in the sintered glass samples showed that negative values in the longitudinal velocity component histogram are consistent with the occurrence of circulation in porous flow. The circulation only happens at high Reynolds numbers (after Forchheimer regime). The transverse velocity component histogram peaks at zero and is symmetric.

Chapter 5

Thermal performance of porous copper

5.1 Effective thermal conductivity of porous copper

The effective thermal conductivity in a porous Cu - fluid system is affected by three heat transfer mechanisms: solid conduction, fluid conduction and natural convection. Heat conduction through the solid phase in porous Cu is dependent on the fraction of the solid phase and the structure of the solid phase. Heat transfer through the fluid phase depends on the properties, principally the viscosity and thermal conductivity, and the motions of the fluid. The effects of fluid phase, porosity, pore size and copper particle size on the effective thermal conductivity of LCS porous copper are investigated in this section.

5.1.1 Effect of fluid phase on thermal conductivity

Effect of the fluid in the porous copper on the effective thermal conductivity of the porous copper system with various porosities and pore sizes are studied. Considering the poor connectivity and presence of isolated pores in low porosity porous samples, fluid contribution studies were only conducted in porous copper samples in the porosity range of 0.55 - 0.80.

Fig. 5.1 shows the effective thermal conductivity of different porous copper in vacuum, air and water as a function of porosity. For any given pore size and porosity, the sample under vacuum has the lowest effective thermal conductivity, while the porous Cu - water system has the highest. This is because in vacuum only the conduction through the solid framework contributes to heat transfer, while with the introduction of fluid, both the solid framework and the fluid contribute to heat transfer. The thermal conductivity of water is 0.6 W/mK, which is more than 20 times higher than the thermal conductivity of air. Therefore, it is not unexpected that the porous Cu - water system performed best among the three systems.

Fluid contribution to the overall thermal conductivity is greatly influenced by the porosity of the porous copper. The absolute contribution of fluid phase is defined as

$$\lambda_{cof} = \lambda_{Cu-f} - \lambda_v \tag{5.1}$$

where λ_{Cu-f} is the effective thermal conductivity of porous copper tested when saturated in water or air, λ_v is the effective thermal conductivity of the solid matrix tested in vacuum.

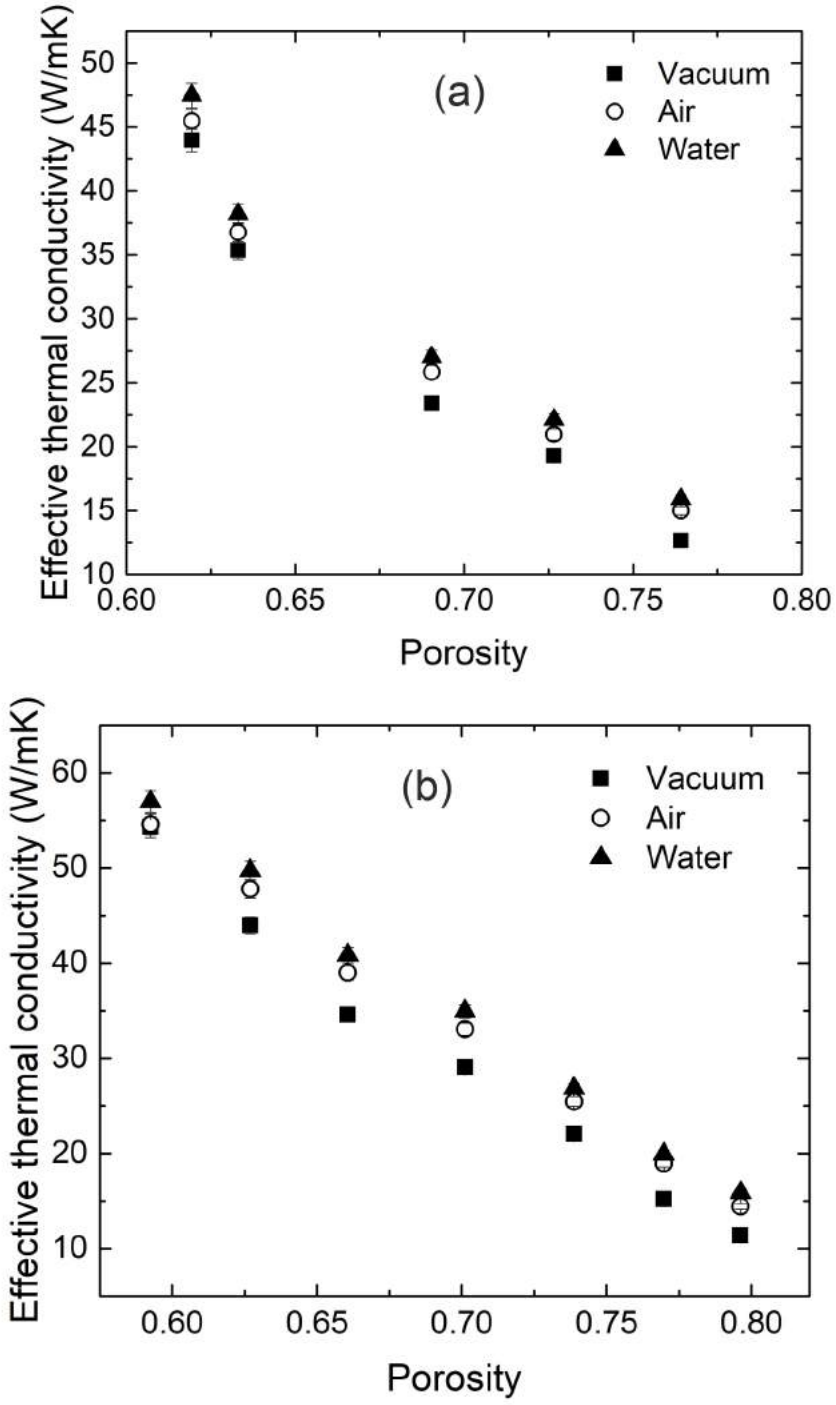

Figure 5.1: The effective thermal conductivity of porous copper samples with various porosities and pore sizes in differnt conditions (vacuum, air and water). Pore size range: (a) 250 - 425 μm, (b) 425 - 710 μm, (c) 710 - 1000 μm and (d) 1000 - 1500 μm. (to be continued)

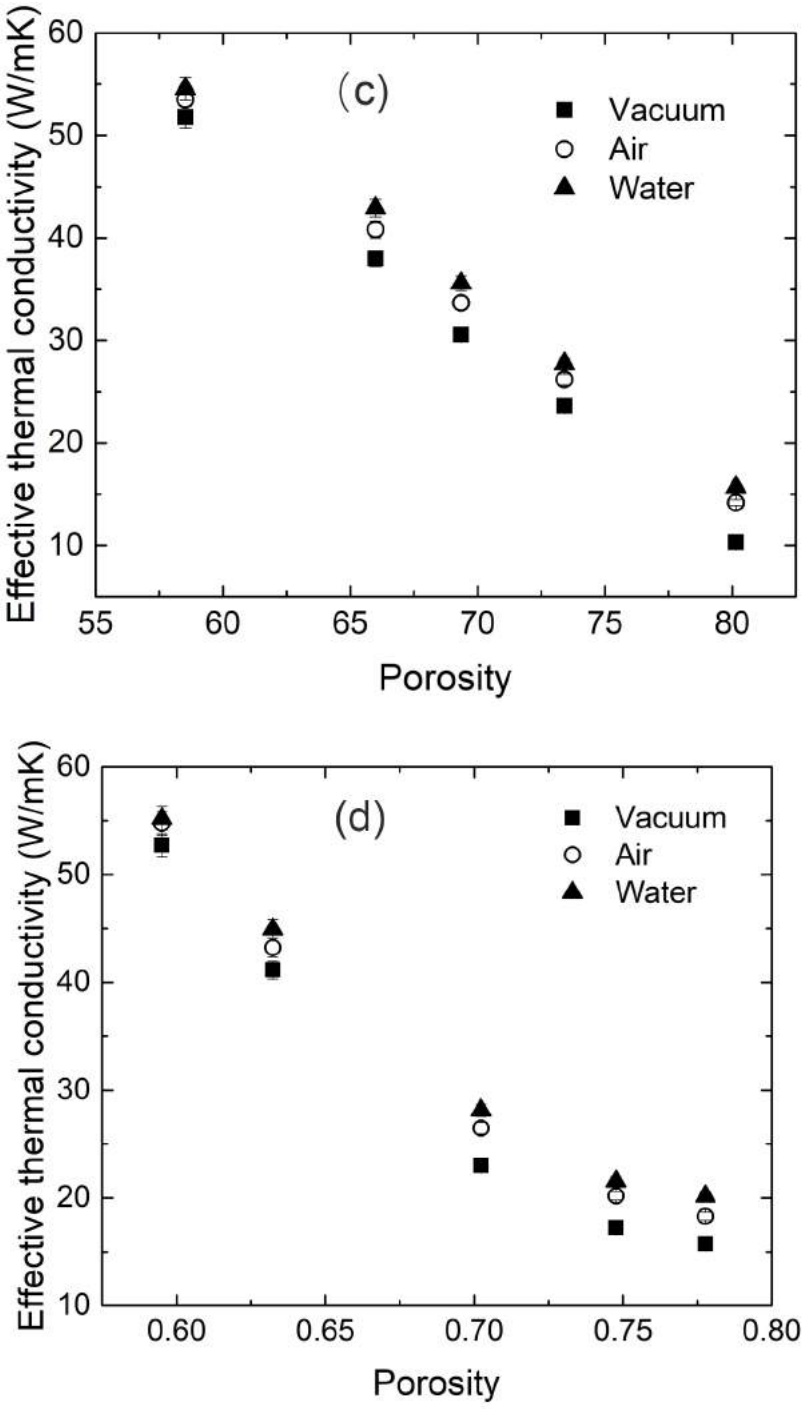

Figure 5.1: (continued) The effective thermal conductivity of porous copper samples with various porosities and pore sizes in differnt conditions (vacuum, air and water). Pore size range: (a) 250 - 425 μm, (b) 425 - 710 μm, (c) 710 - 1000 μm and (d) 1000 - 1500 μm.

The relative contribution of the fluid phase, or percentage contribution, can be defined as

$$\%contribution = \frac{\lambda_{Cu-f} - \lambda_v}{\lambda_{Cu-f}} \times 100 \tag{5.2}$$

Fig. 5.2 shows the absolute contribution of air or water to the effective thermal conductivity of the system at different porosities and pore sizes. The contribution of air or water is much greater than their thermal conductivity, which proves that the contribution is mainly made by convection. Fig. 5.2 also shows that the contribution of water is higher than that of air for all samples. For a given pore size, the effect of porosity on the contribution of fluid is insignificant.

Fig. 5.3 shows the relative contributions of air and water to the effective thermal conductivity of the porous Cu - fluid system at different porosities and pore sizes. It can be seen that the relative contribution of the fluid phase generally increases with porosity. For high porosity samples, such as the sample with a pore size range of 700 - 1000 μm and a porosity of 0.8, the contribution of water can reach 40%. However, for samples with porosities less than 0.65, the contribution is only about 5%. This is because the thermal conductivity of solid matrix is largely dependent on porosity, but fluid convection is less dependent on porosity.

The effect of pore size on the fluid contribution is analysed by the mean absolute contribution of each set of samples with the same pore size, calculated by averaging each sub-figure in Fig. 5.2. Fig. 5.4 shows the mean absolute contribution plotted against the pore size. The fluid contribution first increases with increasing pore size from 250 - 425 μm to 425 - 710 μm and then decreases with increasing pore size

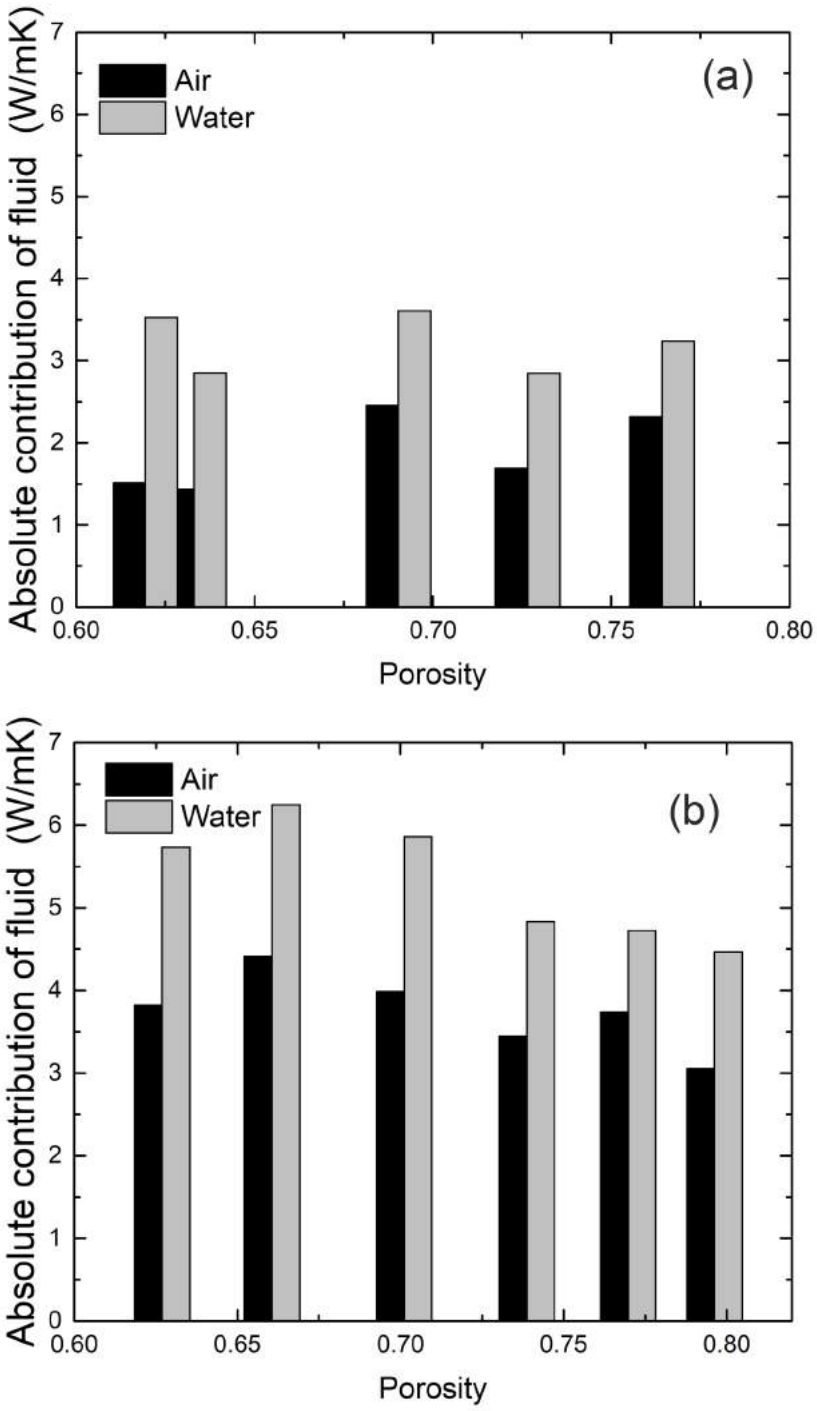

Figure 5.2: Contributions of air and water to the overall effective thermal conductivity at different porosities and pore sizes: (a) 250 - 425 μm, (b) 425 - 710 μm, (c) 710 - 1000 μm and (d) 1000 - 1500 μm. (to be continued)

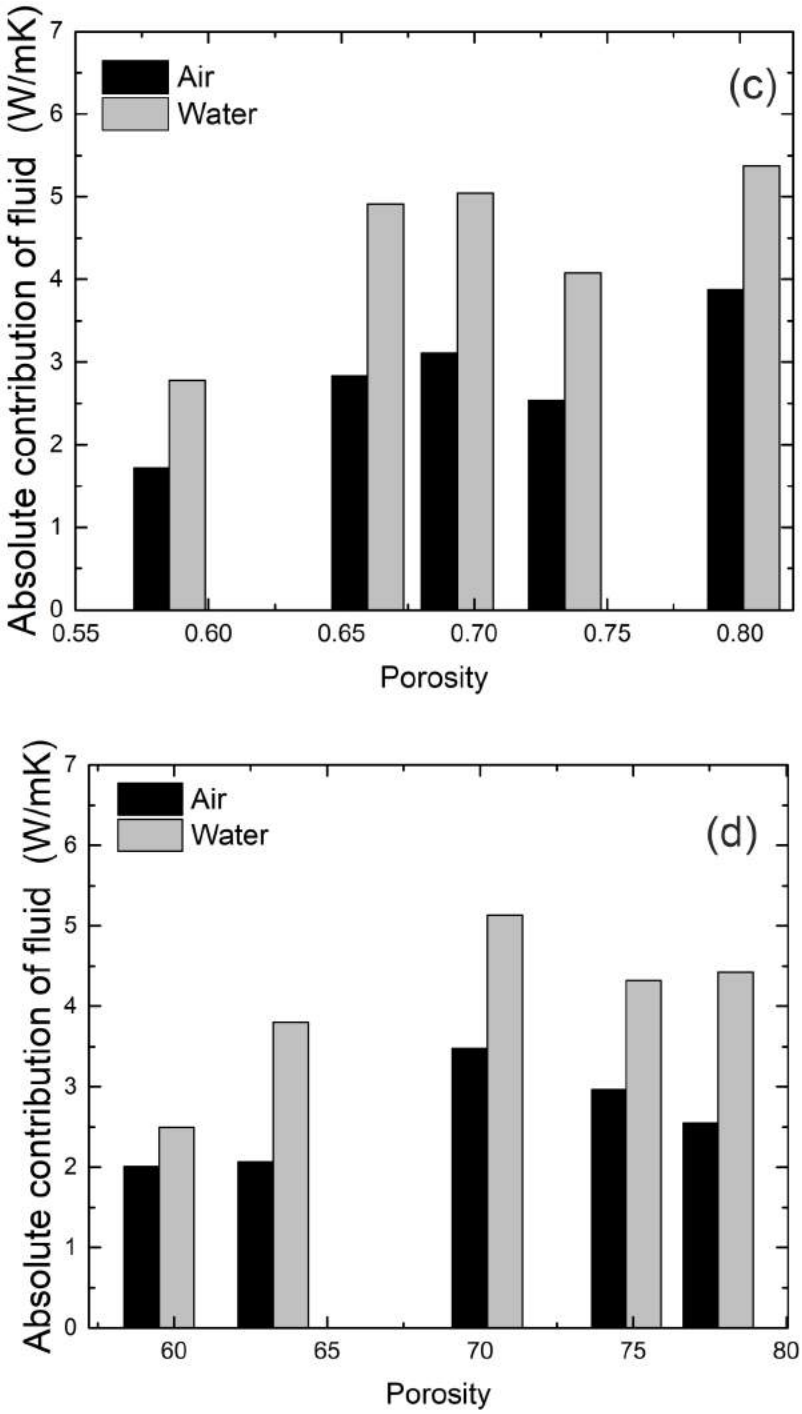

Figure 5.2: (continued) Contributions of air and water to the overall effective thermal conductivity at different porosities and pore sizes: (a) 250 - 425 μm, (b) 425 - 710 μm, (c) 710 - 1000 μm and (d) 1000 - 1500 μm.

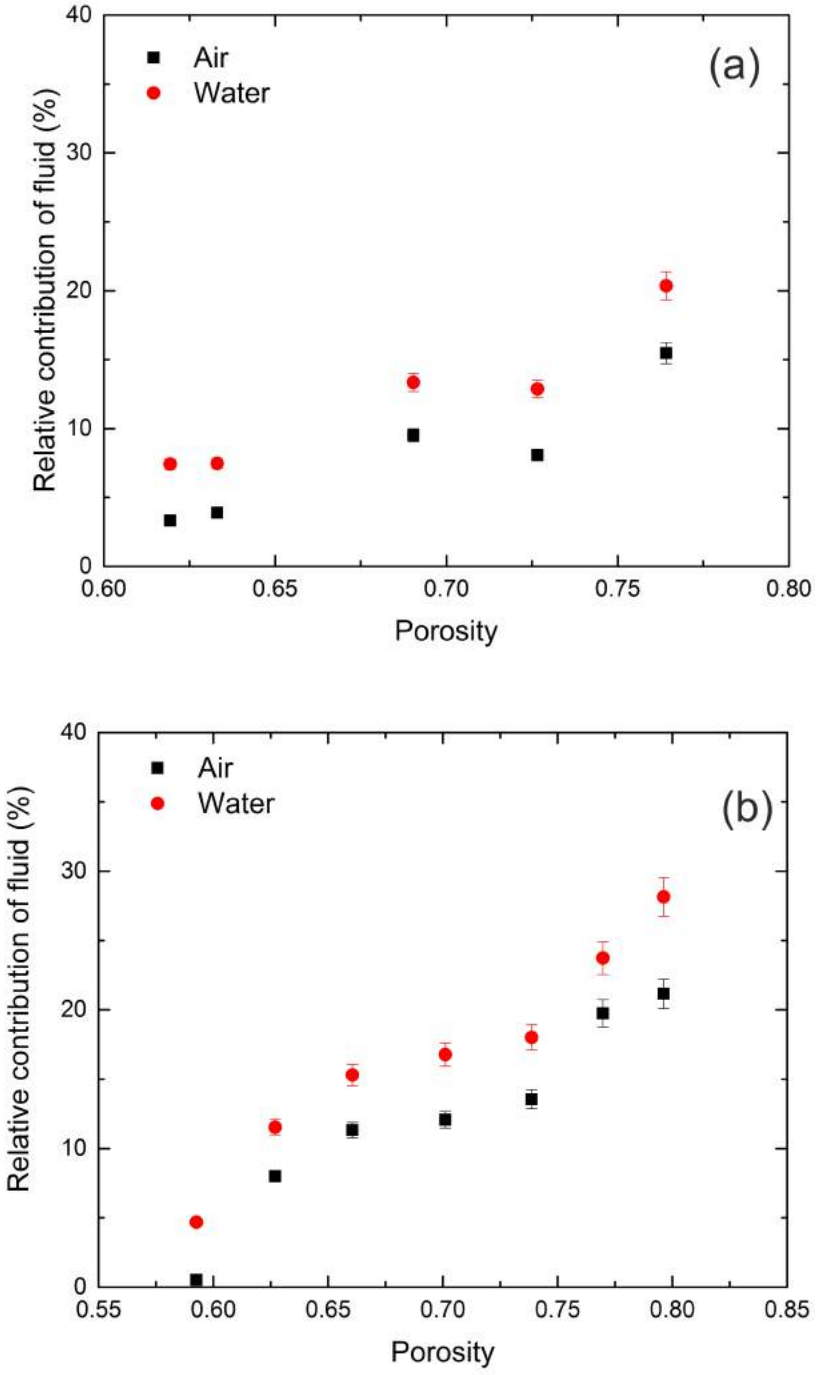

Figure 5.3: Relative contributions of air and water to the overall effective thermal conductivity at different porosities and pore sizes: (a) 250 - 425 μm, (b) 425 - 710 μm, (c) 710 - 1000 μm and (d) 1000 - 1500 μm. (to be continued)

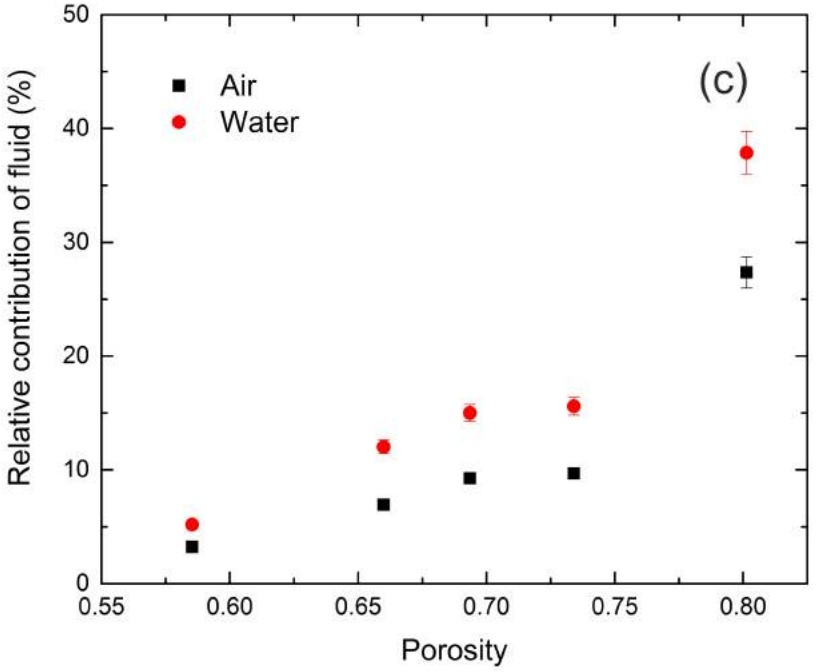

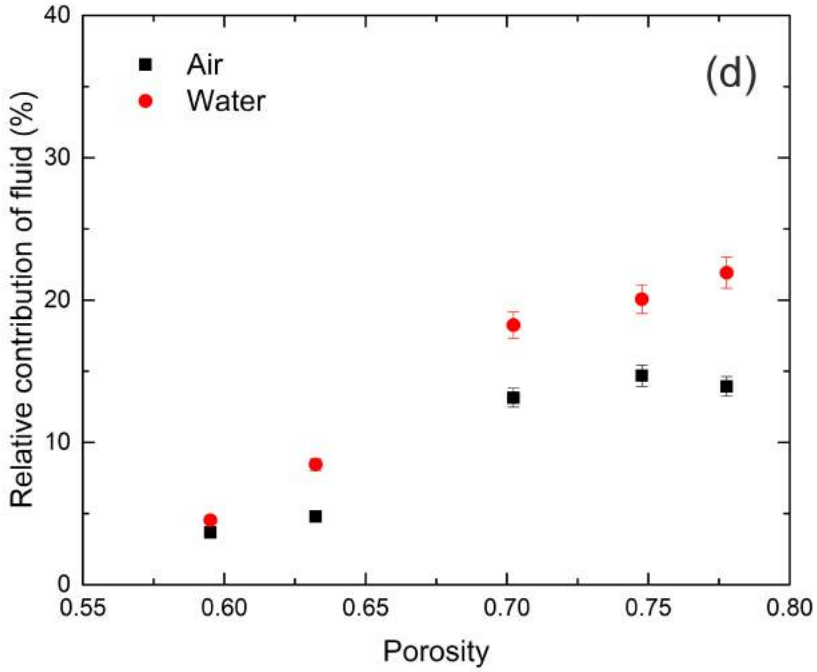

Figure 5.3: (continued) Relative contributions of air and water to the overall effective thermal conductivity at different porosities and pore sizes: (a) 250 - 425 μm, (b) 425 - 710 μm, (c) 710 - 1000 μm and (d) 1000 - 1500 μm.

further. The contributions of air and water have the same trend, both having the minimum and maximum values in the pore size ranges of 250 - 425 μm and 425 - 710 μm, respectively.

Pore size and pore density are normally negatively correlated for a given porosity. Although the porous copper samples with a pore size range of 250 - 425 μm have the highest pore density, which is advantageous for fluid convection, they also have the largest internal surface area and the narrowest channels, which increases the resistance for fluid flow significantly. The porous copper samples with a pore size range of 1000 - 1500 μm have the widest channels and smallest internal surface area, which reduce resistance for fluid movement. However, the low pore density means poor interaction between the fluid and solid phases, so convection is still limited. The porous copper samples with a pore size range of 425 - 710 μm are balanced between pore density and pore size, so they have the strongest fluid convection.

5.1.2 Effect of porosity and pore size on thermal conductivity

The thermal conductivity data of all porous copper samples tested in air are presented in a single plot in Fig. 5.5 to explore the effect of pore size and porosity on the thermal conductivity. The effect of pore size on overall thermal conductivity is negligible, which is consistent with previous observations and experimental results (Bhattacharya et al. 2002, Paek et al. 2000). The effective thermal conductivity decreases sharply as the porosity increases.

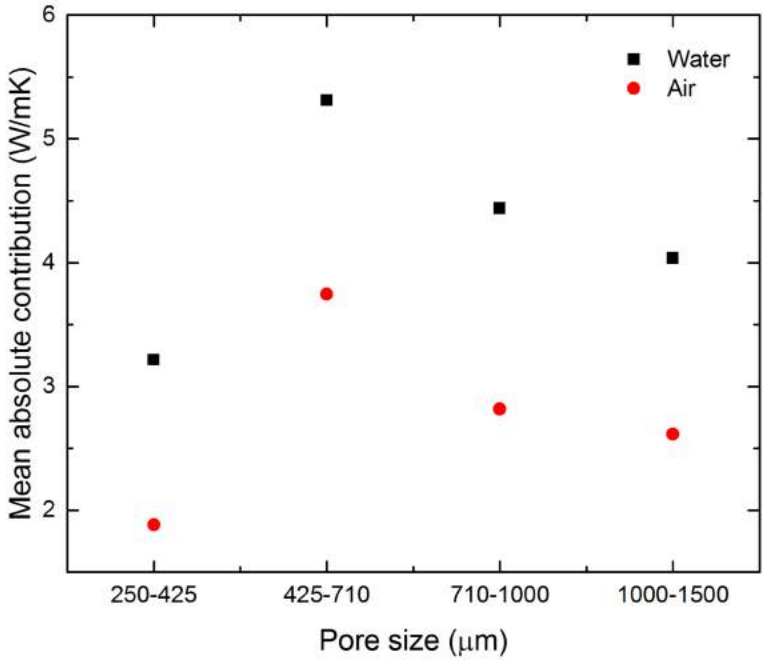

Figure 5.4: Effect of pore size on fluid contribution to the overall thermal conductivity.

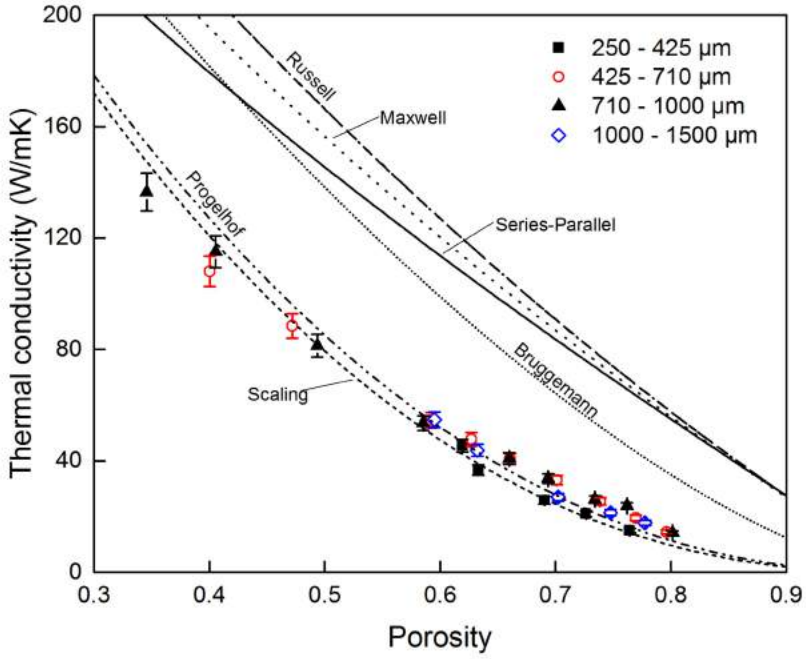

Figure 5.5: Comparison of various thermal conductivity models with experimental data in air condition.

Some empirical and analytical models are summarized and plotted in order to investigate the correlation between porosity and thermal conductivity of porous Cu. These correlations were based either on a composite materials or on a porous metal-fluid system. The common feature for these correlations is that only three parameters are involved: thermal conductivity of the metal used to make the solid framework, λ_s, thermal conductivity of the trapped fluid, λ_f, and the porosity, ϵ, or the relative density of the porous metal, ρ_p/ρ_s, where ρ_p and ρ_s are the densities of porous metal and bulk metal, respectively.

Table 2.2 lists seven of the most referred correlations in the literature. Coincidentally, the Parallel-Series (Leach 1993) and Russell models (Russell 1935) have the same effective thermal conductivity for a given porosity and therefore only six curves are visible in Fig. 5.5. Fig. 5.5 shows that most existing correlations have overestimated the effective thermal conductivity of the porous copper sample. Progelhoff and power law models fit well with the present experimental results.

The power law model can be viewed as a special case of the Progelhoff model, where the solid-to-fluid conductivity ratio is so high that the contribution of fluid phase can be neglected. The power law model suggests a value of n in the range of 1.65 to 1.85, while the Progelhoff model recommends a n of 1.55. In the present study, the value of n for both correlations is around 2.3, which implies a smaller thermal conductivity than the suggested n. This may be attributed to the large quantity of sintering defects in porous copper. The sintered necks are quite small compared to the copper particle diameter, as can be seen from Fig. 5.6. These sintered defects increase the thermal resistance significantly compared with foams fabricated with fluid phase methods (Banhart 2001).

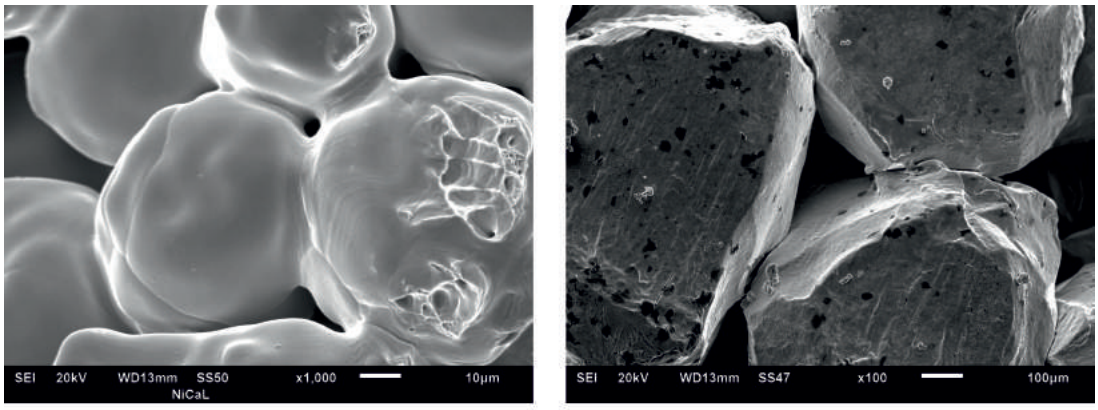

Figure 5.6: Quality of sintered necks for copper particles with different characteristics: (a) shperical particles with diameters of 45 - 70 μm and (b) non-spherical particles with equivalent diameters of 710 - 1000 μm.

5.1.3 Effect of Cu particle size on thermal conductivity

The thermal conductivity of sintered copper samples with various particle size ranges is shown in Fig. 5.7. The left y-axis indicates the absolute thermal conductivity, while the right y-axis indicates the relative thermal conductivity (the ratio of thermal conductivity of sintered Cu to that of pure Cu). The relative thermal conductivity of sintered Cu sample locates between 0.5 and 0.7, which is very low for the relative density of the sintered Cu packed beds (0.85 - 0.89). It can be seen that as the copper particle size increases, the thermal conductivity first increases and then decreases. The sintered Cu sample with the particle diameter range of 45 - 70 μm has the highest thermal conductivity, about 280 W/mK, while the sintered Cu sample with the largest copper particles shows the lowest thermal conductivity, only 208 W/mK.

The large differences in thermal conductivity of sintered copper samples having dif-

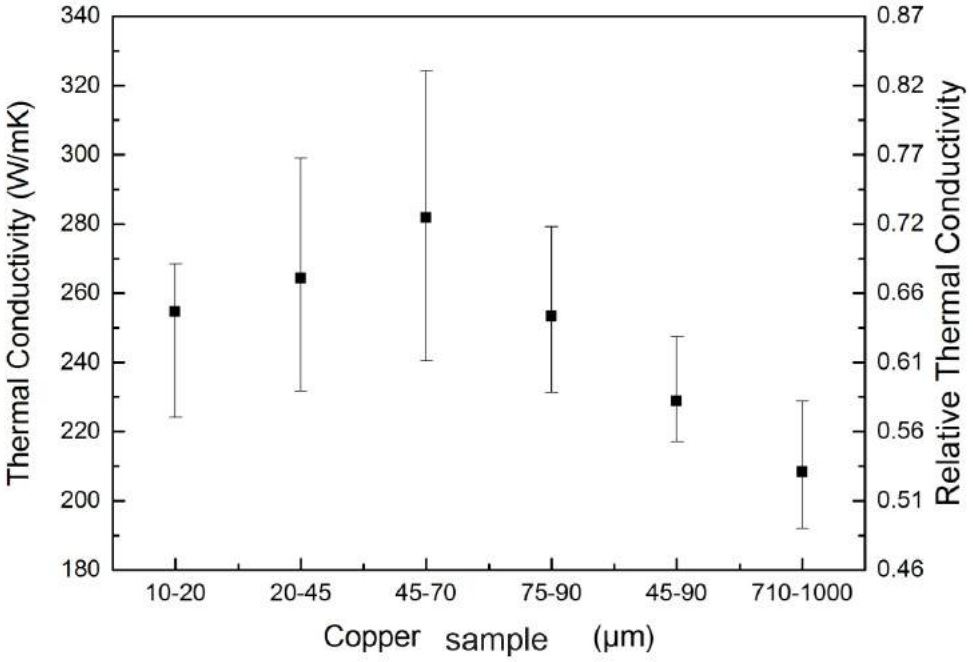

Figure 5.7: Thermal conductivity of sintered copper samles with various copper particle sizes.

ferent Cu particle sizes are likely caused by different quantity and quality of sintered necks. The sintering quality of necks is generally affected by various factors such as oxide film, lubricant, compacting pressure, sintering parameters (temperature and time) and copper particle characteristics (particle size and shape) (Upadhyaya 1997). The quantity of sintered necks is highly dependent on the powder characteristics. In this study, all the processing parameters and sintering parameters were kept the same for all samples and only the particle size was varied. It is well known that smaller spherical particles have a higher surface energy, which promotes sintering and thus the neck quality. Fig. 5.6 shows the sintered neck qualities for different particle sizes and shapes. For the small copper particles (Fig. 5.6 a), it can be seen that they have relatively large necks due to the high surface energy. However, for large non-spherical copper particles, the sintered necks are much smaller, as shown

in Fig. 5.6(b).

Although the high surface energy of fine particles promotes the formation of sintered necks, fine particles introduce more sintered necks than coarse particles in comparison to bulk Cu inside the particles, which can increase the thermal resistance. Therefore, the sintered Cu sample with a particle size of 45 -70 μm has a good balance between neck quality and quantity and shows the best thermal conductivity.

5.2 Heat transfer performance of porous copper under natural convection

The natural convective heat transfer performance of porous copper with various porosities and pore sizes was investigated in this part. The effects of porosity, pore size and orientation were discussed separately in the following sections. The results were compared with existing data and theory.

5.2.1 Effect of porosity on natural convective heat transfer coefficient

Samples with four fixed pore sizes but various porosities from 0.65 to 0.85 were compared to quantify the effect of porosity on natural convective heat transfer coefficient. Fig. 5.8 plots the Nusselt number of porous copper samples with various porosities and pore sizes, tested at horizontal direction, as a function of Rayleigh number. The Nusselt number was calculated from the convective heat transfer coefficient as

follows:

$$Nu = \frac{hL}{k_f} \tag{5.3}$$

where h is the convective heat transfer coefficient, L is the length of the heated section of the porous copper sample in the mean flow direction and k_f is the thermal conductivity of fluid, i.e. water in the present study.

The Rayleigh number is defined as

$$Ra = \frac{g\rho\beta\Delta T D^3}{\alpha\mu} \tag{5.4}$$

where g is gravity acceleration, α is thermal diffusivity of the fluid, β is thermal expansion coefficient of fluid, μ is dynamic viscosity of fluid, ΔT is temperature difference and D is the mean diameter of pores.

Fig. 5.8 shows that the Nusselt number increases with increasing Rayleigh number. For the samples investigated, the optimum porosities for pore size ranges of 250-425 μm, 425-710 μm, 710-1000 μm and 1000-1500 μm are 0.70/0.75, 0.71/0.77, 0.66 and 0.67, respectively. It is found that the sample with the highest porosity has the worst natural convective heat transfer performance among the samples with the same pore size. In addition, except for the sample with the highest porosity, the other samples have a similar performance.

The relationship between Nu and Ra was correlated according to eq. 2.11 and 2.12 (Nield et al. 2006). Since some data are very close, only three correlation lines are

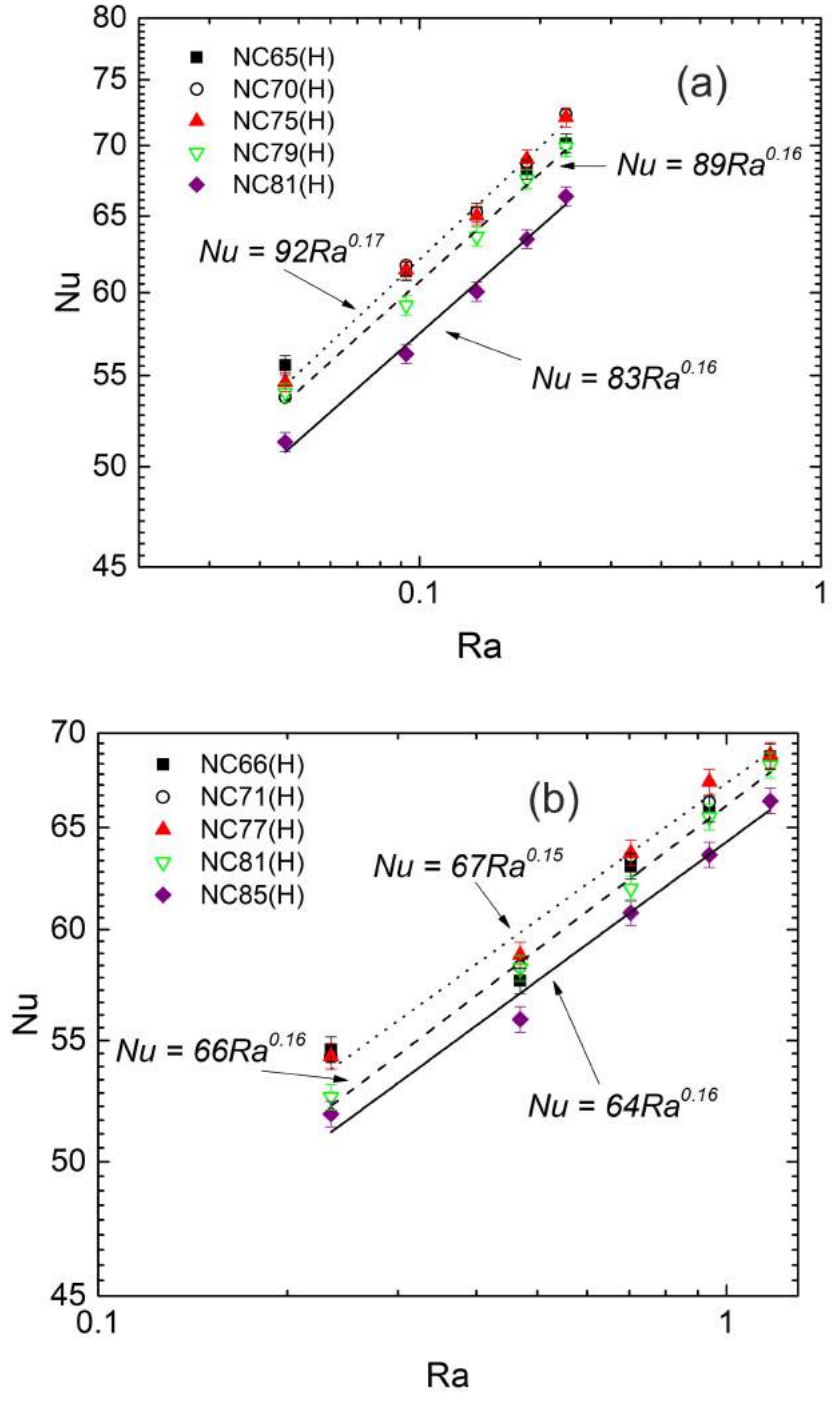

Figure 5.8: Nusselt number plotted as a function of Rayleigh number for porous copper samples at horizontal orientation (the values in the legend represent the porosity of samples). Pore size range: (a) 250 - 425 μm, (b) 425 - 710 μm, (c) 710 - 1000 μm and (d) 1000 - 1500 μm. (to be continued)

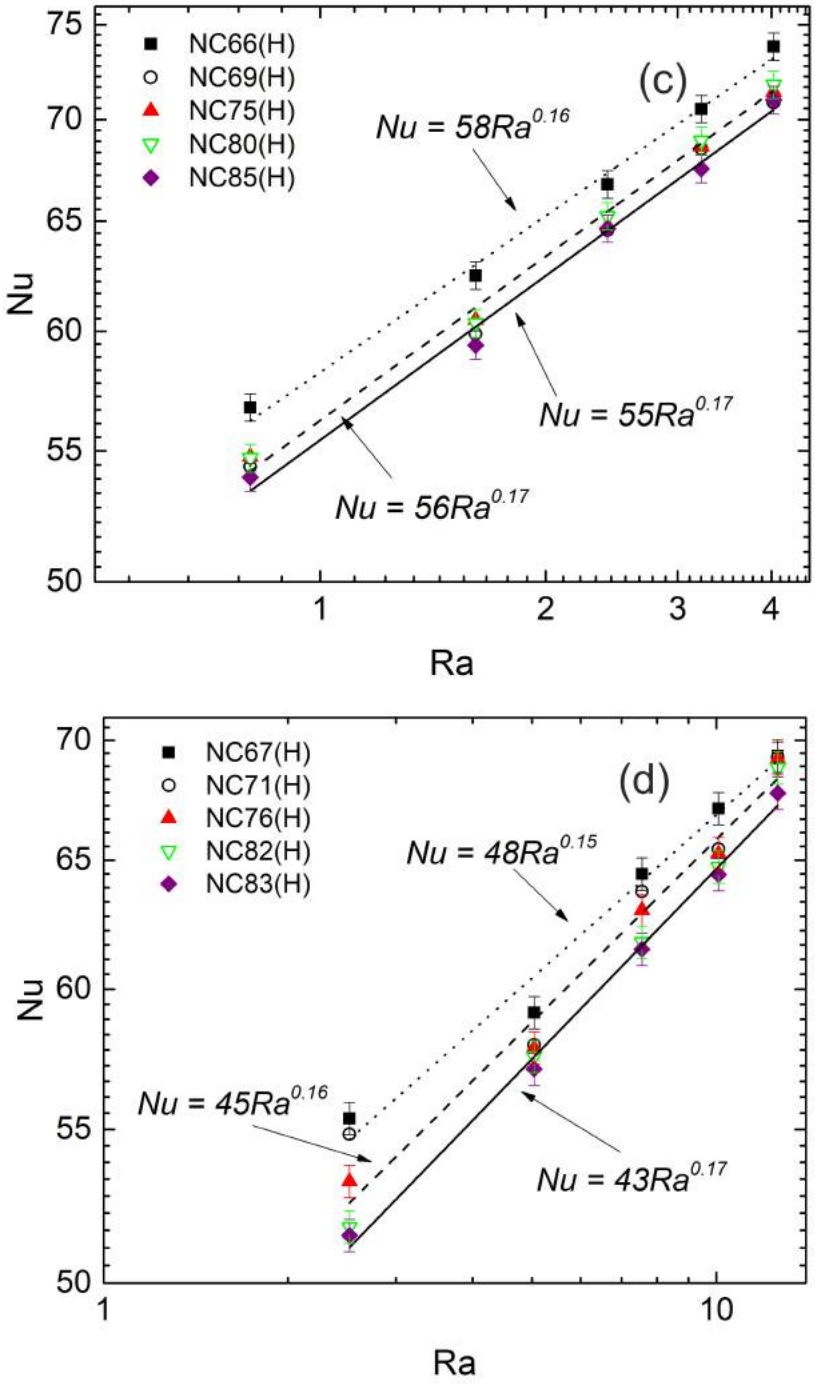

Figure 5.8: (continued) Nusselt number plotted as a function of Rayleigh number for porous copper samples at horizontal orientation (the values in the legend represent the porosity of samples). Pore size range: (a) 250 - 425 μm, (b) 425 - 710 μm, (c) 710 - 1000 μm and (d) 1000 - 1500 μm.

presented in each subfigure in Fig. 5.9. The experimental data agrees well with the power law model, $Nu = C_T Ra^n$, with an exponent value around 0.16. The present exponent is very different from that suggested by the reference Nield et al. (2006). The difference can be caused by the different porous structure in porous medium and different characteristic length in the definition of Rayleigh number. The mean value of factor C_T decreases as pore size increases.

Fig. 5.9 shows the convective heat transfer coefficient as a function of porosity at various temperature differences in order to show the effect of porosity better. It shows that at low porosity (< 0.75), the effect of porosity on heat transfer coefficient is insignificant, while at high porosity, the heat transfer coefficient drops quickly with increasing porosity. Fig. 5.9 also shows that the dependence of heat transfer coefficient on temperature difference decreases with increasing temperature. Take Fig. 5.9(a) as an example, heat transfer coefficient increases by about 4.5 W/m^2K when the temperature difference is increased from 10 K to 20 K, but only by about 2.0 W/m^2K when the temperature difference is increased from 40 K to 50 K. This is because the amount of air entering the porous copper decreases as temperature increases, which weakens the interaction between the air and the solid matrix.

The heat transfer path in the test assembly consists of two parts: heat conduction from the heat source to the solid copper matrix and heat convection from the solid framework to air. Heat conduction mainly depends on the thermal conductivity of the porous sample (solid framework), while convection depends on both the pore space and the internal surface area within the porous sample. Therefore, any of the above factors may affect the cooling performance of porous copper.

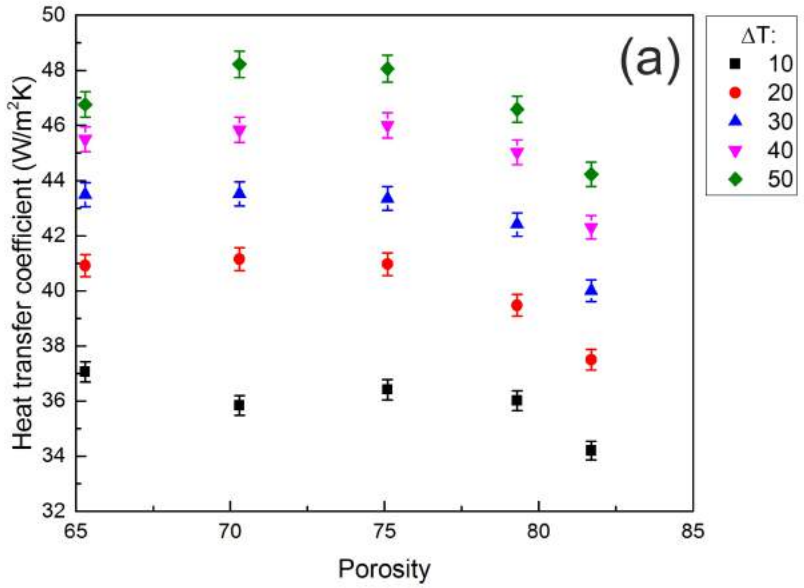

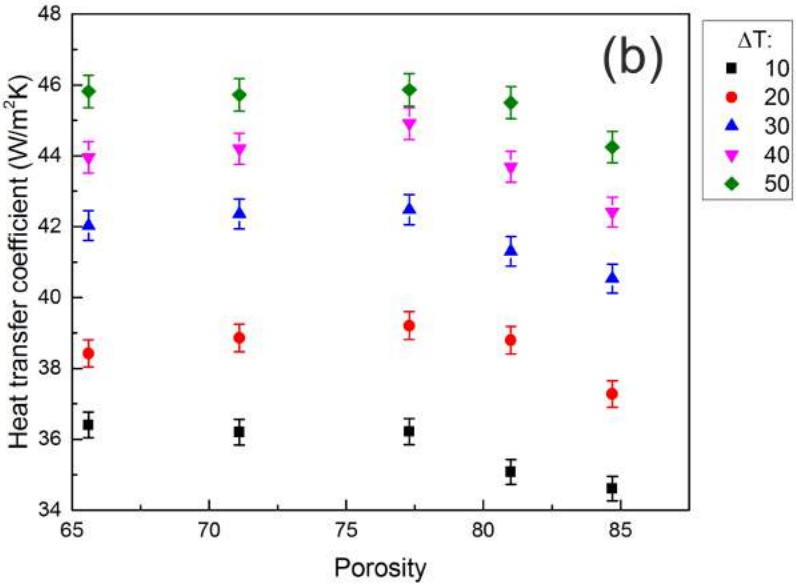

Figure 5.9: Natural convective heat transfer coefficient as a fucntion of porosity at various temperature differences (horizontal orientation). Pore size range: (a) 250 - 425 μm, (b) 425 - 710 μm, (c) 710 - 1000 μm and (d) 1000 - 1500 μm. (to be continued)

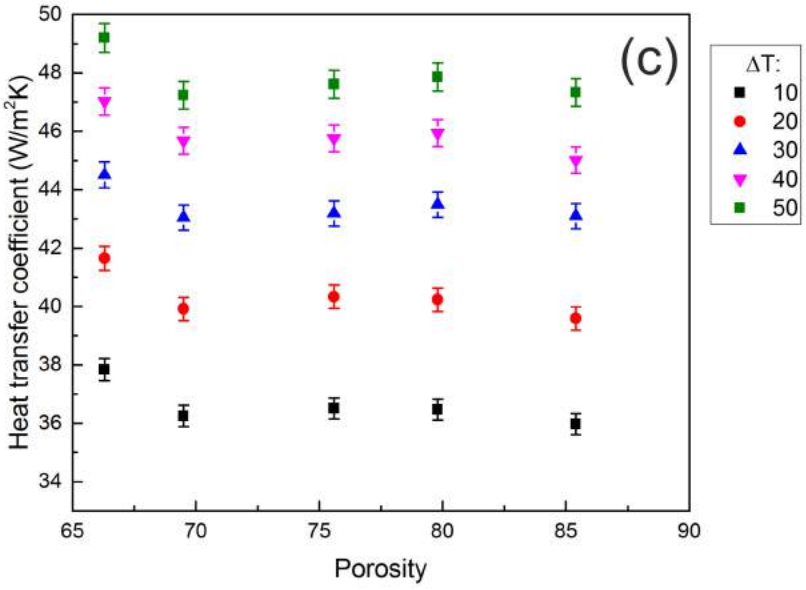

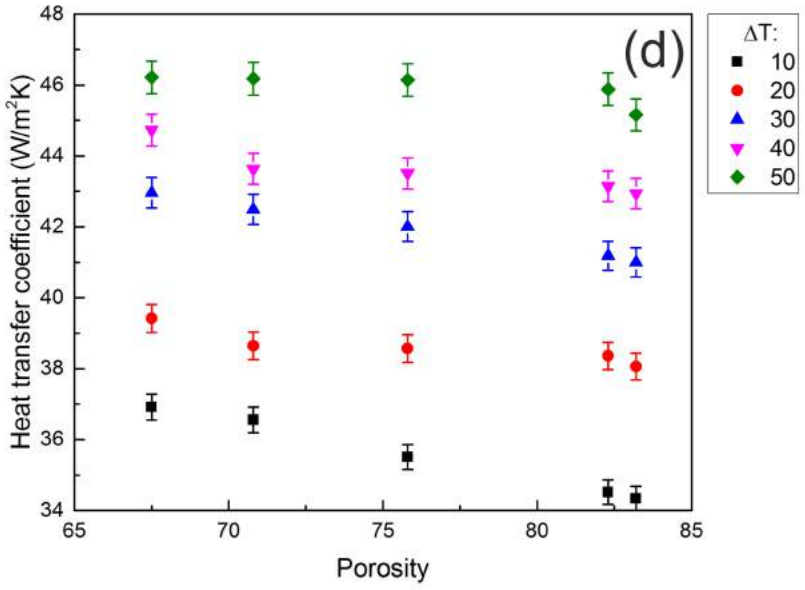

Figure 5.9: (continued) Natural convective heat transfer coefficient as a fucntion of porosity at various temperature differences (horizontal orientation). Pore size range: (a) 250 - 425 μm, (b) 425 - 710 μm, (c) 710 - 1000 μm and (d) 1000 - 1500 μm.

Present (see section 5.1) and previous studies (Thewsey & Zhao 2008, Solórzano et al. 2008, Ashby et al. 2000) investigated the heat conduction in porous metal and found that thermal conductivity decreases exponentially with increasing porosity. According to our experiment, the value of exponent is around 2.3 for porous copper manufactured by the LCS process, which is larger than porous metal made by fluid phase processes (Banhart 2001). This means that the thermal conductivity is more dependent on porosity for LCS porous copper samples. For example, the thermal conductivity of porous copper sample with a porosity of 0.65 is about 40 W/mK, which is approximately 8 times higher than that of a sample with a porosity of 0.85 (see Fig. 5.5).

Although low porosity samples have higher thermal conductivity, the limited pore space within the low porosity samples is not conducive to convection. The low porosity samples also have lower fluid permeability than the high porosity samples, which increases the resistance of fluid entering the porous samples. Therefore, samples with balanced thermal conductivity and convection, e.g., samples with porosities around 0.75 for pore size ranges of 250-425 μm and 425-710 μm, show best natural heat dissipation performance. Samples with pore size ranges of 710-1000 μm and 1000-1500 μm show some deviations because of the effect of pore size, which will be discussed in the next section.

5.2.2 Effect of pore size on natural convective heat transfer coefficient

Fig. 5.10 compares the natural convective heat transfer coefficients of porous copper samples with a similar porosity but different pore sizes at various temperature differences. The samples with pore size of 1000 - 1500 μm have the worst heat transfer performance for all the porosities. The samples having the pore size of 710 - 1000 μm exhibit the best performance for porosities of 0.65, 0.80 and 0.85, while the samples having the pore size of 250 - 425 μm exhibit the best performance for porosities of 0.70 and 0.75. Among the four pore size ranges studied, the effect of pore size on natural convective heat transfer coefficient is not significant as the largest difference between any two samples is less than 10%.

Since the effect of pore size on thermal conductivity is negligible (Fig. 5.5), the pore size affects convection mainly by altering the internal surface area of the porous sample (Diao et al. 2015). For a fixed porosity, a sample with a pore size of 250 - 425 μm has a volumetric surface area 4 times of that of a sample with a pore size of 1000 - 1500 μm (Diao et al. 2015). Furthermore, the small pore structures have lower tortuosity and higher permeability than large pore structures (Diao et al. 2017), i.e., lower flow resistance for fluid in the sample. Therefore, the samples with pore size of 250 - 425 μm show the best for the porosities of 0.70 and 0.75. However, samples with very low (0.65) or very high (0.8 and 0.85) porosities, the effect of thermal conductivity of the solid matrix play an dominant role for the overall heat transfer performance. Therefore, the effect of pore size is not significant for samples within these porosity ranges.

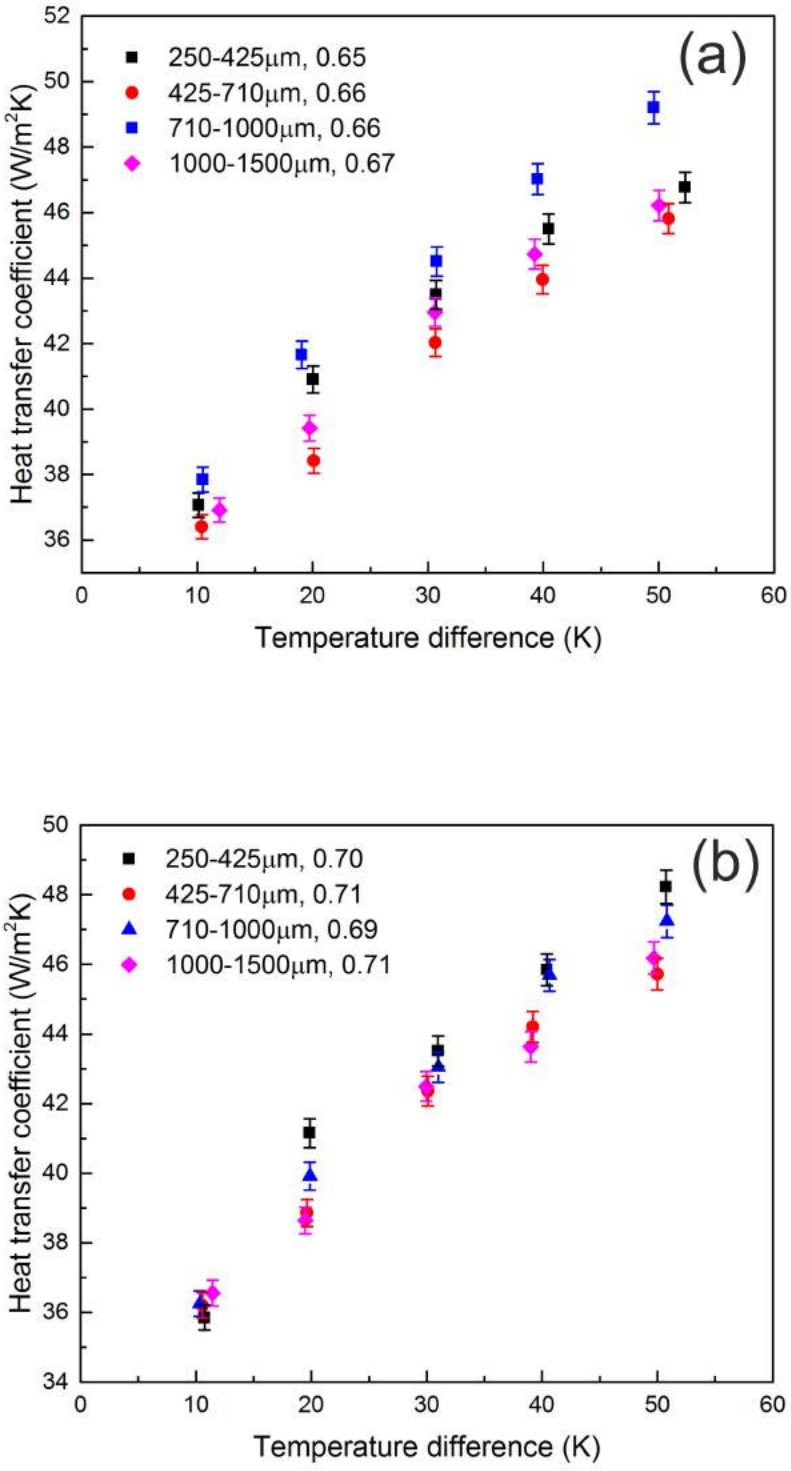

Figure 5.10: Natural convective heat transfer coefficient of sample with similar porosity but different pore sizes plotted as a function of temperature differemce (horizontal direction). (to be continued)

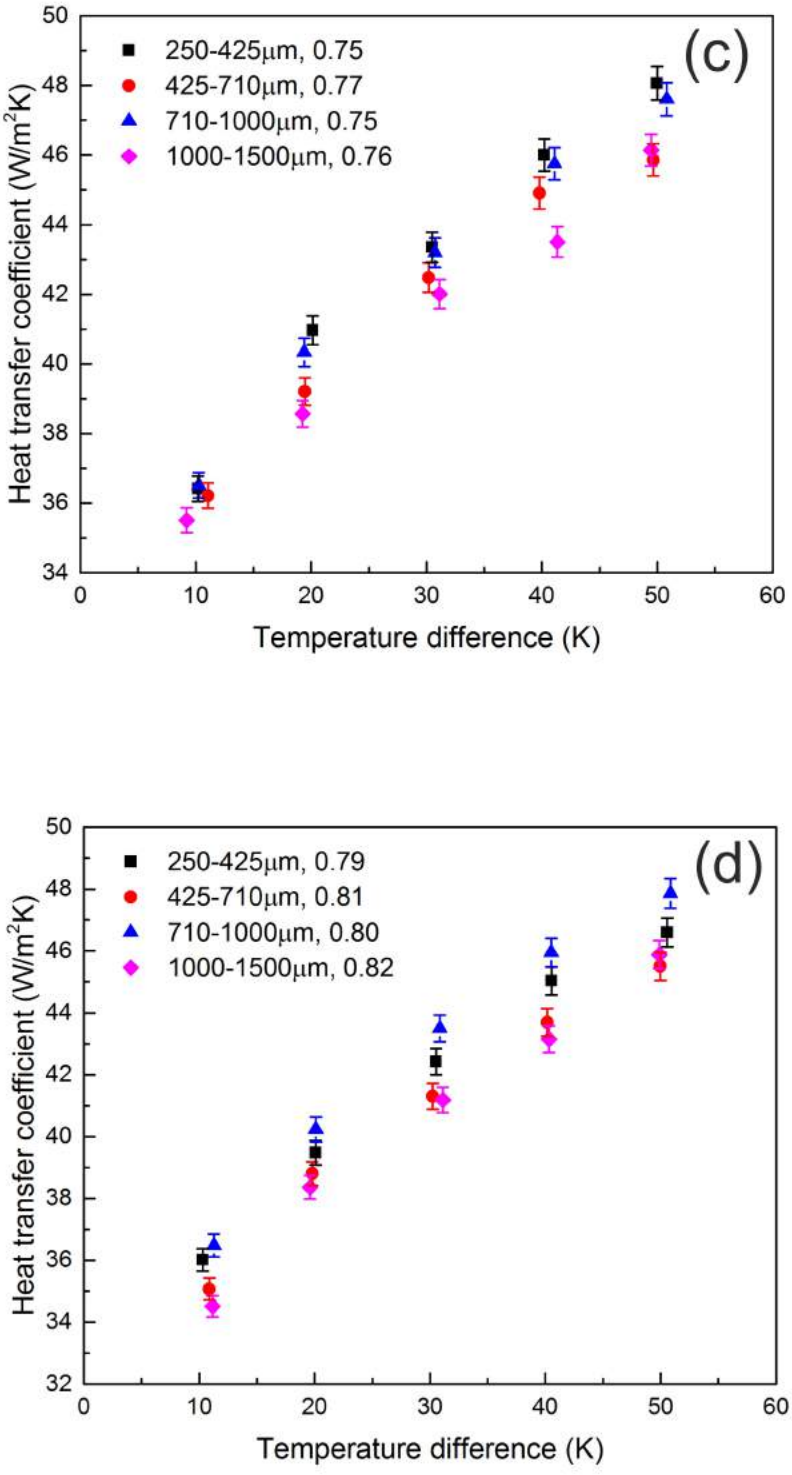

Figure 5.10: (continued) Natural convective heat transfer coefficient of sample with similar porosity but different pore sizes plotted as a function of temperature differemce (horizontal direction). (to be continued)

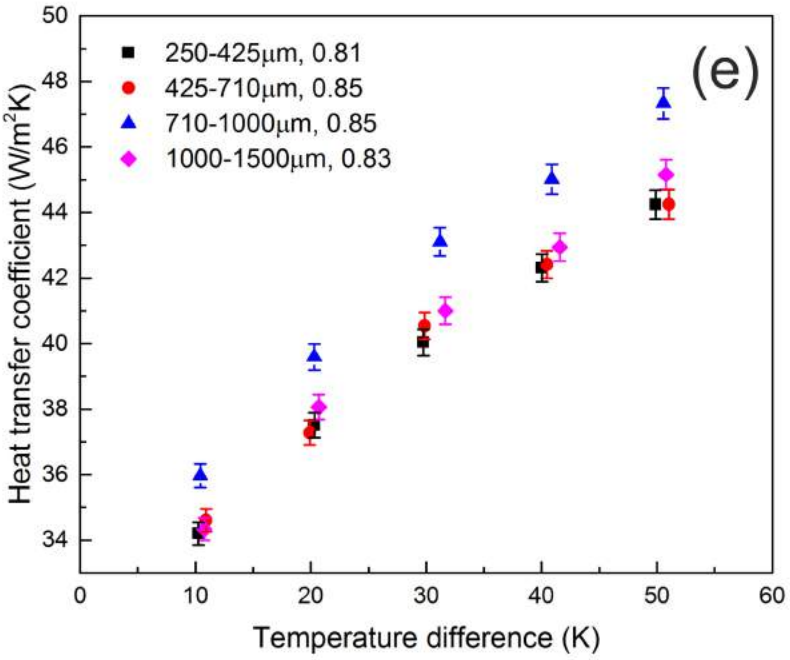

Figure 5.10: (continued) Natural convective heat transfer coefficient of sample with similar porosity but different pore sizes plotted as a function of temperature differemce (horizontal direction).

5.2.3 Effective of orientation on natural convective heat transfer coefficient

Fig.5.11 compares the Nusselt number of selected porous copper samples with different porosities and different pore size ranges measured at horizontal and vertical orientations. The experimental data were correlated with the power law equation and the equations are presented in subfigures. It is found that the data agree well with the power law in both horizontal and vertical orientations, but the values of exponent and factor are different. The present conclusions agree well with what Nield et al. (2006) suggested that the relationship between Nu and Racan be correlated with a similar equation.

As expected, the heat transfer coefficient measured in the vertical orientation is higher than that in the horizontal orientation. However, at low Ra (about 10K and 20K), for samples with pore sizes of 250 - 425 μm and 425 - 710 μm, the Nu of the two directions are similar.

The above results can be explained by the different flow behaviours in the two directions. Heated air always rises in the opposite direction to gravity regardless of the orientation of the porous sample. In the horizontally placed sample, the hot air in the sample rises from the upper surface due to buoyancy force. Cold air around the sample is drawn into the sample from the four vertical surfaces to balance the pressure differential and form a stable circulation system. However, it may be difficult for cold air to reach the centre region (15 mm from the surface) of the sample because the air rises immediately after being heated in the edge region. Therefore, the contributions of the edge and center regions to the heat transfer are different in the horizontal orientation. Similar flow behaviour can be found in the vertically positioned sample. In the vertical orientation, more area within the sample is involved for convective heat transfer. Cold air enters from the bottom and side surfaces and the hot air flows out from the upper surface. In this case, the air can pass through the entire sample when it enters from the bottom surface.

Although the vertically positioned samples are able to let air pass through the whole porous sample, small pore sizes and low temperature differences can still make it hard for air to pass through the porous structure. For samples with the pore size of 250 - 425 μm, the small pore size results in a very high flow resistance. At a small temperature difference, such as 10K and 20K, the driving force from temperature difference may not be great enough to drive air entering the center of the sample.

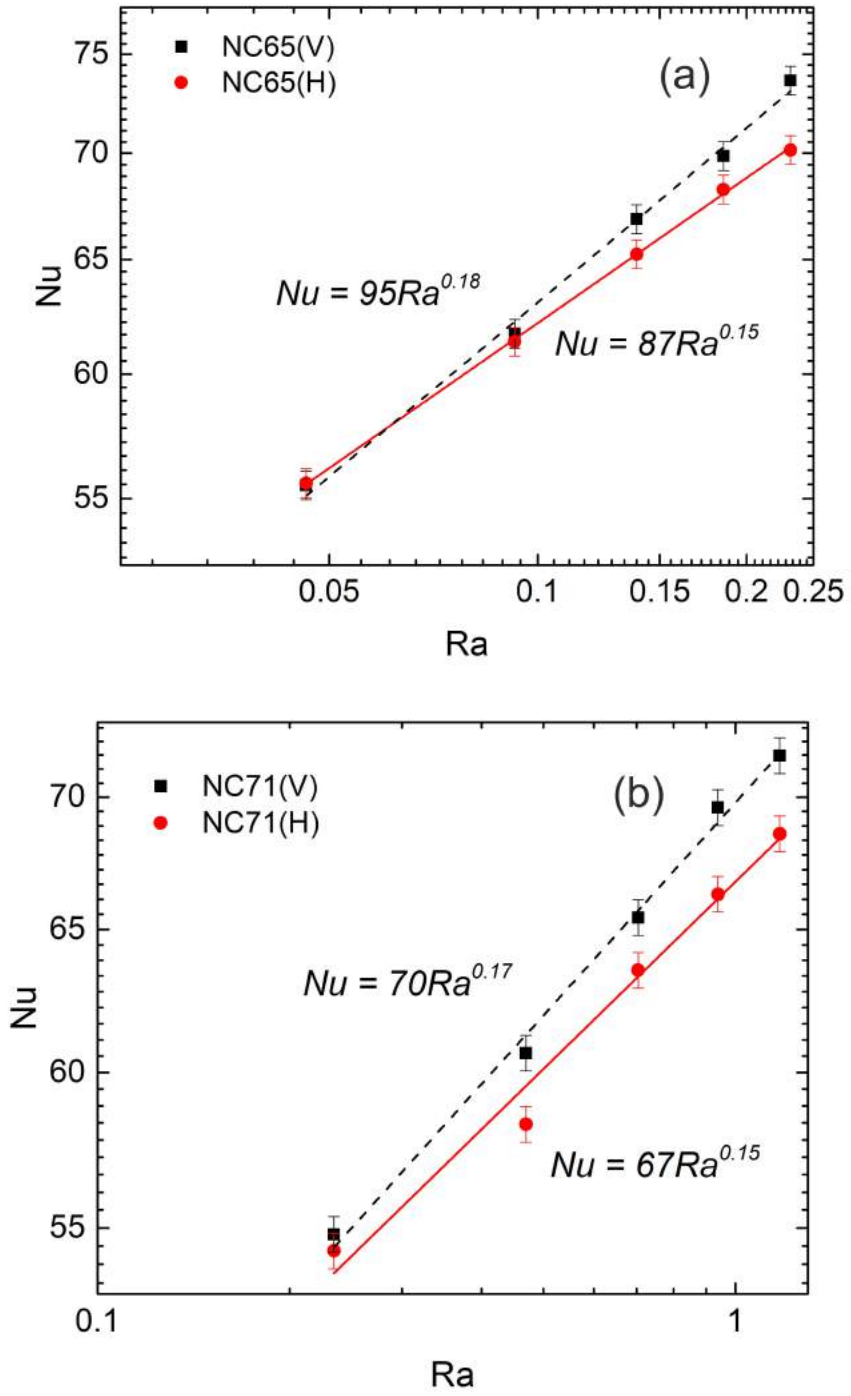

Figure 5.11: Comparison of Nusselt number between horizontal and vertical orientations for selected pore sizes and porosities: (a) 250 - 425 μm, 0.65, (b) 425 - 710 μm, 0.71, (c) 710 - 1000 μm, 0.75 and (d) 1000 - 1500 μm, 0.83. (to be continued)

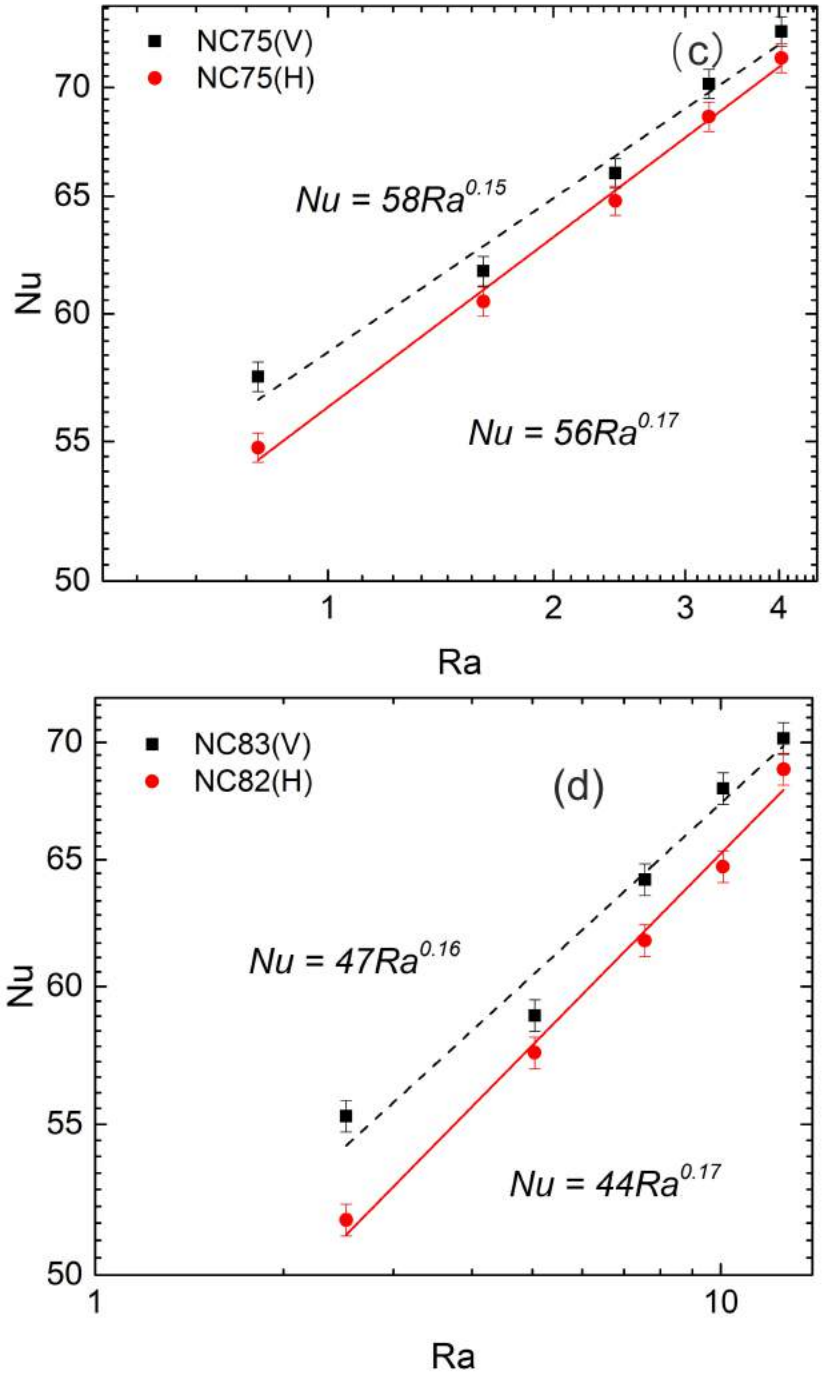

Figure 5.11: (continued) Comparison of Nusselt number between horizontal and vertical orientations for selected pore sizes and porosities: (a) 250 - 425 μm, 0.65, (b) 425 - 710 μm, 0.71, (c) 710 - 1000 μm, 0.75 and (d) 1000 - 1500 μm, 0.83.

Therefore, only convection in the outermost area of the sample occurs. After increasing the temperature difference to 30K, air may be able to penetrate into the sample, but the depth of penetration is still limited. For samples with a lager pore size, e.g. 425 - 710 μm, air could penetrate into the sample at a low temperature difference of 20K, due to decrease in flow resistance.

5.3 Heat transfer performance of porous copper under forced convection

The forced convective heat transfer performance of porous copper is presented in this section. A wide flow rate range is applied to cover all the flow regimes in porous copper sample with different porosities. The effects of porosity and flow regime on heat transfer performance are discussed. A power function is proposed to correlate the Nusselt number and the Reynold number.

5.3.1 Heat transfer coefficient

The convective heat transfer coefficient as a function of Reynolds number for the porous Cu samples is shown in Fig. 5.12. As expected, the convective heat transfer coefficient increases with increasing Reynolds number, which is proportional to the Darcian velocity or water flow rate in the present study. However, the gradient of the curves decreases gradually with increasing Reynolds number. In addition, porosity also has a strong effect on heat transfer performance.

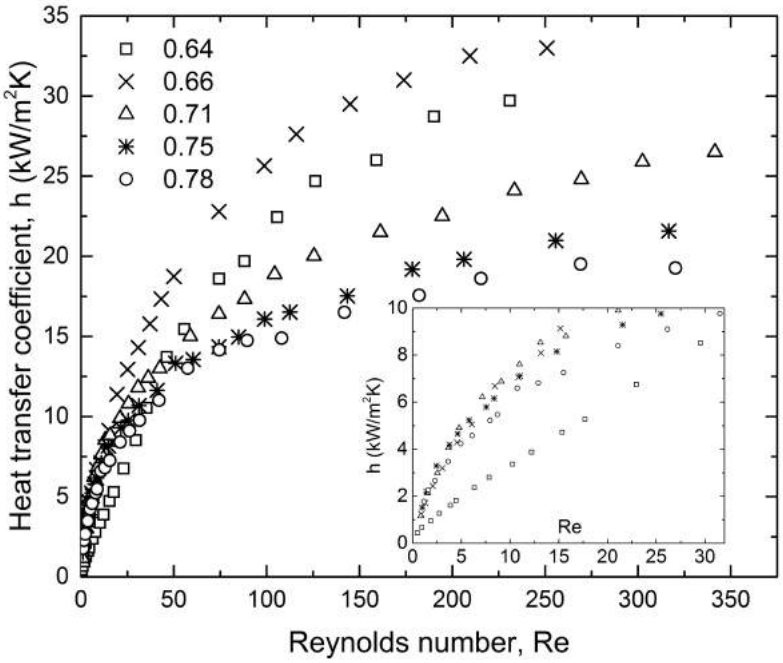

Figure 5.12: Convective heat transfer coefficient versus Reynolds number for porous Cu samples with various porosities. The inset magnifies the plots in the low Reynolds number part.

5.3.2 Nusselt number in different flow regimes

Fig. 5.13 plots Nusselt number as a function of Reynolds number for all porous Cu samples with different porosities. The Nusselt number is plotted as a function of Reynolds number to characterize the heat transfer performance of the porous Cu samples subjected to forced water convection. The relationship between Nusselt and Reynolds numbers was correlated in the form of $Nu = C_T Re^n$ (Eq. 2.17).

Fig. 5.13 shows that each plot can be divided into three sections, with each section fitting well with $Nu = C_T Re^n$. The slope of the fitted lines, i.e. the exponent n, decreases from the first section to the second section and further to the third section, except the sample with a porosity of 0.64, in which n increases from the first section to the second section. Although the three sections for each plot have different

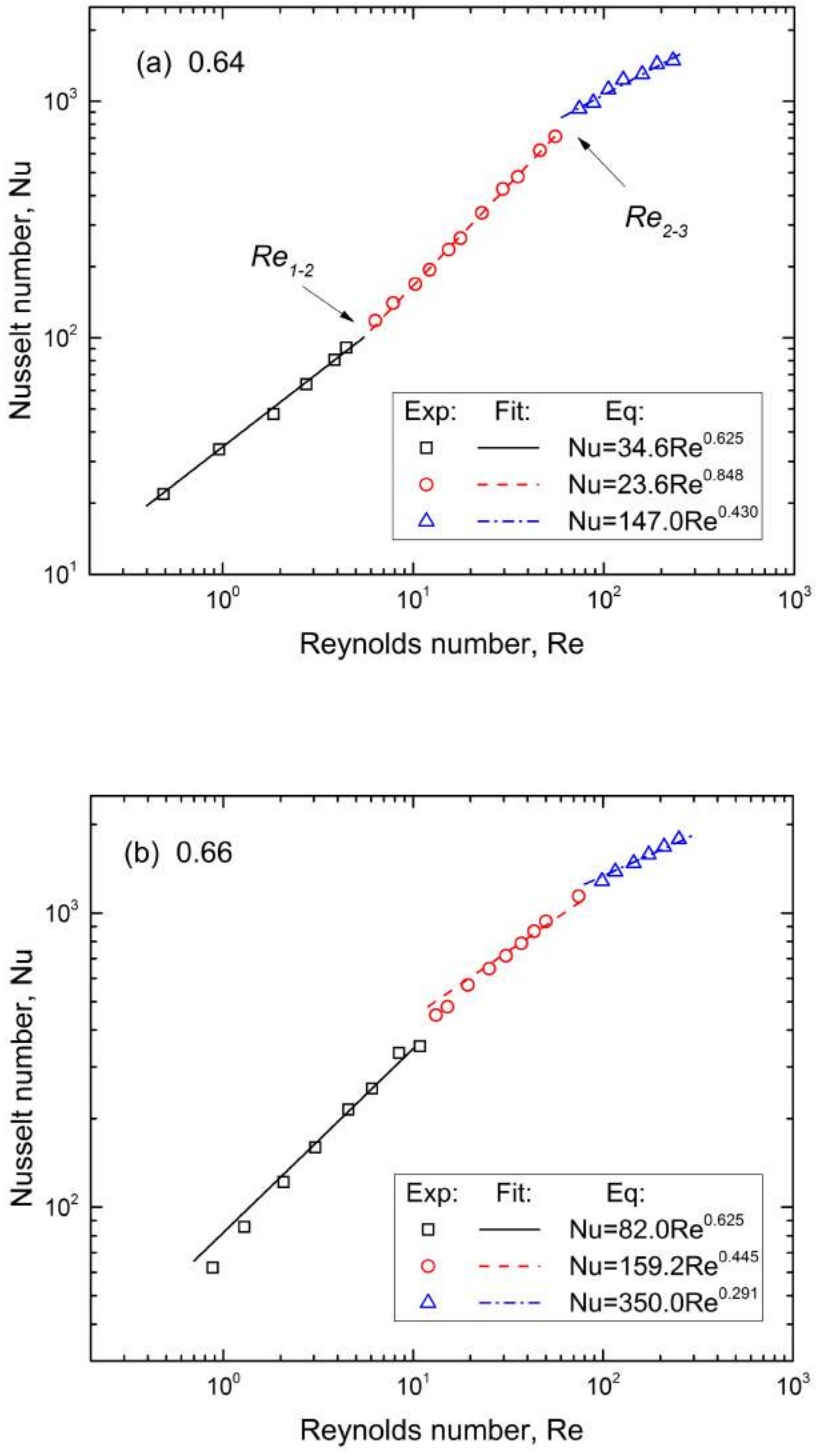

Figure 5.13: Nusselt number as a function of Reynolds number for porous Cu samples with different porosities: (a) 0.64, (b) 0.661, (c) 0.714, (d) 0.753 and (e) 0.782. The data can be correlated by $Nu = C_T Re^n$ in three sections. (to be continued)

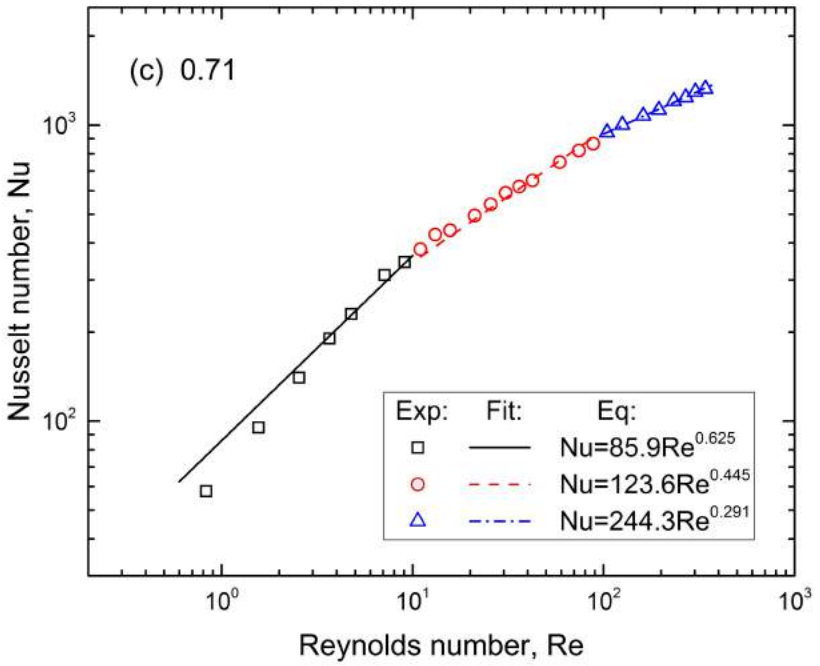

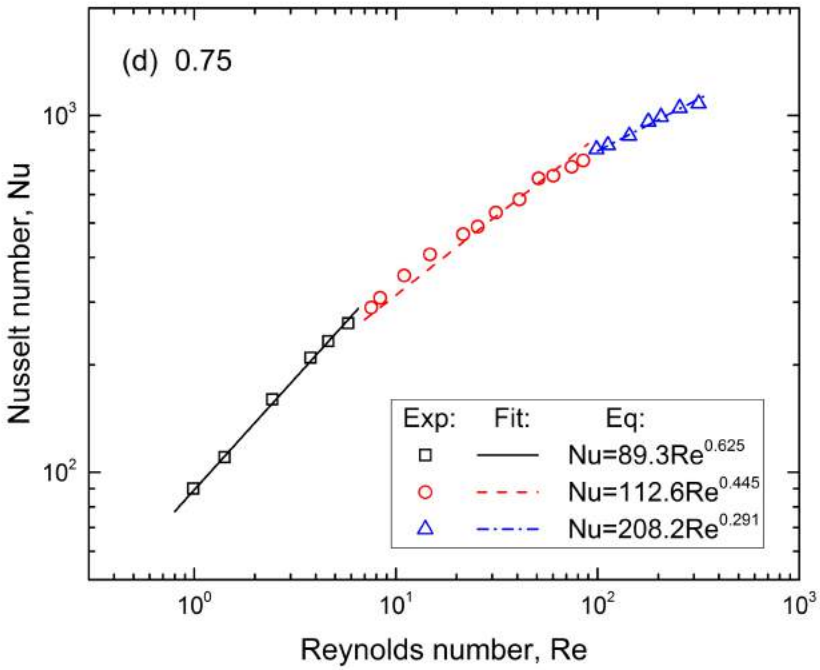

Figure 5.13: (continued) Nusselt number as a function of Reynolds number for porous Cu samples with different porosities: (a) 0.64, (b) 0.661, (c) 0.714, (d) 0.753 and (e) 0.782. The data can be correlated by $Nu = C_T Re^n$ in three sections. (to be continued)

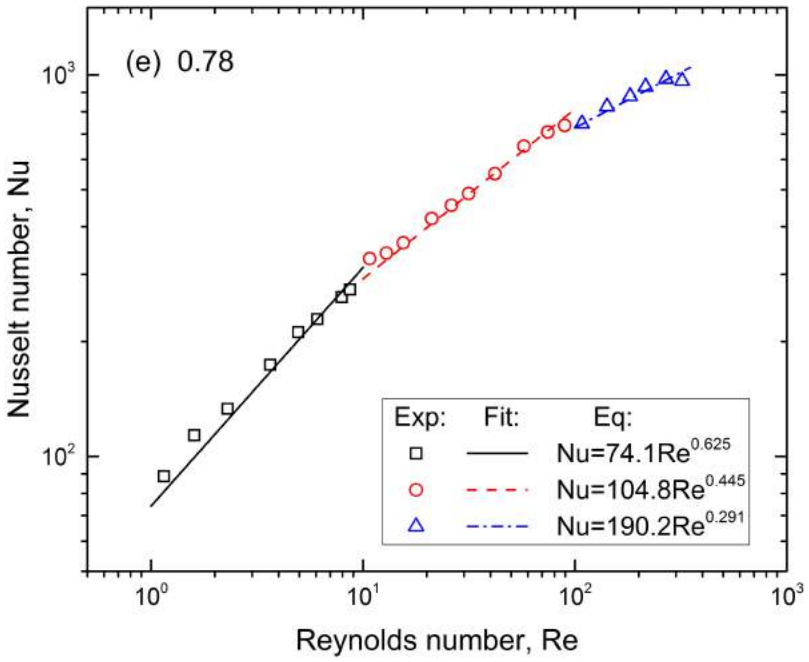

Figure 5.13: (continued) Nusselt number as a function of Reynolds number for porous Cu samples with different porosities: (a) 0.64, (b) 0.661, (c) 0.714, (d) 0.753 and (e) 0.782. The data can be correlated by $Nu = C_T Re^n$ in three sections.

relations, the value of the exponent n for each section tends to be a constant for all porous Cu samples except the one with a porosity of 0.64. In other words, n is largely independent of porosity, except at the relatively low porosity of 0.64.

The value of n not only depends on fluid flow state (flow regimes), but also depends on the porous structure of the porous metal. In packed beds cooled with water under forced convection, the value of n was 0.6 in the study of Wakao & Funazkri (1978), while the value was 1.35 (Re $<$ 100) or 1.04 (Re $>$ 100) in the study of Hwang & Chao (1994). The difference may be caused by the different particle sizes of the packed beds. In sintered fibrous media, the value was found to be 1 (Hunt & Tien 1988) and in the high porosity metal foam, e.g., Al foam, the value was 0.5 (Calmidi & Mahajan 1999). In the LCS porous Cu, however, the value of n ranges from 0.29

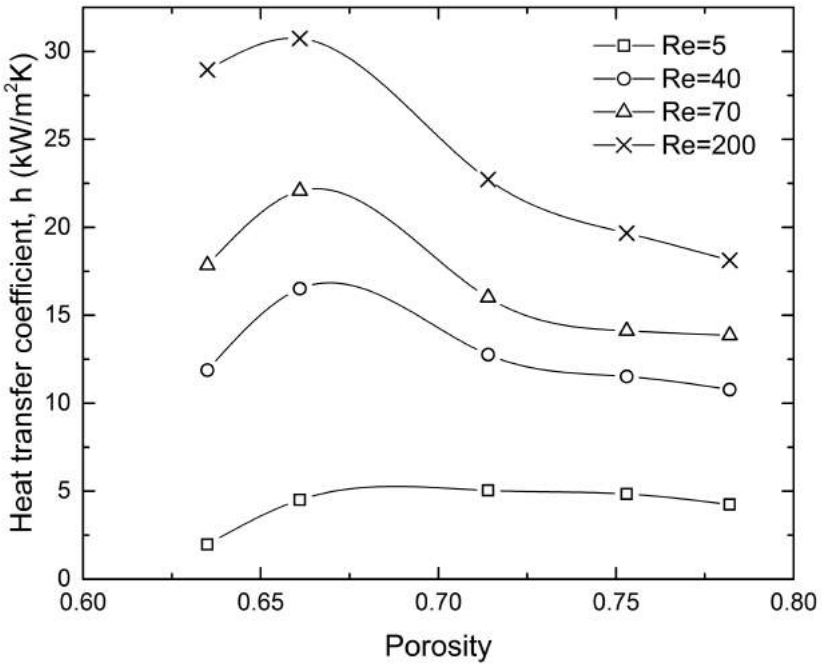

Figure 5.14: Convective heat transfer coefficient versus porosity at various Reynolds numbers.

to 0.85, depending on the porosity and flow regime.

5.3.3 Effect of porosity

Fig. 5.14 shows the variations of heat transfer coefficient with porosity at various Reynolds numbers, or flow rates. The effect of porosity on heat transfer coefficient is dependent on the flow rate. At low flow rates (Re $<$ 10), all samples have a similar heat transfer coefficient except the sample with a porosity of 0.64, which has a lower heat transfer coefficient (see the inset in Fig. 5.12). At high flow rates (Re $>$ 30), the heat transfer coefficient first increases with increasing porosity from 0.64 to 0.66 and then decreases with increasing porosity further.

Fig. 5.15 shows the variations of the correlation parameter C_T versus porosity for the first, second and third sections identified in Fig. 5.13. The trend is similar to that displayed in Fig. 5.14. At low flow rates (Re $<$ 10, first section), all samples have a similar C_T value except the 0.64 porosity sample. At high flow rates (Re $>$ 30, second and third sections), the C_T values first increases with increasing porosity from 0.64 to 0.66 and then decreases with increasing porosity further.

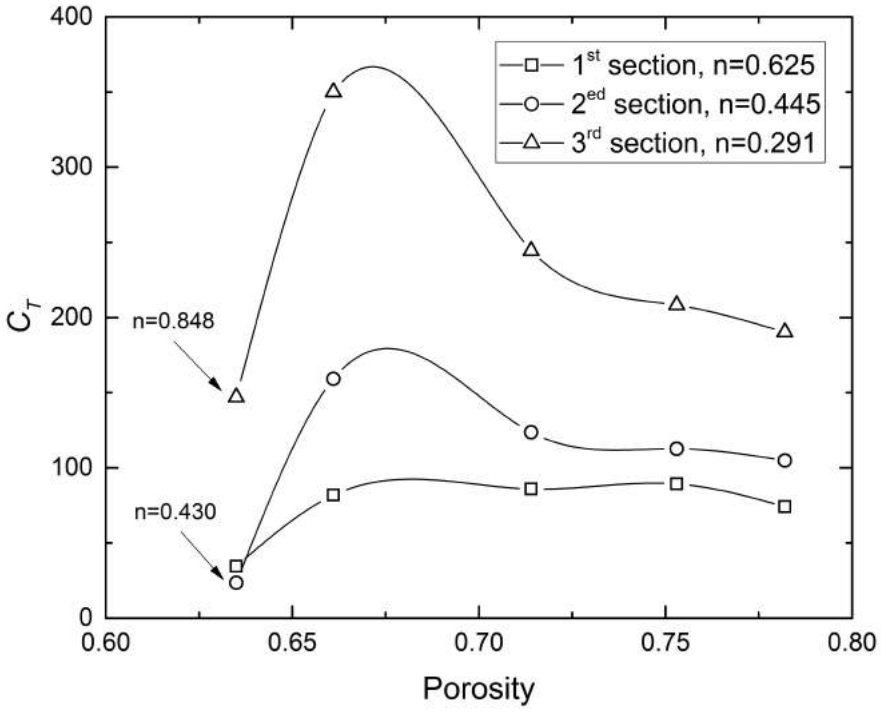

Figure 5.15: Correlation parameter C_T versus porosity for first, second and third sections.

The effect of porosity on heat transfer coefficient or Nusselt number can be understood by considering heat conduction through the solid matrix and heat convection in the fluid flow. Either conduction or convection can be the main factor limiting the overall heat transfer. While conduction is largely determined by porosity, convection is not only dependent on porosity but also affected by flow rate. The heat transfer

performance depends on the coupled effect of porosity and flow rate.

At very low rates (Re < 10), the convective heat transfer at the solid-fluid interface would be the limiting factor. Increasing porosity can increase convection through the fluid, because of the increased amount of fluid, and can therefore increase overall heat transfer in the porous media. However, the heat transfer from the near wall layer to the centre core within the fluid flow is mainly through conduction because of no wakes or vortices to help transfer heat. Therefore, increasing porosity beyond a certain level has no major influence on the convective heat transfer.

At high rates (Re > 10), either conduction in the solid matrix or convection in the fluid flow can be the limiting factor. The samples with a low porosity have a superior thermal conductivity due to the high proportion of solid matrix (Fig. 5.5). However, they have low internal surface area and low fluid permeability (Diao et al. 2015), which reduce the convectional heat transfer from the solid to the coolant. The overall heat transfer coefficient or Nusselt number is limited by the convection contribution and can be low. Conversely, although the samples with a high porosity have good convectional heat transfer from the solid to the coolant and by the moving coolant, they have poor thermal conductivity, which limits the overall heat transfer. As thermal conductivity decreases exponentially with porosity, the overall heat transfer coefficient or Nusselt number becomes lower with increasing porosity.

Fig. 5.14 and 5.15 suggest that the optimum porosity to give the best heat transfer performance is 0.66. At this critical porosity, heat conduction through the solid matrix matches heat convection in the fluid flow, resulting the best overall heat transfer performance (Baloyo & Zhao 2015).

5.3.4 Critical Reynolds numbers

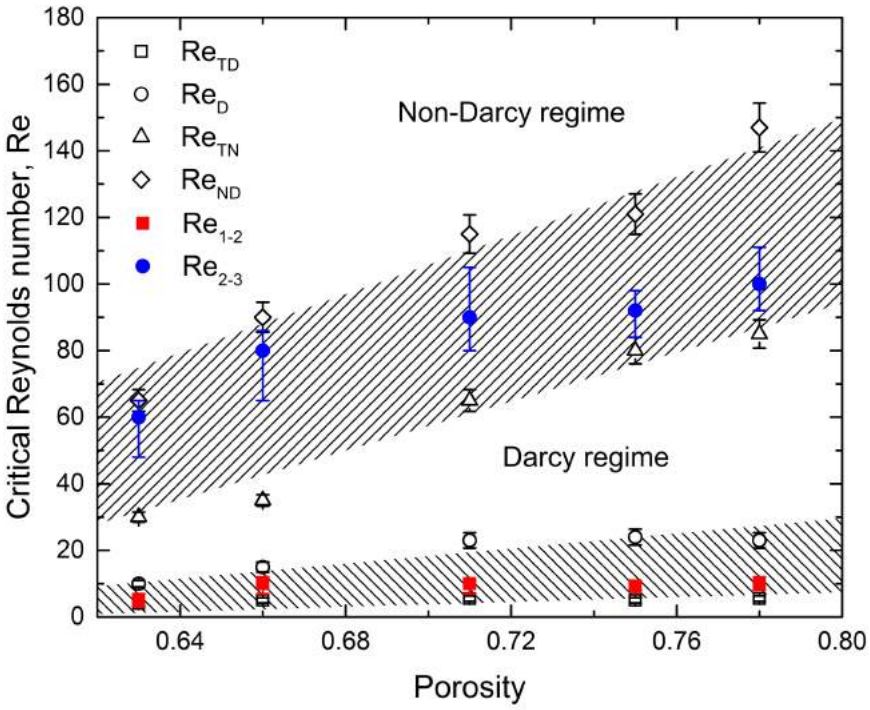

Figure 5.16: Critical Reynolds numbers for flow regimes (Re_{TD}, Re_D, Re_{TN} and Re_{ND}) and transitions between Nusselt number sections (Re_{1-2} and Re_{2-3}) as a function of porosity. The patterned areas show the transition-to-Darcy and transition-to-non-Darcy regimes.

Fig. 5.16 shows the critical Reynolds numbers for the flow regimes and the critical Reynolds numbers for transitions between the three sections in terms of Nusselt number identified in Fig. 5.13, as a function of porosity. The critical Reynolds numbers corresponding to the transitions from the first section to the second section and from the second to the third are designated as Re_{1-2} and Re_{2-3}, respectively. It is shown that Re_{1-2} falls within the transition-to-Darcy regime (Re_{TD} - Re_D), while Re_{2-3} falls within the transition-to-non-Darcy regime (Re_{TN} - Re_{ND}). It can be con-

cluded that the fluid flow behaviour plays an important role in determining the heat transfer performance of in the porous Cu samples. The three sections in terms of Nusselt number correspond broadly to the pre-Darcy, Darcy and non-Darcy regimes.

5.4 Summary

The thermal conductivity, natural convective and forced convective heat transfer coefficient of porous copper samples were experimentally investigated. The fluid convection within the porous copper sample can contribute up to 50% of the thermal conductivity to the porous Cu-fluid system. The contribution of fluid convection increases with the porosity. The relationship between thermal conductivity of porous copper sample and porosity fits well to a power law, with an exponent about 2.3. It also found that the porous copper sample with the copper particle size of 45 - 70 μm has the optimum thermal conductivity.

The natural convective heat transfer coefficient of porous copper increases with temperature difference between the sample and the ambience. The effect of pore size and porosity on the natural convective heat transfer coefficient is not significant. The vertically positioned samples have a higher heat transfer coefficient than horizontally positioned samples because air can pass through the whole sample in a vertical position.

The relationship between forced convective heat transfer and flow rate can be divided into three sections and each section fit well with equation of $Nu = C_t Re^n$. The three sections correspond to pre-Darcy, Darcy and non-Darcy regime, respectively. It is

also found that the porous copper sample with porosity of 0.66 shows the best heat transfer performance.

Chapter 6

Conclusions and future work

6.1 Conclusions

Porous copper samples and porous glass samples with different pore sizes and porosities have been manufactured using the LCS or SDP method. Copper powder with mean diameter of 75 μm and potassium carbonate powder with diameter ranges of 250 - 425 μm, 425 - 710 μm, 710 - 1000 μm and 1000 - 1500 μm, were used as matrix material and space holder, respectively, for fabricating the porous copper samples. Glass powder with a diameter range of 30 - 50 μm and sodium chloride powder with a particle size range of 425 - 710 μm, were used as matrix material and space holder, respectively, for fabricating the porous glass samples. The as-manufactured samples have porosities between 0.5 and 0.85 and pore sizes between 250 μm and 1500 μm in diameter. Sintered copper samples with copper particle sizes of 10 - 20 μm, 20 - 45 μm, 45 - 70 μm, 75 - 90 μm, 100 - 250 μm and 710 - 1000 μm, and porous glass samples with glass particle sizes of 150 - 250 μm, 250 - 425 μm and 425 - 850 μm, were also manufactured. The pressure drop, velocity and fluctuation distribution at the pore scale and heat transfer properties of these porous media were investigated.

6.1.1 Structural properties

The pore morphology of the porous copper and porous glass samples manufactured by the LCS and SDP processes closely matches that of the space holders, demonstrating the capability of these processes in producing porous samples with controllable pore size and pore shape. The large windows between pores and the small voids between the solid particles allowed interconnection of all pores in the whole porous sample. The porous glass samples perfectly mimic the structure of the porous copper samples, demonstrating the feasibility of this method for studying the flow behaviour in porous metal.

6.1.2 Pressure drop, permeability and form drag coefficient

A purpose-built apparatus was used to measure the pressure drop of porous samples. The values of permeability and form drag coefficient were calculated from the pressure drop data. The pressure drop increased with Reynolds number, fitting well with the Forchheimer-extended Darcy equation for all porous media studied in the present study. The pressure drop depends significantly on the porosity of the porous copper and porous glass and particle size of the sintered glass. Both high porosity and large particle size lead to lower pressure drop. In the porous copper and porous glass, the permeability increased and the form drag coefficient decreased with increasing porosity. In the sintered glass, the permeability increased and the form drag coefficient decreased with increasing particle size, and the measured permeability values agreed well with the predicated values from an existing equation.

6.1.3 Velocity and fluctuation distributions

A μ-PIV system was used to characterize the velocity and fluctuation in porous glass samples with different porosities and pore shapes. In the Darcy and Forchheimer regimes, the velocity distributions are similar and they are very different from that in the pre-Darcy and turbulent regimes. The velocity magnitude in the Darcy and Forchheimer regimes increases gradually from the near wall region to the channel center. The velocity profiles along a specific line in the Darcy and Forchheimer regimes almost coincide and are parabolic. In the turbulent regime, velocity distributes more uniformly at the pore scale and the velocity profile along a specific line becomes flatter. The channels/paths involved in fluid transport change as flow rate increases. The channels/paths with high tortuosity are less likely involved in fluid transport at low flow rates as the pressure is not sufficient to overcome the resistance. However, all the channels/paths are involved in fluid transport at high flow rates.

The velocity fluctuation intensity is abnormally high in the near wall region and this is caused by three factors: (1) rough wall surface, (2) normalization by the very low velocity magnitude in the near wall region and (3) high uncertainty of the μ-PIV due to low contrast in the rear wall region. In the central region, the velocity fluctuation intensity is less than 0.1 in the Darcy and Forchheimer regimes, indicating laminar flow, and is larger than 0.1 in the turbulent regime. The transition range identified from the velocity fluctuation is consistent with that identified from the reduced pressure drop.

6.1.4 Thermal conductivity

Thermal conductivity measurements were carried out in vacuum (porous Cu), air (porous Cu - air system) and water (porous Cu - water) conditions. It has been found that the contribution of fluid convection within the porous sample is not negligible for the effective thermal conductivity of the porous Cu - fluid system. Fluid convection can contribute up to 50% of the heat transfer in the porous copper sample with a porosity of 0.8. The thermal conductivity increases with relative density, following a power law, with an exponent of around 2.3. Too large or too small copper particles are not good for the thermal conductivity of porous copper due to poor connectivity or high thermal resistance. The optimum copper particle size range is 45-70μm in terms of thermal conductivity.

6.1.5 Heat transfer performance under natural convection

The natural convective heat transfer coefficient of porous copper samples with different porosities and pore sizes was measured at different temperature differences. The natural convective heat transfer coefficient increases dramatically with increasing temperature difference between sample and ambience. The effect of porosity on natural convective heat transfer performance is not significant for samples with porosity of 0.65 - 0.8. Above 0.8, the natural convective heat transfer coefficient tends to decrease with porosity. For the porous copper samples with pore sizes of 250 - 1500 μm, the effect of pore size on natural convective heat transfer performance is insignificant. The heating direction or the orientation of sample also affects the

heat transfer performance. The sample with heating from side has better cooling performance than heating from bottom for the same heating area.

6.1.6 Heat transfer performance under forced convection

Effects of the flow regime and porosity on the heat transfer coefficient or Nusselt number were investigated under forced convection. The porous copper sample with porosity of 0.66 shows the best forced convective heat transfer coefficient due to its balanced conduction and convection. Flow behaviour has a significant effect on heat transfer performance. The Nusselt number - Reynolds number curve can be divided into three sections and in each section, the relationship between Nusselt number and Reynolds number follows the equation $Nu = C_T Re^n$. The value of n decreases from the first section to the second section and further to the third section, except the sample with a porosity of 0.64. The three sections correspond to the pre-Darcy, Darcy and non-Darcy regime, respectively..

6.2 Future work

The combination of pressure drop and μ-PIV measurements has been proved to be an effective way to study porous flow in a complex structure. Flow behaviour at normal flow rates has been studied extensively with a rich volume of data. Data in the ultra low flow rates (pre-Darcy regime), however, is still limited. Flow visualization and more accurate pressure drop measurements at ultra low flow rates need to be carried out.

The present study is based on a 2D μ-PIV system with a very shallow depth of field, so that only two velocity components were investigated. The porous glass sample, in fact, has a 3D structure and the local structure is different at different directions. Therefore, the flow behaviour in the third direction cannot be tracked with the present system. 3D PIV measurements can be carried out to verify the 2D results and to reveal more details of the flow, e.g., how flow path changes with increasing flow rate.

The refractive index of the working fluid used in the present study does not match well with that of the solid matrix. Alternative working fluid can be used to obtain better images and results. The working fluid used in the present study is Newtonian fluid. Flow behaviour of non-Newtonian fluid in such a complex structure can be investigated. In addition, the effect of pore size on flow behaviour in porous media can also be investigated.

Fluid convection within porous copper samples contributes significantly to the effective thermal conductivity of the porous Cu-fluid system. This is a qualitative conclusion as no direct evidence proves the existence of convection inside porous copper samples. Numerical modelling work may be carried out to investigate the thermal conductivity of a porous metal-fluid system. This will help to evaluate the contribution of convection in porous metal and to understand the fluid dynamics and heat transfer mechanism in the porous metal-fluid system.

The pore size range of the samples used for natural convection measurements is from 250 μm to 1500 μm. It is found that the effect of pore size on convective heat transfer is insignificant within this pore size range. The natural convective heat transfer

performance of LCS porous copper with large pores (2 - 4 mm) can be studied. Regular grooves can also be introduced to the porous copper samples in order to further increase the surface area and to enhance the natural convective heat transfer performance.

Bibliography

Achenbach, E. (1995), 'Heat and flow characteristics of packed beds', *Experimental thermal and fluid science* **10**(1), 17–27.

Afifi, R. & Berbish, N. (1999), 'Experimental investigation of forced convection heat transfer over a horizontal flat plate in a porous medium', *J. Engng. Appl. Sci* **46**, 693–710.

Ahmadi, M., Mostafavi, G. & Bahrami, M. (2014), 'Natural convection from rectangular interrupted fins', *International Journal of Thermal Sciences* **82**, 62–71.

Ali, A. H. H. & Hanaoka, Y. (2002), 'Experimental study on laminar flow forced-convection in a channel with upper v-corrugated plate heated by radiation', *International Journal of Heat and Mass Transfer* **45**(10), 2107–2117.

Ali, M. & Ramadhyani, S. (1992), 'Experiments on convective heat transfer in corrugated channels', *EXPERIMENTAL HEAT TRANSFER An International Journal* **5**(3), 175–193.

Almogbel, M. & Bejan, A. (2000), 'Cylindrical trees of pin fins', *International Journal of Heat and Mass Transfer* **43**(23), 4285–4297.

Ashby, M. F., Evans, T., Fleck, N. A., Hutchinson, J., Wadley, H. & Gibson, L. (2000), *Metal foams: a design guide*, Elsevier.

Babjak, J., Ettel, V. A. & Paserin, V. (1990), 'Method of forming nickel foam'. US Patent 4,957,543.

Bai, K. & Katz, J. (2014), 'On the refractive index of sodium iodide solutions for index matching in piv', *Experiments in fluids* **55**(4), 1704.

Baloyo, J. M. & Zhao, Y. (2015), 'Heat transfer performance of micro-porous copper foams with homogeneous and hybrid structures manufactured by lost carbonate sintering', *MRS Online Proceedings Library Archive* **1779**, 39–44.

Banhart, J. (2001), 'Manufacture, characterisation and application of cellular metals and metal foams', *Progress in materials science* **46**(6), 559–632.

Banhart, J. & Baumeister, J. (1998), 'Production methods for metallic foams', *MRS Online Proceedings Library Archive* **521**.

Bastawros, A.-F. & Evans, A. (1997), 'Characterisation of open-cell aluminum alloy foams as heat sinks for high power electronic devices', *ASME-PUBLICATIONS-HTD* **356**, 1–6.

Baumann, T. & Werth, C. J. (2005), 'Visualization of colloid transport through heterogeneous porous media using magnetic resonance imaging', *Colloids and surfaces A: Physicochemical and engineering aspects* **265**(1-3), 2–10.

Bear, J. (2013), *Dynamics of fluids in porous media*, Courier Corporation.

Bear, J. & Corapcioglu, M. Y. (2012), *Advances in transport phenomena in porous media*, Vol. 128, Springer Science & Business Media.

Bertola, V. & Cafaro, E. (2005), 'Intermediate asymptotic behaviour of fluid flows by scale–size analysis', *Proceedings of the Royal Society A: Mathematical, Physical and Engineering Sciences* **461**(2055), 755–760.

Bhattacharya, A., Calmidi, V. & Mahajan, R. (2002), 'Thermophysical properties of high porosity metal foams', *International Journal of Heat and Mass Transfer* **45**(5), 1017–1031.

Bhattacharya, A. & Mahajan, R. (2006), 'Metal foam and finned metal foam heat sinks for electronics cooling in buoyancy-induced convection', *Journal of electronic packaging* **128**(3), 259–266.

Bhattacharya, A. & Mahajan, R. L. (2002), 'Finned metal foam heat sinks for electronics cooling in forced convection', *Journal of Electronic Packaging* **124**(3), 155–163.

Bonnet, J.-P., Topin, F. & Tadrist, L. (2008), 'Flow laws in metal foams: compressibility and pore size effects', *Transport in Porous Media* **73**(2), 233–254.

Boomsma, K. & Poulikakos, D. (2001), 'On the effective thermal conductivity of a three-dimensionally structured fluid-saturated metal foam', *International Journal of Heat and Mass Transfer* **44**(4), 827–836.

Boomsma, K. & Poulikakos, D. (2002), 'The effects of compression and pore size variations on the liquid flow characteristics in metal foams', *Journal of fluids engineering* **124**(1), 263–272.

Braga, E. J. & De Lemos, M. J. (2005), 'Heat transfer in enclosures having a fixed amount of solid material simulated with heterogeneous and homogeneous models', *International Journal of Heat and Mass Transfer* **48**(23-24), 4748–4765.

Brinkman, H. (1949*a*), 'A calculation of the viscous force exerted by a flowing fluid on a dense swarm of particles', *Flow, Turbulence and Combustion* **1**(1), 27.

Brinkman, H. (1949*b*), 'On the permeability of media consisting of closely packed porous particles', *Flow, Turbulence and Combustion* **1**(1), 81.

Bruggeman, D. (1935), 'Dielectric constant and conductivity of mixtures of isotropic materials', *Ann. Phys.(Leipzig)* **24**, 636–679.

Calmidi, V. & Mahajan, R. (1999), 'The effective thermal conductivity of high porosity fibrous metal foams', *Journal of heat transfer* **121**(2), 466–471.

Calmidi, V. & Mahajan, R. (2000), 'Forced convection in high porosity metal foams', *Journal of heat transfer* **122**(3), 557–565.

Chauveteau, G. & Thirriot, C. (1967), 'Rgimes d'coulement en milieu poreux et limite de la loi de darcy', *Houille Blanche* **22**(1), 1–8. cited By 17.

Cheng, N.-S., Hao, Z. & Tan, S. K. (2008), 'Comparison of quadratic and power law for nonlinear flow through porous media', *Experimental Thermal and Fluid Science* **32**(8), 1538–1547.

Coleman, H. W. & Steele, W. G. (2018), *Experimentation, validation, and uncertainty analysis for engineers*, John Wiley & Sons.

Collishaw, P. & Evans, J. (1994), 'An assessment of expressions for the apparent thermal conductivity of cellular materials', *Journal of materials science* **29**(9), 2261–2273.

Comiti, J., Sabiri, N. & Montillet, A. (2000), 'Experimental characterization of flow regimes in various porous media iii: limit of darcy's or creeping flow regime for newtonian and purely viscous non-newtonian fluids', *Chemical Engineering Science* **55**(15), 3057 – 3061.

Corsan, J. (1984), 'A compact thermal conductivity apparatus for good conductors', *Journal of Physics E: Scientific Instruments* **17**(9), 800.

Dai, Z., Nawaz, K., Park, Y., Chen, Q. & Jacobi, A. (2012), 'A comparison of metal-foam heat exchangers to compact multilouver designs for air-side heat transfer applications', *Heat Transfer Engineering* **33**(1), 21–30.

Darcy, H. (1856), 'Les fontaines publique de la ville de dijon', *Dalmont, Paris* **647**.

Datta, S. S., Chiang, H., Ramakrishnan, T. & Weitz, D. A. (2013), 'Spatial fluctuations of fluid velocities in flow through a three-dimensional porous medium', *Physical review letters* **111**(6), 064501.

Diao, K., Xiao, Z. & Zhao, Y. (2015), 'Specific surface areas of porous cu manufactured by lost carbonate sintering: Measurements by quantitative stereology and cyclic voltammetry', *Materials Chemistry and Physics* **162**, 571–579.

Diao, K., Zhang, L. & Zhao, Y. (2017), 'Measurement of tortuosity of porous cu using a diffusion diaphragm cell', *Measurement* **110**, 335–338.

Dracos, T. (2013), *Three-Dimensional Velocity and Vorticity Measuring and Image Analysis Techniques: Lecture Notes from the Short Course held in Zürich, Switzerland, 3–6 September 1996*, Vol. 4, Springer Science & Business Media.

Dukhan, N. (2006), 'Correlations for the pressure drop for flow through metal foam', *Experiments in fluids* **41**(4), 665–672.

Dukhan, N., Bağcı, Ö. & Özdemir, M. (2014), 'Metal foam hydrodynamics: flow regimes from pre-darcy to turbulent', *International Journal of Heat and Mass Transfer* **77**, 114–123.

Dukhan, N. & Patel, P. (2008), 'Equivalent particle diameter and length scale for pressure drop in porous metals', *Experimental Thermal and Fluid Science* **32**(5), 1059–1067.

Dupuit, J. É. J. (1863), *Études théoriques et pratiques sur le mouvement des eaux dans les canaux découverts et à travers les terrains perméables: avec des considérations relatives au régime des grandes eaux, au débouché à leur donner, et à la marche des alluvions dans les rivières à fond mobile*, Dunod.

Durst, F. (1980), Principles of laser doppler anemometers, *in* 'In Von Karman Inst. of Fluid Dyn. Meas. and Predictions of Complex Turbulent Flows, Vol. 1 11 p (SEE N81-15263 06-34)', Vol. 1.

Dybbs, A. & Edwards, R. (1984), A new look at porous media fluid mechanicsdarcy to turbulent, *in* 'Fundamentals of transport phenomena in porous media', Springer, pp. 199–256.

Dyga, R. & Płaczek, M. (2015), 'Heat transfer through metal foam–fluid system', *Experimental thermal and fluid science* **65**, 1–12.

Effendi, N. S. & Kim, K. J. (2017), 'Orientation effects on natural convective performance of hybrid fin heat sinks', *Applied Thermal Engineering* **123**, 527–536.

Ejlali, A., Ejlali, A., Hooman, K. & Gurgenci, H. (2009), 'Application of high porosity metal foams as air-cooled heat exchangers to high heat load removal systems', *International Communications in Heat and Mass Transfer* **36**(7), 674–679.

Ergun, S. (1952), 'Fluid flow through packed columns', *Chem. Eng. Prog.* **48**, 89–94.

Fand, R., Kim, B., Lam, A. & Phan, R. (1987), 'Resistance to the flow of fluids

through simple and complex porous media whose matrices are composed of randomly packed spheres', *Journal of fluids engineering* **109**(3), 268–273.

Forchheimer, P. (1901), 'Wasserbewegung durch boden', *Z. Ver. Deutsch, Ing.* **45**, 1782–1788.

Fredrich, J. (1999), '3d imaging of porous media using laser scanning confocal microscopy with application to microscale transport processes', *Physics and Chemistry of the Earth, Part A: Solid Earth and Geodesy* **24**(7), 551–561.

García-Moreno, F. (2016), 'Commercial applications of metal foams: Their properties and production', *Materials* **9**(2), 85.

Gibson, L. J. & Ashby, M. F. (1999), *Cellular solids: structure and properties*, Cambridge university press.

Goldstein, R. J. & Kreid, D. (1967), 'Measurement of laminar flow development in a square duct using a laser-doppler flowmeter', *Journal of Applied Mechanics* **34**(4), 813–818.

Han, L. (1960), 'Hydrodynamic entrance lengths for incompressible laminar flow in rectangular ducts', *Journal of Applied Mechanics* **27**(3), 403–409.

Harris, C. (1977), 'Flow through porous media. examination of the immobile fluid model', *Powder Technology* **17**(3), 235 – 252.

Hassan, Y. A. & Dominguez-Ontiveros, E. (2008), 'Flow visualization in a pebble bed reactor experiment using piv and refractive index matching techniques', *Nuclear Engineering and Design* **238**(11), 3080–3085.

Hetsroni, G., Gurevich, M. & Rozenblit, R. (2008), 'Natural convection in metal foam strips with internal heat generation', *Experimental Thermal and Fluid Science* **32**(8), 1740–1747.

Hintz, C., Wagner, I., Sahm, P. & Stoyanov, P. (1999), Investment cast near-net-shape components based on cellular metal materials, *in* 'MetFoam 99: International Conference on Metal Foams and Porous Metal Structures', pp. 153–158.

Horton, C. & Rogers Jr, F. (1945), 'Convection currents in a porous medium', *Journal of Applied Physics* **16**(6), 367–370.

Huang, A. Y., Huang, M. Y., Capart, H. & Chen, R.-H. (2008), 'Optical measurements of pore geometry and fluid velocity in a bed of irregularly packed spheres', *Experiments in Fluids* **45**(2), 309–321.

Huang, R.-T., Sheu, W.-J. & Wang, C.-C. (2008), 'Orientation effect on natural convective performance of square pin fin heat sinks', *International Journal of Heat and Mass Transfer* **51**(9-10), 2368–2376.

Huettel, S. A., Song, A. W., McCarthy, G. et al. (2004), *Functional magnetic resonance imaging*, Vol. 1, Sinauer Associates Sunderland, MA.

Hunt, M. & Tien, C. (1988), 'Effects of thermal dispersion on forced convection in fibrous media', *International Journal of Heat and Mass Transfer* **31**(2), 301–309.

Hutter, C., Büchi, D., Zuber, V. & von Rohr, P. R. (2011), 'Heat transfer in metal foams and designed porous media', *Chemical engineering science* **66**(17), 3806–3814.

Hwang, G. & Chao, C. (1994), 'Heat transfer measurement and analysis for sintered porous channels', *Journal of heat transfer* **116**(2), 456–464.

Incropera, F. P., Lavine, A. S., Bergman, T. L. & DeWitt, D. P. (2007), *Fundamentals of heat and mass transfer*, Wiley.

Irmay, S. (1958), 'On the theoretical derivation of darcy and forchheimer formulas', *Eos, Transactions American Geophysical Union* **39**(4), 702–707.

Jiang, P.-X. (1999), 'Numerical simulation of forced convection heat transfer in porous plate channels using thermal equilibrium and nonthermal equilibrium models', *Numerical Heat Transfer: Part A: Applications* **35**(1), 99–113.

Jiang, P.-X., Wang, Z. & Ren, Z. (1998), Fluid flow and convection heat transfer in a plate channel filled with solid particles, *in* 'International Heat Transfer Conference Digital Library', Begel House Inc.

Jin, I., Kenny, L. & Sang, H. (1991), 'Us patent 4 973 358 (1990)', *PCT Patent WO* **91**, 03578.

Johnston, W., Dybbs, A. & Edwards, R. (1975), 'Measurement of fluid velocity inside porous media with a laser anemometer', *The Physics of fluids* **18**(7), 913–914.

Joseph, D., Nield, D. & Papanicolaou, G. (1982), 'Nonlinear equation governing flow in a saturated porous medium', *Water Resources Research* **18**(4), 1049–1052.

Kaviany, M. (2012), *Principles of heat transfer in porous media*, Springer Science & Business Media.

Kececioglu, I. & Jiang, Y. (1994), 'Flow through porous media of packed spheres saturated with water', *Journal of Fluids Engineering* **116**(1), 164–170.

Kendall, J. M., Lee, M. & Wang, T. (1982), 'Metal shell technology based upon hollow jet instability', *Journal of Vacuum Science and Technology* **20**(4), 1091–1093.

Khashan, S., Al-Amiri, A. & Al-Nimr, M. (2005), 'Assessment of the local thermal non-equilibrium condition in developing forced convection flows through fluid-saturated porous tubes', *Applied thermal engineering* **25**(10), 1429–1445.

Kreith, F., Manglik, R. M. & Bohn, M. S. (2012), *Principles of heat transfer*, Cengage learning.

Kundu, P., Kumar, V. & Mishra, I. (2014), 'Numerical modeling of turbulent flow through isotropic porous media', *International Journal of Heat and Mass Transfer* **75**, 40 – 57.

Kutsovsky, Y., Scriven, L., Davis, H. & Hammer, B. (1996), 'Nmr imaging of velocity profiles and velocity distributions in bead packs', *Physics of Fluids* **8**(4), 863–871.

Lai, F. & Kulacki, F. (1989), 'Thermal dispersion effects on non-darcy convection over horizontal surfaces in saturated porous media', *International journal of heat and mass transfer* **32**(5), 971–976.

Lapwood, E. (1948), Convection of a fluid in a porous medium, *in* 'Mathematical Proceedings of the Cambridge Philosophical Society', Vol. 44, Cambridge University Press, pp. 508–521.

Leach, A. (1993), 'The thermal conductivity of foams. i. models for heat conduction', *Journal of Physics D: Applied Physics* **26**(5), 733.

Lee, D.-Y., Chae, M.-S. & Chung, B.-J. (2017), 'Natural convective heat transfer of heated packed beds', *International Communications in Heat and Mass Transfer* **88**, 54–62.

Li, L. & Ma, W. (2011), 'Experimental study on the effective particle diameter of a packed bed with non-spherical particles', *Transport in porous media* **89**(1), 35–48.

Ling, J. & Dybbs, A. (1992), 'The effect of variable viscosity on forced convection over a flat plate submersed in a porous medium', *Journal of heat transfer* **114**(4), 1063–1065.

Liu, Q. & He, Y.-L. (2017), 'Lattice boltzmann simulations of convection heat transfer in porous media', *Physica A: Statistical Mechanics and its Applications* **465**, 742–753.

Liu, S. & Masliyah, J. H. (2005), Dispersion in porous media, *in* 'Handbook of porous media', CRC Press, pp. 99–160.

Lu, X., Zhao, Y. & Dennis, D. J. (2018), 'Flow measurements in microporous media using micro-particle image velocimetry', *Physical Review Fluids* **3**(10), 104202.

Macdonald, I., El-Sayed, M., Mow, K. & Dullien, F. (1979), 'Flow through porous media-the ergun equation revisited', *Industrial & Engineering Chemistry Fundamentals* **18**(3), 199–208.

Magyari, E., Keller, B. & Pop, I. (2001), 'Exact analytical solutions of forced convection flow in a porous medium', *International communications in heat and mass transfer* **28**(2), 233–241.

Magyari, E. & Rees, D. (2006), 'Effect of viscous dissipation on the darcy free convection boundary-layer flow over a vertical plate with exponential temperature distribution in a porous medium', *Fluid dynamics research* **38**(6), 405.

Mahdi, R. A., Mohammed, H., Munisamy, K. & Saeid, N. (2015), 'Review of convection heat transfer and fluid flow in porous media with nanofluid', *Renewable and Sustainable Energy Reviews* **41**, 715–734.

Mahjoob, S. & Vafai, K. (2008), 'A synthesis of fluid and thermal transport models for metal foam heat exchangers', *International Journal of Heat and Mass Transfer* **51**(15-16), 3701–3711.

Maier, R. S., Kroll, D., Kutsovsky, Y., Davis, H. & Bernard, R. S. (1998), 'Simulation of flow through bead packs using the lattice boltzmann method', *Physics of Fluids* **10**(1), 60–74.

Mandal, D. (2015), 'Hydrodynamics of particles in liquidsolid packed fluidized bed', *Powder Technology* **276**, 18 – 25.

Mandal, D., Vinjamur, M. & Sathiyamoorthy, D. (2013), 'Hydrodynamics of beds of small particles in the voids of coarse particles', *Powder Technology* **235**, 256 – 262.

Maxwell, J. C. (1881), *A treatise on electricity and magnetism*, Vol. 1, Clarendon press.

Meinhart, C. D., Wereley, S. T. & Santiago, J. G. (1999), 'Piv measurements of a microchannel flow', *Experiments in fluids* **27**(5), 414–419.

Merrikh, A. A. & Lage, J. L. (2005), 'Natural convection in an enclosure with disconnected and conducting solid blocks', *International Journal of Heat and Mass Transfer* **48**(7), 1361–1372.

Mishra, P., Singh, D. & Mishra, I. (1975), 'Momentum transfer to newtonian and non-newtonian fluids flowing through packed and fluidized beds', *Chemical Engineering Science* **30**(4), 397–405.

Moghari, M. (2008), 'A numerical study of non-equilibrium convective heat transfer in porous media', *Journal of Enhanced Heat Transfer* **15**(1).

Mokadam, R. (1961), 'Thermodynamic analysis of the darcy law', *Journal of Applied Mechanics* **28**(2), 208–212.

Moutsopoulos, K. N., Papaspyros, I. N. & Tsihrintzis, V. A. (2009), 'Experimental investigation of inertial flow processes in porous media', *Journal of hydrology* **374**(3-4), 242–254.

Nakayama, A. & Ebinuma, C. (1990), 'Transient non-darcy forced convective heat transfer from a flat plate embedded in a fluid-saturated porous medium', *International Journal of Heat and Fluid Flow* **11**(3), 249–253.

Navaei, A., Mohammed, H., Munisamy, K., Yarmand, H. & Gharehkhani, S. (2015), 'Heat transfer enhancement of turbulent nanofluid flow over various types of internally corrugated channels', *Powder technology* **286**, 332–341.

Nield, D. (1996), 'The effect of temperature-dependent viscosity on the onset of convection in a saturated porous medium', *Journal of heat transfer* **118**(3), 803–805.

Nield, D. A., Bejan, A. et al. (2006), *Convection in porous media*, Vol. 3, Springer.

Ochoa-Tapia, J. A. & Whitaker, S. (1995), 'Momentum transfer at the boundary between a porous medium and a homogeneous fluidi. theoretical development', *International Journal of Heat and Mass Transfer* **38**(14), 2635–2646.

Paek, J., Kang, B., Kim, S. & Hyun, J. M. (2000), 'Effective thermal conductivity and permeability of aluminum foam materials', *International Journal of Thermophysics* **21**(2), 453–464.

Pamuk, M. T. & Özdemir, M. (2012), 'Friction factor, permeability and inertial

coefficient of oscillating flow through porous media of packed balls', *Experimental thermal and fluid science* **38**, 134–139.

Patil, V. A. & Liburdy, J. A. (2013), 'Flow characterization using piv measurements in a low aspect ratio randomly packed porous bed', *Experiments in fluids* **54**(4), 1497.

Polubarinova-Koch, P. I. (2015), *Theory of ground water movement*, Princeton University Press.

Progelhof, R. & Throne, J. (1975), 'Cooling of structural foams', *Journal of Cellular Plastics* **11**(3), 152–163.

Progelhof, R., Throne, J. & Ruetsch, R. (1976), 'Methods for predicting the thermal conductivity of composite systems: a review', *Polymer Engineering & Science* **16**(9), 615–625.

Raffel, M., Willert, C. E., Scarano, F., Kähler, C. J., Wereley, S. T. & Kompenhans, J. (2018), *Particle image velocimetry: a practical guide*, Springer.

Ramirez, N. & Saez, A. E. (1990), 'The effect of variable viscosity on boundary-layer heat transfer in a porous medium', *International communications in heat and mass transfer* **17**(4), 477–488.

Rashidi, M., Peurrung, L., Tompson, A. & Kulp, T. (1996), 'Experimental analysis of pore-scale flow and transport in porous media', *Advances in Water Resources* **19**(3), 163–180.

Russell, H. (1935), 'Principles of heat flow in porous insulators', *Journal of the American Ceramic Society* **18**(1-12), 1–5.

Saez, A. E., Perfetti, J. & Rusinek, I. (1991), 'Prediction of effective diffusivities in porous media using spatially periodic models', *Transport in Porous Media* **6**(2), 143–157.

Saleh, S., Thovert, J. & Adler, P. (1992), 'Measurement of two-dimensional velocity fields in porous media by particle image displacement velocimetry', *Experiments in Fluids* **12**(3), 210–212.

Santiago, J. G., Wereley, S. T., Meinhart, C. D., Beebe, D. & Adrian, R. J. (1998), 'A particle image velocimetry system for microfluidics', *Experiments in fluids* **25**(4), 316–319.

Şara, O., Yapıcı, S., Yılmaz, M. & Pekdemir, T. (2001), 'Second law analysis of rectangular channels with square pin-fins', *International Communications in Heat and Mass Transfer* **28**(5), 617–630.

Scala, F. (2013), *Fluidized bed technologies for near-zero emission combustion and gasification*, Elsevier.

Sederman, A., Johns, M., Bramley, A., Alexander, P. & Gladden, L. (1997), 'Magnetic resonance imaging of liquid flow and pore structure within packed beds', *Chemical Engineering Science* **52**(14), 2239–2250.

Sedghi-Asl, M., Rahimi, H. & Salehi, R. (2014), 'Non-darcy flow of water through a packed column test', *Transport in porous media* **101**(2), 215–227.

Sen, D., Nobes, D. S. & Mitra, S. K. (2012), 'Optical measurement of pore scale velocity field inside microporous media', *Microfluidics and nanofluidics* **12**(1-4), 189–200.

Seta, T., Takegoshi, E. & Okui, K. (2006), 'Lattice boltzmann simulation of natural convection in porous media', *Mathematics and Computers in Simulation* **72**(2-6), 195–200.

Shapovalov, V. (2007), Prospective applications of gas-eutectic porous materials (gasars) in usa, *in* 'Materials science forum', Vol. 539, Trans Tech Publ, pp. 1183–1187.

Shapovalov, V. & Withers, J. (2008), Hydrogen technology for porous metals (gasars) production, *in* 'Carbon nanomaterials in clean energy hydrogen systems', Springer, pp. 29–51.

Skochdopole, R. (1961), 'The thermal conductivity of foamed plastics', *Chem. Eng. Prog* **57**(10), 55–59.

Solórzano, E., Reglero, J., Rodríguez-Pérez, M., Lehmhus, D., Wichmann, M. & De Saja, J. (2008), 'An experimental study on the thermal conductivity of aluminium foams by using the transient plane source method', *International journal of heat and mass transfer* **51**(25-26), 6259–6267.

Soni, J., Islam, N. & Basak, P. (1978), 'An experimental evaluation of non-darcian flow in porous media', *Journal of Hydrology* **38**(3-4), 231–241.

Speed, S. E. (1976), 'Foaming of metal by the catalyzed and controlled decomposition of zirconium hydride and titanium hydride'. US Patent 3,981,720.

Surace, R., De Filippis, L., Niini, E., Ludovico, A. & Orkas, J. (2009), 'Morphological investigation of foamed aluminum parts produced by melt gas injection', *Advances in Materials Science and Engineering* **2009**.

Sutherland, J. P., Vassilatos, G., Kubota, H. & Osberg, G. L. (1963), 'The effect of packing on a fluidized bed', *AIChE Journal* **9**(4), 437–441.

Swartzendruber, D. (1962), 'Non-darcy flow behavior in liquid-saturated porous media', *Journal of Geophysical Research* **67**(13), 5205–5213.

Thewsey, D. & Zhao, Y. (2008), 'Thermal conductivity of porous copper manufactured by the lost carbonate sintering process', *physica status solidi (a)* **205**(5), 1126–1131.

Upadhyaya, G. S. (1997), *Powder metallurgy technology*, Cambridge Int Science Publishing.

Vafai, K. & Tien, C. (1981), 'Boundary and inertia effects on flow and heat transfer in porous media', *International Journal of Heat and Mass Transfer* **24**(2), 195–203.

Vafai, K. & Tien, H. (1989), 'A numerical investigation of phase change effects in porous materials', *International journal of heat and mass transfer* **32**(7), 1261–1277.

Valenzuela, J. & Glicksman, L. (1983), Thermal resistance and aging of rigid urethane foam insulation, *in* 'Thermal Insulation, Materials, and Systems for Energy Conservation in the'80s', ASTM International.

Wadley, H. N. (2002), 'Cellular metals manufacturing', *Advanced Engineering Materials* **4**(10), 726–733.

Wakao, N. & Funazkri, T. (1978), 'Effect of fluid dispersion coefficients on particle-to-fluid mass transfer coefficients in packed beds: correlation of sherwood numbers', *Chemical Engineering Science* **33**(10), 1375–1384.

Ward, J. (1964), 'Turbulent flow in porous media', *Journal of the Hydraulics Division* **90**(5), 1–12.

Xiao, Z. & Zhao, Y. (2013), 'Heat transfer coefficient of porous copper with homogeneous and hybrid structures in active cooling', *Journal of Materials Research* **28**(17), 2545–2553.

Yarlagadda, A. & Yoganathan, A. (1989), 'Experimental studies of model porous media fluid dynamics', *Experiments in Fluids* **8**(1-2), 59–71.

Yi, R., Shi, R., Gao, G., Zhang, N., Cui, X., He, Y. & Liu, X. (2009), 'Hollow metallic microspheres: fabrication and characterization', *The Journal of Physical Chemistry C* **113**(4), 1222–1226.

Zerai, B., Saylor, B. Z., Kadambi, J. R., Oliver, M. J., Mazaheri, A. R., Ahmadi, G., Bromhal, G. S. & Smith, D. H. (2005), 'Flow characterization through a network cell using particle image velocimetry', *Transport in porous media* **60**(2), 159–181.

Zhang, L., Mullen, D., Lynn, K. & Zhao, Y. (2009), 'Heat transfer performance of porous copper fabricated by lost carbonate sintering process', *MRS Online Proceedings Library Archive* **1188**.

Zhao, C., Lu, T. & Hodson, H. (2004), 'Thermal radiation in ultralight metal foams with open cells', *International Journal of Heat and Mass Transfer* **47**(14-16), 2927–2939.

Zhao, C., Lu, T. & Hodson, H. (2005), 'Natural convection in metal foams with open cells', *International Journal of Heat and Mass Transfer* **48**(12), 2452–2463.

Zhao, C., Lu, T., Hodson, H. & Jackson, J. (2004), 'The temperature dependence of

effective thermal conductivity of open-celled steel alloy foams', *Materials Science and Engineering: A* **367**(1-2), 123–131.

Zhao, Y., Fung, T., Zhang, L. & Zhang, F. (2005), 'Lost carbonate sintering process for manufacturing metal foams', *Scripta Materialia* **52**(4), 295–298.

Zhao, Y. & Sun, D. (2001), 'A novel sintering-dissolution process for manufacturing al foams', *Scripta materialia* **44**(1), 105–110.